THE UNIVERSITY OF HULL

Establishing a Novel 3-Dimensional Microfluidic Model of Bunyavirus Infection to Characterise Exosome Release from Tumour Cells

being a Thesis submitted for the Degree of Masters by Research in Biomedical Sciences at the University of Hull

By

Danielle Marsh

BSc (Hons) Biomedical Science

October 2022

Acknowledgements

First and foremost, I would like to thank my primary supervisor Professor John Greenman for his expertise, guidance, and support throughout this project. I would also like to express my gratitude to my secondary supervisor, Dr. Cheryl Walter, for her knowledge, patience, and for her time and expertise in teaching me the virology techniques required for this work. Thank-you for being a fantastic supervisory team. I would also like to thank Dr. Victoria Green for sharing her expertise, and for providing the technical training for the methods used to characterise exosomes in this study.

Thank-you to all the PGR students and staff in the Allam 305 and Hardy 131 laboratories, for providing technical training, offering your support, and for contributing to a positive working environment.

Finally, I would like to thank my good friend Hannah Beattie, and partner Chris Sennett, for keeping my spirits high with their unwavering support and reassurance throughout my research.

Abstract

The order *Bunyavirales* represents the largest and most diverse taxonomic grouping of negative-sense RNA viruses, some of which are associated with significant diseases in humans and livestock. The global emergence of these viruses is exacerbated by the lack of any effective therapeutic strategies or licenced vaccines. The major paucity of anti-Bunyaviral drugs and vaccinations, as is the case with many other clinically significant viruses, can partially be attributed to the inability of 2D cell culture systems to recapitulate faithfully the intricacies and complexity of the microenvironment encountered by pathogens in native tissues. This leads to extremely high rates of failure in clinical trials with human subjects.

This study establishes a novel, and physiologically relevant, 3D microfluidic model of *Bunyamwera orthobunyavirus* (BUNV) infection. This model is utilised to investigate the potential involvement of cellular secretory trafficking and exosomes in the poorly understood pathways of Bunyaviral egress. An optimised method of sucrose cushion ultracentrifugation was used to isolate viral particles and exosomes, this was followed by nanoparticle tracking analysis and western blot analysis of the exosome-associated tetraspanins CD63 and CD81. MTS and LDH assays, live/dead cell staining by fluorescence microscopy, and viral plaque assays, identified significant differences in the effects of BUNV infection on cellular metabolism, cell viability and death, and viral kinetics in 2D versus 3D culture models of human tumour cells (HuH-7; hepatocellular carcinoma and A549; lung adenocarcinoma).

BUNV was able to complete a full replication cycle in A549 and HuH-7 spheroids under a flow rate of 2µL/min, for an incubation period of up to 120 hours, as evidenced by infectious viral titres in microfluidic effluent. It was not possible to generate stocks of U87-adapted WT-BUNV, hence, this cell line was not used in the microfluidic model. Significant differences in the metabolic activity of BUNV-infected A549 and HuH-7 cells were found between the 2D and 3D (static) models, with the former showing a greater effect. Although not statistically significant, the data implied that HuH-7 cells secrete CD63 enriched exosomes in response to BUNV infection. Moreover, the metabolic activity of HuH-7 and A549 cells was not affected by BUNV infection in the static 3D model; contrasting with fluorescence microscopy images which illustrated a picture of BUNV-induced cell death. These apparently contradictory results could be explained by the phenomenon of virus-induced mitochondrial-mediated apoptosis.

Future studies which elucidate the nature of the exosomes secreted from BUNV-infected HuH-7 cells, and the intracellular processes which drive their production, will contribute immensely to our understanding of the poorly characterised aspects of the Bunyaviral replication cycle.

List of Abbreviations

Alix	ALG-2-interacting protein
AKAV	Akabane virus
ANDV	Andes virus
ATCC	American Type Culture Collection
Baf A1	Bafilomycin A1
BCA	Bicinchoninic acid
BFA	Brefeldin A
BSA	Bovine serum albumin
BUNV	Bunyamwera virus
CAD	Computer-aided design
CCD	Charge-coupled device
CCHFV	Crimean-Congo Haemorrhagic Fever virus
CEV	California encephalitis virus
CHMP6	Charged multivesicular body protein-6
CL3	Containment level 3
CME	Clathrin-mediated endocytosis
CPE	Cytopathic effect
CPZ	Chloropromazine
CTD	C-terminal domain
DI	Defective interfering (particles)
DMEM	Dulbecco's modified Eagle's medium
DMSO	Dimethyl sulfoxide
DN	Dominant negative
DYN	Dynasore
ECACC	European Collection of Authenticated Cell Cultures
ECL	Enhanced chemiluminescent
ECM	Extracellular matrix
EE	Early endosome
eIF2a	Eukaryotic translation initiation factor 2A
EL	Endolysosome
Endo-H	Endo-β-N-acetylglucosaminidase
ER	Endoplasmic reticulum
ESCRT	Endosomal sorting complexes required for transport
EV	Extracellular vesicle
FBS	Foetal bovine serum
FDA	Fluorescein diacetate
GERV	Germiston virus
HAV	Hepatitis A virus
HBV	Hepatitis B virus
HCMV	Human cytomegalovirus
HCV	Hepatitis C virus
HEV	Hepatitis E virus

HHV-6	Human herpesvirus 6
HIV	Human immunodeficiency virus
HPV	Human papillomavirus
HRP	Horseradish peroxidase
HSPG	Heparan sulfate proteoglycan
HSV	Herpes simplex virus
HTN	Hantaan virus
IAV	Influenza A virus
IFN-β	Interferon-β
IGR	Intergenic regions
ILV	Intraluminal vesicle
INT	Iodonitrotetrazolium chloride
IRF 3	Interferon regulatory factor 3
ISG	Interferon-stimulated gene
LACV	La Crosse virus
LBPA	Lysobiphosphatidic acid
LDH	Lactate dehydrogenase
LE	Late endosome
MCS	Multicellular spheroid
Mda5	Melanoma differentiation-associated protein 5
Mf-IAC	Microfluidic-based immunoaffinity capture
MGM	Megalomycin
MLS	Multilamellar structure
MOI	Multiplicity of infection
MVB	Multivesicular body
MβC	Methyl-β-cyclodextrin
NanoFACS	Nano flow-assisted cell sorting
NF-κB	Nuclear factor-κB
NSm	Non-structural protein, medium gene segment
NSs	Non-structural protein, small gene segment
NTA	Nanoparticle tracking analysis
NTR	Non-translated region
NY-1	New York-1 virus
ORF	Open reading frame
OROV	Oropouche virus
PAMP	Pathogen-associated molecular pattern
PARP	Poly (ADP-ribose) polymerase
PBS	Phosphate buffered saline
PFY	Plaque forming unit
PI	Propidium iodide
PKR	Protein kinase R
PM	Plasma membrane
PMMA	Polymethyl methacrylate
PPF	Particles per frame
PRR	Pattern recognition receptor
PUU	Puumala virus

PVDF	Polyvinylidene difluoride
RER	Rough endoplasmic reticulum
RIG-I	Retinoic acid-inducible gene I
RNAP-II	RNA polymerase II
RNP	Ribonucleoprotein
RSV	Respiratory syncytial virus
RVFV	Rift Valley Fever virus
RWV	Rotating wall vessle
SAP30	Sin3A-associated protein
SARS-CoV-2	Severe acute respiratory syndrome coronavirus 2
SBV	Schmallenberg virus
SDS-PAGE	Sodium dodecyl sulphate polyacrylamide gel electrophoresis
SEO	Seoul virus
SeV	Sendai virus
SFTSV	Severe fever with thrombocytopenia syndrome virus
SNARE	Soluble N-ethylmaleimide-sensitive factor attachment protein receptors
SNV	Sin Nombre virus
ssRNA	Single-stranded RNA
STR	Short tandem repeat
TEA	Tetraethylammonium
TEM	Transmission electron microscopy
TFIIH	Transcription factor II H
TGN	*Trans*-Golgi network
TOSV	Toscana virus
Tsg101	Tumour susceptibility gene 101
ULA	Ultra-low attachment
UUKV	Uukuniemi virus
Vf	Viral factory
Vps4	Vacuolar protein sorting-associated protein 4
WT	Wild type

Table of Contents

List of Figures

List of Tables

List of Equations

Chapter 1: Introduction

1.1 Bunyaviruses

1.1.1 Bunyavirus Classification

Historically, the genus *Orthobunyavirus* was classified under the family *Bunyaviridae,* together with four other genera, *Hantavirus*, *Nairovirus*, *Phlebovirus,* and *Tospovirus*. However, in 2016, the taxonomy was reconsidered by the International Committee on Taxonomy of Viruses which introduced a new order; *Bunyavirales*. This reconsideration was necessary to accommodate the discovery of many novel unclassified, serologically related viruses, owing to recent advances in genome sequencing technologies (Blitvich et al., 2018). The implementation of these taxonomic changes saw the replacement of *Bunyaviridae* with nine new families (Adams et al., 2017). As of May 2019, the order comprises thirteen families (Abudurexiti et al., 2019). In the current taxonomy, the *Orthobunyavirus* genus is classified under the family *Peribunyaviridae*. The *Peribunyaviridae* represent a wide range of enveloped, negative-sense RNA viruses, which possess three distinct genome segments (see section 1.1.3) comprising 11.2-12.5 kb in total (Hughes et al., 2020). The prototype member of the *Orthobunyavirus* genus is Bunyamwera virus (BUNV), formally known as a member of the species *Bunyamwera orthobunyavirus*. Extensive studies using BUNV as a model Bunyavirus have contributed immensely to our understanding of the *Bunyavirales*, since many of the BUNV molecular and cellular characteristics are shared with related pathogens (Barr & Wertz, 2004), including those implicated with serious human diseases (Table 1.1).

1.1.2 Epidemiology & Pathophysiology

The *Bunyavirales* order represents the largest and most diverse taxonomic grouping of negative-sense RNA viruses. These viruses are distributed globally; their incidence is determined by the geographical distributions of the various vectors and vertebrate hosts. All members of the *Bunyavirales* order (except for Hantaviruses and Arenaviruses) are arboviruses i.e., they replicate in, and are transmitted by, haematophagous arthropod vectors such as mosquitoes, ticks, and sandflies. Bunyaviruses infect a variety of plants, protozoans, insects, and animals. Multiple Bunyaviruses are associated with serious diseases in both

livestock and humans, thus posing a potential threat to public health, animal welfare, and food security (Elliott, 2009). There are numerous human pathogens of clinical significance in the *Peribunyaviridae*, *Hantaviridae*, *Nairoviridae*, and *Phenuiviridae* families (Table 1.1). Some clinically noteworthy Bunyaviruses are associated with high morbidity and mortality. Moreover, the global threat posed by the emergence of these viruses is exacerbated by the lack of preventative treatments such as licensed vaccines, in addition to limited therapeutic options (Walter & Barr, 2011). Two inactivated Hantavirus vaccines have been licensed for human use in China and Korea, targeting the Hantaan and Seoul viruses, but these failed to induce a long-lasting response in phase III and IV clinical trials (Song et al., 2016). There are currently two RVFV vaccines, classified as 'investigational new drugs' in the USA; MP-12 and TSI-GSD-200 (Ikegami et al., 2015; Wright et al., 2019). Although MP-12 has been conditionally licenced for animal vaccination, there is currently no RVFV vaccine approved for human use.

Table 1.1. Notable members of the Bunyavirales associated with significant diseases in humans.

Family	Genus	Notable Virus Members	Vector	Geographic Location	Associated Disease	Clinical Manifestations	References
Peribunyaviridae	*Orthobunyavirus*	La Crosse virus (LACV)	Mosquitos (*Aedes spp.*)	North America	La Crosse encephalitis and aseptic meningitis	Fever, nausea, fatigue, seizures, **death (<1% of cases)**	(Thompson et al., 1965; Tatum et al., 1999)
		Jamestown Canyon virus	Mosquitos (*Aedes Coquillettidia*, *Culex*, and *Culiseta spp.*)	North America	Jamestown Canyon meningoencephalitis	Fever, fatigue, headache, respiratory symptoms, confusion, loss of coordination, seizures, **death (<1% of cases)**	(Pastula et al., 2015)
Hantaviridae	*Hantavirus*	Hantaan virus, Dobrava virus, Seoul virus (SEO)	Rodents (field mice)	Asia, Europe	Haemorrhagic fever with renal syndrome (HFRS)	Fever, fatigue, myalgia, uncontrolled bleeding, acute kidney failure, **death (5-15% of cases)**	(CDC; Lee et al., 1978)
		Sin Nombre virus (SNV), New York, and Black Creek Canal	Rodents (deer mice)	Americas	Hantavirus pulmonary syndrome (HPS)	Fever, headaches, myalgia, malaise, cough, shortness of breath, pulmonary oedema, **death (50% of cases)**	(CDC; Nichol et al., 1993; Morzunov et al., 1995)
Nairoviridae	*Nairovirus*	Crimean-Congo Haemorrhagic Fever virus (CCHFV)	Ixodid ticks (primarily *Hyalomma Spp.*), culicoid flies	Asia, Africa, Europe	Crimean-Congo haemorrhagic fever (CCHF)	High fever, headache, joint pain, back pain, red eyes and throat, petechiae on the palate, jaundice, uncontrolled bleeding, **death (10-50% of cases)**	(CDC; Hoogstraal, 1979)
Phenuiviridae	*Phlebovirus*	Rift Valley Fever virus (RVFV)	Mosquitoes (*Aedes Spp.* and *Culex Spp.*)	Africa	Rift valley fever (RVF)	Mild fever, malaise, ocular disease (8-10% cases), encephalitis (<1% cases), haemorrhagic fever (<1% of cases), **death (~10% of cases)**	(WHO; R. Daubney, 1931)

	Severe fever with thrombocytopenia syndrome virus (SFTSV)	Ticks (*Haemaphysalis spp.*), human-human transmission through contact with bodily fluids	East Asia	Severe fever with thrombocytopenia syndrome (SFTS)	High fever, gastrointestinal symptoms, thrombocytopenia, leukopenia, haemorrhagic tendency, lethargy, muscular tremors, convulsions, **death (6-27% of cases)**	(Jiang et al., 2015; Kim et al., 2015; Casel et al., 2021)

Adapted from Soldan and González-Scarano, 2005.

Due to the segmented nature of the Bunyavirus genome (see section 1.1.3), these viruses possess an important evolutionary mechanism for viral persistence; reassortment. Shuffling of gene segments between different viral species generates progeny viruses with novel genome combinations and altered pathogenicity. Bunyaviruses have increased incidence in new and widespread geographical locations due to their capacity for genetic reassortment, in concert with current global events (i.e., climate change, population growth, agricultural expansion, and increased global transportation, (Soldan & González-Scarano, 2005)). As such, Bunyaviruses are considered emerging pathogens with the potential to become the next pandemic perpetrators. To highlight this, in 2011, a novel *Orthobunyavirus* (Schmallenberg virus, SBV) emerged and spread rapidly throughout western Europe (Hoffmann et al., 2012). It was determined that SBV was the culprit in an emerging epizootic associated with previously undescribed congenital defects in sheep and cattle (Lievaart-Peterson et al., 2012; Afonso et al., 2014; Peperkamp et al., 2014). Studies on the demographical and epidemiological data suggest that dispersal of the vector (*Culicoides*) is the principal culprit in the spread of SBV (Sedda & Rogers, 2013; Gubbins et al., 2014). As for all vector-borne diseases, climate and human behaviour are major determinants for the geographical range and survival of vectors, and ultimately, the viruses to which these vectors are susceptible. There has been great concern raised over the emergence of Crimean-Congo Haemorrhagic Fever virus (CCHFV) in several Balkan countries, likely a result of climate changes which favour the survival and reproduction of *Hyalomma* ticks (Maltezou & Papa, 2010). Phylogenetic evidence suggests that certain CCHFV lineages have moved over long distances, potentially owing to the trade of livestock and other anthropogenic factors (Deyde et al., 2006).

1.1.3 *Orthobunyavirus* Structure & Molecular Biology

The *Orthobunyavirus* virion is a small (80-120nm), spherical particle with a lipid bi-layer envelope that encapsulates a tri-segmented genome of single-stranded RNA (ssRNA), with negative polarity (Figure 1.1). The *Orthobunyavirus* genome segments are named with respect to their relative nucleotide length; small (S), medium (M), and large (L). Each segment is encapsidated in the viral nucleocapsid (N) protein to form circular ribonucleoprotein (RNP) complexes, which associate with the L protein (viral RNA-dependent RNA polymerase, RdRp). The lipid envelope, derived from the host cell Golgi complex (see section 1.1.4), is modified

by the insertion of the viral glycoproteins; Gn and Gc. Bowden et al. (2013) utilised electron cryo-tomography and sub-tomogram averaging to reveal the BUNV specific glycoprotein spike array. BUNV spikes protrude 18nm from the membrane surface and comprise trimers of Gn-Gc disulphide-linked heterodimers to form a unique tripodal arrangement.

The overall lengths and organisations of each genome segment are similar across the *Orthobunyavirus*, *Hantavirus*, *Nairovirus*, *Phlebovirus,* and *Tospovirus* genera (Walter & Barr, 2011). Each segment of ssRNA contains a coding region, flanked by non-translated regions (NTRs) at the 3' and 5' termini. Studies have found that the nucleotide sequences within these terminal NTRs are highly conserved, genus-specific, and complementary; allowing for the formation of a 'panhandle' structure that plays a pivotal role in RNA synthesis (see section 1.1.4; (Barr et al., 2003; Barr & Wertz, 2004; Kohl et al., 2004).

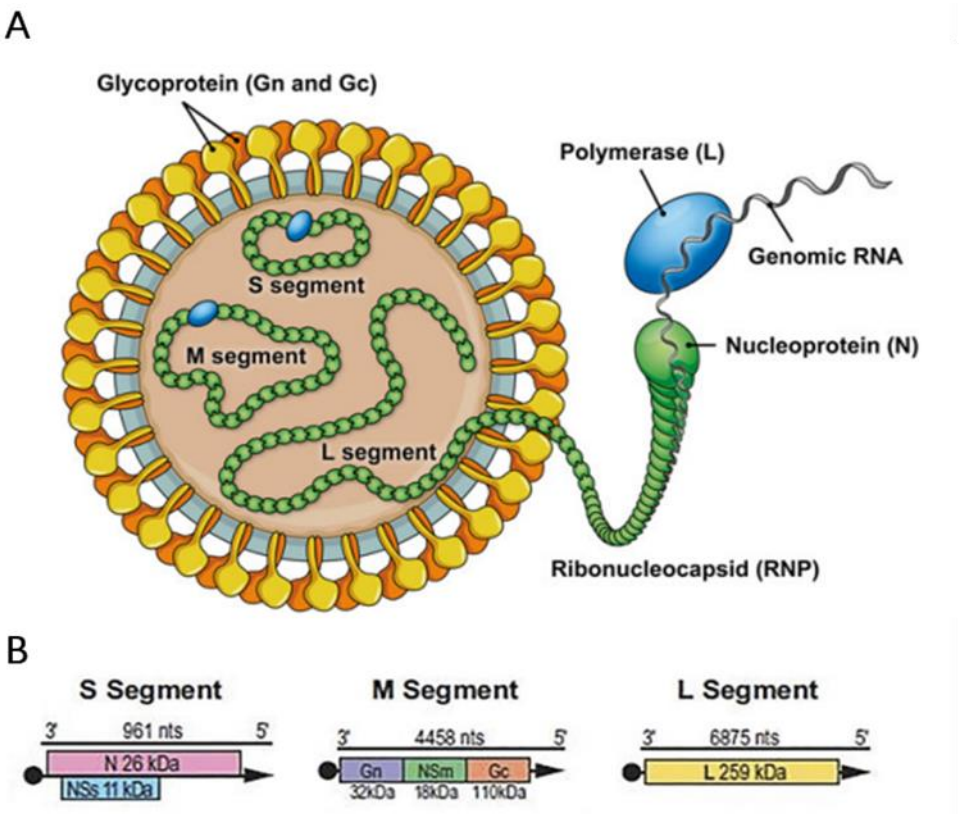

Figure 1.1. A schematic representation of a generic Orthobunyavirus virion with the genome organisation of the prototypic Orthobunyavirus- BUNV. Adapted from ViralZone (Philippe Le Mercier, 2022) and ICTV 2016. (A) *Orthobunyavirus virions are spherical and comprise three negative-sense RNA segments (S, M, and L), encapsidated in viral N protein to form RNP complexes.* ***(B)*** *BUNV-specific genomic RNAs are shown with total nucleotide length above each of the segments. The primary role of the N protein (encoded by the S segment) is to encapsidate the viral RNA-replication products to form RNPs which serve as the template for the viral RdRp (L protein, encoded by the L segment). Like other members of the Orthobunyavirus genus, the BUNV S segment also encodes a non-structural protein (NSs), which participates in the evasion of innate immunity. The M segment of BUNV, as with all other Bunyaviruses encodes a polyprotein precursor, which is proteolytically cleaved by host-cell proteases to generate the Gn and Gc glycoproteins, as well as the non-structural protein NSm- which is thought to play a role in virus assembly (Shi et al., 2006). Arrows represent virion complementary sense RNA.*

1.1.4 Viral Replication

i) Attachment

The initial contact between the viral particle and host cell (viral attachment) involves specific and multivalent interactions between the viral glycoproteins (Gn and Gc) and host cell attachment factors or cell surface receptors (Albornoz et al., 2016). Details of the host cell surface receptor (or receptors), cellular factors, and pathways which mediate Bunyavirus attachment remain poorly characterised and largely uncovered. Table 1.2 details some of the potential receptors/co-factors exploited by Bunyaviruses.

Table 1.2. Some of the documented receptors/co-factors involved in Bunyavirus cell entry.

Genus	Virus Member	Receptor/Co-factor	References
Phlebovirus	SFTSV, RVFV, UUKV	DC-SIGN	(Lozach et al., 2011; Hoffmann et al., 2012; Suda et al., 2016)
Nairovirus	CCHFV		
Orthobunyavirus	LACV	DC-SIGN, Mincle Dectin-1, Dectin-2	(Windhaber et al., 2021)
Phlebovirus	RVFV	HSPG	(de Boer et al., 2012; Murakami et al., 2017)
Orthobunyavirus	SBV, AKAV		
Hantavirus	SNV, NY-1, HTN, SEO, PUU	β3 integrins	(Gavrilovskaya et al., 1998; Gavrilovskaya et al., 1999)

Adapted from Albornoz et al., 2016. DC-SIGN: Dendritic Cell-Specific Intercellular adhesion molecule-3-Grabbing Non-integrin; HSPG: Heparan sulfate proteoglycan; SFTSV: Severe fever with thrombocytopenia syndrome virus; RVFV: Rift Valley fever virus; UUKV: Uukuniemi virus; CCHFV: Crimean-Congo haemorrhagic fever virus; LACV: La Crosse virus; SBV: Schmallenberg virus; AKAV: Akabane virus; SNV: Sin Nombre virus; NY-1: New York-1 virus; HTN: Hantaan virus; SEO: Seoul virus; PUU: Puumala virus.

ii) Penetration

To establish infection, viruses must first gain access to the intracellular environment of the host cell. There are two main strategies by which viruses may achieve entry into the cell: i) receptor-mediated endocytosis, and ii) direct fusion (or endocytosis-independent receptor-mediated entry; Figure 1.2).

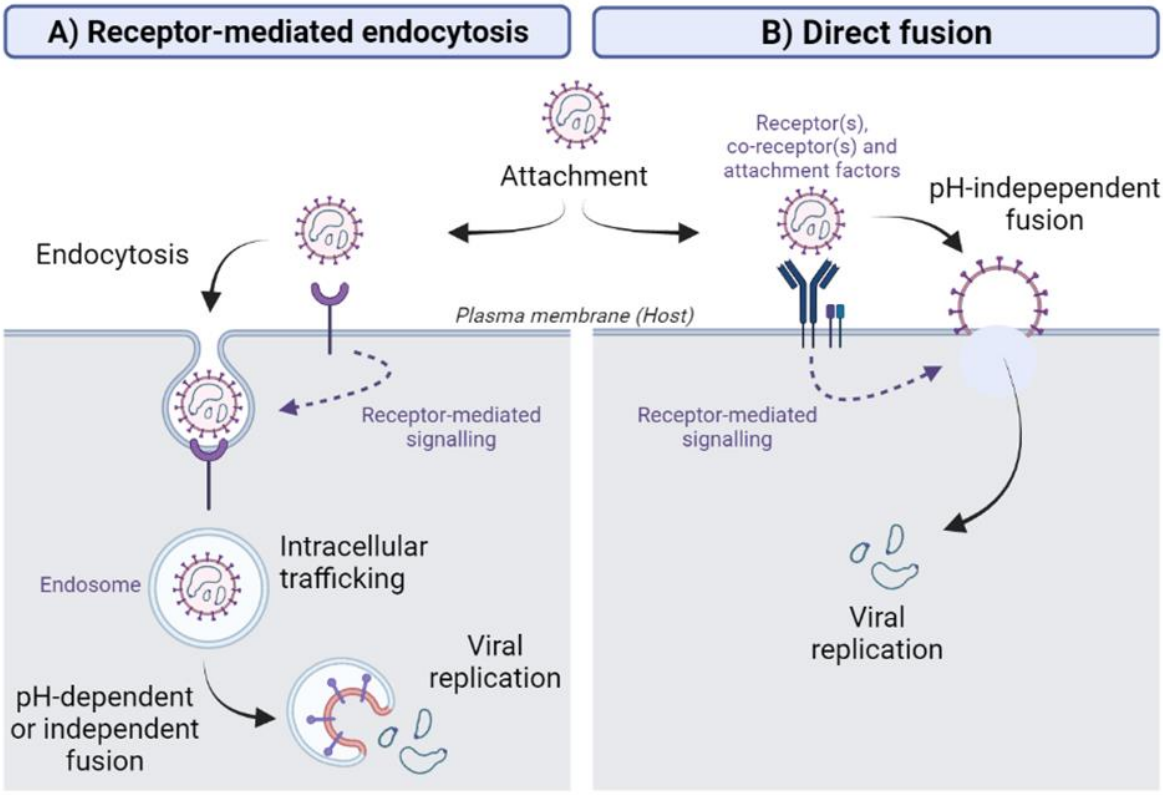

Figure 1.2. Viral entry strategies. Adapted from Boulant et al., 2015, created on Biorender.com. A) *Receptor-mediated endocytosis: viruses exploit host cell endocytic machinery to enter the cell e.g., clathrin-mediated endocytosis employed by members of the Orthobunyavirus, Nairovirus, and Hantavirus genera (Lozach et al., 2010b).* ***B)*** *Direct fusion (or endocytosis-independent receptor-mediated entry): binding to the host cell receptor(s) triggers the viral particle to directly penetrate the plasma membrane. Direct fusion at the plasma membrane is triggered by virus-receptor interaction at a neutral pH, e.g., HIV-1 binding with the CD4 receptor and a co-receptor such as CCR5 or CXCR4 (Kielian & Rey, 2006). This figure is a generalisation depicting enveloped viruses.*

For Bunyaviruses, it is apparent that the physical uptake of particles is reliant on the manipulation of the host-cell endocytic machinery. However, the specific mechanisms which enable the transition between the extracellular and intercellular stage remain poorly understood. Lozach et al., 2010 found that UUKV internalisation is mainly clathrin-independent, however, in rare cases, UUKV particles were observed to associate with clathrin-coated pits and vesicles, suggesting a potential involvement of clathrin-mediated endocytosis (CME) in UUKV infection. There is growing evidence to suggest that several other members of the *Orthobunyavirus* and *Nairovirus* genera subvert CME to penetrate and infect host cells; Figure 1.3 (Santos et al., 2008; Simon et al., 2009; Hollidge et al., 2012; Garrison et al., 2013).

Further investigation is required to elucidate the transition steps between viral attachment at the host-cell surface and the internalisation of the viral particles into early endosomes (EE). The specific endocytic route mediating viral uptake is often determined by the molecular motifs in the cytosolic tails of the host-cell surface receptors to which the virus binds (Boulant et al., 2015). As discussed earlier, Bunyaviruses can utilise a diverse range of cell surface receptors, allowing infection to be established in a variety of different cell types (Table 1.2). As such, these viruses have the capacity to exploit multiple alternative endocytic pathways, which likely impacts viral pathogenicity.

iii) Intracellular Trafficking

Once the Bunyavirus particles have bypassed the host-cell membrane, they are sorted into vesicles and proceed to traffic through the host-cell endocytic machinery until reaching the endosomal compartment which provides the environmental cue(s) to trigger viral fusion and subsequent penetration into the cytosol (Figure 1.3). The process of transport from EE to late endosome (LE) is dynamic and highly complex, involving a magnitude of cellular factors (White & Whittaker, 2016), protein and lipid remodelling, and changes in H+ concentrations within the endosomal vesicles (Scott & Gruenberg, 2011).

The pH dependence of viral fusion reactions can be a major determinant of viral entry sites. For example, viruses with low pH dependencies (i.e., most influenza strains) generally fuse in late endosomes, whereas those with high pH dependencies (~pH 6.0) tend to fuse in early endosomes. Garrison et al. (2013) demonstrate that CCHFV enters cells by CME and infection requires endocytic vesicle acidification, with virus inactivation occurring at pH 6.0 and below. This study also found that CCHFV infection is dependent on the GTPase Rab5 (a key regulator of early endosome biogenesis and membrane trafficking), but not dependent on Rab7 (a regulator of late endocytic trafficking). Several further reports provide evidence to support the requirement for endosomal acidification and trafficking through EEs in the successful infection of other Bunyaviruses (Santos et al., 2008; Lozach et al., 2010b; Hofmann et al., 2013; Bangphoomi et al., 2014; Shtanko et al., 2014). However, endosomal acidification may not be the sole trigger of viral fusion; studies by Hover et al. (2018) suggest that specific cellular potassium (K+) ion concentrations play an important role in the facilitation of BUNV uncoating and RNP release into the cytosol. K+ accumulation within endosomes was found to be regulated by cellular cholesterol abundance (Charlton et al., 2019).

Whilst various data support the view that Bunyaviruses are late-penetrating viruses (i.e., they are dependent on endosomal maturation to establish infection (Lozach et al., 2011a), many of these viruses can infect cells independently of Rab7 (Santos et al., 2008; Hollidge et al., 2012; Garrison et al., 2013; Shtanko et al., 2014). However, Lozach et al. (2010a) show that UUKV enters Rab5-positive EE followed by entry into Rab7-positive and LAMP-1-positive LE. Furthermore, this study shows that acid-activated penetration occurs 20-40 minutes post-internalisation, with a pH threshold of 5.4 for viral fusion, compatible with the timescale and conditions of LE maturation (Figure 1.3). The dispensability of Rab7 in these infections could

be attributed to the escape of viral particles from EE to multivesicular bodies (MVB) during the early stages of the LE maturation process (Scott et al., 2014), as observed in CCHFV infection where viral particles penetrate from MVBs (Shtanko et al., 2014). Further evidence to support the involvement of LE maturation in Bunyavirus entry is the requirement for a functional microtubule network in CCHFV (Simon et al., 2009a) and Hantavirus infection (Ramanathan & Jonsson, 2008). LE maturation is dependent on the transport of endosomes toward the nucleus of the cell-mediated by the microtubule network (Albornoz et al., 2016).

In the ultimate step of this endocytic pathway, Bunyaviruses traverse the endosomal membrane via fusion of the viral envelope, leading to the release of viral material into the cytosol. As mentioned previously, Bunyavirus uncoating, and subsequent release of RNPs into the cytosol, occurs by acid-activated membrane fusion from late endosomes (Figure 1.3). In these models, endosomal acidification results in a conformational change in the viral glycoprotein Gc, which is predicted to contain a class II fusion domain (Garry & Garry, 2004).

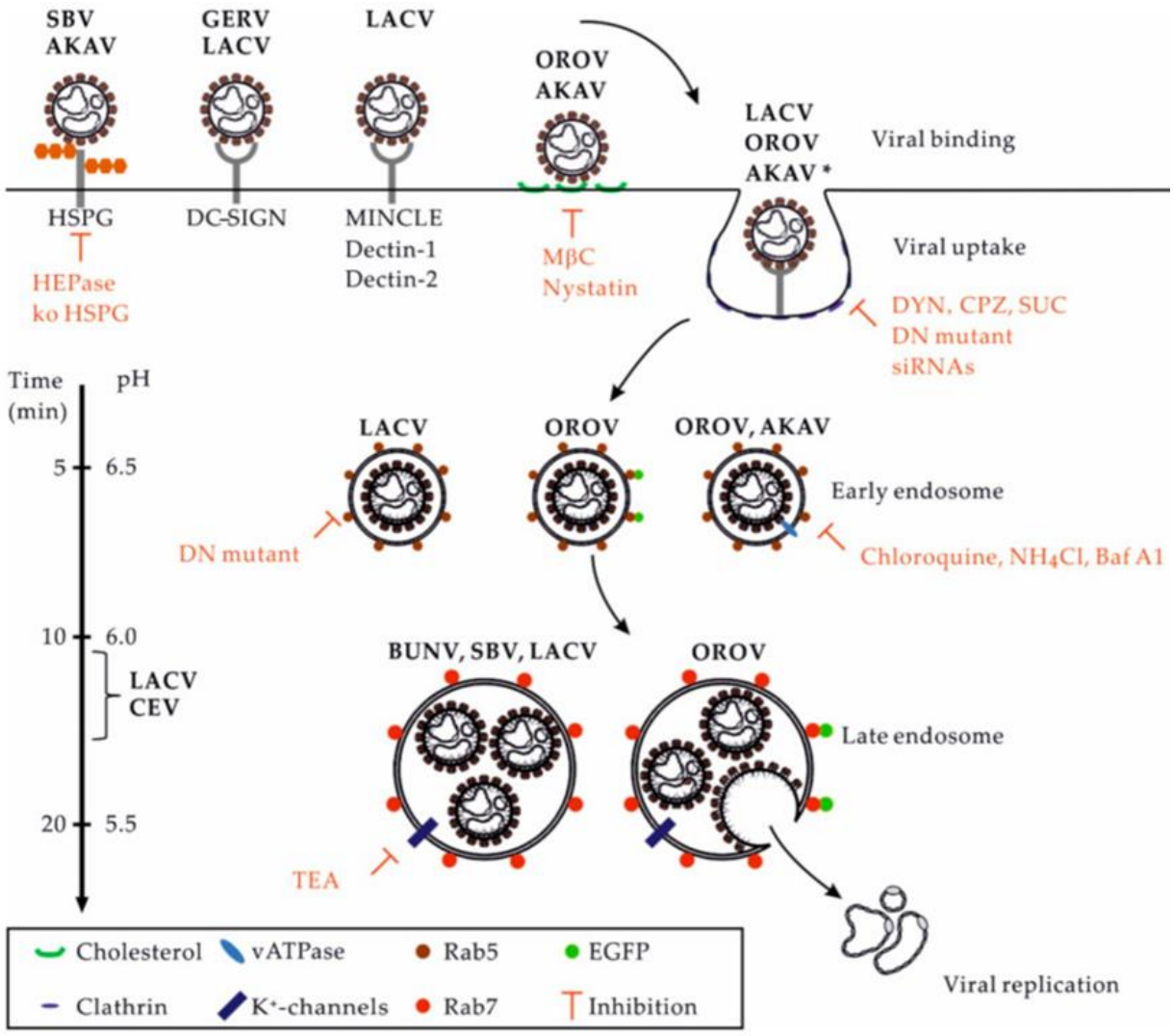

Figure 1.3. Orthobunyavirus entry into mammalian cells (Windhaber et al., 2021). *The left scale shows the time and related pH inside endosomal vesicles. SBV: Schmallenberg virus; AKAV: Akabane virus; GERV: Germiston virus; LACV: La Crosse virus; OROV: Oropouche virus; BUNV: Bunyamwera virus; CEV: California encephalitis virus. The expression of a DN (dominant negative) mutant of Rab5 blocks infection by LACV (Hollidge Bradley et al., 2012). AKAV and OROV infection are sensitive to chloroquine and ammonium chloride (NH_4Cl), which increase the endosomal pH (Santos et al., 2008), as well as H+ ATPases, such as bafilomycin A1 (Baf A1). DYN: dynasore. CPZ: chloropromazine. TEA: tetraethylammonium. MβC: methyl-β-cyclodextrin. SUC: sucrose.*

iv) Transcription and Genome Replication

Bunyaviruses comprise three genomic RNA segments with negative-sense polarity. Together, the viral genomic RNA, N protein and L protein form RNP complexes which constitute the viral transcription and replication machinery (see section 1.1.3). The N and NSs proteins are encoded by the S segment, for Orthobunyaviruses, these proteins are translated from the

same mRNA (Figure 1.4b). However, some bunyaviruses utilise an ambisense gene expression strategy to encode the non-structural proteins. The *Phlebovirus* and *Tospovirus* N and NSs proteins are translated from separate mRNA (Figure 1.4c).

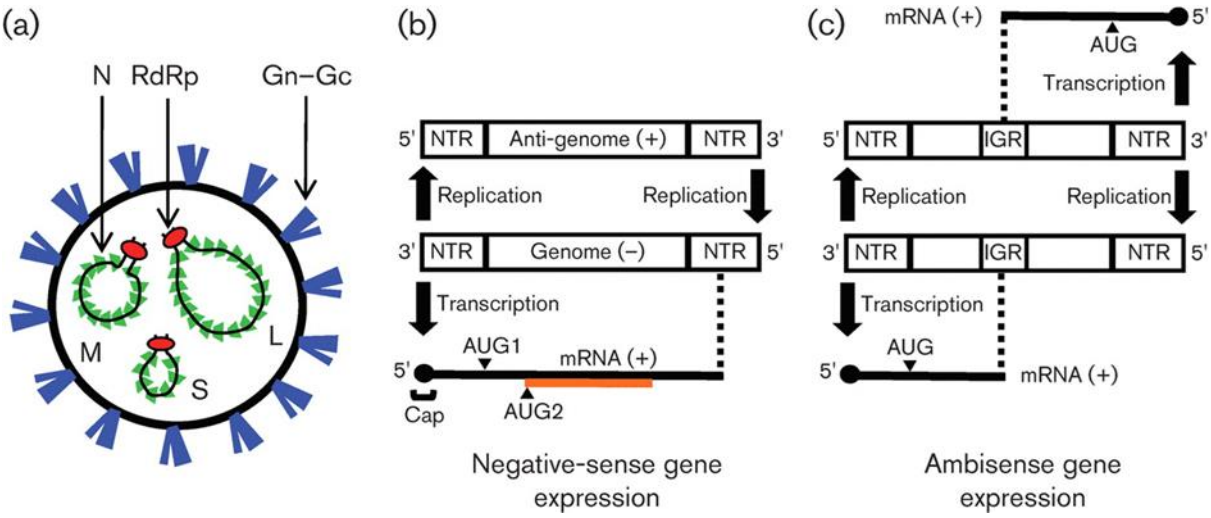

Figure 1.4. A schematic representation of a generic Bunyavirus virion with the transcription and replication strategies of Bunyavirus genome segments (Walter & Barr, 2011). (a) *Bunyavirus virions are spherical particles comprising three RNA segments (S, M and L), each encapsidated in the viral nucleocapsid (N) protein to form circular ribonucleoprotein (RNP) complexes which associate with the L protein (viral RNA-dependent RNA polymerase, RdRp). The viral envelope is decorated with genus-specific spike arrays of Gn-Gc heterodimers.* ***(b)*** *Negative-sense gene expression strategy: vRNA contains a single transcriptional unit flanked by terminal NTRs. This is replicated to generate the transcriptionally silent positive sense antigenome (cRNA), which serves as the template for the synthesis of new generation vRNA. In the S segment, the transcriptional unit may contain overlapping open reading frames (ORFs) which are accessed by alternative initiation codons.* ***(c)*** *Ambisense gene expression strategy: mRNAs are transcribed from cRNA strands as well as vRNA strands. Intergenic regions (IGR) contain transcription termination signals.*

The nucleotide sequences within the NTRs that flank the 3' and 5' termini of each viral genomic RNA (vRNA) segment are responsible for the direction of two RNA synthesis events: i) mRNA transcription and ii) RNA replication. The terminal NTRs for each respective segment (S, M, and L) exhibit highly conserved and complementary sequences (Barr & Wertz, 2004). Barr & Wertz, 2004, demonstrate that inter-terminal complementarity is a requirement for replication and RNA synthesis for the *Orthobunyavirus* BUNV. In this study, optimal replication was achieved by exact complementarity between the 3' and 5' NTRs (Barr & Wertz, 2004). This base-pairing allows for the formation of a 'pan-handle' structure which functions as the promoter of both transcription and replication, as well as circularisation of the genome fragments that most likely acts as protection against innate immune signalling molecules and aids in encapsidation into new virions (Figure 1.5) (Barr & Wertz, 2004; Kohl et al., 2004). Furthermore, conserved, segment-specific nucleotide sequences within the terminal NTRs have been shown to play a pivotal role in determining promoter strength (Flick et al., 2002; Kohl et al., 2004).

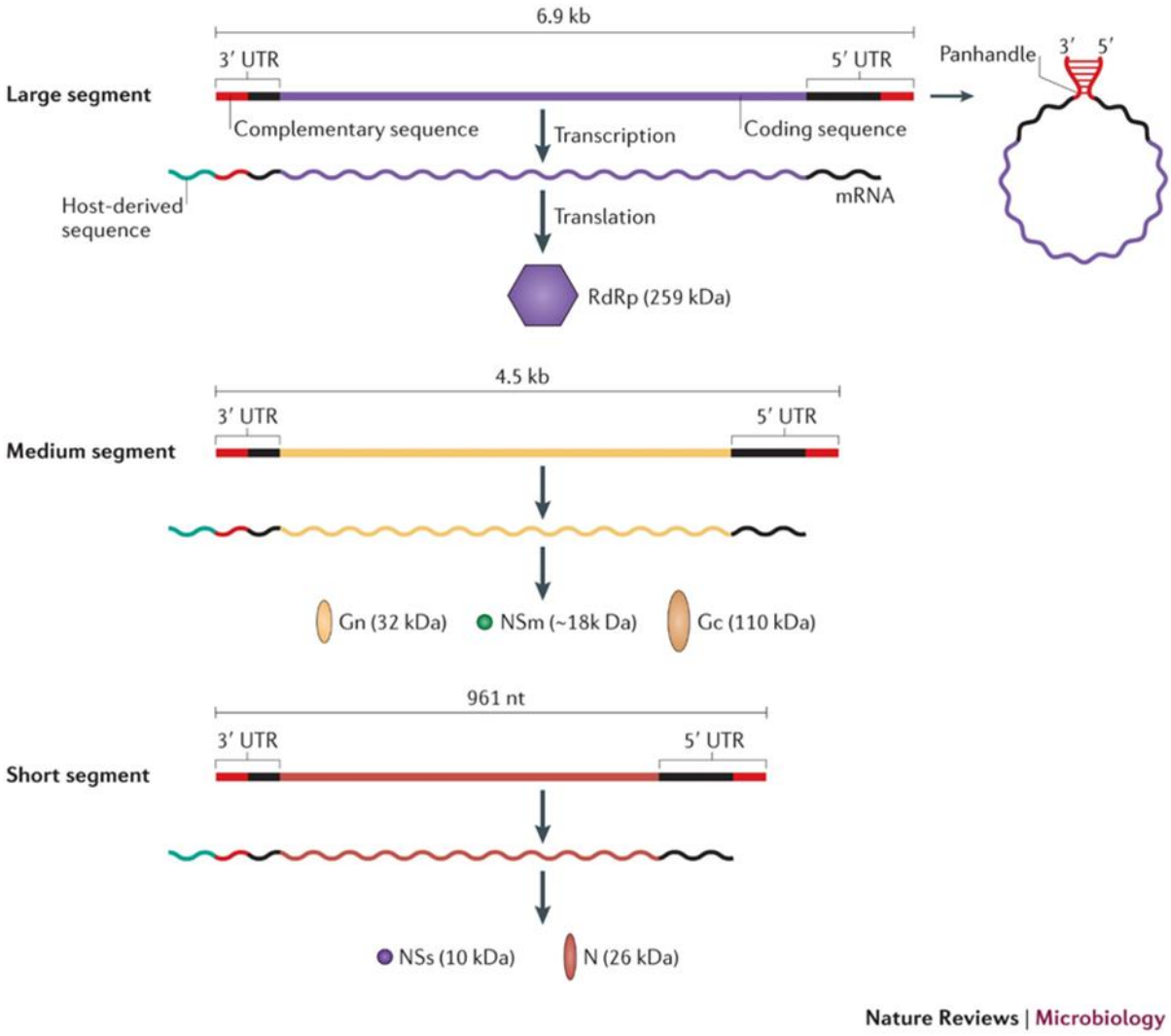

Figure 1.5. Coding strategy of the prototypic Orthobunyavirus- BUNV (Elliott, 2014). *Small (S), medium (M) and large (L) genomic RNA segments are shown with the corresponding nucleotide length above each segment and protein products (with estimated molecular weight) below each segment. Genomic RNAs are transcribed into mRNA (waved lines) with host-derived sequences (green) at the 5′ end obtained via cap-snatching, and 3′ truncations. Complementary 3′ and 5′ terminal sequences (red) result in base-pairing forming a pan-handle structure (top-right), used as a promoter for transcription and replication.*

Primary transcription is the first event to occur after the release of RNPs into the cytosol. The vRNA is transcribed into positive-sense mRNA, catalysed by the viral RdRp (L protein) associated with the RNPs. Initiation of transcription is achieved through a mechanism called 'cap-snatching'; whereby 5'-capped RNA fragments (12-18 nucleotides long) are stolen from host-cell mRNA via endonucleolytic cleavage by the L protein, and used to prime synthesis of viral mRNAs (Patterson et al., 1984; Reguera et al., 2010). This results in the generation of S,

M, and L mRNAs which differ in size from their respective genome templates due to 5' extensions and 3' truncations; presumably, because transcription is terminated before the 5' end of the genomic template is reached. By introducing translational stop codons into BUNV RNA genomes, Barr (2007) demonstrated that ongoing protein synthesis is required to prevent premature transcription termination, a unique feature among negative-sense RNA viruses. This translation-coupled-transcription phenomenon is due to translocating ribosomes, which trail behind the RdRp (Figure 1.6). This movement is proposed to prevent nascent mRNA from engaging with the template and therefore prevent spurious transcription termination through the recognition of termination signals in the coding region (Barr, 2007; Walter & Barr, 2011).

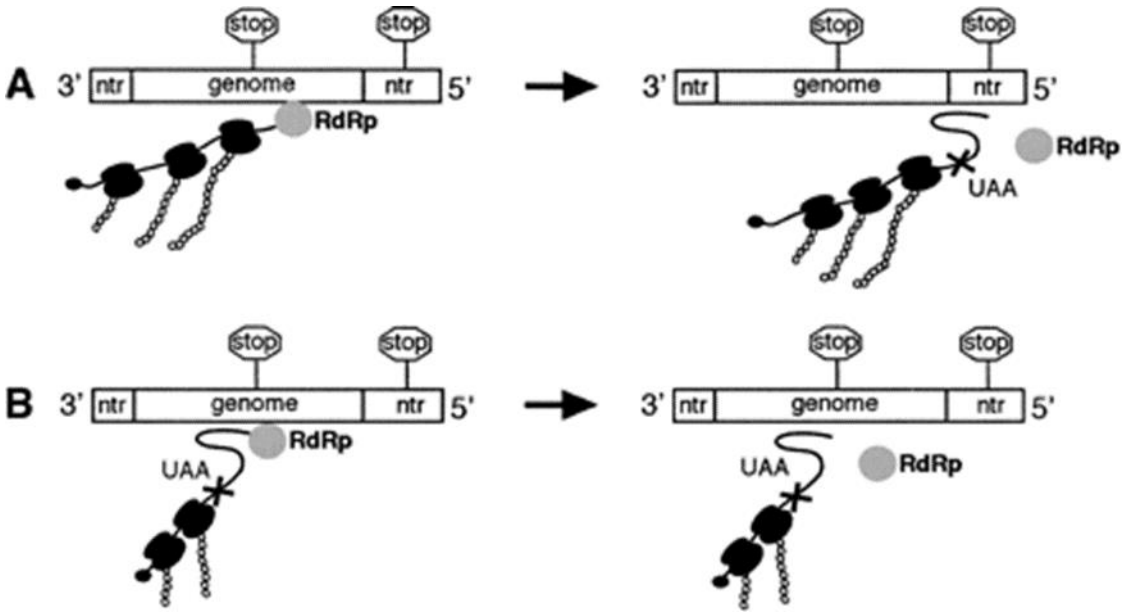

Figure 1.6. Schematic model of Bunyavirus translation-coupled-transcription (Barr, 2007). ***A)*** *In normal translation-coupled-transcription, ribosomes trail behind the RdRp, preventing nascent mRNA from interacting with termination signals (stop signs) in the coding region. Translation stops (represented by a UAA stop codon) when the active termination signals within the NTRs are reached, allowing RNA interactions to occur and RdRp disengages.* ***B)*** *In the absence of translocating ribosomes, i.e., by inhibition with puromycin or cycloheximide, RNA interactions can form with previously silent termination signals in the coding region, resulting in premature transcription termination.*

The mechanisms of transcription termination for Bunyaviruses are poorly defined. The mRNA generated by many Bunyaviruses lack poly(A) tails at their 3' ends, nor do their genomes possess a U-rich tract (used to signal polyadenylation), these are common transcription termination signals in viruses with non-segmented negative-sense genomes (Whelan et al., 2004). It is therefore postulated that Bunyaviruses utilise novel transcription termination mechanisms. Functional analysis of transcription termination of the S-segment of BUNV revealed a 33nt 'termination signal' within the 5' NTR; including a critical hexanucleotide sequence (3'-GUCGAC-5') (Barr et al., 2006). Barr and colleagues also identified a second downstream termination signal containing a pentanucleotide sequence (3'-UGUCG-5'), which overlaps the critical upstream hexanucleotide signal. This sequence is also present in the 5' NTR of the L-segment as well as in the S-segments of several other *Orthobunyavirus* members, which suggests that this transcription termination signal may be conserved across the genus.

Viral RNA replication is a two-stage process whereby *de novo* synthesis generates intermediate positive-sense RNA (cRNA), which serves as the template for the synthesis of new generation vRNA. Both cRNAs and vRNAs interact with the viral N and L proteins, forming new RNPs which undergo further rounds of replication. The molecular mechanisms which drive the switch between transcription and translation are unclear. However, the generation of cRNA and new generation vRNA is coupled with RNP assembly, as stated above, therefore sufficient levels of viral N protein and L protein must be available to encapsidate the nascent cRNA and vRNA. This is supported by Dunn et al. (1995), who showed that only N and L proteins are required for replication. Encapsidation of the cRNA and vRNA is necessary to prevent interactions with the transcription template, and to reduce the accumulation of dsRNA within the cell, an important mechanism of host immune evasion (see section 1.1.5).

v) Virus Assembly & Release

It is generally thought that the assembly of most *Orthobunyavirus* members occurs in the Golgi complex and/or the *trans*-Golgi network (TGN) (Elliott, 2014), which acts as the site of viral replication and maturation of the glycoproteins (Salanueva et al., 2003; Novoa Reyes et al., 2005). Newly formed RNPs are trafficked toward the membranes of the Golgi complex, specifically to regions which have been modified by the insertion of the viral glycoproteins Gn and Gc. It has been proposed that the accumulation of these viral proteins in the Golgi complex is mediated by a Golgi retention signal in the transmembrane domain of the Gn protein (Matsuoka et al., 1994; Shi et al., 2004). Specific interactions between the RNPs and the cytoplasmic tails of the Gn and Gc proteins mediate budding into Golgi-derived vesicles (Shi et al., 2007) which move toward the lumen of the Golgi cisternae. Studies have used Brefeldin A (BFA) to interrogate the role of the Golgi/TGN in Bunyavirus assembly. BFA is a potent inhibitor of protein transport from the ER to the Golgi complex, which induces the redistribution of Golgi-localised proteins to the ER (Sciaky et al., 1997). In these studies, the viral glycoproteins are processed by *cis/medial*-Golgi enzymes but not *trans*-Golgi enzymes (Lippincott-Schwartz et al., 1989; Chen et al., 1991). BFA was found to block viral particle release, but it does not interfere with intracellular virion assembly (Chen et al., 1991; Barbosa et al., 2020).

Salanueva et al. (2003) utilised cryomicroscopy methods to study the morphogenesis of BUNV in BHK-21 and Vero cells. This study shows that the first structural maturation step occurs within the Golgi stacks, where dense, compact structures form from immature precursors observed as annular particles. Using the macrolide antibiotic Megalomycin (MGM), which reversibly alters the *trans* side of the Golgi complex, Salanueva et al. (2003) show that this maturation step is dependent on the presence of a functional *trans*-Golgi. This was supported in a further study by Novoa Reyes et al. (2005), who show that the maturation of the viral forms is accompanied by the acquisition of endo-β-N-acetylglucosaminidase H (Endo-H) resistance in the glycoproteins Gn and Gc. This suggests that the sugar residues on Gn and Gc are processed during trafficking through the Golgi stacks to the *trans*-Golgi.

Furthermore, Salanueva et al. (2003) document the formation of 'viral factory' units (Vf), noted as a novel viral structure consisting of tubular elements built within the Golgi complex, which form connections with mitochondria. The observation that cellular architecture is

dramatically modified in BUNV infection is supported in a further study by Fontana et al. (2008), who utilised 3D ultrastructural imaging and molecular mapping to characterise the BUNV Vf. Both viral and cellular components (NSm and actin) are required for the assembly of viral tubes. These viral tubes are built within the Golgi stacks and anchor to mitochondria and rough endoplasmic reticulum (RER) cisternae, forming a multifunctional unit which acts as a structural framework connecting viral replication and morphogenesis (Figure 1.7).

Additional studies support that, as the infection cycle progresses, the Golgi complex undergoes a spectacular morphological change. In infection with the *Orthobunyavirus* OROV, the Golgi cisternae become enlarged and acquire an MVB-like appearance (Barbosa et al., 2018). These Vfs were also shown to form connections with mitochondria and RER, as observed by Salanueva et al. (2003) and Fontana et al. (2008). The OROV Vf lacks typical endosomal markers but is enriched with proteins involved in MVB biogenesis; the endosomal sorting complexes required for transport (ESCRT) proteins. The ESCRT machinery has been shown to mediate the membrane remodelling events required for Vf biogenesis and is required for effective infectious viral particle production (Barbosa et al., 2018; Barbosa et al., 2020). Since the discovery that Human Immunodeficiency Virus (HIV-1) recruits ESCRT machinery to facilitate viral budding and release (Garrus et al., 2001), the ESCRT pathway has been shown to be manipulated as a major escape route by many diverse enveloped and non-enveloped viruses (Votteler & Sundquist, 2013; Meng & Lever, 2021). The complex network of proteins forming the ESCRT machinery, and its associated factors mediate scission of membrane necks which results in the budding of vesicles toward the cytoplasm (termed 'reverse topology' membrane scission (Schöneberg et al., 2017)). This differs from classical vesiculation processes such as endocytosis; whereby membrane fission, catalysed by dynamin, results in vesicle budding away from the cytoplasm (Votteler & Sundquist, 2013). The 'reverse topology' membrane remodelling events that occur during the maturation of early endosomes into multivesicular bodies (MVBs), mediated by ESCRT machinery (see section 1.2.2), are closely linked to the topology of enveloped virus budding. As such, many

enveloped viruses have evolved to usurp this machinery; this is discussed further in section 1.2.3.

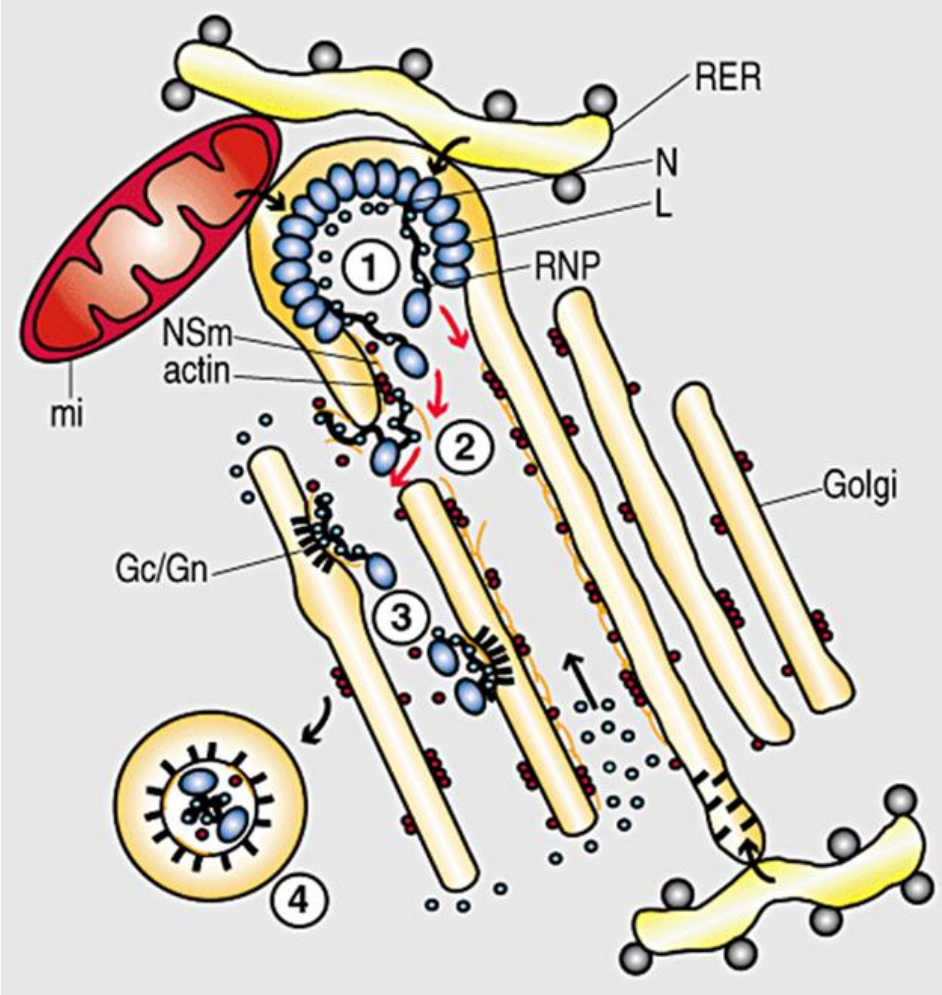

Figure 1.7. Assembly of the Bunyavirus viral factory (Vf) (Fontana et al., 2008). *Viral tubes assemble in Golgi stacks using the endogenous actin-containing matrix and viral NSm as a scaffold. The viral tubes form connections to mitochondria and RER cisternae, providing links to the cellular factors and machinery required for viral replication and assembly.*

Traditionally, after virion budding through the Golgi cisternae and subsequent maturation, it is believed that virus-containing vesicles are trafficked to the plasma membrane and secreted via the exocytic pathway, where virus-containing vesicle membranes fuse with the plasma membrane resulting in the release of infectious virions. This is supported by Rowe et al. (2008), who show colocalization of Rab8 and Rab11 with the *Hantavirus* ANDV. These Rab-GTPases regulate vesicular trafficking from the TGN and recycling endosomes to the plasma

membrane in an ESCRT-independent manner (Chen et al., 1998). In this study, downregulation of both Rab11a alone and Rab11a/Rab11b combined resulted in decreased ANDV secretion (Rowe et al., 2008). However, various other exocytic routes may be employed by Bunyaviruses during egress. For example, a study by (Yan et al., 2022) shows that SFTSV exploits autophagic flux for assembly and egress.

Transmission electron microscopy has revealed the presence of multilamellar structures and filament bundles (containing actin) at the surface of cells during BUNV release. Furthermore, the disruption of actin filaments with cytochalasin D massively reduces the extracellular viral titre (Sanz-Sánchez & Risco, 2013), indicating that actin plays a vital role in viral egress and propagation. Further study is certainly required to more intricately elucidate how Bunyaviruses exploit the exocytic machinery to escape the cell and propagate infection.

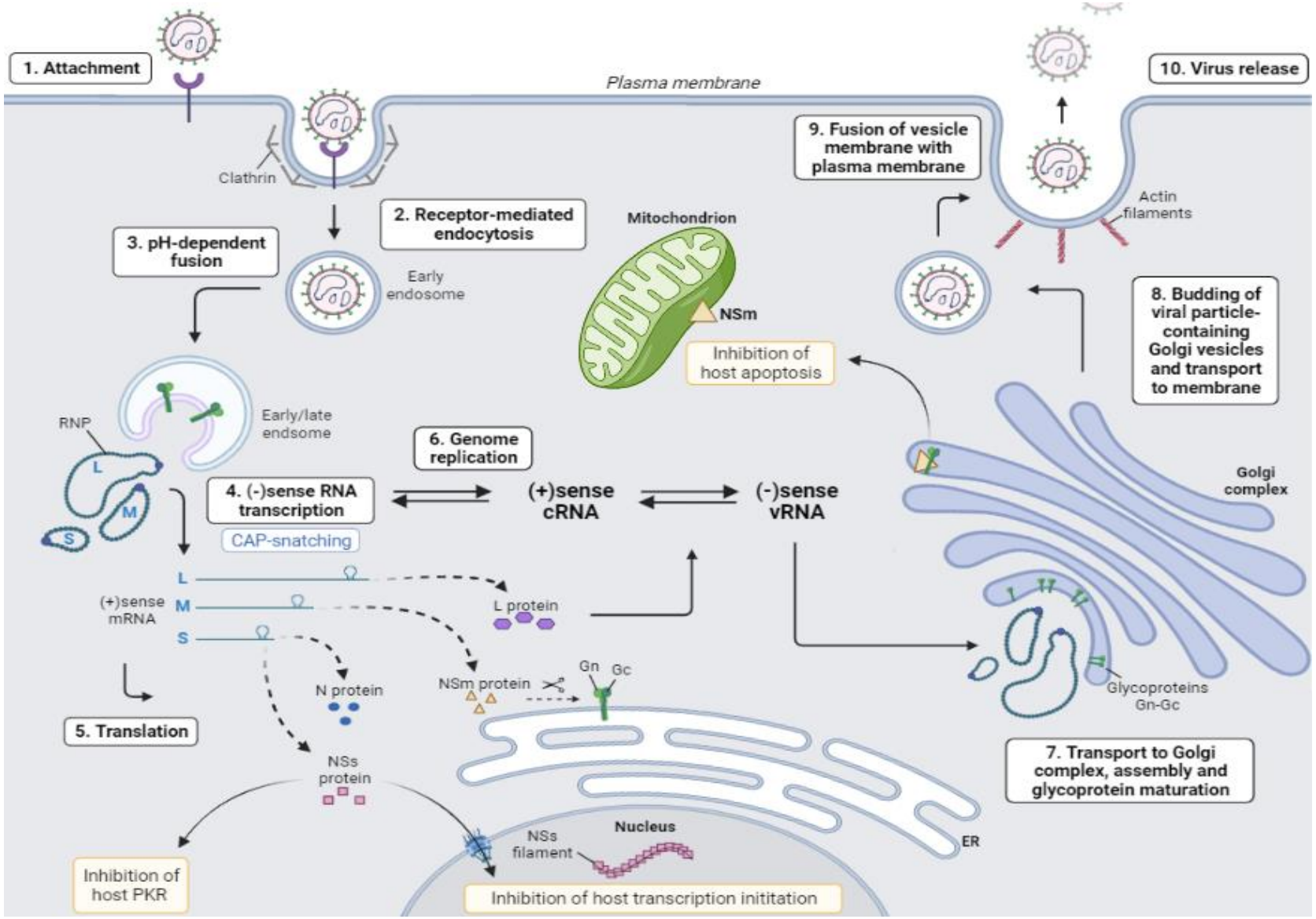

Figure 1.8. A schematic overview of the Orthobunyavirus life cycle, created on Biorender.com. *Orthobunyaviruses may exploit various exocytic pathways to mediate viral egress (8-10), including the ESCRT-pathway, resulting in MVB fusion and release of vesicles containing one or more virions into the extracellular medium (see section 1.2.3).*

1.1.5 Mechanisms of Immune Evasion

i) *Active Innate Response Suppression*

Most members of the *Orthobunyavirus* genus encode the non-structural protein NSs. These NSs proteins have multiple functions during the viral replication cycle and have been found to be a major virulence factor. A study using a recombinant BUNV lacking NSs showed decreased plaque size and viral titre compared to wild-type (wt) BUNV (Bridgen et al., 2001). Indicating that, although not essential for viral replication, NSs contribute to viral pathogenesis. Using a minireplicon system, Weber et al. (2001) demonstrate that the Bunyavirus NSs protein downregulates the activity of the viral RdRp and inhibits viral RNA synthesis. It is suggested that this could perhaps be a mechanism to evade immune detection.

In viral infection, pathogen-associated molecular patterns (PAMPs), such as 5'-triphosphorylated RNA and dsRNA, are recognised by pattern recognition receptors (PRRs). Binding to PRRs induces the activation of a signalling cascade which promotes the transcription of interferon-β (IFN-β), ultimately leading to the upregulation of IFN-stimulated genes (ISGs) which restrict viral replication (Figure 1.9). The culmination of the hundreds of ISGs induced by the IFN response is an extremely powerful defence against viral infection, but individually, the inhibitory effect of these ISGs is relatively low (Elliott, 2014). Carlton-Smith and Elliott (2012) show that the restriction of BUNV replication is dependent on the accumulated effects of at least three ISGs (PKR, MTAP44, and viperin). Several studies have shown that the NSs proteins encoded by the Orthobunyaviruses BUNV, LACV, and SBV are IFN induction antagonists (Figure 1.10) (Weber et al., 2002; Blakqori et al., 2007; Hart et al., 2009; Elliott et al., 2013).

In BUNV and LACV infection, inhibition of the IFN response occurs downstream of transcription factor activation. Using chromatin immunoprecipitation, Thomas et al. (2004) show that, in mammalian cells, the BUNV NSs prevent the phosphorylation of serine 2 in the heptapeptide repeats within the C-terminal domain (CTD) of RNA polymerase II (RNAP II). This results in blocked transcription, and consequently IFN-β synthesis, by inhibiting mRNA elongation and 3' processing (Thomas et al., 2004). It is believed that this inhibition is mediated by the interaction between the C-terminus of NSs and the Mediator protein Med8

(Léonard et al., 2006). In LACV infection, NSs trigger the proteasomal degradation of the hyperphosphorylated form of RNAP II by exploiting the DNA damage response pathway (Verbruggen et al., 2011).

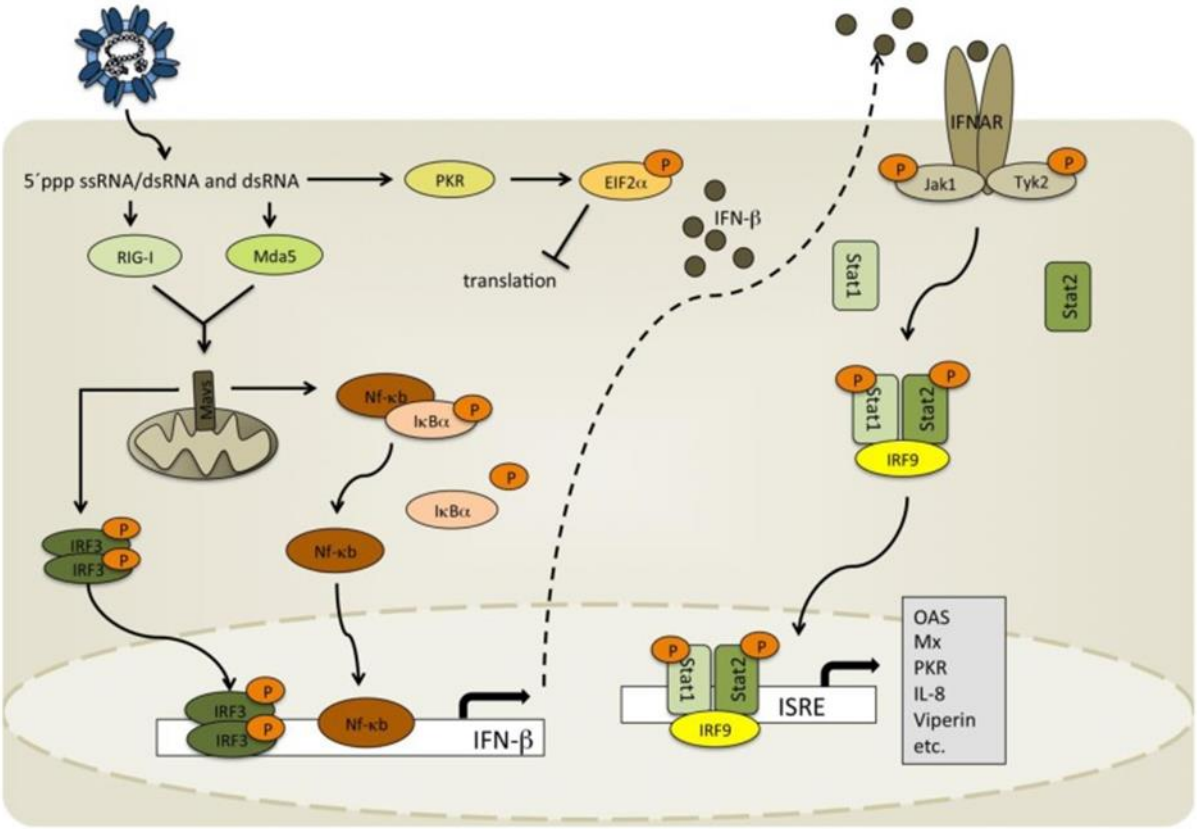

Figure 1.9. Pathway of IFN-β transcription activation and induction of ISGs (Eifan et al., 2013). *Viral 5'-triphosphorylated RNA or dsRNA are recognised by the RNA helicases; retinoic acid-inducible gene I (RIG-I), and melanoma differentiation-associated protein 5 (Mda5). This binding results in the activation and translocation of several transcription factors: including IFN regulatory factor 3 (IRF 3), and nuclear factor-κB (NF-κB) into the nucleus. Here, IRF 3 and NF-κB promote transcription of IFN-β, which is transported out of the cell. Binding of IFN-β to IFN receptors triggers the activation of the JAK/STAT signal transduction pathways which results in the transcription of many different ISGs, functioning together to restrict viral replication and propagation.*

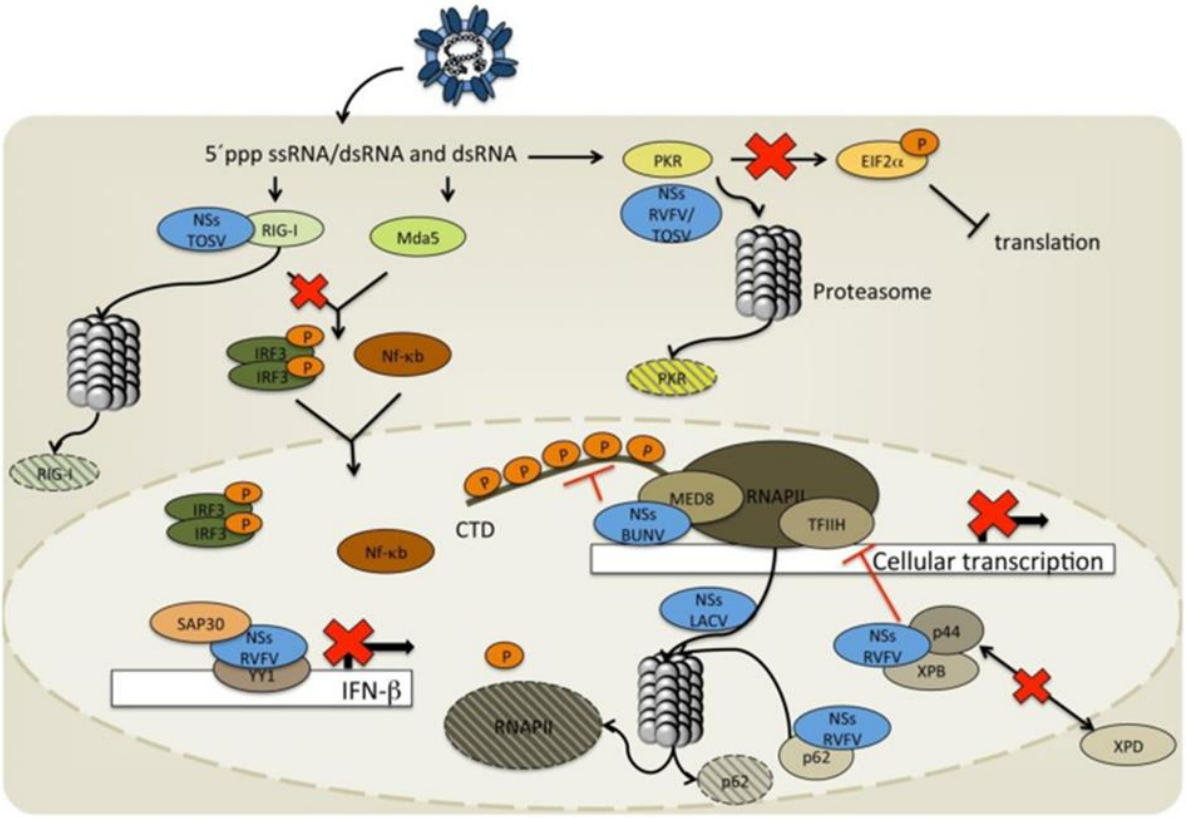

Figure 1.10. Mechanisms of Orthobunyavirus and Phlebovirus NSs protein interference with the host innate immune response (Eifan et al., 2013). *Rift Valley Fever Virus (RVFV) and Toscana virus (TOSV) NSs induce proteasome degradation of protein kinase R (PKR), inhibiting phosphorylation of eukaryotic translation initiation factor 2A (eIF2a), thus facilitating viral translation. TOSV NSs inhibit the activation of IRF-3 by proteasome-mediated degradation of RIG-I (Gori-Savellini et al., 2013), interfering with IFN-β production. In RVFV infection, NSs interact with Sin3A-associated protein (SAP30), resulting in the formation of a protein complex with the transcriptional repressor Yin Yang 1 (YY1) on the IFN-β promoter, inhibiting transcription activation (Le May et al., 2008). Furthermore, RVFV NSs suppress the transcription of host mRNA through interaction with transcription factor II H (TFIIH) components, preventing TFIIH subunit assembly (Le May et al., 2004). The NSs of Bunyamwera virus (BUNV) and La Crosse virus (LACV) inhibits cellular transcription by targeting RNA polymerase II (RNAP II). For BUNV, this inhibition occurs via the prevention of serine 2 phosphorylation in the RNAP II C-terminal domain (CTD), mediated by the interaction between NSs and the Mediator component Med8. LACV NSs trigger proteasomal degradation of the transcriptionally active form of RNAP II, via the DNA damage response pathway (Verbruggen et al., 2011).*

ii) Immune Evasion

Emerging evidence suggests that viruses across many different families have evolved to exploit extracellular vesicles (EVs), to many varying downstream effects; including modulation of the host immune responses (discussed further in section 1.2.3). When assessed cumulatively, viral components contained within EVs have the potential to increase viral persistence through, disguising viral genomes, decoying the immune system, and increasing viral infection in uninfected cells (Figure 1.11) (Anderson et al., 2016). Interestingly, recent evidence suggests that several Bunyaviruses exploit EVs to mediate their receptor-mediated transmission (Silvas et al., 2015), and to module host immune responses (Ahsan et al., 2016; Alem et al., 2021). Recent observations providing evidence to support the conservation of these functions across different virus families suggest that EVs may play an important, previously unappreciated, role in viral disease.

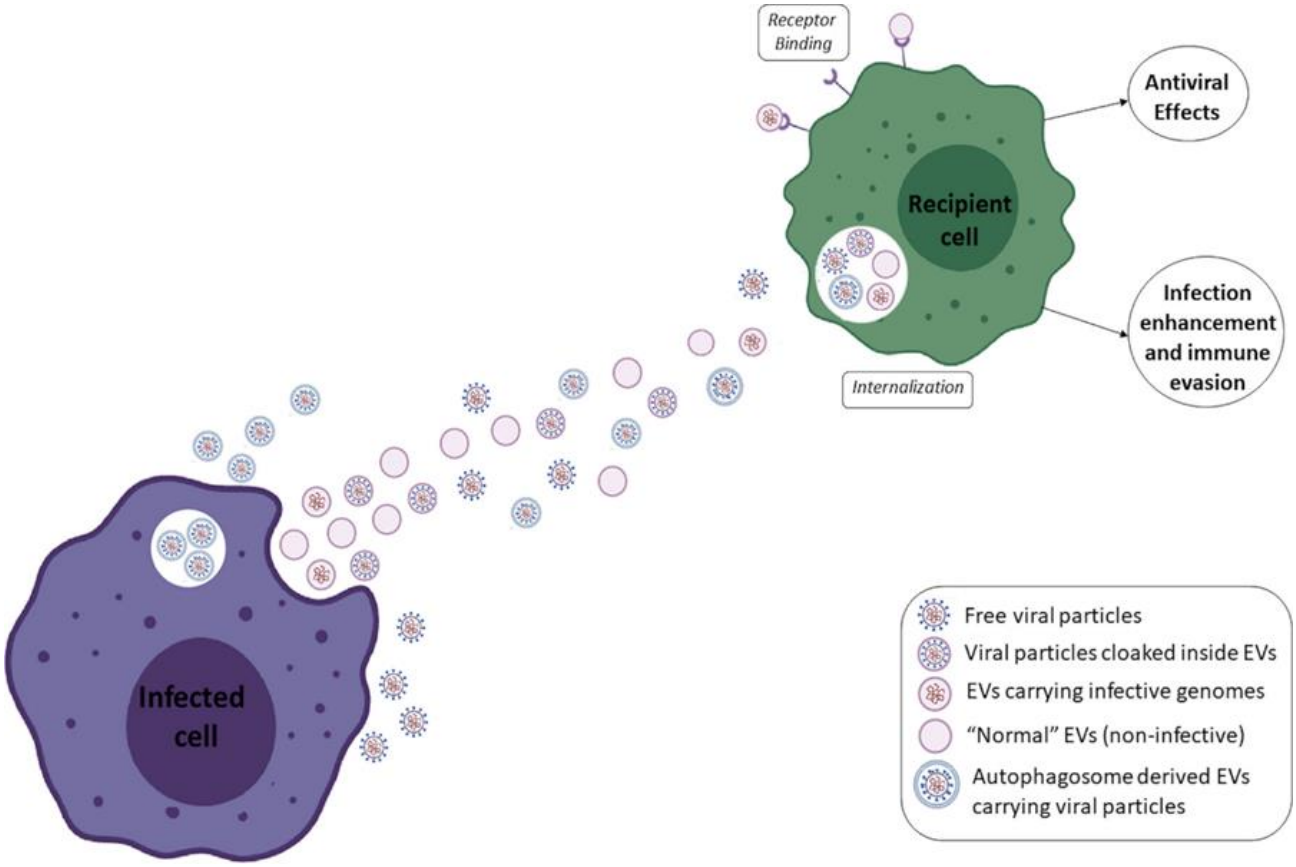

Figure 1.11. Schematic representation of the potential interplay between viruses, viral components, and extracellular vesicles (EVs) (Martins & Alves, 2020).

1.2 Extracellular Vesicles

1.2.1 Characterisation of Extracellular Vesicles

Extracellular vesicles (EVs) is the generic term used to describe particles which are naturally secreted from cells that are delimited by a lipid bilayer and are unable to replicate (Théry et al., 2018). Originally, EVs were thought to serve as 'waste carriers'; assisting in the secretion of un-needed compounds from within the cell (Johnstone et al., 1987). However, as evidenced by an increasing number of high-profile publications, we now know that EVs are 'information carriers', playing a significant role in cell-cell communication in multiple physiological pathways including cancer, aging, obesity, cardiovascular, autoimmune and infectious diseases (Yáñez-Mó et al., 2015; Bebelman et al., 2018; Théry et al., 2018; Ipinmoroti & Matthews, 2020; Ancel & Feige, 2021; Yin et al., 2021).

EVs are a heterogenous group; there is currently no consensus on markers that distinguish EV subtypes definitively, and the nomenclature is still being defined by the research community. Overlaps in the internal composition, size, surface markers, and similarities in morphology between different EV subtypes (see Figure 1.12) have posed a significant challenge in the development of a precise EV classification system (Gould & Raposo, 2013; Kowal et al., 2016). Studies have utilised electron microscopy methods to gain insight into the biogenesis of the different EV subtypes (Théry et al., 2006; Raposo & Stoorvogel, 2013; Zhang et al., 2019), based on this knowledge, EVs are commonly divided into two subgroups: microvesicles and exosomes (Figure 1.12).

However, it must be noted that the current classification system is not without limitations; in particular, this system overlooks the possibility that EV biogenesis many differ between cell-types. For example, Jurkat T-cells possess plasma membrane domains enriched with exosome proteins, from which EVs with exosome characteristics have been shown to directly bud (Booth et al., 2006). In these T-cells, it has been shown that endosomal trafficking, mediated by Rab27a, directs HIV budding at the plasma membrane (Gerber et al., 2015). It is likely that this mechanism is manipulated for the biogenesis of exosomes at the plasma membrane, in T-cells specifically, implying that an EV classification system based primarily on the mechanism of EV biogenesis would be inappropriate.

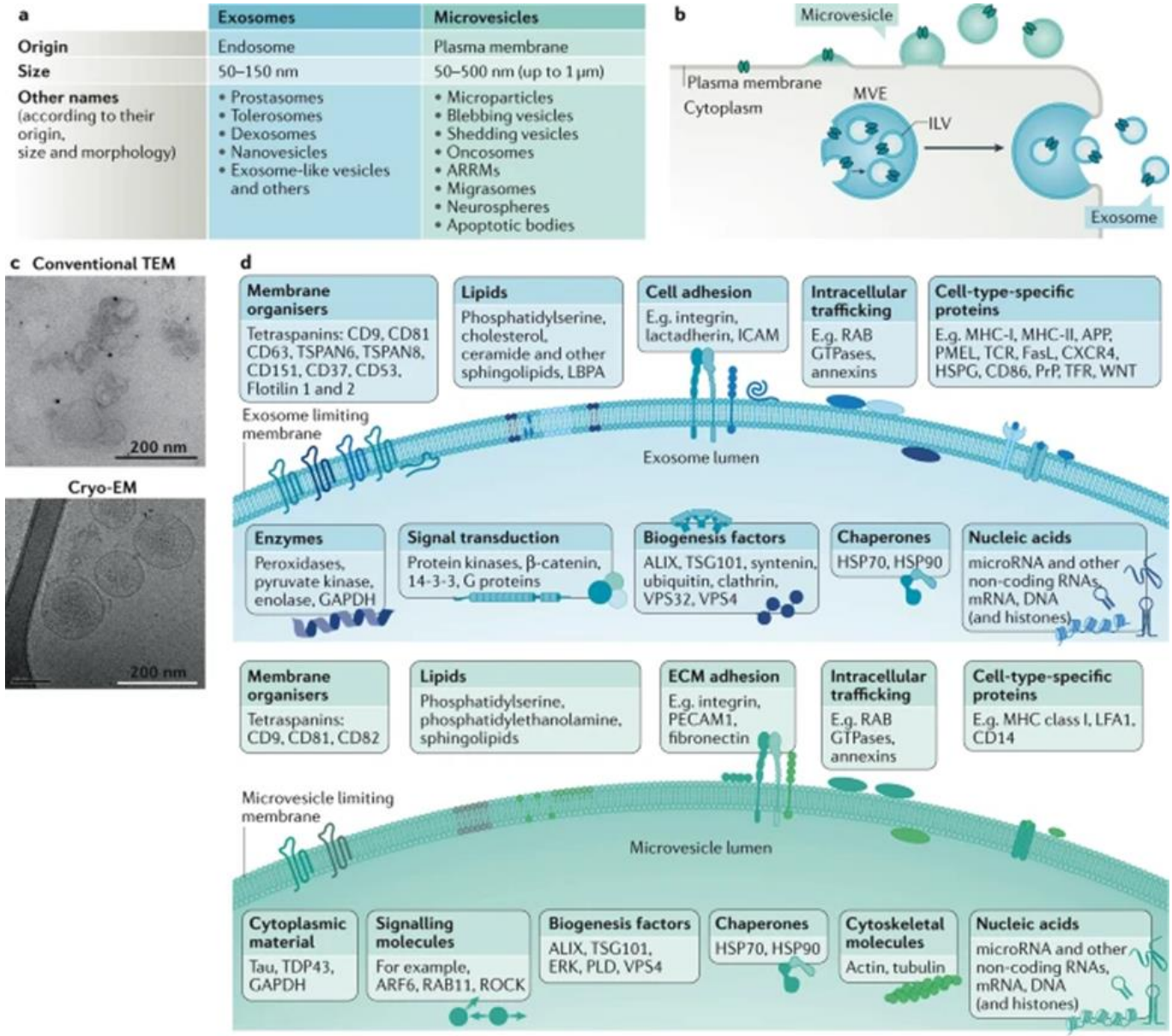

Figure 1.12. Characterisation of extracellular vesicles (van Niel et al., 2018). (a) *EVs are roughly divided into two main categories: microvesicles and exosomes, based on their size, cellular origin, and morphology.* ***(b)*** *Microvesicles originate from direct budding of the plasma membrane. Exosomes originate from the inward budding of the limiting membrane of endocytic compartments (forming intraluminal vesicles; ILVs), the vesicle-containing endosomes, termed multivesicular bodies (MVBs), eventually fuse with the plasma membrane, releasing their internal vesicles (i.e., exosomes) into the extracellular medium.* ***(c)*** *Microvesicles observed by conventional transmission electron microscopy (TEM, top) and cryo-electron microscopy (cryo-EM, bottom). Microvesicles appear as round, double membraned structures when viewed in a near-native state by cryo-EM.* ***(d)*** *The internal cargo and surface composition of microvesicles and exosomes.*

1.2.2 Exosome Biogenesis

In recent years, exosomes have attracted great attention in the research community. This is owing to the discovery that exosomes contain a complex biological cargo (proteins, lipids, and nucleic acids; see Figure 1.12), which they are able to deliver to recipient cells, over long distances, ultimately resulting in the reprogramming of the target cells (Zhang et al., 2019). Since exosomes are released from most eukaryotic cells, differences in the type, function and the physiological or pathological state of the donor cell confer differences in the cargo within the exosomes it produces (Zhang et al., 2019). Exosomes, therefore, not only represent a novel mechanism of intercellular communication, playing a pivotal role in numerous cellular processes, including immune responses and signal transduction (Gangoda et al., 2015; Greening et al., 2015a), they may also be used as prognostic biomarkers for disease; acting as a 'signature' to the cellular processes occurring within the donor cell.

As detailed in section 1.2.1, exosomes are formed from the inward budding of the MVB membrane, forming ILVs, which are secreted by exocytosis into the extracellular medium following fusion of the MVB membrane with the plasma membrane (Hessvik & Llorente, 2018). MVBs can also be trafficked to the TGN for endosome recycling, or be targeted for degradation; either by direct fusion with lysosomes, or fusion with autolysosomes followed by lysosomes (Kalluri & LeBleu, 2020). It is speculated that specific ILV cargoes and markers influence the fate of the MVB; i.e., whether it will follow a pathway for recycling, secretion or degradation (Gurung et al., 2021).

During ILV formation, lipids and membrane-associated proteins are clustered in microdomains on the MVB limiting membrane. This promotes the recruitment of the cell-type/state specific cytosolic components scheduled for secretion (Ostrowski et al., 2010), which are sequestered through scission of the ILVs into the MVB lumen, mediated by ESCRT-dependent or ESCRT-independent mechanisms (Babst, 2011). The ESCRT pathway is largely considered to be the primary mechanism of exosome biogenesis (Hurley, 2008; Henne et al., 2011; Villarroya-Beltri et al., 2014; Hurley, 2015). However, studies have also shown that MVBs containing CD63 decorated ILVs can form in the absence of all four ESCRT complexes (Stuffers et al., 2009), favouring alternative, ESCRT-independent, exosome biogenesis pathways.

The exosome biogenesis pathway is summarised in Figure 1.13. This is a finely tuned and highly complex process, which varies significantly depending on cargoes, cell type, and other pathological and physiological stimuli (van Niel et al., 2018).

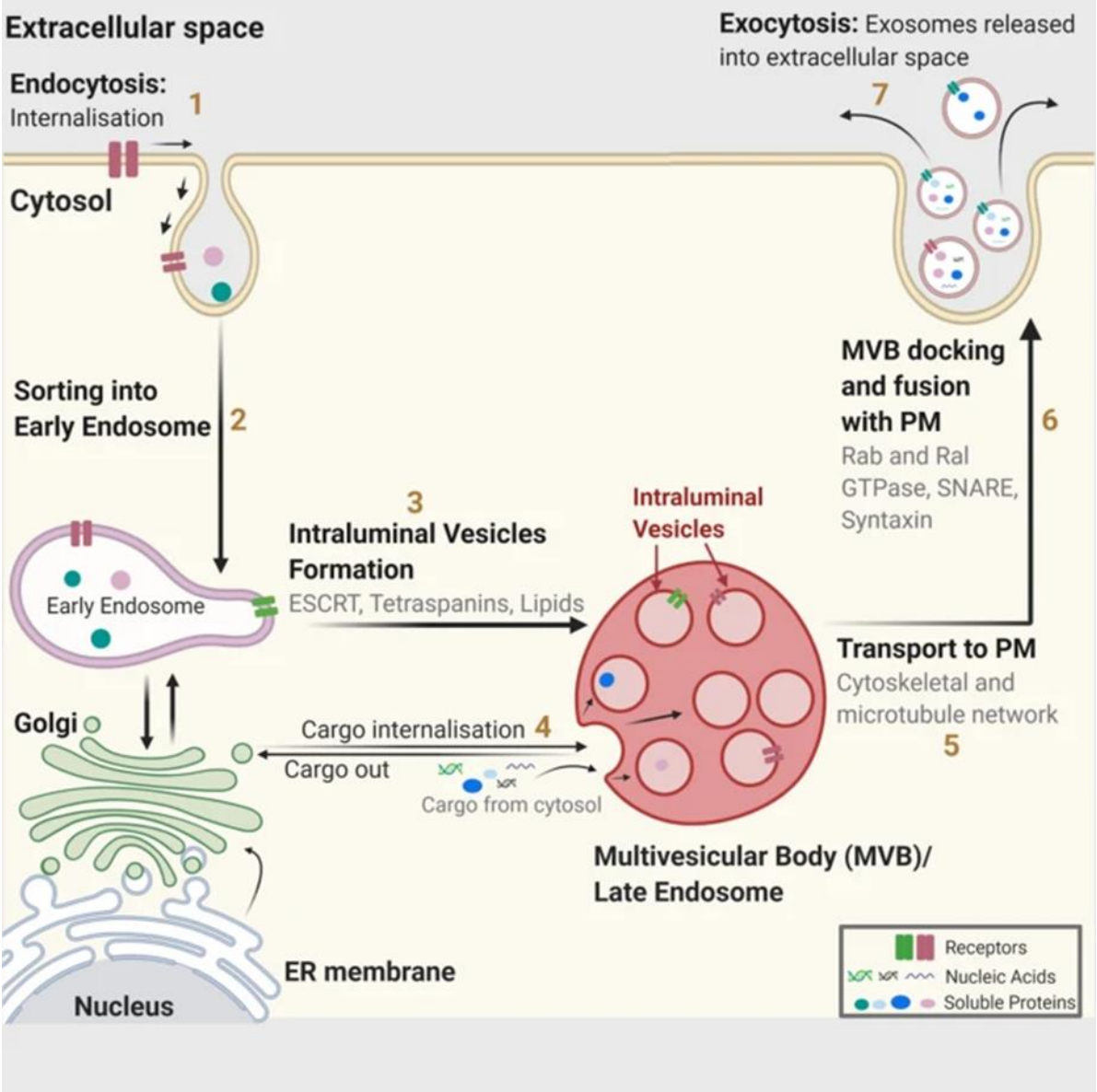

Figure 1.13. Exosome biogenesis pathways (Gurung et al., 2021). (1) *Cargoes (proteins, lipids, and other cytosolic components) are internalised and* ***(2)*** *sorted into early endosomes (EEs).* ***(3)*** *EEs mature into late endosomes (LEs; otherwise known as multivesicular bodies (MVBs)) containing many intraluminal vesicles (ILVs). The formation of these ILVs is mainly driven by ESCRT machinery, comprising 5 core complexes: ESCRT-o, -I, -II, -III and vacuolar protein sorting-associated protein 4 (Vps4). ESCRT-o recognises ubiquitinated cargoes and recruits ESCRT-I by interacting with the tumour susceptibility gene 101 (Tsg101) subunit. ESCRT-I and -II promote the budding of the MVB membrane at the ubiquitinated protein microdomains. ESCRT-II interacts with the charged multivesicular body protein-6 (CHMP6)*

subunit of ESCRT-III, recruiting CHMP4 and CHMP3 to perform budding and vesicle neck fission to form ILVs. Vps4 then catalyses the disassembly of ESCRT-III. ***(4)*** *Cargoes, delivered from the trans-Golgi and cytosol, are sequestered into ILVs (simultaneously with* ***(3)****). Sorting of cargoes and ILV formation is influenced by interactions between the adaptor protein; syntenin, the heparan sulfate proteoglycan; syndecan, and ALG-2-interacting protein X (Alix). Syntenin binds syndecan with ALIX through LYPX(n)L motifs (Baietti et al., 2012), this acts as an intermediate between ESCRT-I and ESCRT-II, assisting in cargo selection (Zhang et al., 2019). Alix directly recruits ESCRT-III through interaction with lysobiphosphatidic acid (LBPA; (Larios et al., 2020), thus providing an additional ILV formation pathway, independent to the canonical ubiquitin-dependent ESCRT pathway. ESCRT-independent pathways of exosome biogenesis have also been documented which involve lipid-raft microdomains (Skryabin et al., 2020). Ceramides, due to their cone-shaped structure, can induce spontaneous negative curvature of the MVB membrane, promoting domain-induced budding (Trajkovic et al., 2008). Tetraspanins, commonly used as exosome biomarkers, can also participate in ESCRT-independent exosome biogenesis and cargo selection (van Niel et al., 2011; Perez-Hernandez et al., 2013).* ***(5)*** *MVBs are trafficked to the plasma membrane via the cytoskeletal and microtubule network.* ***(6)*** *MVBs fuse with the plasma membrane (PM) and* ***(7)*** *ILVs contained within the MVB are secreted as exosomes. SNARE proteins and their effectors (Rab GTPases) play an important role in MVB trafficking to the PM and the subsequent docking and secretion of exosomes. Rab27b regulates the trafficking of MVBs toward the PM, and both Rab27a and Rab27b are required for MVB docking (Ostrowski et al., 2010; van Niel et al., 2018). However, Rab27 isoforms are not expressed by all cell types, implying that different cells have adapted diverse mechanisms for exosome secretion. This is highlighted in studies which show that Rab35 and Rab11 are involved in MVB docking and exosome secretion (Hsu et al., 2010a; Koles et al., 2012).*

1.2.3 Exosomes in Viral Disease

In recent years, several studies have recognised the crucial roles of exosomes in viral pathogenesis and immunity (Chahar et al., 2015; Madison et al., 2015; Ahsan et al., 2016; van Dongen et al., 2016). The discovery that these roles are conserved across diverse virus families suggests that they have greater importance in viral pathogenesis than previously appreciated; representing a source of viral antigen that could potentially be used as a biomarker for disease (Anderson et al., 2016). Furthermore, exosomes have the potential to act as carriers for targeted drug/gene delivery due to their low immunogenicity and cell penetration capacity (Andaloussi et al., 2013; Anderson et al., 2016; Chen et al., 2021; Popowski et al., 2021).

i) Hijacking the Exosome Biogenesis Pathway

The cellular machinery involved in the exosome biogenesis pathway (see section 1.2.2) is often hijacked by viruses, particularly enveloped viruses, for their transmission, assembly, and egress to produce new progeny (Anderson et al., 2016). Clathrin-mediated endocytosis is employed by many viruses, including some Bunyaviruses, to allow viruses to traffic through the host-cell endocytic machinery (see section 1.1.4). Studies have shown that Hepatitis C (HCV) and Hepatitis A (HAV) are able to incorporate their full-length RNA genomes into ILVs within MVBs. These ILVs, when secreted as exosomes, can establish infection in naïve cells, highlighting a novel route of transmission which permits the evasion of antibody-mediated immune responses (Ramakrishnaiah et al., 2013; Longatti, 2015; Longatti et al., 2015). Human immunodeficiency virus (HIV-1) can also manipulate host endocytic machinery to mediate the delivery of viral cargo into uninfected cells. Gould et al. (2003) proposed the 'Trojan horse' exosome hypothesis; this suggested that retroviruses had evolved to exploit the endosomal system to mediate their receptor-independent transmission. This was supported in studies by Wiley and Gummuluru (2006) who show that exosome-associated HIV-1 particles, derived from immature dendritic cells, can establish infection in CD4+ T cells with higher infectivity than cell-free virus particles.

An increasing body of evidence suggests that viruses can manipulate the endosomal ESCRT machinery to effect membrane fission during egress (Votteler & Sundquist, 2013). It has also

been reported that some viruses utilise Rab GTPases to facilitate their assembly and egress (Alenquer & Amorim, 2015) (Figure 1.14).

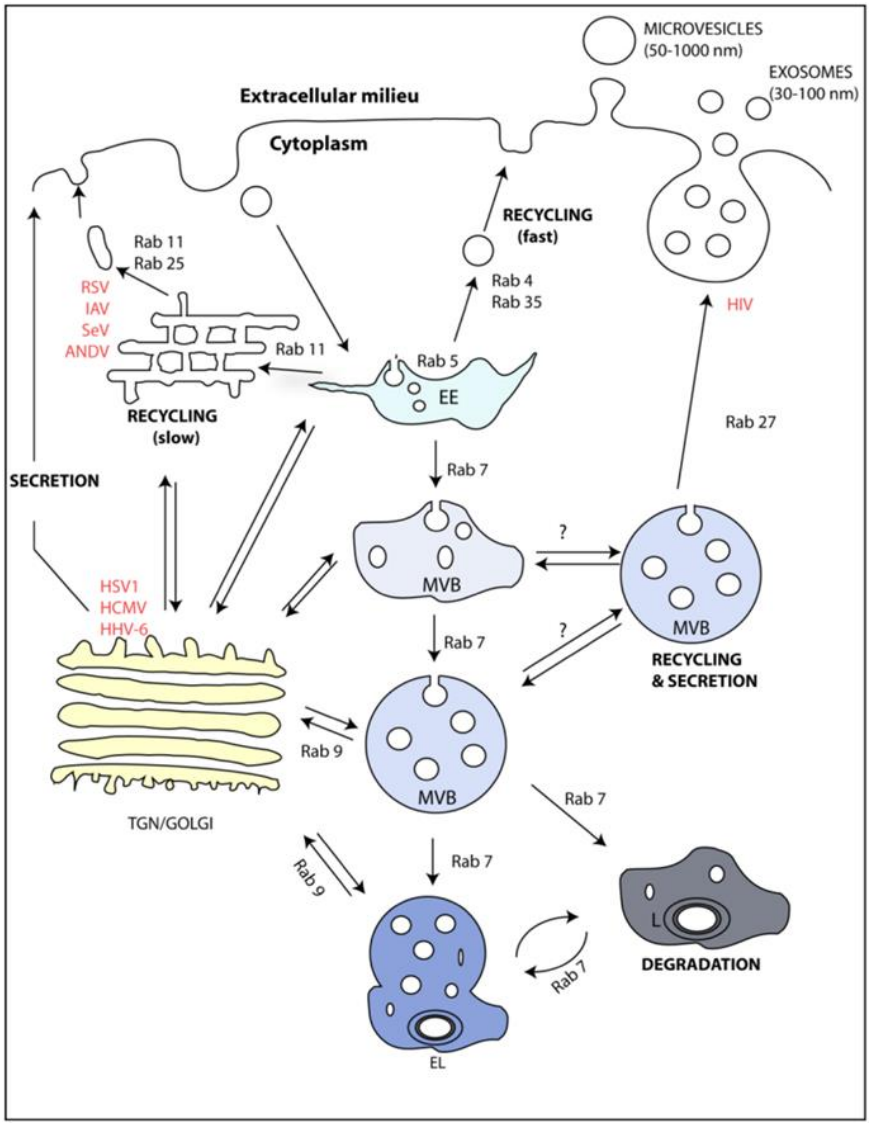

Figure 1.14. Rab GTPases exploited by viruses in the exosome biogenesis pathway (Alenquer & Amorim, 2015). *Endocytosed cargo is transported into early endosomes (EE). These form recycling endosomes or multivesicular bodies (MVBs). MVBs fuse with either lysosomes to produce endolysosomes (EL), or the plasma membrane to secrete their intraluminal vesicles (ILVs) as exosomes into the extracellular milieu. Each endocytic compartment is characterised by the enrichment of specific Rab GTPases. Influenza A virus (IAV), respiratory syncytial virus (RSV), Sendai virus (SeV), and Andes virus (ANDV) manipulate Rab11 to transport progeny RNA to the cell surface. Rab27 (a/b) are required for the assembly of human immunodeficiency virus (HIV), herpes simplex virus 1 (HSV1), and human cytomegalovirus (HCMV). Human herpesvirus 6 (HHV-6) infection increases MVB formation. HHV-6 virions have been shown to be present in MVBs and are secreted alongside exosomes upon fusion of the MVB with the plasma membrane.*

ii) Exosomes in Bunyavirus Infection

Despite the increasing body of research into the role of exosomes in viral disease, the functions of exosomes in the replication and pathogenesis of single-stranded RNA viruses, such as Bunyaviruses, remains largely unexplored.

Studies by Silvas et al. (2015) found that extracellular vesicles produced by SFTSV-infected cells harboured infectious virions. Silvas et al., 2015 confirmed, using live cell imaging, that the SFTSV virions harboured within CD63-immunoprecipitated exosomes were effectively transported to uninfected neighbouring cells, where the virus was able to sustain efficient replication. This demonstrates that SFTSV can exploit exosomes to mediate receptor-independent transmission. This could serve as a potential avenue to investigate novel therapeutic strategies against this virus, and potentially related pathogens, which may hijack the endosomal cellular machineries to establish infection by employing a similar mechanism. Moreover, future studies which further reveal the roles of exosomes in Bunyavirus infection may help to elucidate and define poorly understood aspects of the Bunyaviral replication cycle, particularly the mechanisms by which these viruses' egress to produce new infectious progeny and establish infection in naïve cells.

Further to this, Alem et al. (2021) show that exosomes produced from cells infected with the *Phlebovirus* RVFV serve a novel protective function. In this study it was shown that exosomes isolated from RVFV-infected cells induced RIG-I mediated activation of IFN-β response (see section 1.1.5), resulting in the activation of autophagy in exosome-treated naïve cells. It is suggested that this mechanism of innate immune response regulation is associated with the presence of viral RNA sequences and proteins such as N- and NSs, packaged within the exosomes secreted from RVFV infected cells, as detected by Ahsan et al. (2016). Interestingly, in the study by Ahsan et al. (2016), naïve immune cells (T-cells and monocytes) treated with some exosome preparations from RVFV infected cells underwent apoptosis through poly (ADP-ribose) polymerase (PARP) cleavage and caspase 3 activation. Collectively, these data suggest that exosomes play a multidimensional role in RVFV infection, including regulation of host immunity, and likely contribute significantly to viral pathogenesis.

Further research is certainly required to elucidate whether these mechanisms of receptor-independent transmission and host immune regulation, mediated by exosomes, are

conserved across the *Bunyavirales.* Importantly, further mechanistic insights into the functions of exosomes in the pathogenesis and persistence of Bunyavirus infection may support the much-needed development of effective vaccines and novel therapeutic agents.

1.3 Cellular Modelling

1.3.1 2D vs 3D Cell Culture

Currently, most of our knowledge regarding host-virus interactions, and our understanding of the molecular mechanisms of viral pathogenesis and aetiology, are based upon studies using traditional 2D culture systems. Such systems, utilising eukaryotic cells cultured as single monolayers on flat glass or plastic substrates, have been established for viral characterisation and propagation since the 1940s (Enders et al., 1949). Whilst these conventional 2D culture systems have contributed tremendously to fundamental investigations into a multitude of viral diseases, they lack the ability to accurately reflect the complexity of the *in vivo* microenvironment encountered by viral pathogens. The inability of 2D systems to recapitulate the intricacies of native tissues has impeded the study of fastidious viruses, and contributed to high rates of failure in vaccine and antiviral drug development (Lawko et al., 2021).

To overcome this, various 3D cell culture models have been developed (Table 1.3), which bridge the gap between simplified 2D culture systems and costly animal models (and their associated ethical issues), providing a more physiologically relevant platform for the *in vitro* study of human viruses. Such model systems can more accurately reflect *in vivo* cell morphology, proliferation, and differentiation compared to conventional 2D culture (Edmondson et al., 2014; Antoni et al., 2015). Moreover, cells in multicellular spheroid (MCS) models (see Table 1.3) exist in a highly interactive 3D microenvironment, wherein the cell-cell/cell-ECM interactions and concentration gradients regulate cell function and behaviour, in addition to providing a permeability barrier through which drugs must penetrate.

However, it must be noted that these 3D platforms are not without limitations; they are unable to mimic the entire complexity of native tissues. For example, the normal vasculature, fluid flows, internal tensions, tissue heterogeneity, and immune responses observed *in vivo* are not mimicked by all 3D models. Some of the currently available 3D model systems used for the study of mammalian viruses are detailed in Table 1.3, with their respective advantages and limitations.

Table 1.3. Advantages and limitations of different 3D cell culture systems used for the study of human viruses.

Model		Technique	Advantages	Limitations	References
MCS culture 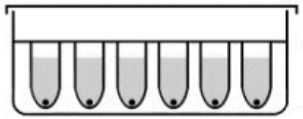	**Aggregation based**	ULA plates pre-coated with ultra-hydrophilic polymer allow spontaneous spheroid formation.	• High-throughput • Ease of use • Spheroids can be easily extracted from culture medium for further experiments • Fast and uniform spheroid formation	• Expensive • Not all cell lines form tight spheroids	(Kapałczyńska et al., 2018)
	**Hanging drop**	Cells self-organise into spheroids on inverted substrates due to gravitational forces.	• Easily accessible spheroids • Co-culture possible • Fast spheroid formation	• Labour intensive • Time consuming • Difficult to exchange culture medium	(Frey et al., 2014)
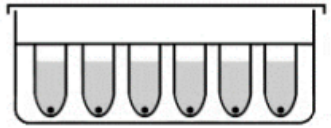	**Liquid overlay**	Round-bottom plates are coated with a hydrophilic substance such as agarose which encourages spheroid formation.	• Inexpensive • High throughput • Easy to perform	• Spheroid size/shape variability (heterogenous spheroid formation) • Not all cell lines form spheroids	(Sennett, 2019; Pinto et al., 2020)
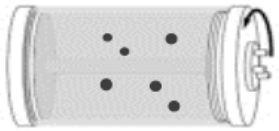	**RWV**	Cells are incubated in a RWV which creates a microgravity promoting cell aggregation into spheroids.	• Large scale spheroid production	• Constant agitation prevents visualisation • Produces spheroids with varying sizes/shapes	(Antoni et al., 2015)

				• Requires specialised equipment	
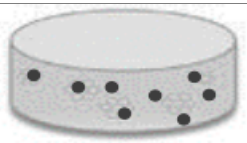	**Scaffold/Matrix based**	Cells are seeded onto 3D scaffolds which mimic the ECM. Natural polymers such as: hydrogel, collagen, Matrigel, laminin, gelatin, hyaluronate, and chitosan can be used.	• Mimics ECM • Co-culture possible • Easy to set-up	• Expensive ECM gels • Labour intensive	(Breslin & O'Driscoll, 2013)
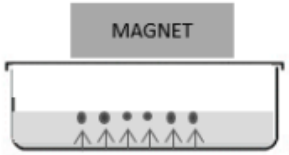	**Magnetic levitation**	Cells form 3D structures based on magnetic levitation in the presence of hydrogels containing magnetic nanoparticles.	• Fast and uniform spheroid formation • Non-toxic • Does not induce inflammatory response by the cultured cells • Co-culture possible	• Low throughput • Expensive (requires the preparation of magnetic nanoparticles)	(Souza et al., 2010; Haisler et al., 2013; Tseng et al., 2013)
Organotypic epithelial raft culture		Epithelial cells are placed on a dermal equivalent (composed of collagen and fibroblasts) and cultured at the air-liquid interface to full differentiation.	• Suits the study of epitheliotropic or fastidious viruses	• Expensive • Time consuming and labour intensive	(Meyers, 1996; Andrei et al., 2010)
Microfluidic 3D cell culture 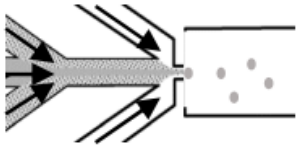		Spheroids/cells are formed/maintained within devices which allow precise control of fluid flow at a microlitre scale. A free perfusion system, allows distribution of oxygen and nutrients as well as the elimination of waste.	• Mimics vasculature and shear stresses • Generates gradients as observed *in vivo* (oxygen, growth factors, etc.) • Co-culture possible	• Specialised equipment required • Difficult to set-up • Limited number of cells	(Sennett, 2019; Pinto et al., 2020)

3D perfusion cell culture 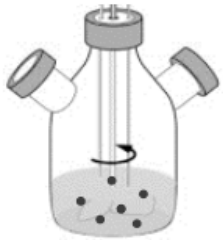	Cells are cultured in a rotating wall bioreactor while continuously exchanging culture medium.	• Large scale spheroid production • Generates gradients as observed *in vivo* (oxygen, growth factors, etc.) • Can control physiological chemostatic conditions	• Expensive • High shear forces • Spheroid size/shape variation • Specialised equipment required	(Martin & Vermette, 2005; Li & Cui, 2014)

Adapted from Harb et al. (2021), He et al. (2016) and Pinto et al. (2020). MCS: Multicellular spheroid. RWV: rotating wall vessel bioreactor. ECM: extracellular matrix.

1.3.2 3D Cell Culture Model Applications in Virology

The study of human papillomavirus (HPV) has been revolutionised by the development of organotypic epithelial raft cultures (see Table 1.3), since HPV replication is strictly liked to the differentiation of the host epithelium (Andrei et al., 2010). Organic epithelial raft cultures, which generate a stratified and differentiated epithelium, have been further employed to study the interactions of HPV with other epitheliotropic viruses, such as HSV (Meyers et al., 2003) and adeno-associated virus (Hermonat et al., 2005). Moreover, these models have been utilised to evaluate the efficiency of antiviral compounds targeting HPV (Andrei et al., 2010; Satsuka et al., 2010), HIV (Israr et al., 2010; 2011), and HSV (Balzarini et al., 2013).

Furthermore, 3D cell culture models have been increasing utilised in the field of HCV research. MCS models of HuH-7.5 and HuH-7 cells have been successfully established using scaffold-based techniques and RWV bioreactors (Cho et al., 2009; Sainz et al., 2009; Rajalakshmy et al., 2015). These MCS models were highly permissive to HCV infection, and supported HCV replication; thus, providing a more physiologically relevant platform to study HCV biology, host-virus interactions, and anti-HCV therapeutics (Liu et al., 2014). As such, these models could be implemented as an alternative to primary hepatocytes (Rajalakshmy et al., 2015). The replication cycle of hepatitis E virus (HEV) remains poorly understood, largely owing to the limitations of cell culture systems and animal models (Osterman et al., 2015) and the difficulties of *in vitro* propagation of HEV. Berto et al. (2013) show that HEV can replicate efficiently in a 3D human hepatoblastoma PLC/PRF/5 model (using RWV). Interestingly, replication was not supported in the conventional 2D monolayer system (Berto et al., 2013). This highlights the potential of RWV 3D culture systems for the *in vitro* cultivation and study of fastidious viruses.

In recent years, 3D cell culture models have also gained increasing attention in the study of respiratory virus infections, including the severe acute respiratory syndrome coronavirus 2 (SARS-CoV-2) (Monteil et al., 2020; Salahudeen et al., 2020; Harb et al., 2021). The urgent need for a physiologically relevant platform to allow the early screening of vaccines was illustrated by the recent SARS-CoV-2 outbreak, which catalysed an international effort to produce an effective vaccine. The process of vaccine development is time-consuming and costly, with only a small percentage of vaccines progressing from preclinical testing to human trials (Thomas et al., 2016). This low rate of success may be partially attributed to the poor

ability of 2D culture systems, used in the early stages of vaccine development, to accurately predict *in vivo* responses (He et al., 2016; Lawko et al., 2021). Furthermore, whist animal models have contributed greatly to the study of human diseases and drug development, they are unable to effectively model human pathophysiology and, unsurprisingly, up to 80% of therapeutics which pass preclinical *in vivo* trials fail during clinical trials with human subjects (Miller & Spence, 2017). This further highlights the relevance of 3D culture models, which can more accurately embody the physical, biological, and chemical properties of the *in vivo* microenvironment which influence disease pathology and therapeutic responses (Edmondson et al., 2014; Langhans, 2018; Lawko et al., 2021).

In addition to those discussed above, 3D cell culture systems have been utilised for various virological applications using numerous other human viruses; these are summarised in Table 1.4. Such models have proved invaluable in the advancement of our knowledge regarding host-virus interactions and viral pathogenesis, in addition to the culture of previously difficult-to-grow viruses, and even in the identification and screening of novel therapeutics (He et al., 2016). Whilst these emerging 3D culture technologies are gaining widespread attention in the viral research community, no such model has yet been utilised to study Bunyaviruses. The development of a 3D model of Bunyavirus infection may prove a valuable tool, given that much of the Bunyavirus life-cycle remains to be elucidated (see section 1.1.4), and the current lack of any effective vaccine or therapeutic agents (see section 1.1.2).

Table 1.4. 3D cell culture applications in human virology.

Virus	3D Culture Model	Cell Type	Applications	References
HPV	OERC	Primary human keratinocytes	• HPV interactions with cancer/other viruses • Propagation and infection • Replication cycle • Assessing the efficacy of therapeutics	(Fang et al., 2006; Andrei et al., 2010)
HIV	OERC	Gingival keratinocytes	• Effects of antiretroviral drugs	(Israr et al., 2010; 2011)
HSV	OERC	HaCaT keratinocytes	• Viral replication and spread	(Hukkanen et al., 1999)
HCV	RWV	Huh-7	• HCV life cycle	(Murakami et al., 2006; Sainz et al., 2009)
	Scaffold-based	HuS-E/2/ Huh-7.5	• Effects of anti-HCV drugs	(Aly et al., 2009)
HEV	RWV bioreactors	PLC/PRF/5	• Replication and propagation	(Berto et al., 2013)
VZV	OERC	Primary human keratinocytes	• Effects of antiviral drugs	(Andrei et al., 2005; Goodwin et al., 2013)
	RWV bioreactor	Human neural progenitor cells	• Infection	(Goodwin et al., 2013)
AdV	OERC	Primary human keratinocytes	• Adenovirus mutants	(Noya et al., 2003)
	3D organoids	HEK-293	• Adenovirus vectors	(Wang et al., 2014)
NoV	RWV bioreactor	Int-407, Caco-2	• Viral replication	(Straub et al., 2007; Straub et al., 2011)

Adapted from He et al. (2016). HPV: Human papillomavirus. HIV: Human immunodeficiency virus. HSV: Herpes simplex virus. HCV: Hepatitis C virus. HEV: Hepatitis E virus. VZV: Varicella-zoster virus. AdV: Adenovirus. NoV: Norovirus. OERC: Organotypic epithelial raft culture. RWV: Rotating wall vessel.

1.4 Thesis Aims

This project aims to establish a flowing 3D culture model using A549 and HuH-7 cells; that is permissive to infection with BUNV. This project will investigate whether this model can be utilised for downstream extraction and isolation of BUNV virions and exosomes for subsequent characterisation by western blotting and nanoparticle tracking analysis. Given that no such 3D model has been utilised for the study of Bunyaviruses, this project aims to provide the underpinning data required for successful maintenance of BUNV-infected multicellular spheroids (under flowing conditions). Therefore, the project objectives are as follows:

1. To optimise a differential ultracentrifugation protocol for the isolation of purified exosomes and viral particles.
2. To determine the effects of BUNV infection on cell viability in 2D versus 3D culture models.
3. To assess whether multicellular spheroids infected with BUNV can be maintained in a viable state under flowing conditions.
4. To determine if BUNV-infection induces exosome release, and to characterise differences in the exosome 'signature' between cells (+/- BUNV infection), in 2D versus 3D (microfluidic) cell culture models.

Chapter 2: Materials and Methods

2.1 Tissue Culture

2.1.1 Maintaining Mammalian Cell Lines

Human glioblastoma cells (U-87 MG) and human lung adenocarcinoma cells (A549) were purchased from the European Collection of Authenticated Cell Cultures (ECACC 89081402 and ECACC 86012804, respectively). The human hepatoma-derived HuH-7 cell line was provided by Prof. Mark Harris (University of Leeds). All cell lines were cultured in Dulbecco's modified Eagle's medium (DMEM) with 25mM HEPES and 4.5g/L Glucose (Fisher Scientific, Loughborough, UK). The culture medium was supplemented with a 1x Penicillin-Streptomycin solution (Lonza, Burton on Trent, UK), to a final concentration of 100 units/mL penicillin and 100µg/mL streptomycin. The medium was also supplemented with 10% (v/v) heat-inactivated foetal bovine serum (FBS; Labtech, Heathfield, UK). A549 and HuH-7 cells were additionally supplemented with 4mM L-Glutamine (Lonza), and HuH-7 cells were cultured in media with added non-essential amino acids (100µM NEAA; Lonza).

All cell lines were handled under sterile conditions in a class II biological safety cabinet per the Advisory Committee on Dangerous Pathogens (UK) guidelines. Furthermore, all cell lines were regularly screened in-house for mycoplasma infection.

Following the ECACC recommended sub-culture routine, U-87 MG and A549 cells were split 1:3 - 1:6 once sub-confluent (70 - 80%). HuH-7 cells were split 1:3 - 1:5 once sub-confluent. Stocks of each cell line were preserved at a low passage number in FBS with 10% (v/v) Dimethyl sulfoxide (DMSO; Thermo Fisher Scientific, Lancashire, UK), and stored in liquid nitrogen. Both U-87 MG cells and HuH-7 cells were maintained in continuous culture until reaching passage 35, and A549 cells were cultured to passage 30 before reviving an earlier cryostock. When split 1:4, A549 cells and HuH-7 cells reached the desired confluency after 4-5 days of incubation at 37°C, 5% CO_2. U-87 MG cells, when split 1:4, required 3 days of incubation to reach the desired confluency.

Once the desired confluency was reached (determined by light microscopy at 10x magnification), the supernatant was discarded into 1% Rely+On™ Virkon™ and the monolayer rinsed with 5mL phosphate-buffered saline (PBS). To detach the cell monolayers, 2mL 0.25%

trypsin (Thermo Fisher Scientific) was added to the flask followed by incubation at 37°C, 5% CO_2 for 3 - 10 minutes. U-87 MG cells required less incubation time with trypsin than HuH-7 and A549 cells. Typically, all U-87 MG cells had completely detached after 3 minutes of incubation; HuH-7 cells took approximately 5 minutes to detach, and A549 cells often required 5 - 10 minutes of incubation with trypsin for cells to fully disassociate from the adherent base.

For U-87 MG cells, 3mL appropriate media was added to the flasks to neutralise the trypsin once all cells had detached. The resulting cell suspension was transferred into a 15mL tube (Sarstedt, Leicester, UK) and centrifuged at 400 x *g* for 4 minutes at room temperature to form a pellet of cells. Without disrupting the cell pellet, the supernatant was discarded; the cell pellet was then resuspended by aspirating with an appropriate volume of fresh media. Cell suspensions were divided equally between culture flasks (1mL/flask). For the HuH-7 and A549 cells, 8mL appropriate fresh media was added to neutralise the 2mL trypsin in the flasks. The cell suspension was aspirated using a serological pipette (Sarstedt) to ensure a homogenous solution, and an appropriate volume of cell suspension was transferred into a new flask, i.e., 2.5mL to obtain a split ratio of 1:4.

Cell lines in continuous culture were maintained in 75cm^2 adherent tissue culture flasks (Sarstedt) with filter caps to allow for consistent gas exchange whilst providing a barrier against micro-organisms. Cells were trypsinised for the minimum time required for all cells to detach from the base of the flasks to reduce cell damage and degradation of cell surface proteins (Lai et al., 2022). An enzymatic approach was chosen over non-enzymatic means of cell detachment (i.e., using a dissociation buffer), as this is recommended for the routine serial passage of strongly adherent cell lines; such as those used in this study (Heng et al., 2009). Furthermore, using trypsin to dissociate cells, as opposed to a dissociation buffer (which operates by chelating free calcium and magnesium ions in solution), prevents complications related to salt carry-over in subsequent infection experiments. Care was taken to ensure that all cells had detached by gently tapping the side of the flask and examining the cells under a light microscope before neutralising the trypsin. This ensured that less adherent cell populations were not being unintentionally propagated. Cells cultured in T75 flasks were supplemented with 20mL of appropriate media, maintained in a 37°C, 5% CO_2 incubator and inspected daily for confluency and contamination.

2.1.2 Cell Line Authentication

To verify the identity of the U-87 MG and HuH-7 cell lines, they were sent to a UKAS accredited genetic testing laboratory (NorthGene™, Biofortuna Limited, Deeside, UK), for authentication using Short Tandem Repeat (STR) analysis. DNA profiles were generated and compared to profiles on the American Type Culture Collection (ATCC) database.

A 100% match was found for the U-87 MG cells. The HuH-7 cell line has never been deposited on the ATCC, so a matching percentage was not provided. However, 6 out of the 9 STR loci tested matched the DNA profile (STR-PCR data) listed on the European Collection of Authenticated Cell Cultures (ECACC) database. The matching loci were as follows: Amelogenin: X, CSF1PO: 11, D13S317: 10, D16S539: 10, THO1: 7, vWA: 16,18. Differences in the genome profiles generated between laboratories could be attributed to the clonal evolution of cells during long-term cell culture (Kasai et al., 2016). The HuH-7 cell line consists of highly heterogenous cell populations; this is evidenced by Blight et al. (2002), who report that Hepatitis C virus (HCV) replication is only supported in certain subpopulations of HuH-7 cells. Due to this heterogeneity, an accurate genome profile has not been available for the HuH-7 cell line, since its establishment in 1982 (Nakabayashi et al., 1982).

The A549 cells, a gift from L. Sadofsky (University of Hull), were not sent for authentication as they were recently purchased from the ECACC, which are subject to scrutiny to ensure the integrity of their cell lines.

2.1.3 Cell Counting

Cell monolayers were detached from tissue culture flasks as described in section 2.1.1. Cells were counted using a haemocytometer (Hawksley, Sussex, UK) viewed at x10 magnification; 10µL cell suspension was homogenised with 10µL Trypan Blue (Sigma-Aldrich, Gillingham, UK) in a 0.5mL polypropylene tube. 10µL of the resulting solution was pipetted into the counting chamber. Only live (unstained) cells were counted in all 4 sets of 16 squares using a hand tally counter (Figure 2.1). A system was followed whereby cells which lay on the boundary of the bottom and left lines were not included in the total cell count. The concentration of cells/mL was calculated using Equation 1.

Equation 1. Calculating cell concentration.

$$no.cells/mL = \left(\left(\frac{no.cells\ counted}{4}\right) x\ 2\right) x\ 10^4$$

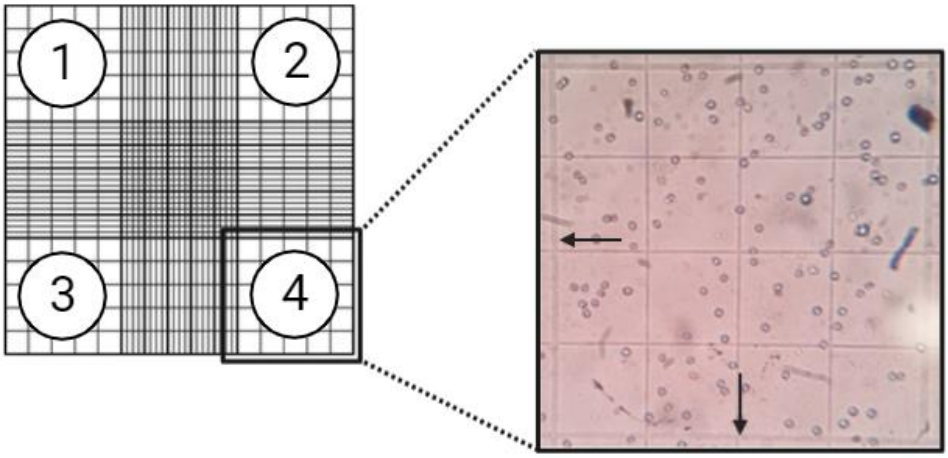

Figure 2.1 Haemocytometer grid. *The haemocytometer is divided into 9 major squares, each 1mm2 in size. The four corner squares (1 – 4) are further divided into 4 x 4 grids. When the cover glass is applied, the volume of each chamber (1 - 4) equals 0.1mm3 (10^{-4}mL). The zoom callout (square 4) shows A549 cells in the counting chamber of the haemocytometer, viewed under a light microscope at x10 magnification. Arrows point to the bottom and left boundary lines, cells on this boundary are not included in the total cell count*

2.1.4 2D Monolayer Cell Culture

Cells were seeded into CytoOne® 6-well plates (Starlab, Milton Keynes, UK) to perform subsequent 2D BUNV infection experiments, i.e., to adapt BUNV to the other cell lines used in this study (see section 2.3.4), and to obtain the '2D' samples for western blotting (see section 2.8.1). In 6-well plates, cells were seeded at a density of 0.4 x 10^6 cells/well in 1mL and supplemented with 2mL media to obtain 70-80% confluent monolayers after 24 hours of incubation at 37°C, 5% CO2 (Table 2.1).

For the analysis of cell viability in 2D culture (+/- BUNV infection) via MTS assay (see section 2.5.2), cells were seeded into 96 well flat-bottom plates (Sarstedt) at a density of 5,000 cells/well in 100µL.

To obtain the correct seeding density, cells were dissociated using trypsin once 70-80% confluent and neutralised as described in section 2.1.1. Once neutralised, the resulting cell suspensions were centrifuged at room temperature for 4 minutes at 400 *x g*, the supernatant was discarded, and the pellet resuspended in 1mL of fresh media. Cells were counted as described in section 2.1.3, and cell concentration was calculated using Equation 1 (see section 2.1.3).

Equation 2 was used to determine the dilution factor required to obtain the desired cell count per 1mL of cell suspension for seeding into 6-well plates.

Equation 2. Calculating the dilution factor required when adding 1mL/well.

$$Dilution\ Factor = \frac{no.\ cells/mL}{(\ desired\ cell\ count)} - 1$$

For seeding into 96-well plates, the 'desired cell count' was multiplied by 10 (Equation 3) since only 100µL of cell suspension was to be added to each well in the plate. For each calculation, '1' must be subtracted from the result to account for the 1mL of media used to resuspend the cells. The dilution factor refers to the volume of fresh media which must be added to the 1mL cell suspension to obtain the desired cell density in 1mL (6 well) or 100µL (96 well) of cell suspension.

Equation 3. Calculating the dilution factor required when adding 100µL/well.

$$Dilution\ Factor = \frac{no.\ cells/ml}{(\ 10\ x\ desired\ cell\ count)} - 1$$

Table 2.1. Seeding densities for 2D cell culture.

	Surface area of well (cm^2)	**Average no. cells/well at 100% confluency**	**Seeding density**
6-Well Plate	9.6	1.2×10^6	4×10^5
96-Well Flat-Bottom Plate	0.32	4×10^4	5×10^3

2.1.5 3D Spheroid Cell Culture

Ultra-Low Attachment (ULA) plates (Corning, Flintshire, UK) were used to facilitate the formation of uniform U-87 MG, HuH-7 and A549 spheroids (Figure 2.2), due to their ease of use and the well-documented ability for each of these cell lines to form 3D spheroids using this anchorage-independent technique (Khawar et al., 2018; Saleh et al., 2020; Collins et al., 2021). U-87-MG, HuH-7 and A549 cells were harvested, counted, and resuspended as described in section 2.1.4.

The optimal seeding densities and incubation times for HuH-7 and A549 cells were determined by spheroid growth analyses as described in section 2.2.1. U-87 spheroid growth optimisation has been conducted extensively at the University of Hull; therefore, no further 3D culture optimisation of this cell line was required for this study.

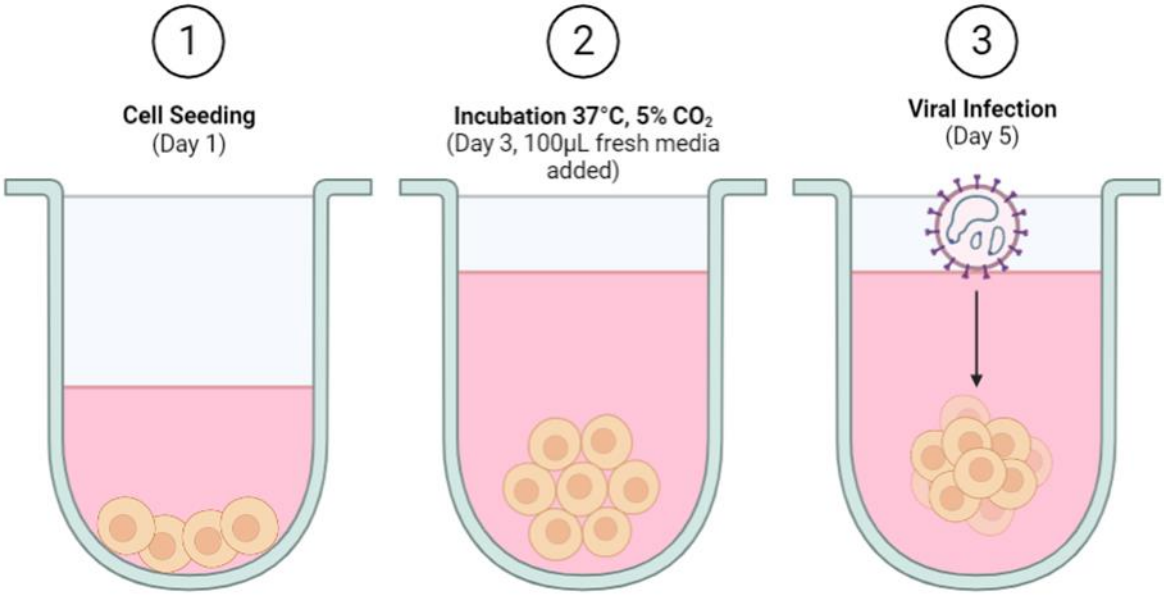

Figure 2.2. A549 and HuH-7 3D spheroid cell culture using an ultra-low attachment (ULA) plate. *Cells are seeded into wells in 100µL of culture medium. After 3 days of incubation at 37°C, 5% CO_2, the forming spheroids are supplemented with an additional 100µL fresh culture medium. The media is refreshed every 2 days thereafter, by carefully removing 100µL of spent media from each well and adding 100µL of fresh media. A549 and HuH-7 spheroids remain in the 37°C, 5% CO_2 incubator for 5 days post-seeding. After allowing 5 days for spheroid growth, infection with BUNV is performed for subsequent experiments.*

2.2 Spheroid Growth Analysis

2.2.1 A549 & HuH-7 Spheroid Optimisation

To determine the optimal 3D culture conditions to form HuH-7 and A549 spheroids, images of spheroids (seeded at varying cell densities) were taken using the PC software-operated colony counter GelCount™ by Oxford Optronix for 10 days post-seeding. The horizontal and vertical diameter of each of the spheroids was measured using ImageJ software (Figure 2.3) to obtain an average spheroid diameter.

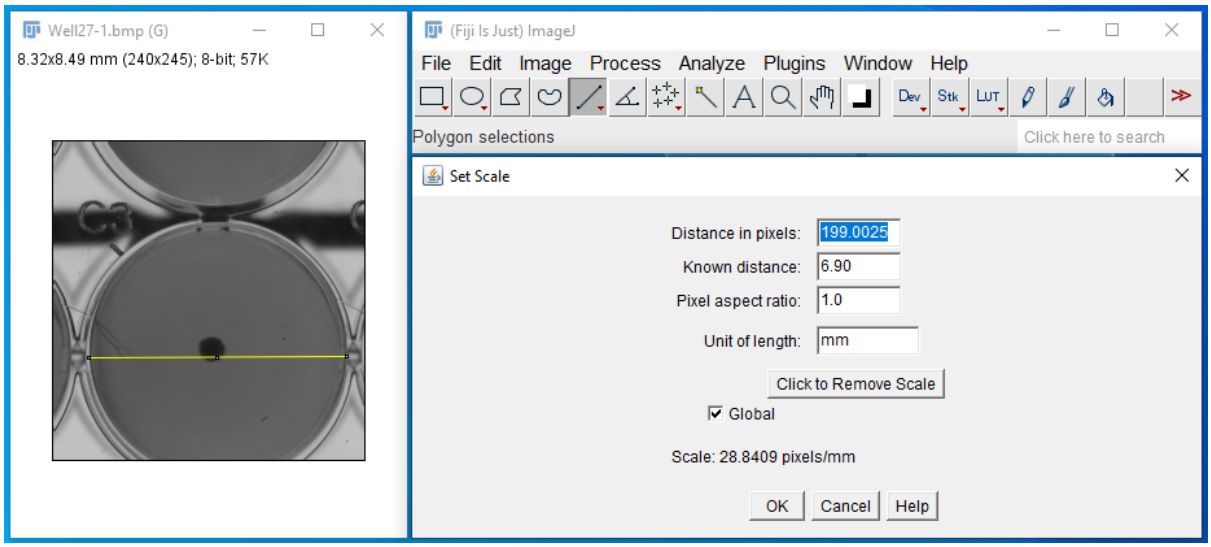

Figure 2.3. Setting the scale on ImageJ software to measure the spheroid diameter. *The horizontal diameter of the well (yellow line) is measured. The distance in pixels, calculated by ImageJ, is divided by the known diameter of the well (6.9mm) to provide a scale (pixels/mm). After setting the scale, future spheroid measurements are converted into the selected unit of length (mm).*

Seeding density was calculated and ULA plates were seeded as described in section 2.1.5. After 3 days of incubation, an additional 100µL of appropriate fresh media (see section 2.1.1) was added to each well, resulting in a total well volume of 200µL. The media was refreshed every 2 days thereafter as described in section 2.1.5.

2.2.2 Effects of Reduced-Serum Conditions on Spheroid Growth

A549 and HuH-7 cells were seeded into ULA plates at a density of 30,000 and 5,000 cells/well, respectively, and maintained in a 37°C, 5% CO_2 incubator for 5 days. The forming spheroids were supplemented with 100µL of fresh media (DMEM, + 10% (v/v) FBS, as shown in Figure 2.2, after 3 days of incubation. After 5 days, the media in each well (200µL) was carefully removed, without disrupting the spheroids. Each spheroid was then washed with 100µL PBS, before being supplemented with 200µL fresh media (DMEM, +2% (v/v) FBS, -P/S, +4mM L-Glutamine). The 2% (v/v) FBS media was refreshed every 2 days thereafter, as described in section 2.1.5.

The spheroids were imaged on the GelCount™ colony counter 24, 48, 72, 120, 168, and 240 hours following their transition into the reduced-serum media. During this period, the spheroids were maintained in a 33°C, 5% CO_2 incubator. For each cell line, 10 spheroids were analysed using ImageJ software as described in section 2.2.1.

2.3 Infection of Mammalian Cells with BUNV

2.3.1 Virus Containing Media

The cell culture medium used for experiments involving BUNV was as described in section 2.1.1, except that no P/S was added to the media. Also, the FBS concentration was reduced to 2% (v/v) for all cell lines, as recommended by the ATCC, since components within the FBS can interfere with viral attachment and replication (Hossain et al., 2008; Qin et al., 2013). Reducing FBS concentration to 2% (v/v) for BUNV infection experiments is widely reported in the literature (Hover et al., 2016; Varela et al., 2017; Hover et al., 2018; Shen et al., 2018; Mastrodomenico et al., 2019). For experiments in which supernatant was collected for EV isolation (see section 22.7), the culture medium was supplemented with 2% (v/v) exosome-depleted FBS (Thermo Fisher Scientific). Exosomes are present in the serum used for tissue culture; by utilising exosome-depleted FBS, we ensure that the exosomes purified from conditioned media are derived from the cultured cells and are not contaminated by exogenous exosomes present in the culture medium (Shelke et al., 2014).

2.3.2 BUNV Titration Method – Plaque Assay

Wild type (WT) BUNV was rescued from cloned complementary DNAs which were originally reverse engineered by Bridgen and Elliott (1996) and a kind gift from J. Barr (University of Leeds). Stocks of WT-BUNV were stored at -80°C in 1mL, 100µL, and 20µL aliquots in A549/HuH-7 derived spent media. The virus stocks were propagated in A549 cells and HuH-7 cells (see section 2.3.4), and the viral titre was determined by plaque assay. Methylcellulose (1.6% (w/v) in dH_2O; Scientific Laboratory Supplies Ltd, Nottingham, UK) was utilised as the liquid-overlay matrix to immobilise plaques, and crystal violet to stain plaques for ease of visualisation. To generate further stocks of WT-BUNV, sub-confluent (70-80%) monolayers of A549/HuH-7 cells were infected with a serial dilution of WT-BUNV (Figure 2.4), in a 6-well plate format. To each well, 1mL virus-containing media (10^{-5} - 10^{-7}, in duplicate) was added before incubation at 33°C, 5% CO_2 for 1 hour. To ensure equal virus adhesion distribution, the plates were rocked gently every 15 minutes during this incubation period.

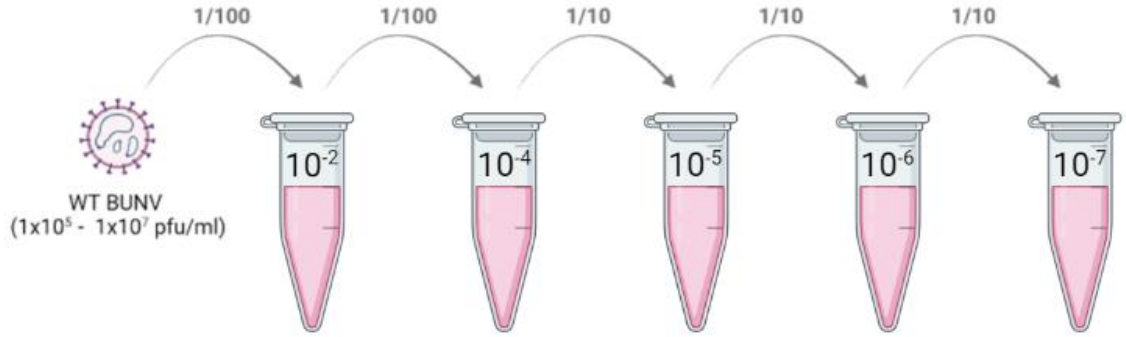

Figure 2.4. BUNV serial dilution, created on Biorender.com. *Sub-confluent monolayers of A549/HuH-7 cells in each well of the 6-well plate are infected with 1mL of diluted virus (10^{-5}, 10^{-6}, and 10^{-7}, in duplicate).*

After 1 hour, the supernatant containing any unbound viral particles was discarded into 1% Chemgene. A 1:1 solution of 1.6% (w/v) methylcellulose in dH_2O, and DMEM (as described in 2.3.1) was then gently added to the infected cells (4mL/well). To allow the formation of plaques, cells were left to incubate (at 33°C, 5% CO_2) for 5 days.

After 5 days of incubation, most of the methylcellulose/media overlay was carefully aspirated off and the monolayers then fixed with two rounds of 10% formaldehyde (Sigma-Aldrich) in PBS. To each well, 2mL 10% formaldehyde was added; the plate was then left at room temperature for 10 minutes before aspirating off this solution and fixing again with 2mL/well 10% formaldehyde for an additional 10 minutes. The second fixing step was found to reduce monolayer destruction and the lifting of cells. The cell monolayers were then rinsed once with PBS, and twice with dH_2O. To stain, 1mL of 0.1% (w/v) crystal violet made up in 20% ethanol was added to each well. The plates were then placed on a plate rocker at room temperature for one hour. After one hour, the stain was removed, and each well was washed with dH_2O and dried before counting plaques.

By utilising the 6-well plate format, two technical replicates were acquired for each dilution (10^{-5} – 10^{-7}). The average number of plaques was calculated for each dilution to determine viral concentration. The total plaque forming units (pfu) per mL were calculated by taking the average number of plaques for a dilution and the inverse of the dilution factor (Equation 4).

Equation 4. Calculating total pfu/mL.

$$\frac{Average\ no.plaques}{Dilution\ x\ Volume} = Pfu/mL$$

2.3.3 Calculating Multiplicity of Infection (MOI)

The multiplicity of infection (MOI) refers to the number of viral particles per cell, i.e., when performing an infection at an MOI of 1, the viral stock is diluted so that the number of viral particles (usually diluted in 1mL of media) is equivalent to the number of cells which are to be infected. Detailed below is an example calculation to determine the amount of viral stock (titre: 1 x 10^7 pfu/mL) needed to infect a confluent 6-well plate (approximately 1.2 x 10^6 cells/well) at an MOI of 1, using 1mL diluted virus per well.

<u>MOI 1 calculation (6-well plate):</u>

1) Desired MOI **(1)** x no. of cells per well **(1.2 x 10^6)** = total pfu/mL needed **(1.2 x 10^6)**
2) Total pfu/mL needed **(1.2 x 10^6)** / stock titre **(1 x 10^7 pfu/mL)** = volume of stock needed in 1mL of media for an MOI of 1 **(0.12mL)**
3) To generate enough diluted virus, the volume of stock required is multiplied by 6 (as there are 6x wells): **0.12mL x 6 = 0.72mL**

Therefore, 0.72mL of viral stock is diluted in 5.28mL media. To infect the cells at an MOI of 1, 1mL of the diluted virus is added per well.

2.3.4 Generating Stocks of HuH-7 and U-87 MG Adapted BUNV

i) HuH-7 Adaptation

A549 propagated viral stocks of WT-BUNV (titre: 3.7 x 10^7 pfu/mL) were used to generate further virus stocks which were adapted to the HuH-7 cell line. For this adaptation, sub-confluent monolayers of HuH-7 cells (in a 6-well plate) were infected with BUNV at MOIs increasing 10-fold from 0.01 to 1; 2x wells were infected at each MOI. Infection with BUNV can be successfully achieved at MOIs ranging from 0.1- 10 (Newton Susan et al., 1981; Szemiel et al., 2012; Shi et al., 2016; Hover et al., 2018; Heitmann et al., 2021). A low MOI range was used for these adaptation experiments, to allow the cells to enter an antiviral state before lysis, mimicking natural infection. Using high MOIs can quickly lead to the formation of defective interfering (DI) particles (first observed by von Magnus (1954) as "incomplete" virus particles). Using lower MOI ranges in infection experiments avoids the generation of significant quantities of DI particles, which interfere with viral replication through diverse mechanisms (Yang et al., 2019).

MOI was calculated as described in section 2.3.3, and 1mL of the diluted virus was added per well. This was followed by incubation at 33°C, 5% CO_2 for 1 hour, with gentle rocking every 15 minutes to ensure even distribution of the viral particles. After 1 hour, the virus-containing supernatant was discarded, and each well was supplemented with 4mL fresh medium (as described in section 2.3.1).

The infected HuH-7 cells were then incubated at 33°C, 5% CO_2 for 5 days, and monitored daily for any cytopathic effect (CPE). After 5 days, the spent media was collected from each well and the viral titre was determined by plaque assay as described in section 2.3.2, using HuH-7 cells in the plaquing plates to yield an accurate titre. However, as lower viral titres were expected in this initial adaptation experiment, the dilution ranges used for these titrations were 10^{-4}, 10^{-5}, and 10^{-6}. A separate plaque assay plate was set up to titre the supernatant collected from each well in the original infection plate (a total of 6x plaque assay plates).

ii) U-87 MG Adaptation

The same process as described above for BUNV adaptation to HuH-7 cells was conducted using U-87 MG cells. However, when monitoring CPE at 72 hours post-infection (72hpi), monolayer destruction and extensive lifting of the U-87 MG cells was observed at all MOIs used (0.01, 0.1, and 1). Therefore, the supernatant from each well was collected at 72hpi (as opposed to 120hpi used for HuH-7 adaptation) and centrifuged at 400 *x g* for 5 minutes (at 4°C) to remove the dead cells. The pellet of dead cells was discarded, and the viral titre of each supernatant was assessed by plaque assay as detailed above. As described for HuH-7 BUNV adaptation, U-87 MG cells were used in the plaquing plates to yield accurate titre. However, the same destruction of the monolayer and extensive lifting of U-87 MG cells were observed in the plaque assay plates, therefore no plaques could be counted.

Further plaque assays were performed with altered conditions to attempt to generate stocks of U-87 MG adapted WT-BUNV, as detailed in section 3.1.3. However, due to time constraints, it was not possible to generate U-87 MG adapted BUNV stocks, therefore, all infection experiments are conducted using the A549 and HuH-7 cell lines, for which virus stocks had been successfully obtained.

2.3.5 Infecting 3D Spheroids with BUNV

Spheroids were seeded into ULA plates as described in section 2.1.5. Infection with BUNV was performed on day 5 (post-seeding) when uniform spheroids had formed (Figure 2.2). The MOI was calculated as described in section 2.3.3, using the initial seeding density (see ***Table 3.1***) as an approximation for the number of cells/well.

Firstly, the spent media in each well of the ULA plate was carefully removed without disrupting the spheroids (200µL). The spheroids were then washed with 100µL of PBS to remove any residual traces of P/S. Infection was then performed by adding 100µL/well of diluted virus - MOIs increasing 10-fold from 0.1 – 10 were used for viability analyses (see sections 22.5 and 22.6), and for exosome characterisation (see section 22.8).

Since only 100µL of the diluted virus was added to each spheroid (as opposed to 1mL for 2D infections), the total pfu/mL needed (see section 2.3.3 – MOI calculation (2)) was multiplied

by 10. The spheroids were incubated with the diluted virus for 2 hours at 33°C, 5% CO_2; a longer incubation period was utilised due to the lower surface area: volume ratio of the spheroids, compared to cell monolayers. After 2 hours, the supernatant containing the diluted virus was carefully removed, and the spheroids were supplemented with 200µL of fresh culture medium (+2% (v/v) FBS, -P/S). The media was refreshed every 2 days thereafter, as described in section 2.1.5, and the infected spheroids were maintained in a 33°C, 5% CO_2 incubator.

2.4 Microfluidic Cell Culture

2.4.1 Chip Assembly

The polymethyl methacrylate (PMMA) chips used to house the spheroids in the microfluidic culture model were designed, laser cut, and chloroform bonded at the University of Hull. PMMA sheets (Kingston Plastics, Hull, UK) were purchased at three thicknesses: 12mm, 5mm and 3mm. Each component of the microfluidic chip was drawn using the computer-aided design (CAD) software SolidWorks (Waltham, USA). The chip components were then laser cut using a Laserscript LS6840 PRO CO_2 laser cutting machine (HPC Laser Ltd, Halifax, UK), following the cutting pathways exported from SolidWorks (Figure 2.5).

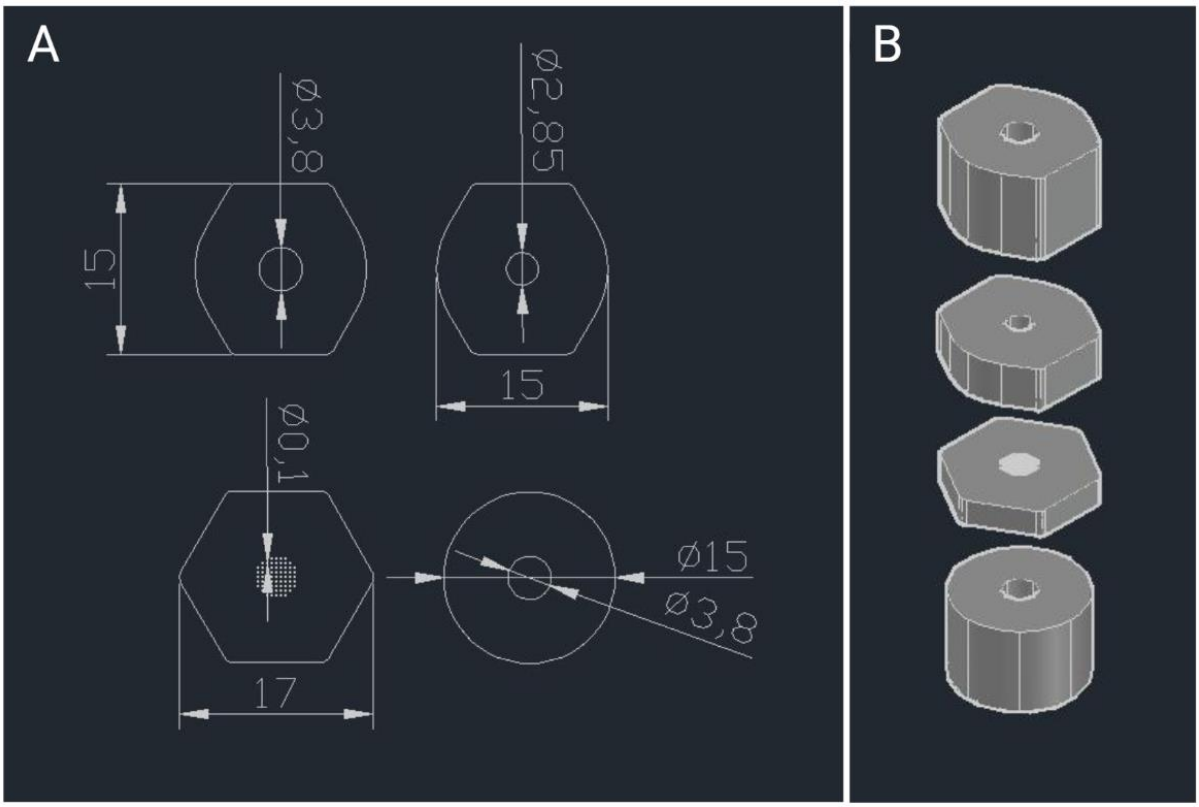

Figure 2.5. Microfluidic chip components. ***A:*** *SolidWorks blueprint for laser cutting including component dimensions (millimetres).* ***B:*** *SolidWorks 3D render; components are bonded in the orientation shown. Components are as follows (B; top-bottom): inlet, tissue chamber, grid matrix, outlet.*

The chips were then assembled using a solvent-bonding technique (Lin et al., 2007). Firstly, the components were correctly orientated by test fitting Luer connectors into the inlet and outlet components. The grid matrix (see Figure 2.5) was orientated so that the holes tapered toward the outlet. A 100µL pipette tip was utilised to dispense a small volume of chloroform (Sigma-Aldrich) onto one component, on the surface to which the next component was to be joined. Care was taken to ensure that the chloroform did not enter the channels at the centre of each component, particularly in the grid matrix, to prevent blockages. The adjoining component was then carefully aligned, and pressure was applied by hand for 2 minutes to ensure a strong bond. This process was repeated until all four components had been joined. chloroform was then gently pipetted around the circumference of each join-point, and the assembled chips were stood upright, and left overnight in a fume-cupboard to allow the chloroform to evaporate.

Before use, the chips were tested for leaks. To do this, the input and output tubing (see section 2.4.2) was firmly connected to the chips, followed by infusion with dH_2O at 20µL/min for 4 hours. During the test infusion period, the chips were placed on absorbent paper so that any leaks could be easily identified. If a leak was found, chloroform was applied once again to the join points, and the components were firmly clamped together using a screw clamp before drying overnight. Once dried, the chips were then test-infused again to ensure that the leakage was repaired.

2.4.2 Microfluidic Device Set-up

All microfluidic device assembly was performed under sterile conditions in the containment level 3 (CL3) laboratory. All tubing and adaptors used for microfluidic culture were purchased from Ibidi (Germany). To prepare the input tubing, 0.8mm silicone tubing was evenly cut into 15cm long sections, and each end of the tubing was firmly pushed over the barbs of 1x Luer lock connector female and 1x elbow Luer connector male. The outlet tubing; 1.6mm silicone tubing was also divided into 15cm long sections. However, each section of outlet tubing was connected to 1x elbow Luer connector male only, with the other end of the tubing left open to allow for effluent collection.

The tubing was connected to the inlet and outlet components of the PMMA chip (see section 2.4.1) via the elbow connectors. A 20mL syringe (BD Plastics Ltd, Sunderland, UK) filled with 70% (v/v) ethanol in dH_2O was then attached to the Luer lock connector of the inlet tubing, and each chip was flushed with 5mL to sterilise. The chips were then rinsed by flushing with 5mL dH_2O, followed by 5mL pre-warmed media (+2% (v/v) FBS, -P/S, see section 2.3.1). Next, 20mL syringes (1x per experimental condition) were filled with the pre-warmed media, and each syringe was connected to a 0.2µM syringe filter. To prevent the introduction of air bubbles into the chips, the filled syringes (containing approximately 2mL surplus media) were gently pressed until a meniscus formed at the top of the syringe filter. The syringe was then connected to the input Luer, and any excess media was flushed through the chip so that each syringe read exactly 20mL. The protocol used for the assembly of the microfluidic devices, and the flow dynamics used in this study are based on previous optimisation studies conducted at the University of Hull (Sennett, 2019).

Spheroids were infected/mock infected as described in section 2.1.5. After the 2-hour infection period, each spheroid in the ULA plate was supplemented with 200µL fresh media (+2% (v/v) FBS, -P/S), and immediately transferred into chips. To transfer the spheroids into the chips, the outlet tubing was held in an elevated position, above the inlet component, so that the input tubing could be removed without draining media from the chip (Figure 2.6). Spheroids were collected from the ULA plate and gently transferred into the tissue chamber, 4x spheroids (for each experimental condition used) were placed into each chip. A 1000µL pipette tip was utilised for this transfer; this was found to limit mechanical stress and reduce spheroid damage/disaggregation.

Once 4x spheroids had been successfully transferred into the tissue chamber, surplus media from the ULA plate was gently added into the inlet until a meniscus was formed. The 20mL syringe (attached to the input tubing) was then lightly pressed so that a meniscus formed at the tip of the input Luer. The menisci at the input Luer and inlet component were joined, to prevent air bubble formation, and the input tubing was firmly pressed into the inlet (Figure 2.6).

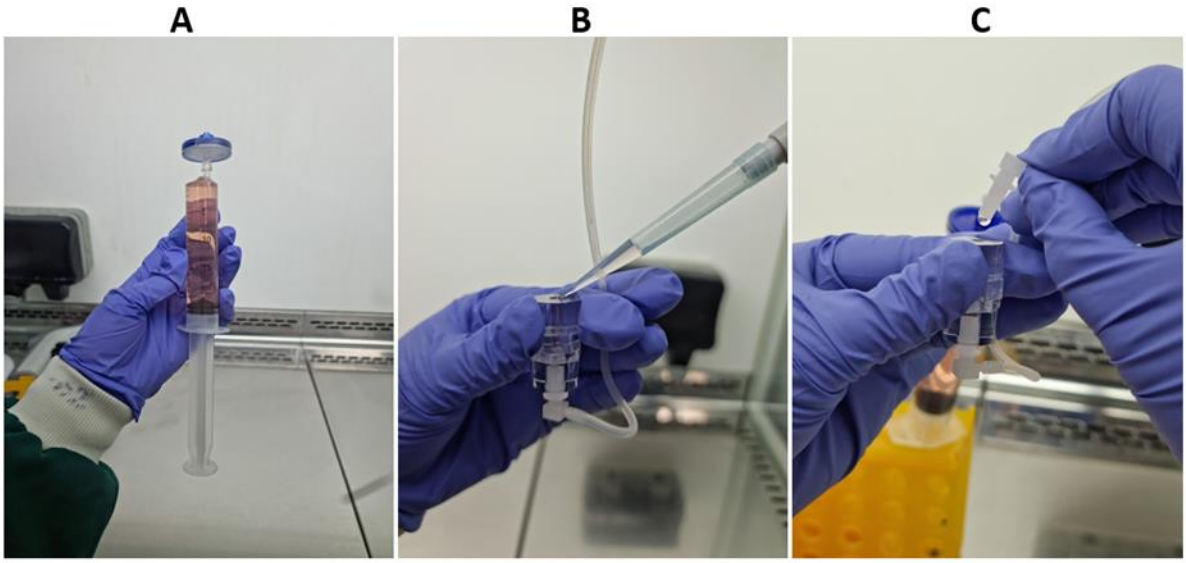

Figure 2.6. Microfluidic chip set-up process. ***A:*** *A 20mL syringe is filled to the stop with prewarmed media. A 20µM syringe filter is connected and air bubbles removed before flushing the surplus media through the chip so that the syringe reads exactly 20mL.* ***B:*** *The output tubing is elevated above the input so that media is retained in a closed system to allow spheroids to be transferred into the tissue chamber.* ***C:*** *Menisci at the tip of the input Luer and the inlet component are joined and firmly pressed together to complete the chip set-up.*

The assembled microfluidic devices were held in the correct orientation, with the inlet at the top, using a custom-built, 3D-printed, chip holder. The open ends of the output tubing were fed into corresponding, labelled, 15mL polypropylene tubes to allow for effluent collection. A hole was made in the lid of each 15mL tube so that the output tubing could be fed through; a small pinhole was also made in the lid of each tube to prevent pressure build-up. Each syringe, containing 20mL media, was then secured onto a Harvard Apparatus PHD 2000 Infusion Pump, contained within a 33°C, 5% CO_2 incubator (Figure 2.7). For all experiments, an infusion rate of 2µL/min was used.

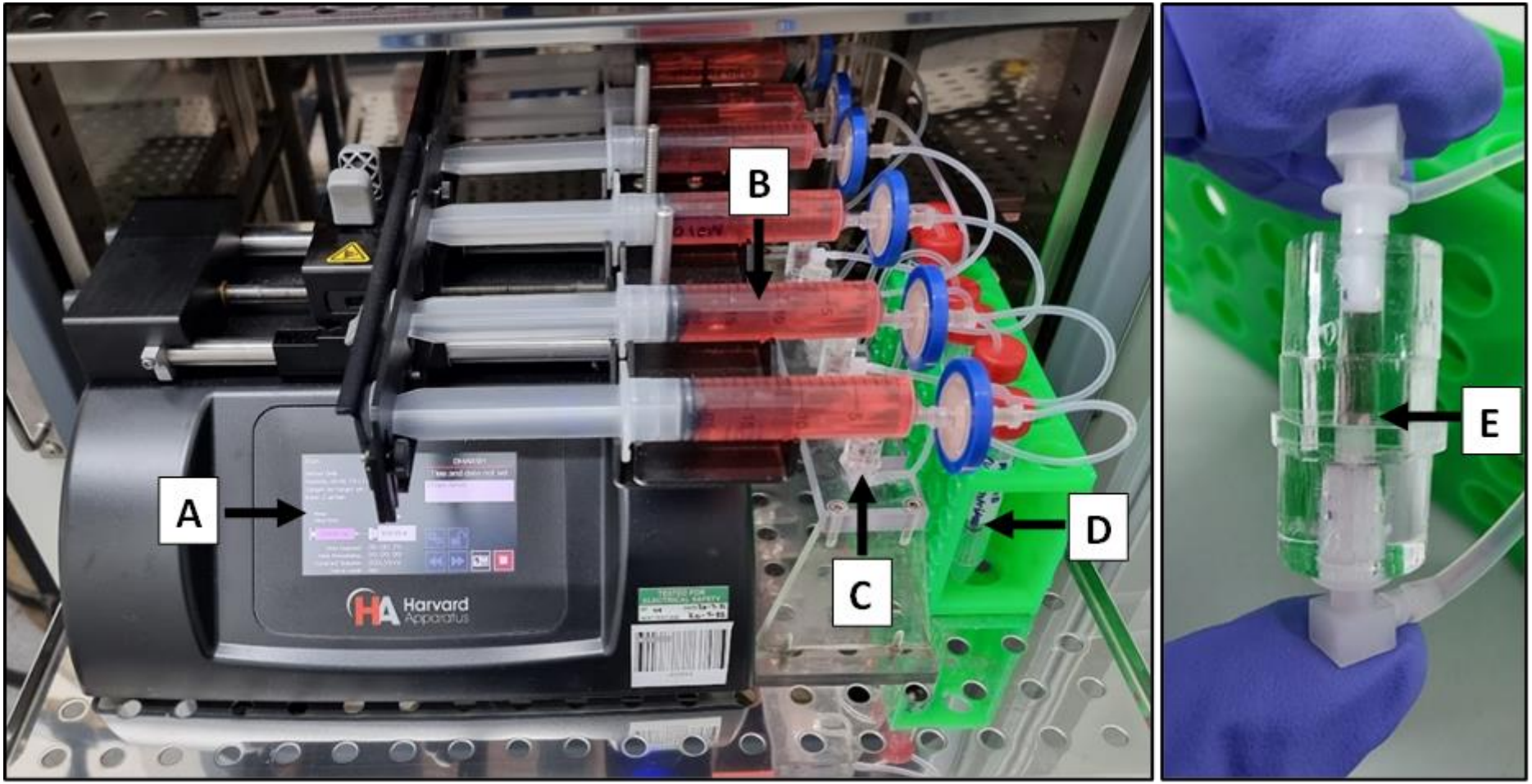

Figure 2.7. Microfluidic device set-up inside of a 33°C, 5% CO_2 incubator. ***A:*** *Harvard Apparatus PHD 2000 Infusion pump control screen, infusion is set at 2µL/min. Flow rate is calculated based on the syringe diameter which is manually input into the infusion pump.* ***B:*** *20mL syringe containing assay medium (+2% (v/v) FBS, -P/S), attached to a 0.2µM sterile filter.* ***C:*** *Assembled PMMA microfluidic chips containing 4x spheroids, held in correct orientation by a custom-build holder.* ***D:*** *Labelled 15mL polypropylene tubes into which microfluidic effluent is collected.* ***E:*** *Coalesced A549 spheroids contained within a chip, after 120-hours of media infusion.*

2.5 Investigating the Effects of BUNV Infection on Cell Viability in 2D vs 3D (Static) Cell Cultures

2.5.1 Fluorescence Microscopy (with Live/Dead Staining)

Fluorescence microscopy was utilised to assess the effects of BUNV infection on cell viability and cell death in 3D (static) cultures of A549 and HuH-7 cells. To do this, spheroids were infected as described in section 2.3.5. Control 'uninfected' (mock-infected) spheroids were analysed alongside spheroids infected with BUNV at MOIs of 0.1, 1 and 10. After 24, 72, and 120 hours of incubation (post-infection), 3x spheroids (for each cell line and MOI used) were treated with a fluorescein diacetate (FDA) and propidium iodide (PI) staining solution (Table 2.2) and analysed under a fluorescence microscope at 5x magnification using Zen software (Zeiss, Germany).

FDA is taken up by the cells forming the spheroids and, in viable cells, the non-fluorescent FDA is converted into the green-fluorescent metabolite fluorescein, in an esterase-dependent reaction. PI is unable to pass through the membranes of living cells, however, loss of integrity in the membranes of damaged/dead cells makes them permissive to the PI. In these damaged/dead cells, PI binds to DNA by intercalating with the bases. Simultaneous staining with FDA and PI, therefore, allows for two-colour discrimination of living and dead cells in a population (Jones & Senft, 1985).

A 5% (w/v) FDA stock was prepared by dissolving 5mg FDA (Sigma-Aldrich) in 1mL acetone in a 15mL polypropylene tube. The tube was wrapped in foil to prevent UV degradation and stored at -20°C (for up to 2 weeks). The PI stock was prepared by adding 1mL of PBS to 2mg PI (Sigma-Aldrich) in the UV-resistant glass vial in which the PI arrived. The 2% (w/v) PI stock was stored at 4°C per the manufacturer's recommendations.

The FDA/PI staining solution was prepared as shown in Table 2.2.

Table 2.2. FDA/PI staining solution.

Reagent	Volume (µL)
PBS	5000
FDA (5mg/mL)	8
PI (2mg/mL)	50

PBS: Phosphate-buffered saline, FDA: Fluorescein diacetate, PI: Propidium iodide.

Before staining, the spheroids were transferred from the ULA plate into a 96-well flat bottom plate, and each spheroid was washed with 200µL PBS. The FDA/PI staining solution (Table 2.2) was then added (200µL/well), followed by incubation at 33°C, 5% CO_2, for 15 minutes. After 15 minutes, the staining solution was carefully removed, and each spheroid was washed twice with PBS.

The spheroids were immediately analysed under the fluorescent microscope using pre-set filters for fluorescein (green laser - 488nm excitation), and PI (red laser - 540nm excitation). The images were then digitally overlaid, and a scale bar was added using the Zeiss Zen software.

2.5.2 MTS Assay

i) MTS Assay Principle

The effects of BUNV infection on cell viability in 2D vs 3D (static) cell cultures were determined by MTS assay. This assay is based on the conversion of the MTS tetrazolium compound by NAD(P)H-dependent dehydrogenase enzymes in metabolically active (viable) cells. The coloured formazan product which is formed from the reduction of the MTS tetrazolium compound is soluble in the cell culture medium and can be quantified by recording the absorbance at 490nm.

ii) Performing the MTS Assay

A convenient 'One Solution' MTS assay was used in this study; eliminating the solubilisation steps which are required in the more time-consuming MTT assay. The MTS reagent: CellTiter 96® Aqueous One Solution Cell Proliferation Assay (Promega, Southampton, UK) was utilised per the manufacturer's standard operating procedure. To prevent UV and freeze/thaw degradation of the MTS reagent, 1mL aliquots were stored at -20°C in UV-resistant polypropylene tubes (Sarstedt). The volume of MTS reagent required for each assay was calculated and thawed before use.

A549 and HuH-7 cells were seeded into 2x 96-well flat bottom plates (2D culture), and 2x ULA plates (3D culture) as described in sections 2.1.4 and 2.1.5, respectively. The plates were

incubated at 37°C, 5% CO_2 for 3 days (2D culture) or 5 days (3D culture), before performing infections with BUNV as described in section 2.3. For 2D investigations, confluent monolayers of A549 and HuH-7 cells were infected with BUNV at MOIs of 0.1, 1, and 10 (20x wells for each MOI used). For the 'uninfected control', 20x wells were mock-infected with plain cell culture medium (-P/S, +2% (v/v) FBS). For 3D investigations, 20x spheroids (of each cell line) were infected/mock-infected, using the same experimental conditions as detailed above for 2D culture.

Each well (2D & 3D) was supplemented with 200µL fresh media (-P/S, +2% (v/v) FBS) following infection/mock-infection, the media was refreshed every 2 days thereafter. When setting up the plates for each MTS assay, 20x 'no cell' control wells were also included to assess for interference from the assay medium when recording the absorbance, these wells contained cell culture medium (-P/S, +2% (v/v) FBS) only. An example MTS assay plate set-up is shown in Figure 2.8, the same plate organisation was used for both 2D (flat-bottom) and 3D (ULA) plates.

The MTS assay was performed at 24, 72, 120, 168 and 240 hours post-BUNV infection. At each time point, 3x wells for each experimental condition were assessed, including the uninfected and media ('no cell') controls. Firstly, 100µL of spent media was removed from each of the wells which were to be assessed. Care was taken when removing media from the wells in the ULA plate to ensure that spheroids were not lost or damaged. Only 15x spheroids of each condition were required to obtain MTS data in triplicate for each time-point. The remaining 5x spheroids served as 'spares'; these could be used to replace spheroids which may be lost/damaged during media changes.

For both 2D and 3D cultures, 20µL of the MTS reagent was added to each well containing the samples in 100µL of culture medium. The plates were incubated at 33°C, 5% CO_2 for 1 hour (2D culture) or 4 hours (3D culture). A longer incubation time was required for 3D samples due to their lower surface area: volume ratio, compared to 2D culture. At the end of the incubation period, the plates were placed on a plate shaker for 30 seconds at 300rpm to disperse the soluble formazan (produced by cellular reduction of MTS) throughout the cell culture medium. Then, 80µL of culture medium from each well was carefully transferred into corresponding wells in a fresh, flat-bottomed, 96-well plate. A multichannel pipette was utilised to ensure consistent pipetting volume. Finally, the absorbance was recorded at

490nm using BioTek Gen5 software on a Biotek Synergy HT 96-well plate reader. The data was exported into Microsoft Excel™ format for subsequent analysis. To account for any interferences caused by the measuring plate, the absorbance was also recorded at 590nm, corrected absorbance is obtained by subtracting these values from the 490nm readings.

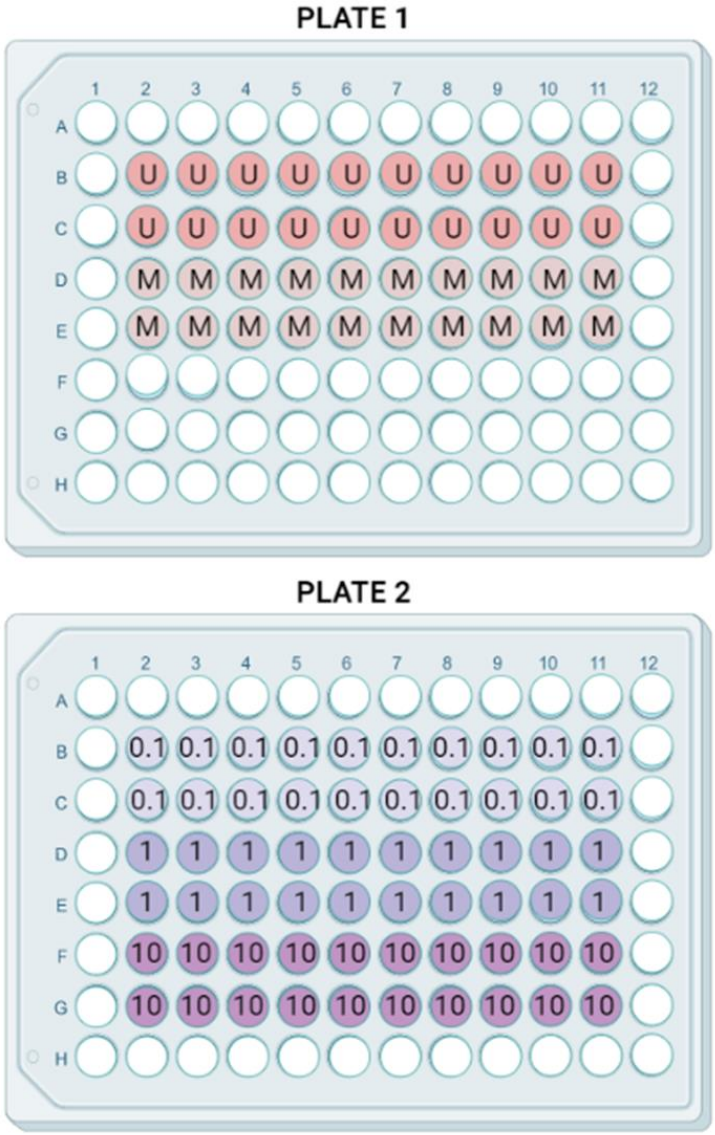

Figure 2.8. Example 96-well plate set-up for the MTS assay. *Uninfected control cells/spheroids and media only ('no cell') controls were maintained in a separate plate (plate 1) to the infected wells (plate 2), to avoid contamination with BUNV. U: Uninfected control cell monolayers/ spheroids. M: 'no cell' control wells containing assay medium only. 0.1: infected with BUNV at an MOI of 0.1. 1: infected with BUNV at an MOI of 1. 10: infected with BUNV at an MOI of 10. The white wells on the perimeters of each plate contained PBS to prevent evaporation from the wells in the centre of each plate.*

iii) Analysing MTS Assay Data

After obtaining corrected absorbances (by subtracting the 590nm recording), the average absorbance (of the three technical replicates) was calculated for each experimental condition, including controls. The average of the 'no cell' control wells was subtracted from the average absorbance values for each sample condition (uninfected, MOI 0.1, MOI 1, and MOI 10), to account for background interference from the assay medium. Relative MTS activity was expressed as a percentage relative to the uninfected control samples, for which MTS activity was considered to be 100% for comparison purposes.

2.6 Assessing the Viability of BUNV-Infected Multicellular Spheroids On-Chip (Under Flow Conditions)

2.6.1 LDH Assay (Cell Lysis & Cell Death)

i) LDH Assay Principle

The enzyme lactate dehydrogenase (LDH) catalyses the conversion of lactate to pyruvate (Figure 2.9) and is highly prevalent in the cell cytosol. When the plasma membrane of a cell becomes damaged (e.g., when a cell lyses), LDH is released into the supernatant. LDH, therefore, is commonly used as a biological marker of cell death (Kaja et al., 2017; Kumar et al., 2018). This study used an LDH assay kit (Cytotoxicity Detection Kit Plus, LDH, Roche, Hertfordshire, UK) to assess cell death and cell lysis. This colourimetric assay utilises a series of enzymatic reactions, resulting in the formation of a soluble formazan dye, at room temperature, which is measured spectrophotometrically at 490nm. An increase in the amount of LDH activity (resulting from increased cell death/membrane damage) directly correlates to the amount of formazan produced during the assay period. This information can be used to calculate LDH release and quantitively assess cell death and cell lysis.

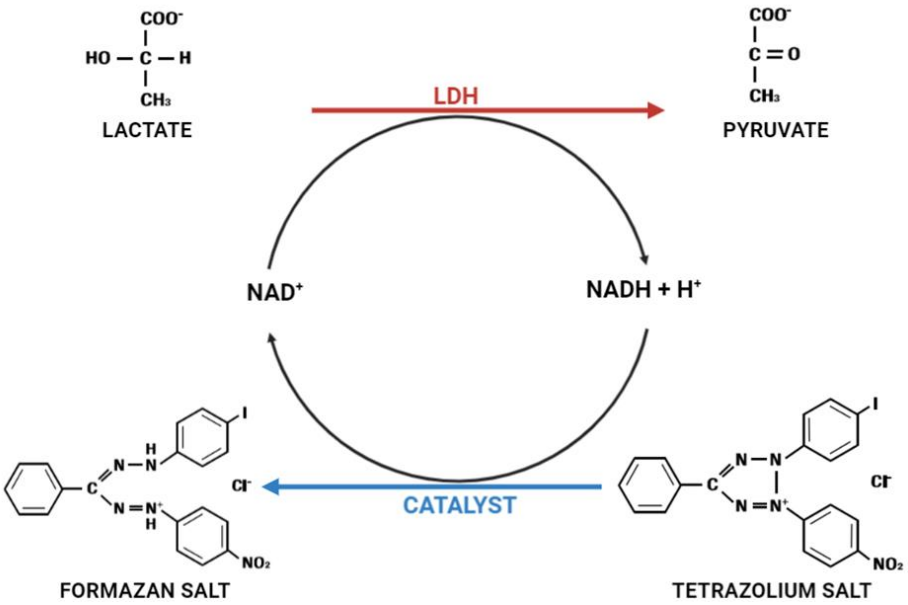

Figure 2.9. Schematic diagram of the LDH assay reaction, created on Biorender.com. *Step 1 (red arrow): LDH reduces NAD+ to NADH + H^+ by oxidation of lactate to pyruvate. Step 2 (blue arrow): two hydrogen atoms are transferred from NADH + H^+ to the tetrazolium salt (2-[4-iodophenyl]-3-[4-nitrophenyl]-5-phenyltetrazolium chloride) by the catalyst (Diaphorase/NAD+ mixture).*

ii) Performing the LDH Assay

The LDH assay was performed on effluent collected from microfluidic devices, set up as described in section 2.4.2. The first effluent sample was collected 24hpi, by removing the 15mL tube containing the effluent and feeding the outlet tubing of the microfluidic device into a fresh, sterile 15mL tube. This process was repeated every 24 hours thereafter for a total incubation period of 120 hours, yielding a total of 5 effluent samples for LDH analysis. The effluent was collected at the same time each day to ensure that sample volumes were consistent for comparability. Using a flow rate of 2µL/minute gave a total effluent volume of approximately 2.8mL per day, considering evaporation. When the final effluent sample was collected (at 120hpi), the microfluidic device was disassembled, and the spheroids contained within the 'uninfected' (mock-infected) control chip were pooled into a sterile 1.5mL tube and lysed by adding 100µL lysis solution (provided in the Cytotoxicity Detection Kit Plus). The uninfected spheroid lysate was then transferred into a 7mL Bijou container, diluted in 2.7mL 1% (w/v) BSA (PAA Cell Culture Company, Cambridge, UK) made up in PBS, and used as the LDH positive control (Figure 2.10).

Fresh stock solutions of all reagents required for the LDH assay were prepared immediately before their use. The catalyst (Diaphorase/NAD+ mixture), dye solution (iodonitrotetrazolium chloride (INT) and sodium lactate), stop solution (1M HCl), and lysis solution was stored at -20°C and thawed at room temperature before the commencement of the assay. To reconstitute the catalyst, 1mL ddH_20 was added to the lyophilised sample, the solution was mixed by gently inverting the bottle, and then left to incubate at room temperature for 10 minutes before use. The reaction mixture was prepared by mixing 250µL reconstituted catalyst with 11.25mL dye solution. Finally, a 1.0 unit/mL LDH standard was prepared by adding 0.5µL L-LDH (Roche) to 1.375mL assay medium (DMEM, +2% (v/v) FBS, -P/S).

Once all reagents had been prepared, a 96-well flat-bottomed plate was set up as shown in Figure 2.10. Firstly, 100µL assay medium was added to wells B-H, 1-3. To the first three wells of the plate (horizontally, A1-3), 200µL/well 1.0 unit/mL LDH was added. A doubling dilution was then performed by taking 100µL 1.0 unit/mL LDH standard from wells A1-3 and adding it to the 100µL media in wells B1-3 (0.5 unit/mL LDH standard). A multi-channel pipette was utilised to ensure consistency of pipetting volume. This process was repeated moving vertically down the plate, until reaching the bottom 3 wells (H1-3, 0.0078125 unit/mL LDH

standard), where the surplus 100µL of the resulting solutions was discarded, leaving each well containing 100µL LDH standard of known concentration.

After the LDH standard doubling dilution had been performed, 100µL/well of the 1% (w/v) BSA in PBS was added to the plate in triplicate, to assess for any spontaneous LDH release in the spheroid lysate (positive control) diluent. Likewise, 100µL/well plain assay medium was added to the plate in triplicate, to assess for background LDH release in the assay reagents, this is to be subtracted from the data obtained for the effluent samples and LDH standards. Next, 100µL/well of the uninfected spheroid lysate was added in triplicate. Since the uninfected spheroids represent 'healthy' cells, it is expected that high quantities of LDH will be released from within the cells upon forced membrane damage (using the lysis solution). After the background LDH release controls and positive control were loaded onto the plate, 100µL/well of the effluent samples were loaded, in triplicate.

Once all samples had been loaded onto the plate, 100µL of the reaction mixture was added to each well. The plate was then incubated at room temperature, and protected from light, for 15-30 minutes. After 15 minutes, the plate was checked, and if a visible gradient of colour was seen in the LDH standards the assay was stopped. If no clear gradient was observed, the plate was returned to incubate and checked every 5 minutes, until the maximum incubation time of 30 minutes. To stop the reaction, 50µL of the stop solution was added to each well. Before recording the absorbance, the plate was inspected for bubbles which, if present, were removed using a microlancet. The absorbance was then recorded at 490nm using BioTek Gen5 software on a BioTek Synergy HT 96-well plate reader. The absorbance was also

recorded at 590nm, which was subtracted from the 490nm readings to yield corrected absorbances, removing any interferences from the assay plate.

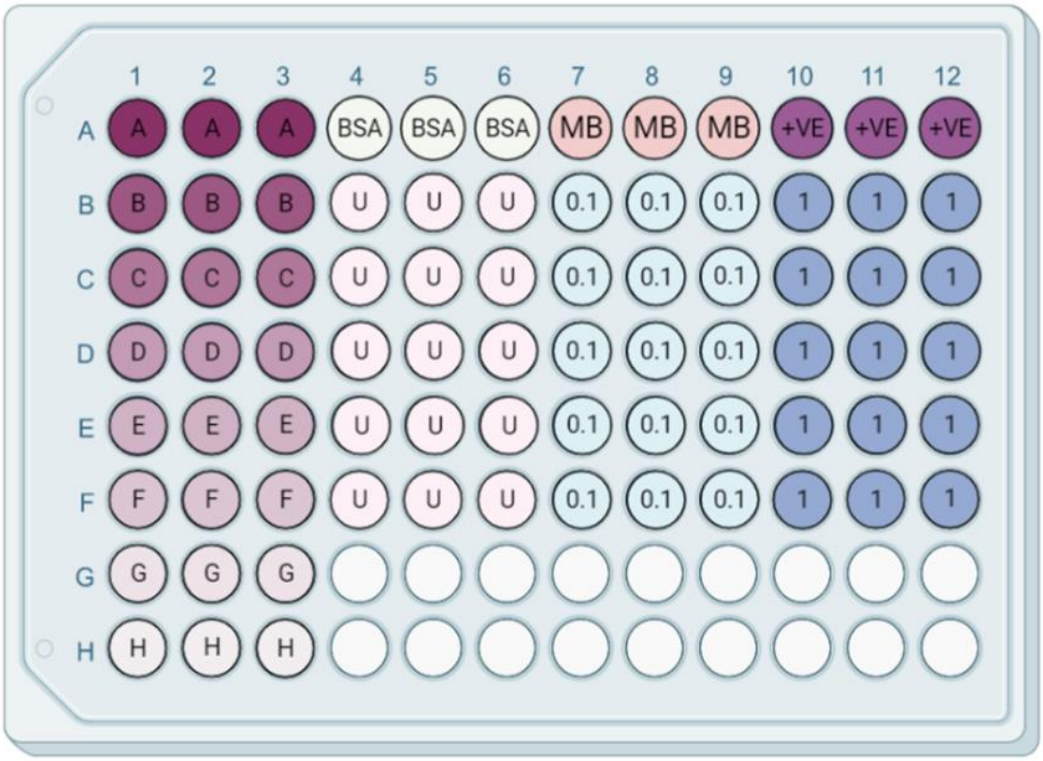

Figure 2.10. Example set-up of a 96-well plate for the LDH assay, created on Biorender.com. *Wells A-H, 1-3 contain a doubling dilution of LDH standard. A: 1.0 unit/mL, B: 0.5 unit/mL, C: 0.25 unit/mL, D: 0.125 unit/mL, E: 0.0625 unit/mL, F: 0.03125 unit/mL, G: 0.015625 unit/mL, H: 0.0078125 unit/mL. BSA: 1% (w/v) BSA in PBS (BSA blank). MB: plain assay medium (media blank). +VE: positive control, uninfected spheroid lysate. U: effluent samples collected from the chip containing uninfected spheroids. 0.1: effluent samples collected from the chip containing spheroids which were infected at an MOI of 0.1. 1: effluent samples collected from the chip containing spheroids which were infected at an MOI of 1. Moving vertically down the plate, wells B-F, 4-12 correspond to the time-points of effluent collection, i.e., B4-B12 samples were collected 24 hours post-infection with BUNV, C4-C12 samples 48 hours post-infection etc.*

iii) Analysing LDH Assay Data

Absorbance data were exported from Gen5 into an excel file, where the 590nm recordings were subtracted from the 490nm recordings before calculating averages for each of the samples (triplicates), including the standards and controls. The average of the media blank was subtracted from the averages of all samples and LDH standards, and the BSA blank average was subtracted from the average of the positive control lysate. After the corrected absorbance values had been obtained, a standard curve was generated using the known concentration values of the LDH standards (X-axis) and their respective absorbance (Y-axis) (Figure 2.11). A logarithmic trend line was added to the curve, and the equation of the line was rearranged to find X (see Figure 2.11). This equation was then used to convert the average absorbance recordings for each of the effluent samples (and positive control lysate) into units/mL of LDH released. This data was then plotted onto a graph to illustrate LDH release over time (24-120hpi), for each of the experimental conditions (uninfected, MOI 0.1, and MOI 1).

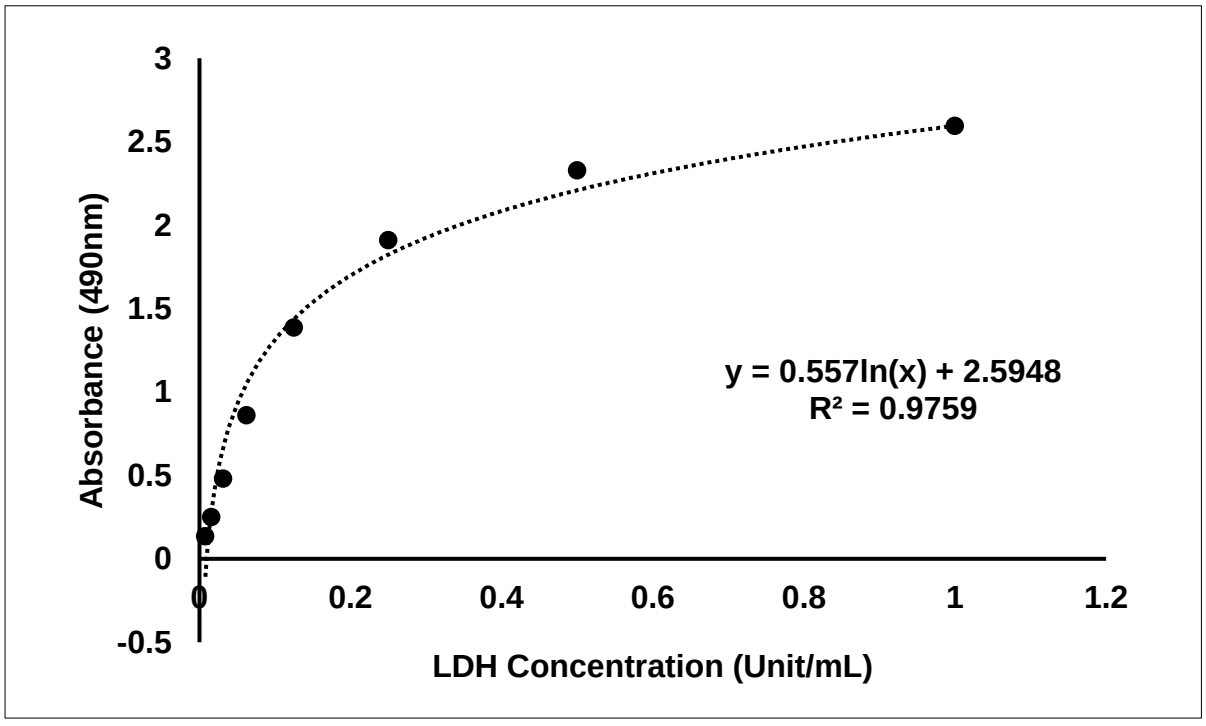

Figure 2.11. Example LDH standard curve. *To calculate the concentration of LDH released in test samples a logarithmic trend line is added, and the equation is rearranged to calculate (x) as follows (excel format): x= exp((y-2.5948)/0.557).*

2.7 Isolating Exosomes & Viral Particles from Cell Culture Medium

2.7.1 Standard Ultracentrifugation vs Sucrose Cushion Ultracentrifugation

Differential ultracentrifugation is a commonly used technique which enables the separation and isolation of cells, sub-cellular components (i.e., organelles, proteins, and nucleic acids), and other biological objects such as viruses (Théry et al., 2006). When a homogenous solution containing a mixture of biological components is subject to several successive rounds of centrifugation, each with increasing relative centrifugal force (x *g*) and duration, the components can be selectively isolated and differentiated based on their differences in size and density, and thus their sedimentation rates. Differential ultracentrifugation is widely employed in the field of EV research and is well defined for exosome isolation (Théry et al., 2006; György et al., 2011; Momen-Heravi et al., 2013; Livshits et al., 2015).

A differential ultracentrifugation procedure (as shown in Figure 2.12) adapted from Théry et al. (2006) was used to isolate exosomes and BUNV virions in this study. Although not essential for the isolation of exosomes, an additional purification step in the final (ultracentrifugation) stages using a sucrose cushion is recommended to remove contaminants such as large protein aggregates and proteins non-specifically associated with exosomes. To optimise a differential ultracentrifugation protocol for the isolation of exosomes and BUNV virions, both standard ultracentrifugation, and ultracentrifugation using a sucrose cushion were performed.

For optimisation, A549 and HuH-7 cells were seeded into 2x 6-well plates per cell line. One plate (for each cell line) was mock-infected with a plain culture medium; the second plate was infected with BUNV at an MOI of 0.1 (see section 2.3.3). Each well was supplemented with 4mL media (+2% (v/v) exosome depleted FBS, see section 2.3.1) and incubated at 33°C, 5% CO_2 for 5 days. After 5 days, the supernatant from each plate was collected and pooled into

a single sterile 50mL tube per experimental condition (a total of 4 samples). The samples were then subjected to differential ultracentrifugation as depicted in Figure 2.12.

The first centrifugation step (400 x *g* for 10 minutes at 4°C) eliminates any dead cells contained within the collected supernatant. The pellets produced from this step were discarded and the supernatant was transferred into fresh tubes (1x tube per experimental condition) and further clarified by centrifugation at 2,000 x *g* for 10 minutes at 4°C to remove large cell debris. The clarified supernatant resulting from the second centrifugation step was then aliquoted into corresponding labelled 1.5mL tubes and centrifuged at 10,000 x *g* for 30 minutes at 4°C in a benchtop microfuge to remove apoptotic bodies.

Without disrupting the pellet, the supernatant contained within the 1.5mL tubes was then pooled into corresponding labelled OptiSeal polypropylene 4.7mL centrifuge tubes (Beckman Coulter Ltd, High Wycombe, UK). The OptiSeal tubes were weighed to ensure balance (variations of <0.01g were accepted) and sealed by inserting the OptiSeal spacer and cap (Beckman Coulter Ltd, High Wycombe, UK) before being placed into a TLA-110 fixed-angle rotor (Beckman Coulter Ltd, High Wycombe, UK). Samples were then ultracentrifuged at 100,000 x *g* for 1 hour at 4°C using a Beckman Optima MAX-XP ultracentrifuge.

The samples were divided at this stage to compare the standard ultracentrifugation and sucrose cushion ultracentrifugation methods. For each experimental condition, half of the clarified supernatant was subject to standard ultracentrifugation, and the remaining half was prepared by ultracentrifugation with a sucrose cushion, as shown in Figure 2.12.

Filtered PBS was used as the sample diluent to prevent contamination with exogenous exosomes/nanoparticles. This is also the rationale for using exosome-depleted FBS in the cell culture medium. The filtered PBS was prepared by passing sterile PBS through a 20nm Whatman® Anotop® syringe filter (Merck Life Science Ltd, Gillingham, UK). For the 'standard ultracentrifugation' samples, the pellet (which is not visible at this stage) was washed with 1mL 20nm-filtered PBS; a pipette with a gel loading tip (Fisher Scientific) was utilised to gently scrape the bottom of the OptiSeal tube to ensure that the pellet was thoroughly resuspended.

The OptiSeal tubes were then filled with 20nm-filtered PBS, balanced, sealed, and ultracentrifuged again.

Similarly, the partially purified pellets which were to be subject to the additional sucrose cushion purification step were resuspended in 1mL 20nm-filtered PBS as described above. However, before centrifugation, these resuspended pellet solutions were transferred into a new OptiSeal tube, which had been loaded with a 1mL cushion of 30% (w/v) sucrose made up in 20nm-filtered PBS (Figure 2.12). The tube was then filled with 20nm-filtered PBS, without disrupting the interface, before ultracentrifugation. The sucrose cushion (containing the exosomes and viral particles) was collected and transferred into a fresh OptiSeal tube, and washed with 20nm-filtered PBS, before a final round of ultracentrifugation.

For both the 'standard ultracentrifugation' and 'sucrose cushion ultracentrifugation' samples, the pellets of purified exosomes/viral particles were left to dry for 20 minutes by placing the OptiSeal tubes upside-down in a rack. After 20 minutes, the pellets were lysed as described in section 22.82.8.1 (i). The total protein concentration of each exosome/viral particle preparation was quantified by BCA assay (see section 2.8.1 – (ii)), and the two differential ultracentrifugation protocols were compared by immunoblotting for exosome markers and viral proteins, as described in section 22.82.8.1.

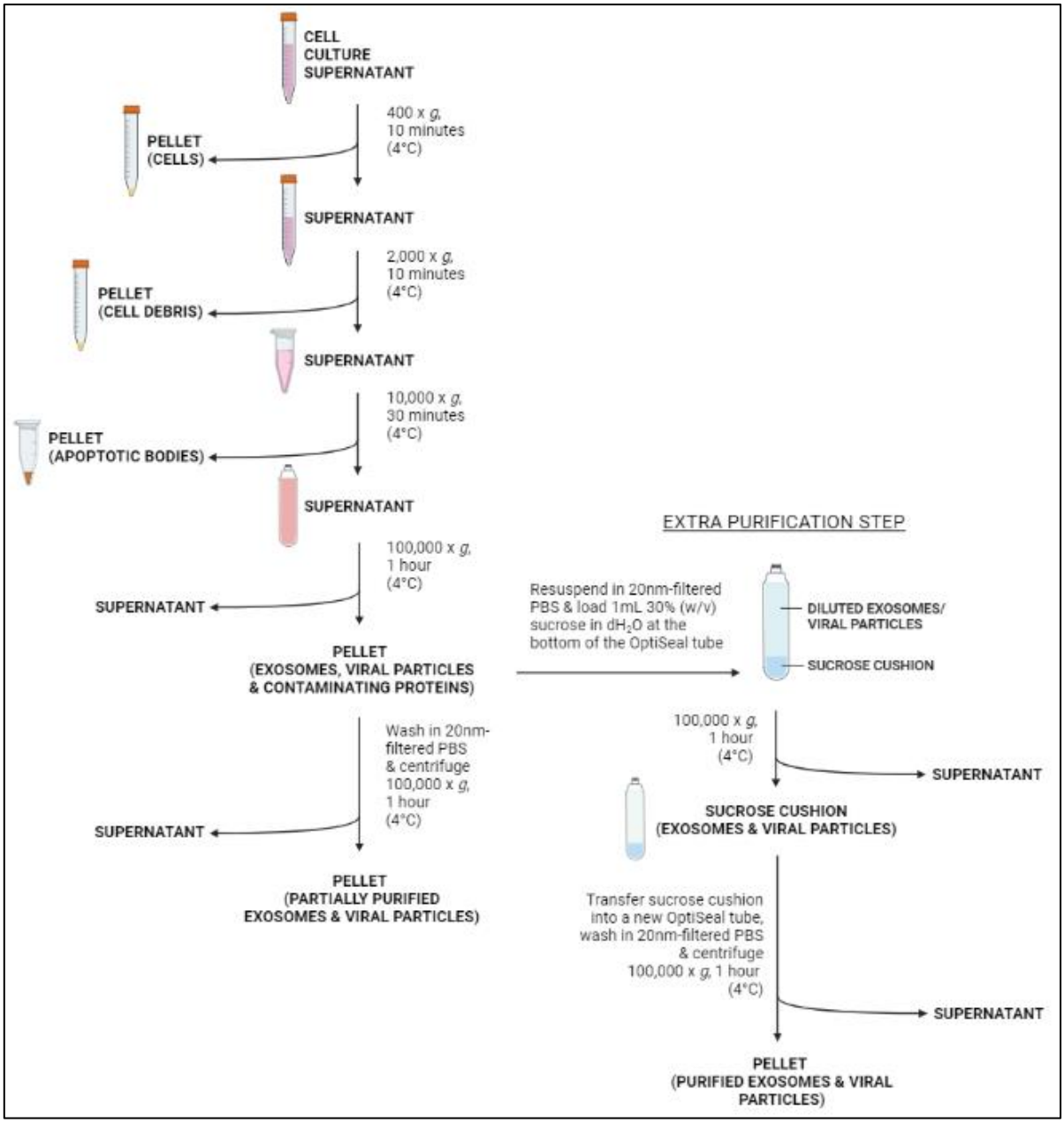

Figure 2.12. Flow chart for the differential ultracentrifugation procedure used to isolate exosomes and viral particles (Adapted from Théry et al. (2006), created on Biorender.com). *Curved arrows represent material that is discarded after centrifugation. The speed and duration of each centrifugation is indicated next to the downwards facing arrows. In the first three centrifugation stages, the pellets are discarded, and the supernatant is saved for the next stage. For standard ultracentrifugation (without the extra purification step), the supernatant is discarded after each 100,000 x g centrifugation, and the pellet is saved. Similarly, in sucrose cushion ultracentrifugation (extra purification step displayed on the bottom right), the supernatant is discarded after each 100,000 x g centrifugation. However, after the penultimate 100,000 x g centrifugation, the sucrose cushion is transferred into a fresh ultracentrifuge tube, and the pellet (containing contaminating proteins) is discarded.*

2.7.2 Isolating Exosomes & BUNV Virions for Western Blotting

For experiments in which supernatant/microfluidic effluent was to be collected for exosome isolation, all cells were cultured in medium as described in section 2.3.1, whereby the 10% (v/v) FBS is replaced with 2% (v/v) exosome-depleted FBS.

The supernatant was collected from cells (+/- BUNV infection) cultured in 6-well plates for 2D investigations. For 3D investigations, microfluidic effluent was collected from chips containing spheroids (+/- BUNV infection, see section 2.4.2). Both supernatant and effluent were collected at 120hpi; uninfected control samples were also collected after 120 hours incubation at 33°C, 5% CO_2. A flow rate of 2µL/minute yields approximately 2.8mL effluent every 24 hours, due to evaporation, effluent volumes were observed to be ~12 – 13mL when collected after 120 hours of incubation. To keep this consistent, for 2D investigations, 1x 6 well plate was used for each experimental condition (i.e., 6x wells containing uninfected cells, 6x wells containing cells infected at MOI 0.1, etc), and each well was supplemented with 2mL media to total 12mL when collected and pooled.

For 2D investigations, a total of 16 samples were prepared for western blotting analysis. These samples were prepared as follows; 4x 6-well plates were seeded with A549 cells as described in section 2.1.4. One plate was mock-infected with plain culture medium, the second plate was infected with BUNV at an MOI of 0.1, the third was infected at an MOI of 1, and the final plate was infected at an MOI of 10 (see section 2.3.3).

After 120 hours of incubation at 33°C, 5% CO_2, the supernatant was removed from each plate and pooled into a corresponding 15mL tube. This supernatant was then subject to differential ultracentrifugation with sucrose cushion purification as shown in Figure 2.12. The resulting pellets of purified exosomes/viral particles were lysed as described in section 2.8.1 (i). After removing the supernatant from each 6-well plate, the cell monolayers were also lysed and pooled. The total protein concentration in each sample was determined by BCA assay (see section 2.8.1– (ii)). The samples were stored at -80°C and thawed on ice immediately before western blotting. A total of 8 samples were produced from A549 2D culture: 4x whole cell lysates, and 4x purified exosome/viral particle preparations. The same process was repeated using HuH-7 cells to produce an additional 8 samples for western blotting.

Likewise, for 3D investigations, a total of 16 samples were prepared. Both A549 and HuH-7 cells were seeded into respective ULA plates to generate spheroids as described in section 2.1.5. For each cell line, 14x spheroids were mock-infected with plain culture medium, 14x spheroids were infected with BUNV at an MOI of 0.1, 14x spheroids at MOI 1, and 14x spheroids at MOI 10 (as described in section 2.3.5). Immediately post-infection, 4x spheroids (each MOI) were transplanted into microfluidic chips (see section 2.4.2), and the remaining spheroids were supplemented with 200µL fresh media and placed in a 33°C, 5% CO_2 incubator. The media in the ULA plate was refreshed every 2 days thereafter as described in section 2.1.5. The microfluidic pump was set to infuse 2µL/minute and, after 120 hours of incubation, the infusion was stopped and the effluent from each chip was collected. Exosomes/viral particles were isolated from microfluidic effluent by sucrose cushion ultracentrifugation (Figure 2.12), lysed, quantified, and stored as described above for 2D investigations. For the '3D whole cell lysate' samples, 10x spheroids (each MOI) were pooled from the ULA plate after 120 hours of incubation and lysed as described in section 2.8.1 (i).

2.7.3 Isolating Exosomes & BUNV Virions for Nanoparticle Tracking Analysis

A549 and HuH-7 spheroids were infected with BUNV at MOIs of 0.1, 1, and 1, as described in section 2.3.5. Immediately post-infection, 4x spheroids (of each cell line and MOI) were transferred into microfluidic devices (see section 2.4.2). For each cell line, an 'uninfected' control chip was also prepared; this chip contained 4x spheroids mock-infected with plain culture medium (+2% (v/v) exosome-depleted FBS, -P/S). After all the devices had been assembled and secured onto the infusion pump, the outlet tubing was fed into corresponding, labelled 15mL polypropylene tubes, and the infusion was started (2µL/min).

The microfluidic effluent was collected every 24 hours, from the commencement of the infusion. At each effluent collection, the infusion was paused, before removing the outlet tubing from the collection tubes, and feeding it into fresh, sterile 15mL tubes.

Nanoparticle tracking analysis (NTA; see section 2.8.2) was performed on the samples collected at 24hpi, 72hpi, and 120hpi. The samples collected at 48hpi and 96hpi were not utilised for any subsequent analysis, however, effluent collection every 24 hours ensured that sample volume was kept consistent (approx. 2.8mL). Each effluent sample was stored at -80°C until all samples had been collected. The final effluent samples (120hpi) were also frozen at -80°C, before isolating the exosomes/viral particles, so that each sample had been subject to the same experimental conditions.

Exosomes and viral particles (released from the cells forming the spheroids) are contained within the effluent samples. These were isolated using the differential ultracentrifugation protocol (with sucrose cushion purification) shown in Figure 2.12. All samples were thawed on ice prior to ultracentrifugation. The pellets of purified exosomes/viral particles were dried for 20 minutes, before resuspending in 1mL 2% (v/v) formaldehyde, made up in 20nm-filtered PBS. NTA was performed immediately after sample preparation to prevent sample degradation.

2.8 Exosome Characterisation

2.8.1 Western Blotting

i) Preparing Cell Lysates

RadioImmunoPrecipitation Assay (RIPA) buffer was used as the cell lysis and protein solubilisation buffer in this study, to allow for the extraction of cytoplasmic, nuclear and membrane proteins for subsequent western blotting. Transmembrane proteins, e.g., the tetraspanins CD63 and CD81, can be difficult to extract from lysates, particularly those with ≥4 membrane-spanning regions (Kowal et al., 2017). RIPA buffer is harsher than other common protein extraction buffers, and therefore is well suited for this purpose (Muinao et al., 2018; Subedi et al., 2019). RIPA buffer was prepared as detailed in Table 2.3, before use, 1x cOmplete™, Mini, EDTA-free Protease Inhibitor Cocktail tablet (Merck Life Science Ltd, Gillingham, UK) was dissolved in 10mL RIPA lysis buffer solution. The RIPA buffer was sterilised by filtering through a Sartorius Minisart™ 0.2 µm syringe filter (Fisher Scientific) and stored at 4°C.

Table 2.3. RadioImmunoPrecipitation Assay (RIPA) lysis buffer recipe.

Reagent	Volume (µL)	Final concentration
NP-40	100	1.0% (w/v)
Sodium deoxycholate	500	0.5% (w/v)
SDS	100	0.1% (w/v)
NaCl	300	150mM
Tris, pH 8.0	500	50mM
ddH_2O	8,500	

NP-40: Nonidet P40, SDS: sodium dodecyl sulfate, NaCl: sodium chloride.

To prepare the 2D whole cell lysates, cell media was gently removed from each well in the 6-well plate, and the cells were washed with 1mL/well PBS, before adding RIPA buffer (100µL/well). Cell monolayers were detached using cell scrapers (Sarstedt) into the lysis buffer. The lysates were then collected and pooled into a single, sterile, labelled 1.5mL polypropylene tube, per experimental condition (uninfected, MOI 0.1, MOI 1, and MOI 10). The pooled lysates were incubated on ice for 10 minutes to complete the lysis process. During

this incubation, the lysates were agitated by aspirating with a 100µL pipette tip to further break apart the cells. After 10 minutes, the lysates were centrifuged at 13,000 x *g* for 2 minutes to sediment whole cells, cellular debris, and insoluble carbohydrates, which can interfere with electrophoresis. Finally, the supernatant was transferred into fresh, corresponding, labelled 1.5mL tubes and stored at -80°C.

For 3D whole cell lysates, 10x spheroids (each experimental condition) were collected, using a 1000µL pipette tip, and pooled into corresponding labelled 1.5mL tubes. The media was carefully discarded, and the spheroids were washed by adding 1mL PBS to each tube. This was followed by centrifugation at 400 x *g* for 2 minutes, to pellet the spheroids, the PBS was then carefully discarded. To lyse the spheroids, 100µL RIPA buffer was added to each tube containing 10x spheroids. A 100µL pipette tip was used to aspirate the lysate to encourage spheroid disaggregation. The spheroid lysates were incubated on ice for 10 minutes, then centrifuged at 13,000 x *g* for 2 minutes, transferred into new tubes, and stored at -80°C as described above for the preparation of 2D lysates.

Lastly, to prepare the 'purified EV' lysates, 100µL RIPA buffer was added to Optiseal tubes containing dried pellets of purified exosomes and viral particles, isolated by ultracentrifugation with a sucrose cushion, as shown in Figure 2.12. A gel loading tip was used to scrape the bottom/sides of the Optiseal tube, to ensure that the pelleted exosomes/ viral particles were thoroughly resuspended in the lysis buffer. The lysates were then transferred into labelled 1.5mL tubes and incubated on ice for 10 minutes, followed by sonication for 3 minutes, and finally centrifugation at 16, 000 x *g* for 15 minutes. All lysates were stored at -80°C until use, and freeze/thawed twice (once for protein quantification, and once for western blotting).

ii) BCA Assay

A colourimetric, two-step Pierce BCA Protein Assay Kit (Thermo Fisher Scientific) was used to determine the protein concentration of lysates in this study. This assay is based on the reduction of Cu^{2+} to Cu^{1+} in the presence of peptides containing ≥3 amino acid residues, in an alkaline medium. In the first step of the assay, the 'biuret reaction', a light blue-coloured chelate complex is formed from the reaction between the peptides and cupric ions. In the

second step of the assay (the colour development reaction), the chelation of two bicinchoninic acid (BCA) molecules with one cuprous ion (Cu^{1+}, formed in step one), results in the formation of a water-soluble, purple-coloured complex (Figure 2.13), which can be quantified spectrophotometrically.

A serial dilution was performed on a 2000µg/mL BSA stock solution to produce a series of BSA standards of known concentration (Table 2.4). The absorbance values obtained from the BSA standards were used to generate a standard curve, from which the protein concentration in sample lysates could be determined. Sample lysates were thawed on ice prior to the commencement of the BCA assay. The BCA working reagent (included in the Pierce BCA Protein Assay Kit) was prepared by mixing BCA reagent (A) with BCA reagent (B) in a 50mL tube at a ratio of 50:1 (A: B), per the manufacturer's protocol. The volume of working regent required was calculated using Equation 5:

Equation 5. Calculating the volume of working reagent required for the BCA assay.

$$\begin{aligned}&\left(no.standards + no.\ unknowns\ (lystaes)\right) * \left(no.of\ replicates\ (3)\right)\\ &* \left(volume\ of\ working\ reagent\ per\ sample\ (200\mu L)\right)\\ &= total\ volume\ of\ working\ reagent\ required\end{aligned}$$

Table 2.4. Preparation of the BSA standards.

Tube	BSA (µL)	ddH_2O (µL)	Final BSA concentration (µg/mL)
A	100, stock	0	2000
B	112.5, stock	32.5	1500
C	97.5, stock	97.5	1000
D	52.5, tube B	52.5	750
E	97.5, tube C	97.5	500
F	97.5 tube E	97.5	250
G	97.5, tube F	97.5	125
H	30, tube G	120	25
I	0	120	0

BSA: Bovine serum albumin.

The BSA standards were loaded onto a 96-well flat bottom plate in triplicate (25µL/well). Due to the limited volume of the sample lysates, only 3µL of lysate was added to each well (in triplicate). The wells containing 3µL lysate, of unknown protein concentration, were then diluted with 22µL of ddH_2O; this dilution was accounted for when calculating protein concentration based on the absorbance recordings obtained for the BSA standards. Once all standards/samples had been loaded onto the plate, the working reagent was added (200µL/well). A multichannel pipette was utilised to ensure consistent pipetting volume. The assay plate was then protected from light, and incubated at 37°C, 5% CO_2, for 30 minutes, before recording the absorbance at 595nm using a Biotek Synergy HT 96-well plate reader.

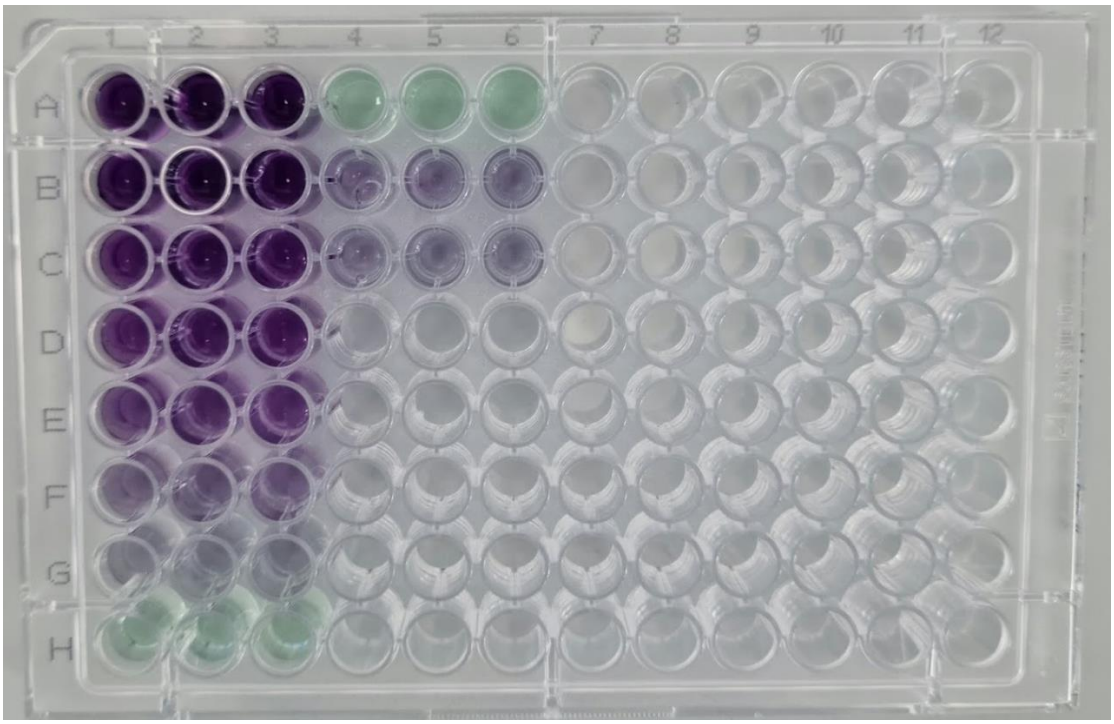

Figure 2.13. An example BCA assay plate. *A clear gradient of colour is seen in the BSA standards after 30 minutes incubation at 37°C, 5% CO_2. A1-A3; 2000 µg/mL BSA. B1-B3; 1500µg/mL BSA. C1-C3; 1000µg/mL BSA. D1-D3; 750µg/mL BSA. E1-E3; 500µg/mL BSA. F1-F3; 250µg/mL BSA. G1-G3; 125µg/mL BSA. H1-H3; 25µg/mL BSA. A4-A6; 0µg/mL BSA. B4-B6; A549 3D whole cell lysate (uninfected). C4-C6; HuH-7 3D whole cell lysate (uninfected).*

iii) Gel Electrophoresis

Proteins contained within the sample lysates were separated based on their molecular weight using discontinuous sodium dodecyl sulphate polyacrylamide gel electrophoresis (SDS-PAGE). All western blotting reagents were purchased from Thermofisher, unless otherwise

attributed. The NuPAGE® Bis-Tris Electrophoresis System was used, following the protocol described by Kowal et al. (2017). This system operates at a neutral pH, which minimises protein modifications and promotes protein stability during electrophoresis, resulting in sharper band resolution compared to the highly alkaline Laemmli system (Laemmli, 1970). Denaturing, but non-reducing conditions were used to resolve the proteins – this is important for the detection of the tetraspanins CD63 and CD81, as the epitope recognised by the antibodies to these proteins relies on correct protein folding mediated by Cys-Cys disulfide bonds, which are broken by reducing agents (Théry et al., 2018).

The lysate was measured to achieve a protein concentration of 30µg/well (quantified by BCA assay - see above) and added to an equal volume of 2x Bolt™ LDS Sample Buffer, containing no reducing agent. Each lysate/sample buffer mixture was then heated at 70°C for 10 minutes, to denature the proteins. After 10 minutes, the samples were immediately transferred onto ice to incubate whilst the Bolt system gel running tank was set up. The chambers of the tank were filled with 1x NuPAGE™ MES SDS Running Buffer. The comb and tape were removed from pre-cast NuPAGE® Bis-Tris, 4-12% Mini Protein gels before placing the gels into the tank. A small amount of 2x Bolt™ LDS Sample Buffer was pipetted into each well, to check for any deformities. Each well was then washed several times with 1x MES buffer, before loading samples and markers. Two molecular weight markers were loaded onto each gel; a chemiluminescent substrate compatible marker - Invitrogen™ MagicMark™ XP Western Protein Standard (3µL, Fisher Scientific), which contains an IgG binding site, and a colourimetric marker - SeeBlue™ Plus2 Pre-stained Protein Standard (6µL). The pre-stained colourimetric marker was used to visualise and confirm protein separation; this marker was also used as the molecular weight reference when imaging for BUNV N protein, using the ChemiDoc MP Imaging System (discussed below). After loading all samples and standards, the gels were run at 150V for approximately 40 minutes, until the dye front had reached the end of the gel (Figure 2.14).

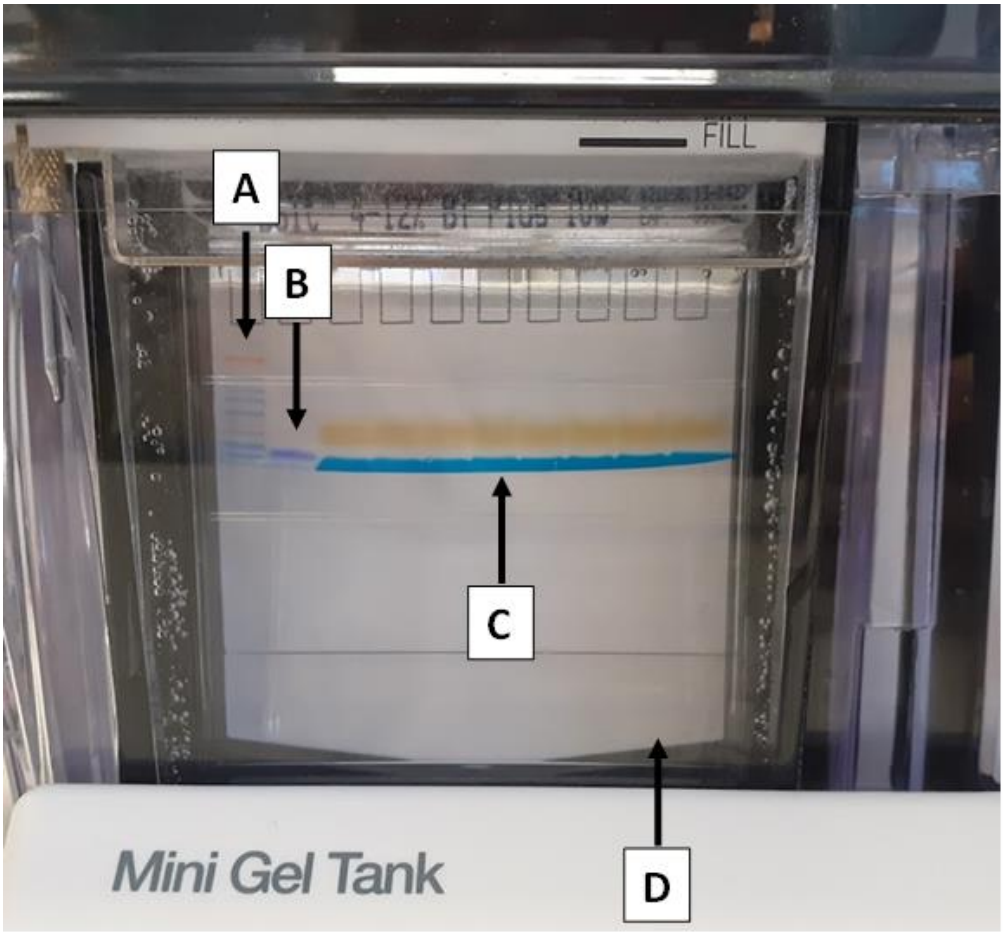

Figure 2.14. Protein standards and samples running at 150V through a NuPAGE® Bis-Tris, 4-12% Mini Protein gel. ***A:*** *colourimetric ladder showing protein separation as expected.* ***B:*** *chemiluminescent ladder.* ***C:*** *dye front.* ***D:*** *the end of the gel, the power supply is turned off when the dye front (C) reaches this point.*

iv) Gel Transfer

Once run sufficiently, the gel was released from the cassette and the separated proteins were transferred onto a polyvinylidene difluoride (PVDF) membrane, using the Bio-Rad Turbo Transfer System. The bottom portion of a Trans-Blot Turbo Mini PVDF Transfer Pack (Bio-Rad, Hertfordshire, UK) was placed into the Trans-Blot drawer; this portion consists of a buffer-saturated ion reservoir stack and a prewetted 0.2µm PVDF membrane. The gel was carefully placed on top of the PVDF membrane, and then, the top portion of the transfer pack (the second buffer-saturated ion reservoir stack), was applied on top of the gel. A plastic roller was used to remove any air bubbles before assembling the lid of the Trans-Blot drawer. A pre-programmed standard transfer at 25V for 30 minutes was used, per the manufacturer's recommendations.

v) Membrane Preparation; Blocking and Antibody Incubation

Once the membrane transfer had completed, the gels were discarded and the membrane (containing the separated proteins) was placed into a plastic tub and covered with blocking buffer (5% (w/v) non-fat dried milk powder (Marvel) dissolved in PBS-Tween 20 (PBS-T; 0.1% (v/v) Tween 20, Sigma-Aldrich). The membranes were incubated with blocking buffer for 1 hour, with end-to-end rocking at 4°C, to prevent non-specific antibody binding.

After 1 hour, the blocking buffer was discarded, before adding 5mL of an antibody-dependent concentration of primary antibody (Table 2.5), diluted in 5% (w/v) milk in PBS-T (0.1% (v/v) Tween-20). The membranes were incubated with the primary antibody overnight, at 4°C, with gentle rocking. The primary antibody was removed following the overnight incubation, and each membrane was washed 3x with PBS-T (0.1% (v/v) Tween 20), for 10 minutes. The membranes were then incubated with secondary antibody (or IgGκ HRP binding protein for CD63/CD81 detection), diluted in 5% (w/v) milk in PBS-T as detailed in Table 2.5, for 1 hour at room temperature with gentle rocking. All secondary antibodies used are conjugated to horseradish peroxidase (HRP), to allow for chemiluminescent detection of the proteins of interest. After 1 hour, the secondary antibody/ IgGκ HRP binding protein was discarded, and the membranes were washed again with PBS-T (3x 10-minute washes).

The proteins of interest were then detected using enhanced chemiluminescent (ECL) HRP substrates. These substrates consist of a stable peroxide solution and an enhanced luminol solution which, when mixed 1:1 and incubated with a blot containing HRP-conjugated probes, produce a chemical reaction that emits light at 425nm. The emitted light can be captured on X-ray film or using charge-coupled device (CCD) imaging.

Table 2.5. Antibodies used for western blotting, including type, species, clonality, dilution, and supplier information.

Antibody	Type	Species	Clonality	Dilution	Supplier	Catalogue No.
Anti-CD63	Primary	Mouse	Monoclonal	1:1000	Santa Cruz Biotechnology, Inc	sc-5275
Anti-CD81	Primary	Mouse	Monoclonal	1:500	Santa Cruz Biotechnology, Inc	sc-70803
Anti-α-tubulin	Primary	Mouse	Monoclonal	1:1000	Proteintech	6603I-I-Ig
Anti-BUNV N	Primary	Sheep	Polyclonal	1:5000	A kind gift from J. Barr	N/A
Anti-Mouse	Secondary	Rabbit	Polyclonal	1:2500	Dako	P0260
Anti-Sheep	Secondary	Donkey	Polyclonal	1:5000	Abcam	ab97125
m-IgGκ BP-HRP	Mouse IgGκ light chain binding protein	Mouse	N/A	1:2500	Santa Cruz Biotechnology, Inc	sc-516102

vi) Developing a Film (Exosome Markers - CD63 and CD81)

Signal West Stable (SSWS) peroxide solution was used as the ECL substrate for the detection of the tetraspanins CD63 and CD81, due to its high sensitivity and long signal duration, enabling the detection of low abundant protein targets in limited sample volumes. SSWS peroxide solution was prepared by mixing components A and B at a 1:1 ratio. The washed CD63/CD81 probed membranes were incubated at room temperature with 2mL SSWS peroxide solution, and protected from light, for 5 minutes. The membrane was then drained by blotting the edge onto absorbent paper, before being placed in the correct orientation between two pieces of transparent projector film.

Membranes were secured into a developing cassette and transported into a dark room – with only red safe light. A piece of X-ray film (CL-XPosure™ Film, 5 x 7 inches) was placed on top of the membrane, in one swift motion, before securing the developing cassette. As each piece of X-ray film was removed from the packaging, the top left corner was cut so that the film could be correctly orientated once developed. The SSWS ECL substrate has a signal duration of up to 24 hours; as faint signals were observed when the films were exposed for 5 minutes and 60 minutes, each film was left to expose in the developing cassette overnight.

After exposing overnight, the film was carefully removed from the cassette and transferred into a tray containing developer solution (Ilfosol 3; Ilford, Cheshire, UK). The film was gently agitated and, once bands appeared, the film was transferred into a second tray containing 10% (v/v) acetic acid and agitated again for a few seconds. Finally, the developed film was placed into a third tray containing a fixer solution (Rapid Fixer; Ilford), before rinsing under cold, running water, and hanging to dry.

vii) CCD Imaging (BUNV N Protein)

For the detection of BUNV N protein, Clarity Western ECL Substrate (Bio-Rad) was prepared by mixing the Clarity Western Peroxide Reagent (A) with the Clarity Western Luminol/Enhancer Reagent (B), at a 1:1 ratio. Membranes, which had been probed for BUNV N-protein using anti-BUNV N protein primary antibody (1:5000) and anti-sheep HRP-conjugated secondary antibody (1:5000), as described above, were then incubated with 7mL of the ECL substrate, for 5 minutes at room temperature. After 5 minutes, the ECL substrate was discarded, and the membrane was secured between two clean acetate sheets; any air bubbles were carefully removed. The membrane was then imaged using a Bio-Rad Chemidoc™ MP Imaging System and processed with Image Lab™ Software.

viii) Densitometry Analysis

Densitometry analysis was performed using ImageJ software. Relative band intensity was calculated as a percentage relative to the 'uninfected' (mock-infected) controls.

2.8.2 Nanoparticle Tracking Analysis (NTA)

NTA was performed using the NanoSight LM10 instrument (Malvern Panalytical Ltd, Malvern, UK) following the manufacturer's instructions. This technology provides information on the size distribution and concentration of nanoparticles (small particles 10nm-1000nm), such as exosomes and viral particles, in a liquid suspension. NTA measures the Brownian motion (the random movement of particles resulting from collisions with molecules of the surrounding medium) of each particle, in real-time, on a frame-to-frame basis. Size distribution and concentration values are automatically determined by a dedicated particle tracking programme within the NTA 3.4 software, which performs calculations using the Stokes-Einstein equation.

Exosomes and viral particles were isolated from microfluidic effluent by differential ultracentrifugation as described in section 2.7.3. Each sample was diluted 1:10 with 20nm-filtered PBS to obtain an appropriate particle per frame (ppf) range for NTA; the NanoSight LM10 measures particles in the range of 10^6-10^9 particles/mL, which is approximately 20-100 ppf.

The capture and image processing settings were set according to the manufacturer's software guide, as follows:

Capture settings: 3x 60 seconds, camera level: 16, screen gain: 1.

Image processing settings: screen gain: 10, detection threshold: 5.

2.9 Statistical Analysis

Statistical analyses were performed using GraphPad Prism 8 (GraphPad Software, Inc., San Diego, CA). A two-way ANOVA with Tukey's post hoc analysis was performed to determine the statistical significance of the differences in spheroid diameter between different seeding densities (section 3.1.1), and between the different FBS concentrations used (section 3.1.2). Two-way ANOVA with Tukey's post hoc analysis was also performed to assess the significance of the differences in MTS activity (section 3.2.1) and CD63/CD81 expression (section 3.3.1) between infected/uninfected cells, at the different assay time-points. All statistical analyses used a cut-off value of $p<0.05$. Data are presented as mean ± 2SEM unless otherwise stated. All conditions were tested in triplicate in three independent experiments unless otherwise stated.

Chapter 3: Results

3.1 Technical Optimisation

3.1.1 Spheroid Growth Optimisation

HuH-7 and A549 cells were seeded at a range of densities based on those reported in the literature for successful spheroid formation, using the anchorage-independent ULA plate technique as described in section 2.1.5. For HuH-7 spheroid optimisation, cells were seeded at 5,000, 10,000, and 15,000 cells/well in 100µL (Khawar et al., 2018). To form A549 spheroids, a greater seeding density was required; for optimisation, seeding densities of 20,000, 25,000, and 30,000 cells/well in 100µL were used (Ekert et al., 2014; Saleh et al., 2020).

After seeding, the ULA plates were incubated for 3 days at 37°C, 5% CO_2 to allow spheroids to form, before imaging. The spheroids were imaged using the colony counter GelCount™ by Oxford Optronix every 24 hours, from day 3 (post-seeding), for a period of 10 days (excluding days 8 and 9). Spheroid measurements were determined at each time point using ImageJ software, as described in section 2.2.1. Three ULA plates for each cell line were seeded, imaged, and analysed; each plate was seeded with cells at differing passages. Within each plate, 10 technical replicates were analysed for each seeding density; the same 10 spheroids were measured at each time point for comparability. This non-invasive imaging technology was utilised to allow the same spheroids to be assessed throughout the course of the experiment, without interfering with the growth of the spheroids.

A statistically significant difference in spheroid diameter between initial seeding densities was found for A549 spheroids, P=0.0055 (two-way ANOVA overall interaction P value). However, no statistically significant difference between initial seeding density and spheroid diameter was found for HuH-7 spheroids, P=0.2528.

On day 3 (post-seeding), both A549 and HuH-7 cells had formed spheroids (see Figure 3.1 (ii) and Figure 3.2 (ii), respectively). Tukey's multiple comparisons confirmed that A549 spheroids seeded at 30,000 cells/well were significantly larger than those seeded at 25,000 cells/well (P=0.0031), and those seeded at 20,000 cells/well (P=0.0010) on day 3. In contrast on day 3, there was no significant difference in the diameter of HuH-7 spheroids seeded at

15,000 cells/well compared to those seeded at 10,000 cells/well (P=0.8826), or those seeded at 5,000 cells/well (P=0.1342). For both A549 and HuH-7 spheroids, there was no significant difference in spheroid diameter (on day 3) between the two lowest seeding densities; P=0.0831 and P=0.2513, respectively.

A549 spheroids were larger than HuH-7 spheroids on days 3 and 4, at all seeding densities used. However, A549 spheroids (at all seeding densities) decreased in size throughout the time course of the experiment (Figure 3.1 (i)), whereas HuH-7 spheroids became larger at all densities (Figure 3.2 (i)). On days 6, 7, and 10, all HuH-7 spheroids were larger than the A549 spheroids. Day 5 (post-seeding), therefore, was chosen as the optimal incubation time to perform subsequent experiments on both A549 and HuH-7 spheroids as, at this time point, the spheroids formed from both cell lines were similar in size.

Optimal seeding densities of 30,000 cells/well and 5,000 cells/well were chosen for seeding A549 and HuH-7 cells, respectively (Table 3.1). This decision was based on the observation that the spheroids seeded at these densities formed the most uniform and spherical bodies. The spheroids seeded at the other densities often formed heterogeneous shapes, with less distinctive peripheries (see Figure 3.1 (ii, B) and Figure 3.2 (ii, C)). Furthermore, on day 5 (optimal incubation time), the A549 spheroids seeded at 30,000 cells/well were the largest (0.595mm ± 0.0163). Larger spheroids are easier to handle in subsequent experiments, e.g., when transferring the spheroids into microfluidic chips (see section 2.4.2) and are also less likely to be lost during media changes, washes, staining etc. There was little difference in the diameter of HuH-7 spheroids between seeding densities on day 5. As such, the lowest seeding density (5,000 cells/well) was chosen so that more spheroids could be generated from lower cell counts.

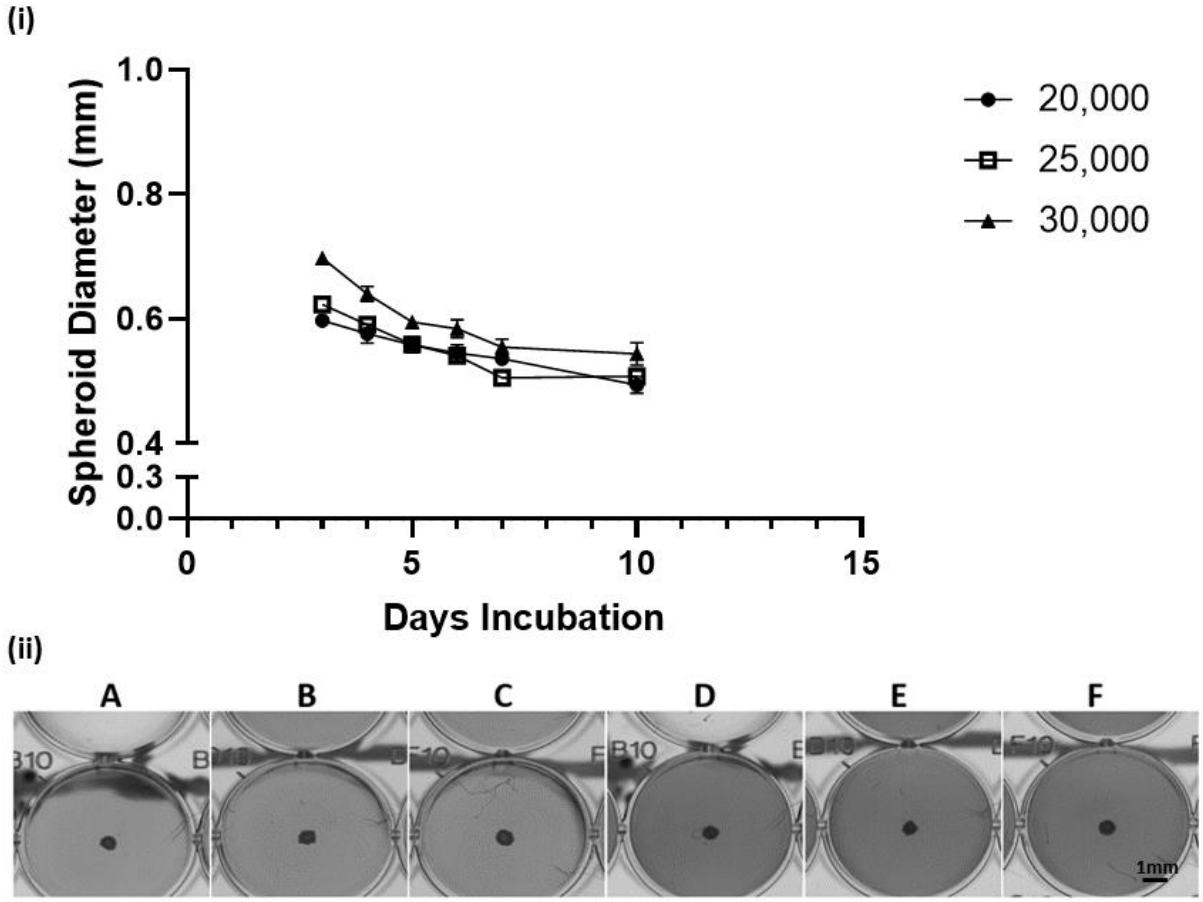

Figure 3.1. Growth of A549 spheroids seeded at varying densities. ***(i)*** *A549 spheroid diameter measurements. Spheroid diameter (mm) was measured using ImageJ software on days 3, 4, 5, 6, 7, and 10 (post-seeding). The vertical and horizontal diameter was obtained, and averaged, for each spheroid at each time point (n= 10). Each data point represents the average spheroid diameter calculated from three independent experiments (n=3). Error bars represent ± 2 standard deviations. A549 spheroids decrease in diameter from day 3 (post-seeding), until day 7, when the diameter plateaued.* ***(ii)*** *GelCount™ images of A549 spheroids seeded into a ULA plate at varying densities. The representative images shown were taken on day 3 post-seeding (A-C) and day 5 post-seeding (D-F). Seeding densities are as follows: A & D; 20,000 cells/well, B & E; 25,000 cells/well, C & F; 30,000 cells/well.*

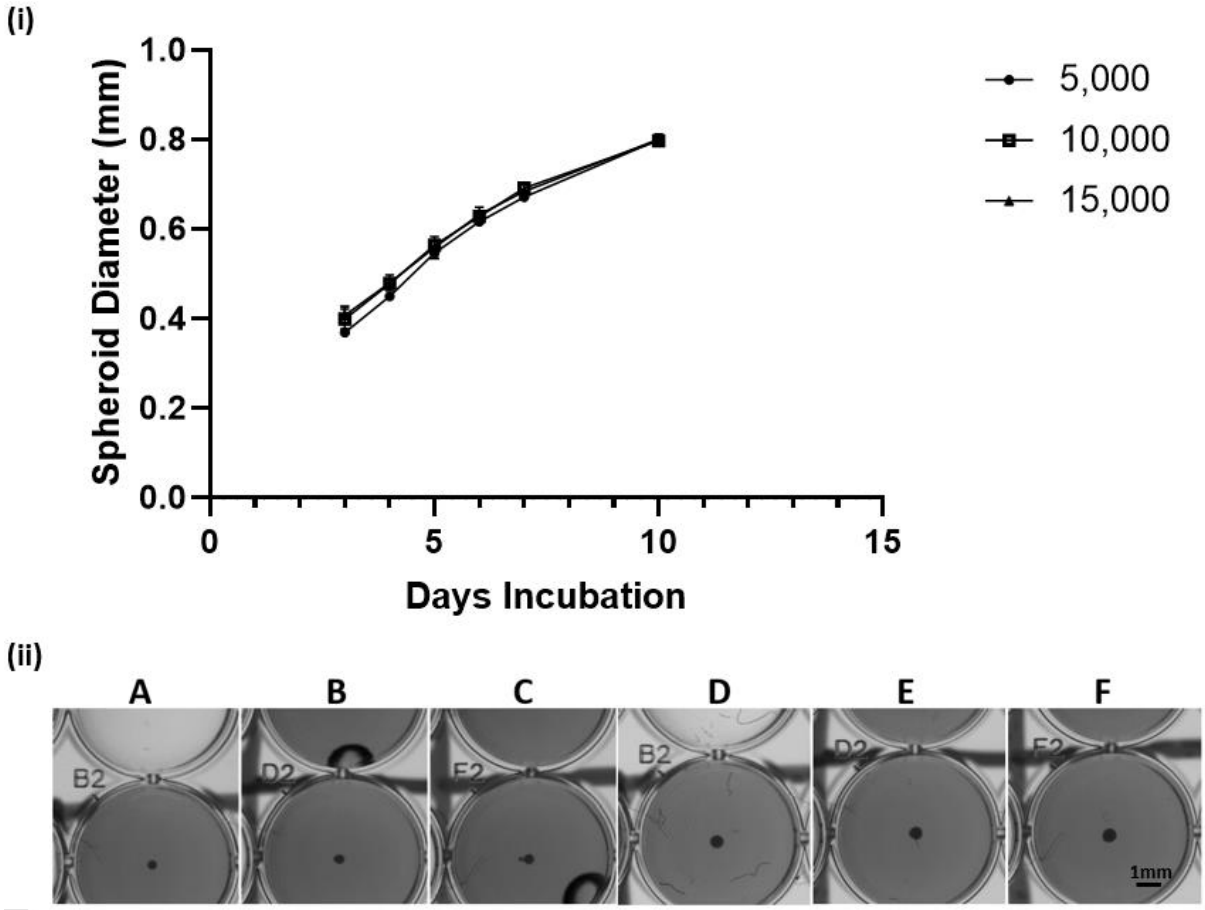

Figure 3.2. Growth of HuH-7 spheroids seeded at varying densities. ***(i)*** *HuH-7 spheroids diameter measurements. Each data point represents the average spheroid diameter calculated from three independent experiments (n=3). In each experiment, a total of 10 spheroids (each density) were measured at each time point, and the average diameter was obtained. Error bars represent ± 2 standard deviations. HuH-7 spheroids increase steadily in diameter from day 3 (post-seeding). By day 10, all spheroids reached a maximal diameter, regardless of the initial seeding density.* ***(ii)*** *GelCount™ images of HuH-7 spheroids seeded into a ULA plate at varying densities. The representative images shown were taken on day 3 post-seeding (A-C) and day 5 post-seeding (D-F). Seeding densities are as follows: A & D; 5,000 cells/well, B & E; 10,000 cells/well, C & F; 15,000 cells/well.*

Table 3.1 shows the seeding densities used for each cell line, and the number of days incubation at 37°C, 5% CO_2 that is required for the formation of spheroids which are uniform in both size and sphericity.

Table 3.1. Optimal seeding densities and incubation times for the formation of uniform U-87 MG, HuH-7 and A549 spheroids.

Cell Line	Seeding Density (100µL/ well)	Days Incubation (37°C, 5% CO_2)
U-87 MG	20,000	3
HuH-7	5,000	5
A549	30,000	5

The optimal seeding density and incubation for U-87 MG spheroid formation is as described in previous optimisation studies (Sennett, 2019).

3.1.2 The Effects of Reduced Serum Conditions on Spheroid Growth

When performing infections with BUNV, the cell culture medium is replaced with fresh medium, containing a reduced concentration (2% (v/v)) of FBS, as described in section 2.3.1. To assess whether reduced-serum conditions impact spheroid growth, both A549 and HuH-7 spheroids were treated with reduced-serum media and maintained in a 33°C, 5% CO_2 incubator, as described in section 2.2.2, to replicate the conditions used for BUNV infections. Spheroid growth was analysed as described in section 2.2.1.

No statistically significant difference in spheroid diameter was observed for A549 spheroids between the two concentrations of FBS (10% vs 2% (v/v)), at any of the time points (see Figure 3.3 (i)), P=0.1793. There was, however, a significant difference in HuH-7 spheroid diameter between the two FBS concentrations at 96 hours (post media transition, see Figure 3.3 (ii)), P=0.0118. Since no significant difference in HuH-7 spheroid diameter was found at 120, 168, and 240 hours (P=0.2727, P=0.9269, and P=0.9977, respectively), it was determined that the observed difference was likely a result of spheroid size variation caused by a disruption to the spheroids during the media change at 72 hours (post-transition).

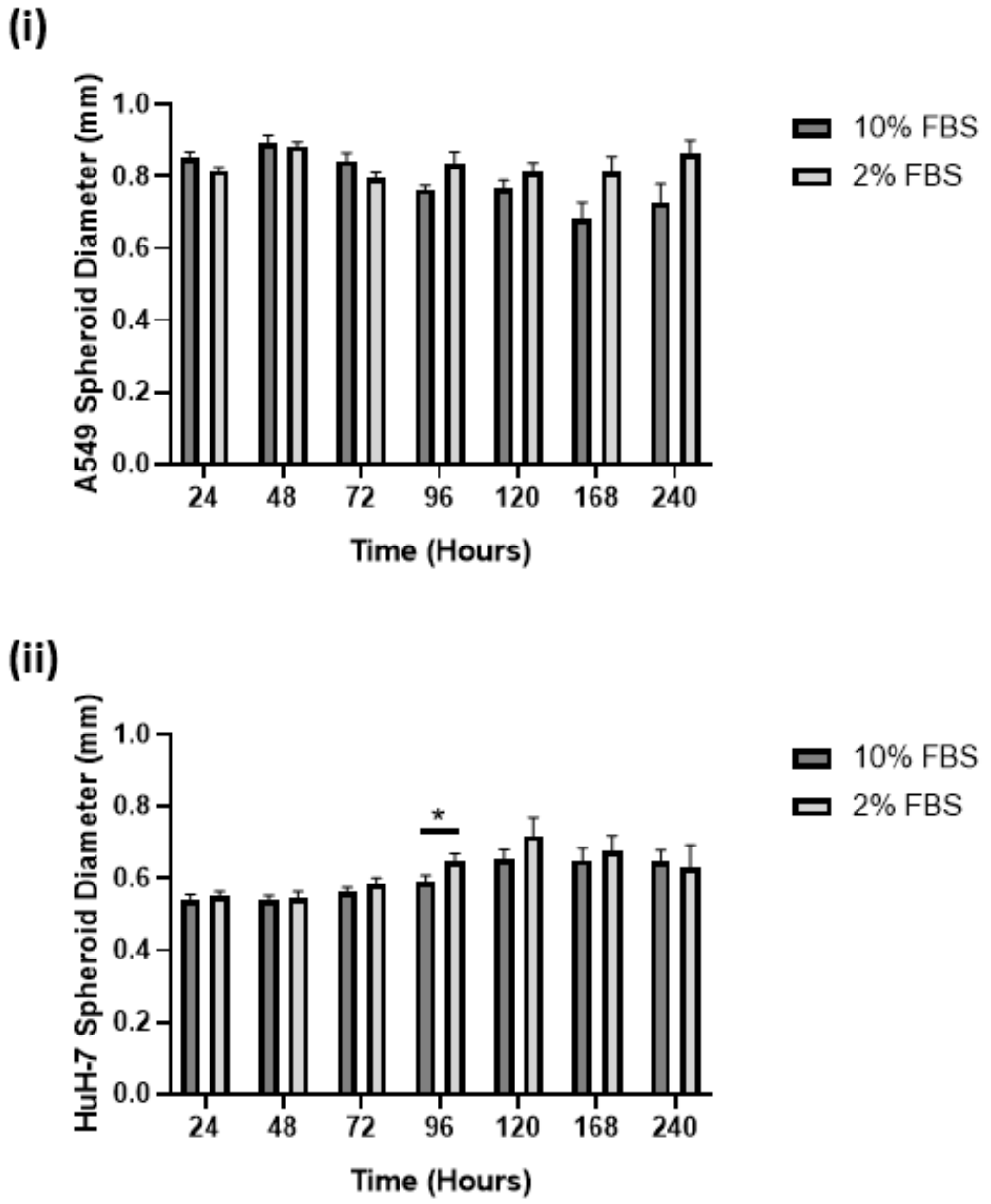

Figure 3.3. The effects of reduced serum conditions on A549 and HuH-7 spheroid growth. *Spheroid measurements were determined using ImageJ software. Time (X-axis) refers to the number of hours after transitioning the spheroids into new media (containing 10% or 2% (v/v) FBS), followed by incubation at 33°C, 5% CO_2.* ***(i)*** *The effects of reduced serum conditions on A549 spheroid growth. No significant difference in A549 spheroid diameter is observed between FBS concentrations at all time points.* ***(ii)*** *The effects of reduced serum conditions on HuH-7 spheroid growth. A significant difference in HuH-7 spheroid diameter is observed between FBS concentrations at 96 hours, P=0.0118. No statistically significant differences in HuH-7 spheroid diameter are observed at all other time points. Error bars represent the standard error of the mean (SEM), n=5.*

3.1.3 BUNV Adaptation to HuH-7 and U-87 MG Cells

i) BUNV Adaptation to HuH-7 Cells – Worked Calculation

Stocks of WT-BUNV adapted to the HuH-7 cell line were generated as described in section 2.3.4. Very few plaques were observed in the titre plates for the supernatant collected from HuH-7 cells infected at the higher MOIs (0.01 and 1), this is likely due the generation of defective interfering (DI) particles, as discussed in section 2.3.4. The plaque assay performed on the supernatant collected from the cells infected at an MOI of 0.001 produced more visible plaques, giving an acceptable titre. This adaptation yielded an initial titre of 1.6×10^6 pfu/mL. The HuH-7 adapted WT-BUNV stock calculation is detailed below; this calculation uses Equation 4.

HuH-7 adapted WT-BUNV stock pfu/mL calculation:

1) Average no. plaques in the 10^{-5} wells: (19 + 15) / 2 = **17**

   $17 / (0.00001 \times 1) =$ **1.7×10^6**

2) Average no. plaques in the 10^{-6} wells: (1 + 2) / 2 = **1.5**

   $1.5 / (0.000001 \times 1) =$ **1.5×10^6**

3) Average pfu/mL = $((1.7 \times 10^6) + (1.5 \times 10^6)) / 2 =$ **1.6×10^6 pfu/mL**

Following repeated infection of HuH-7 cells using this initial virus stock, subsequent HuH-7 adapted WT-BUNV stocks were titred at 2.6×10^7 pfu/mL.

ii) BUNV Adaptation to U-87 MG Cells

As described in section 2.3.4, extensive lifting of U-87 MG cells was observed for all MOIs used at 72hpi when performing the initial adaptation experiment (Figure 3.4 (A)). This same lifting was observed in the plaque assay plate when attempting to titre the supernatant (Figure 3.4 (B)), meaning that viral titre could not be determined. Therefore, the plaque assay conditions were altered to attempt to generate a U-87 MG-adapted BUNV stock.

Firstly, lower starting MOIs were used in the initial infection plate (0.0001, 0.001, 0.01). Despite observing reduced cell lifting at 72hpi with these lower MOIs, no plaques could be observed in the plaque assay plates, again, due to extensive destruction and lifting of the monolayers. This lower MOI experiment was then repeated, instead allowing 20 minutes of virus-cell contact (as opposed to 1 hour) with fixing and staining of the cell monolayers after 72 hours of incubation with the methylcellulose/media overlay, as opposed to 120 hours (see section 2.3.2). Still, U-87 MG monolayers appeared to lift in the plaque assay plates, and no plaques could be visualised. Infection of U-87 MG cells with BUNV was repeated once again, using the lower MOIs, reduced virus-cell contact, and supplementing the monolayers in the plaque assay plates with 6mL methylcellulose/media overlay instead of 4mL. Again, after 72 hours of incubation at 33°C, 5% CO_2, cell lifting was observed, and viral titre could not be determined.

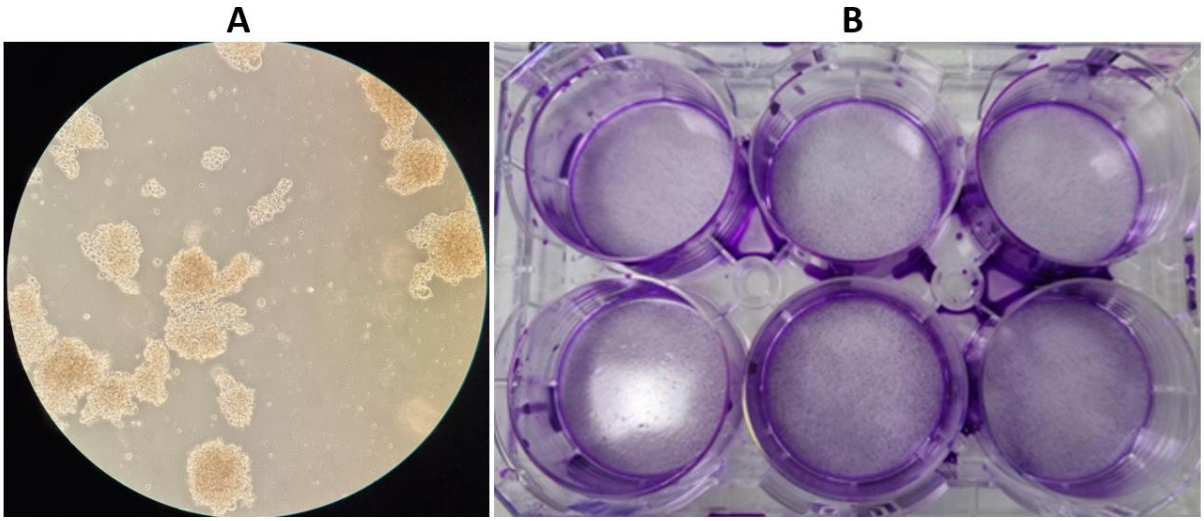

Figure 3.4. Extensive lifting and destruction of U-87 MG monolayers following infection with BUNV. ***A:*** *U-87 MG cells, 72hpi (MOI 0.01), viewed under a light microscope at 10x magnification.* ***B:*** *A crystal-violet stained plaque assay plate showing extreme destruction of U-87 MG monolayers. U-87 MG cells were seeded in the plaque assay plate and treated with a serial dilution of clarified virus-containing supernatant collected from the well shown in (A). After 120 hours of incubation at 33°C, 5% CO_2, with a methylcellulose/media overlay, the cells were fixed twice with 10% formaldehyde, washed, and stained with crystal violet.*

Finally, a mock infection was performed to investigate whether the observed CPE was a result of BUNV infection, the plaque assay conditions (reduced FBS medium/methylcellulose overlay, 33°C incubation, or staining). Or, whether the observed CPE was due to a U-87 MG-

cytotoxic component contained within the A549-derived spent media (in which the viral stock is maintained).

To do this, A549 cells were seeded into a 6-well plate as described in section 2.1.4. After 24 hours, the media was replaced with fresh media containing 2% (v/v) FBS, without P/S. The near-confluent A549 cells were then incubated at 33°C, 5% CO_2 for five days, and the resulting spent media was used to mimic the infection conditions previously used on U-87 MG monolayers. U-87 MG cells were seeded into a 6-well plate, and after allowing 24 hours for 70-80% confluent monolayers to form, each well was treated with 1mL of the A549-derived spent media, for one hour, to mimic the conditions used in BUNV infection experiments. After one hour, the media was removed, and each well (containing the mock-infected U-87 MG cells) was supplemented with 4mL fresh media (-P/S, +2% (v/v) FBS). The plate was incubated at 33°C, 5% CO_2, and inspected daily for CPE.

This mock-infection appeared to not affect the U-87 MG cells, which continued to proliferate and appear healthy under microscopic examination (Figure 3.5). It was therefore determined that the observed lifting was likely a result of infection with BUNV, and the conditions used to perform the plaque assay. As previously stated in section 2.3.4, it was not possible to generate a U-87 MG adapted BUNV stock in an appropriate time frame for the project, therefore, future infection experiments are conducted using the A549 and HuH-7 cell lines only.

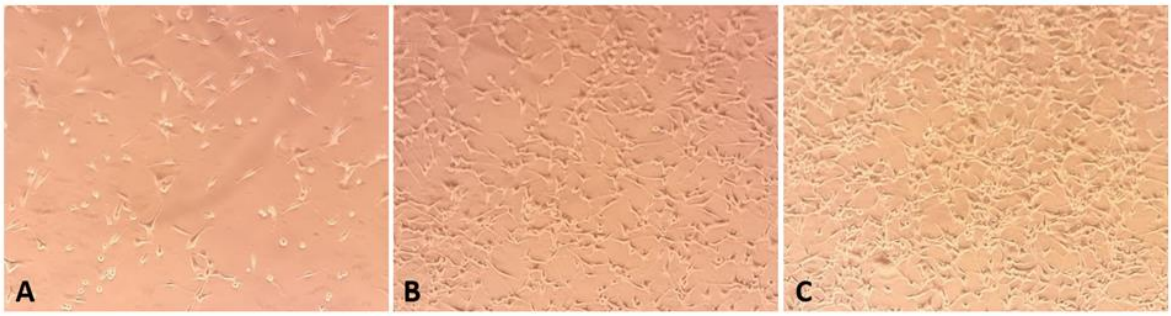

Figure 3.5. U-87 MG cells post mock-infection with A549-derived spent media. Viewed under a light microscope at 10x magnification. ***A:*** *24 hours post mock-infection.* ***B:*** *120 hours post mock-infection.* ***C:*** *168 hours post mock-infection. U-87 MG cells maintain typical morphology and continue to proliferate after being mock-infected with A549-derived spent media. No extensive lifting was observed. Images are representative of 6x U-87 MG monolayers subject to the same experimental conditions.*

3.1.4 Comparison of Ultracentrifugation Protocols

To optimise an ultracentrifugation protocol for the isolation of exosomes and BUNV virions, supernatant was collected from A549 and HuH-7 cells (+/- BUNV infection) as described in section 2.7.1. The collected supernatant was divided; half was subject to a standard ultracentrifugation procedure, and the remaining half was further purified using a sucrose cushion in an additional ultracentrifugation step (see Figure 2.12). The use of sucrose cushion ultracentrifugation for the purification of BUNV virions is well described in the literature (Habjan et al., 2009; Guardado-Calvo et al., 2016; Huang et al., 2016; Mastrodomenico et al., 2019; Mo et al., 2020). Although not essential to obtain reasonably pure exosome pellets (Théry et al., 2006), the use of a sucrose cushion has been shown to effectively separate exosomes from aggregated proteins and high density nucleic acids contaminants, which are present in the exosome pellets produced from differential ultracentrifugation alone (Momen-Heravi et al., 2013; Witwer et al., 2013; Gupta et al., 2018).

Pellets of exosomes/viral particles, prepared using both ultracentrifugation methods, were lysed, and the protein concentration was quantified by BCA assay as described in section 2.8.1. Protein concentration was greater in all samples prepared by ultracentrifugation with a sucrose cushion, compared to those prepared by standard ultracentrifugation (Figure 3.6).

The proteins contained within the lysates were separated using SDS-PAGE; due to the low protein concentration of the 'standard ultracentrifugation' samples (Figure 3.6), only 10µg/well of each sample was loaded, to ensure a fair comparison. The membrane was probed for the exosome marker CD63, as well as BUNV N protein, as described in section 2.8.1 (Figure 3.7).

A lower expression of CD63 was observed in the samples prepared by sucrose cushion ultracentrifugation, compared to those prepared by standard ultracentrifugation (Figure 3.7 (iii)). Similarly, BUNV N protein expression was less intense in the HuH-7 sample prepared with a sucrose cushion (55.7%), relative to the sample which had been prepared without a sucrose cushion (Figure 3.7 (iv)). In contrast, very little BUNV N protein was detected in the BUNV-infected A549 sample which was subject to standard ultracentrifugation. Relative to the A549 sample prepared by standard ultracentrifugation, BUNV N protein expression in the A549 sample prepared with sucrose cushion purification was 6x more intense.

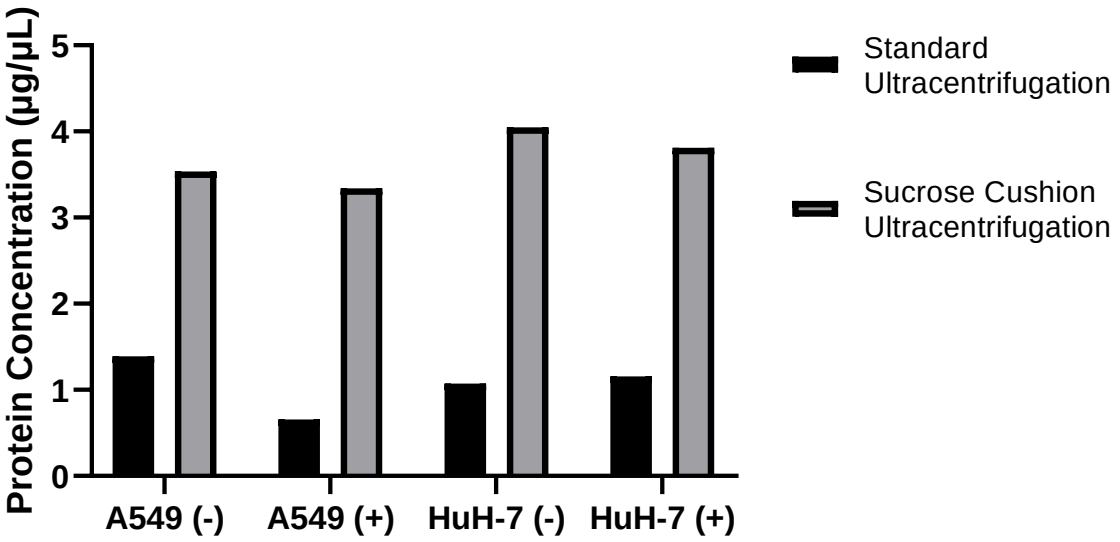

Figure 3.6. Differences in protein concentration between samples prepared by standard ultracentrifugation versus ultracentrifugation with a 30% sucrose cushion. *A549 and HuH-7 cells were mock-infected (-) or infected with BUNV at an MOI of 0.1 (+) and incubated at 33°C, 5% CO_2. After 5 days, exosomes/viral particles were isolated from the A549/HuH-7 spent media by either standard ultracentrifugation, or ultracentrifugation with a sucrose cushion. Protein concentration was determined by BCA assay (n=1).*

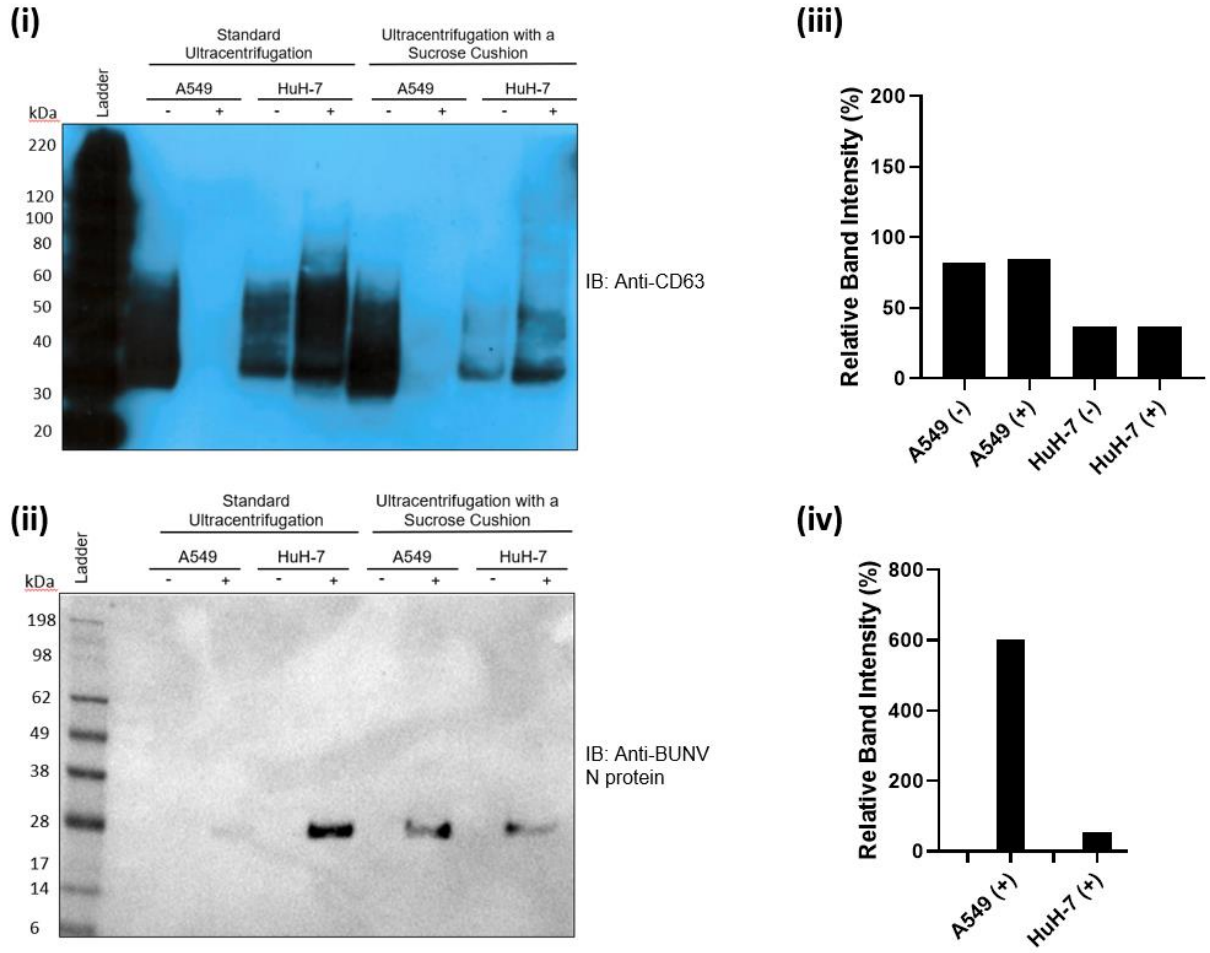

Figure 3.7. Western blot analysis of CD63 and BUNV N protein to compare exosome/viral particle isolation techniques. ***(i)*** *Western blot for CD63; exosomes were purified from A549 and HuH-7 supernatant by standard ultracentrifugation and ultracentrifugation with a 30% sucrose cushion. Cells were mock-infected (-) or infected with BUNV at an MOI of 0.1 (+), and incubated at 33°C, 5% CO_2, for 120 hours before collecting the supernatant for ultracentrifugation. Proteins were separated by denaturing but non-reducing SDS-PAGE. Protein concentration was normalised by BCA assay, and 10µg of protein was loaded for each sample.* ***(ii)*** *The membrane used in blot (i) was stripped, blocked and re-probed for BUNV N protein.* ***(iii)*** *Densitometry analysis, using ImageJ, of the detected CD63 bands. Each bar represents the relative intensity of the bands observed for the samples prepared by ultracentrifugation with a sucrose cushion. Intensity is expressed as a percentage relative to the standard ultracentrifugation samples (n=1).* ***(iv)*** *Densitometry analysis of the detected BUNV N protein bands, intensity is expressed as a percentage relative to the standard ultracentrifugation samples (n=1).*

3.2 The Effects of BUNV Infection in 2D, 3D (Static), and 3D Microfluidic Culture Models

3.2.1 Metabolic Activity - MTS Assay

The effects of BUNV infection on the metabolic activity of A549 and HuH-7 cells in 2D and 3D (static) cell cultures was determined by MTS assay as described in section 2.5.2. In addition to uninfected control cells/spheroids, the absorbance correlating to MTS activity was also recorded for "no cell" control wells, containing assay medium only. At each time point (24-, 72-, 120-, 168-, and 240-hpi with BUNV), the absorbance was recorded in triplicate for each condition (media only, uninfected, MOI 0.1, MOI 1, and MOI 10) and the average MTS absorbance and thus levels of metabolic activity was determined. The average absorbance value obtained from the wells containing media only was subtracted from the average absorbance recorded for each experimental condition, at each time point, to account for spurious MTS activity or interference in the assay medium.

To assess the effects of BUNV infection on metabolic activity, the average absorbance values obtained for each sample infected with BUNV were expressed as a percentage relative to the uninfected control sample, at each respective time point. To allow comparison, the MTS (metabolic) activity in the uninfected control samples was considered as 100% at each time point (Figure 3.8). Data are presented as mean ± 2SEM.

i) BUNV Infection Decreases Metabolic Activity in A549 Cells Cultured as 2D Monolayers

In A549 cells cultured as 2D monolayers, there was a significant difference in MTS activity between cells infected with BUNV at an MOI of 0.1 and those infected at an MOI of 10 at 24hpi ($P=0.0080$), 72hpi ($P<0.0001$), and 120hpi ($P<0.0001$). Infecting A549 monolayers with BUNV at an MOI of 10 had the most profound effect on MTS activity of the three MOIs used (Figure 3.8 (i)); these cells consistently showed the lowest rates of MTS activity. However, no significant difference in MTS activity was found between cells infected at an MOI of 0.1 and those infected at an MOI of 10 at 168hpi ($P=0.5906$), and 120hpi ($P=0.4894$). Likewise, MTS activity was significantly higher in cells infected at an MOI of 1 compared to those infected at

an MOI of 10 at 24-, 72, and 120hpi (P=0.0010, P<0.0001, P<0.0001, respectively), and at 168- and 240hpi, there was no significant difference in MTS activity between cells infected at an MOI of 1 and those infected at an MOI of 10 (P>0.9999, P=0.9118, respectively; Figure 3.8 (i)). Furthermore, no significant difference in MTS activity was found, at any time point, between cells infected at MOI 0.1 and MOI 1. The relative MTS activity decreased in 2D cultures of A549 cells infected at MOI 0.1 from 95.92% ± 6.36% at 120-hpi to 36.98% ± 4.88% at 168-hpi. Similarly, 2D A549 cells infected at an MOI of 1 showed a decrease in relative MTS activity between 120- and 168-hpi; from 109.28% ± 1.78%, to 28.31% ± 3.22%. The relative MTS activity was similar across all three MOIs used at the final two time-points; with little variation in MTS activity between 168- and 240-hpi for each MOI used (Figure 3.8 (i)).

ii) BUNV Infection Has Little Effect on the Metabolic Activity in A549 Spheroids Until 240hpi

In contrast to 2D culture, increasing MOI appeared to have little effect on the relative MTS activity in A549 cells cultured as 3D spheroids (Figure 3.8 (ii)). At 24-, 72, 120-, and 168-hpi, no significant difference in MTS activity was found between each of the MOIs used. However, at 240hpi, the relative MTS activity was significantly lower in spheroids infected at an MOI of 1, compared to those infected at an MOI of 0.1 (P=0.0381). Interestingly, no significant difference in MTS activity was found between spheroids infected at MOI 0.1 and those infected at MOI 10 at 240hpi (P=0.0670); it is possible that this may be influenced by the limited number of replicates (n=3). Further in contrast to 2D culture, the relative MTS activity in A549 spheroids infected at MOIs of 0.1 and 1 increased between 120- and 168hpi (Figure 3.8 (ii)); the relative MTS activity of the spheroids infected at MOI 0.1 increased from 111.49% ± 5.94% to 129.29% ± 8.30%, and the relative MTS activity of those infected at MOI 1 increased from 121.4% ± 9.15% to 129.40% ± 6.89%. For each MOI used, the relative MTS activity decreased between 168- and 240-hpi (Figure 3.8 (ii)).

iii) BUNV Infection Induces Sporadic Changes to the Metabolic Activity in HuH-7 2D Cultures

In 2D cultures of HuH-7 cells, there was no significant difference in the relative MTS activity between each of the MOIs used at 24-, 168-, and 240hpi. However, at 72hpi, the cells infected with BUNV at MOI 0.1 showed significantly greater MTS activity compared to those infected at MOI 10 (P=0.0017), and those infected at MOI 1 (P=0.0079) (Figure 3.8 (iii)). No significant difference in MTS activity was found between cells infected at MOI 1 and those infected at MOI 10 at 72hpi (P=0.7039). However, between 72- and 120-hpi, the relative MTS activity of cells infected at MOI 0.1 decreased from 112.33% ± 3.78% to 92.34% ± 2.64%. Likewise, the relative MTS activity of the cells infected at MOI 1 decreased from 102.62% ± 1.49% to 88.82% ± 2.10% (Figure 3.8 (iii)). Contrastingly, little change in the relative MTS activity was observed in cells infected at MOI 10 between 72- and 120-hpi. As such, at 120hpi, the cells infected at MOI 10 show significantly higher MTS activity than the cells infected at MOI 1 (P=0.0030), and those infected at MOI 0.1 (P=0.451) (Figure 3.8 (iii)). There was no significant difference in the relative MTS activity between cells infected at MOI 1 and cells infected at MOI 0.1 at 120hpi (P=0.4852).

iii) BUNV Infection Has Little Effect on the Metabolic Activity in HuH-7 Spheroids

Interestingly, in 3D cultures of HuH-7 cells, there was no significant difference in the relative MTS activity between all MOIs used at any time point during the assay period (Figure 3.8 (iv)). Between 24- and 72-hpi, the relative MTS activity of all the infected HuH-7 spheroids appeared to decrease. This was followed by an increase in MTS activity (at all MOIs used) between 72- and 120-hpi, and a further increase in MTS activity (at all MOIs used) between 120- and 168-hpi. Between 168- and 240-hpi, the relative MTS activity of spheroids infected at MOI 10, and those infected at MOI 1 increased again (MOI 1: 107.29% ± 6.20% to 126.50% ± 9.24%, MOI 10: 115.94% ± 4.86% to 119.90% ± 6.14%). In contrast, the spheroids infected at MOI 0.1 showed a decreased relative MTS activity between 168hpi (117.62% ± 13.30%) and 240hpi (107.43% ± 1.01%).

iv) The Metabolic Activity in A549 and HuH-7 3D Cultures is More Variable than in 2D Cultures

To better understand the observed effects of BUNV infection on metabolic activity (as detailed above) the MTS absorbance data produced from the uninfected controls was further interrogated. The MTS activity of each A549/HuH-7 uninfected control (2D and 3D; at 72-, 120-, 168-, and 240-hpi) was expressed as a percentage relative to respective uninfected control at 24hpi, for which the MTS activity was considered as 100% (Figure 3.9).

For both A549 and HuH-7 2D cell cultures, there was no significant difference in the MTS activity of uninfected controls throughout the course of the experiment. However, in 3D cultures of both A549 and HuH-7 cells, the relative MTS activity of the uninfected controls appeared to fluctuate (Figure 3.9). The relative MTS activity of uninfected A549 spheroids at 240hpi was significantly greater than that at 72hpi ($P=0.0344$), and that at 120hpi ($P=0.0239$). However, there was no significant difference in the MTS activity of the uninfected A549 spheroids at 168hpi, compared to that at 240hpi ($P=0.0606$). As previously mentioned, this is likely influenced by the limited number of replicates ($n=3$).

Likewise, in 3D cultures of HuH-7 cells, the relative MTS activity of mock-infected ('uninfected') spheroids appears to vary throughout the assay period. A significant difference in MTS activity was found between HuH-7 spheroids measured at 72hpi, compared to those measured at 168hpi ($P=0.0103$), and between those measured at 168hpi compared to 240hpi ($P=0.0287$).

In 3D cultures of both A549 and HuH-7 cells, the relative MTS activity of uninfected spheroids appears to decrease consecutively between 72- and 168-hpi, with an increase in MTS activity observed in both cell lines between 168- and 240hpi. It is possible that the observed decrease in MTS activity may be a result of spheroid damage, inflicted during media changes (Cui et al., 2017; Han et al., 2021). As detailed in section 2.5.2, media changes were performed every 2 days following infection/mock-infection, coinciding with the MTS measurements at 72, 120, and 168 hours. The final media change was performed 216 hours after the initial infection/mock-infection, giving the spheroids 24 hours to recover from any damage caused during the media change, before recording the final MTS measurement at 240 hours.

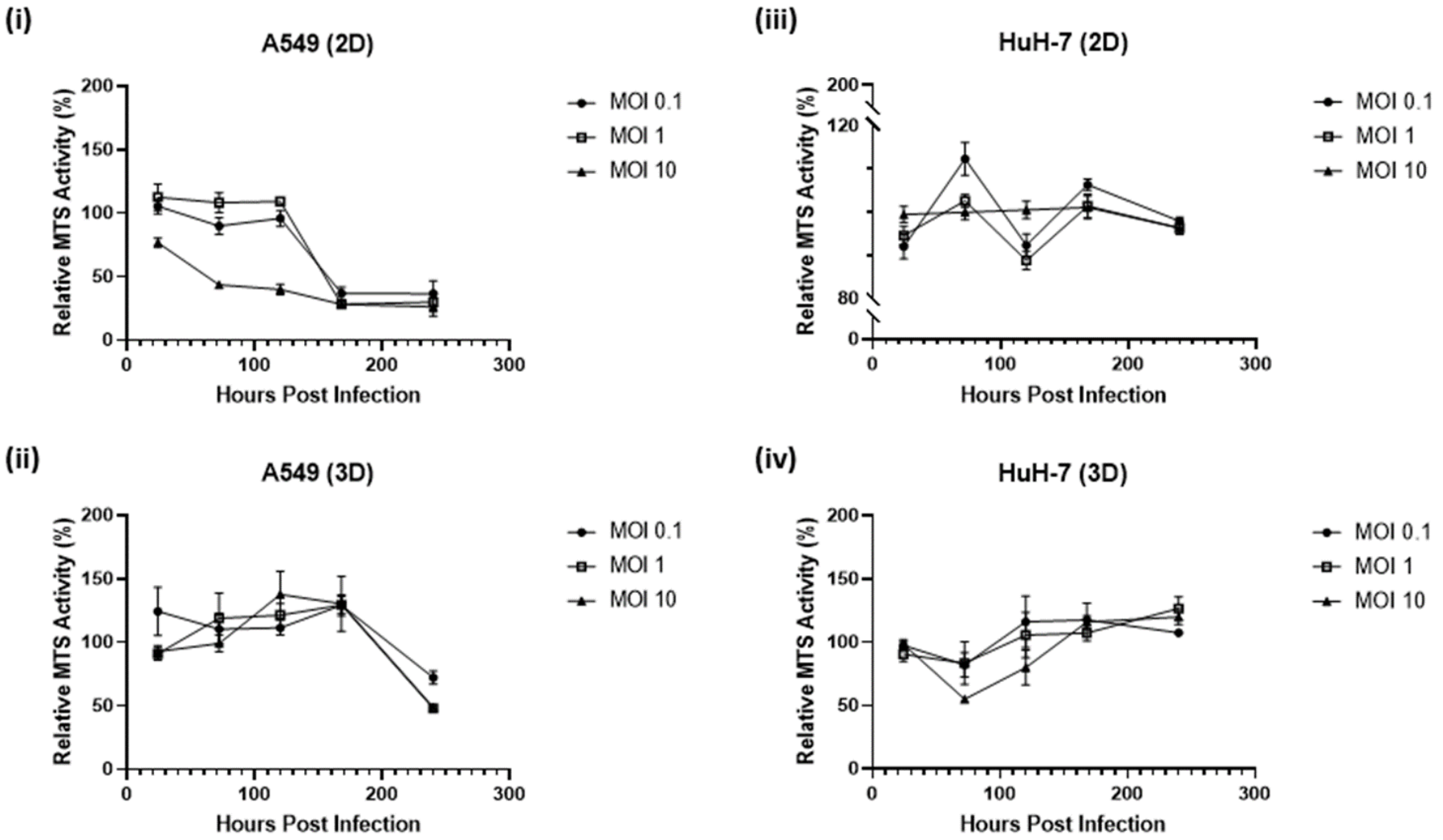

Figure 3.8. The effects of BUNV infection on the metabolic activity of A549 and HuH-7 cells cultured as 2D monolayers versus 3D spheroids. *Cells/spheroids were infected with BUNV at MOIs of 0.1, 1, and 10, and the effects on cellular metabolic activity were assessed via MTS assay at 24-, 72-, 120-, 168- and 240-hpi. MTS activity (i.e., metabolic activity) is expressed as a percentage relative to MTS activity of the 'uninfected' (mock-infected) cells/spheroids which, at each time point, was considered as 100%.* ***(i)*** *The relative MTS activity of A549 monolayers infected with BUNV at varying MOIs.* ***(ii)*** *The relative MTS activity of A549 spheroids.* ***(iii)*** *The relative MTS activity of HuH-7 cell monolayers.* ***(iv)*** *The relative MTS activity of HuH-7 spheroids. Data are presented as mean ± 2SEM, n=3.*

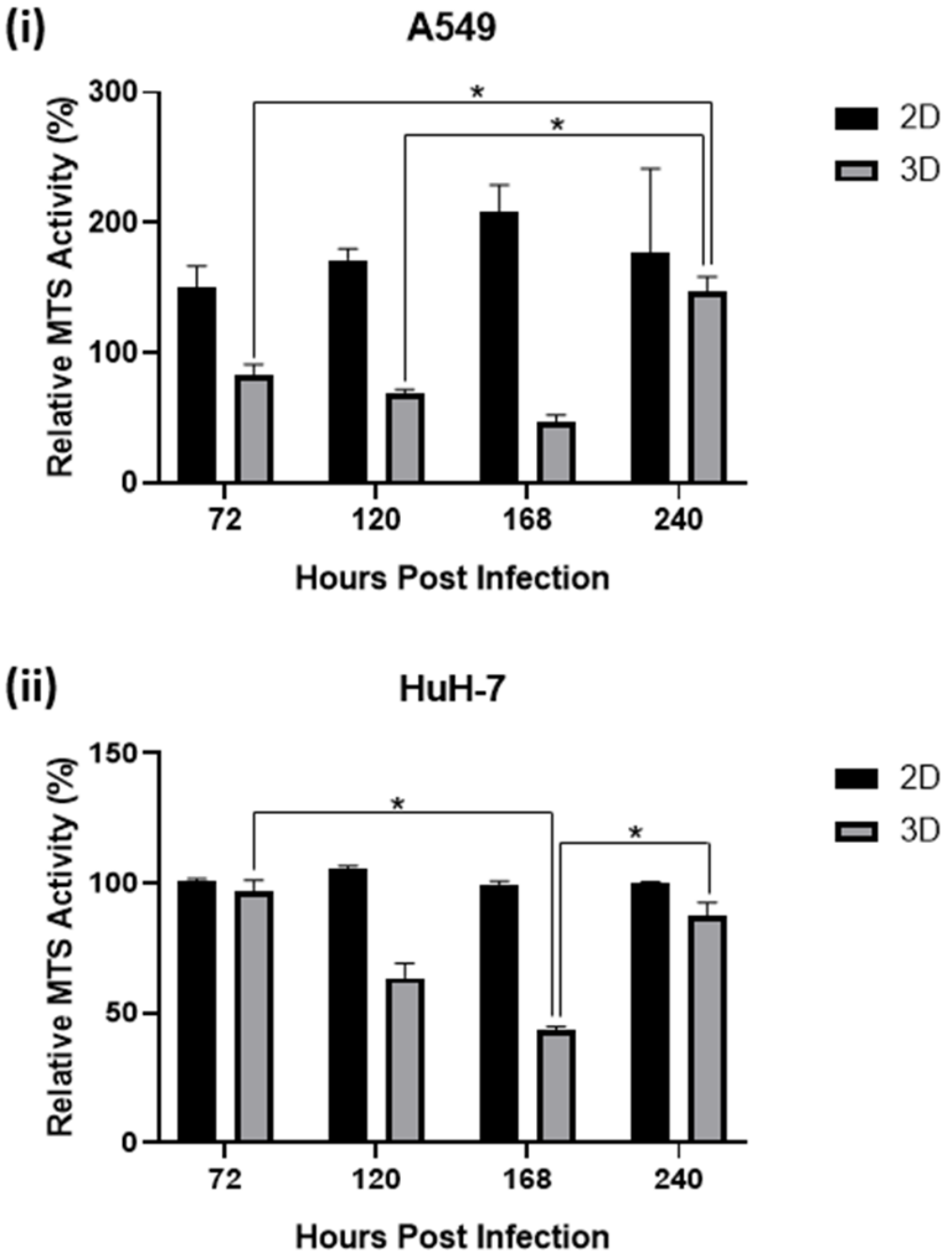

Figure 3.9. The effects of time on the relative MTS activity of the 'uninfected' A549 and HuH-7 controls. *A549* ***(i)*** *and HuH-7* ***(ii)*** *cell monolayers and 3D spheroids were mock-infected with plain cell culture medium, and the metabolic activity was assessed via MTS assay at 24-, 72-, 120-, 168-, and 240-hours post mock-infection. Relative MTS activity is expressed as a percentage relative to the MTS absorbance recorded at 24 hours (post mock-infection), for the respective cells/spheroids, which was considered as 100%. Data are presented as mean ± 2SEM, n=3.*

3.2.2 Fluorescence Microscopy (with FDA & PI Staining)

Fluorescence microscopy with fluorescein diacetate/propidium iodide (FDA/PI) staining was utilised to allow the qualitative assessment of live and dead cells in A549/HuH-7 (static) spheroids, infected with BUNV as described in section 2.3.5. Mock-infected ('uninfected' control) spheroids were imaged alongside spheroids infected with BUNV at MOIs of 0.1, 1, and 10 at each time point. At each time point, 3x spheroids (each cell line and MOI) were treated with an FDA/PI staining solution and imaged as described in section 2.5.1. Figure 3.10 shows representative images of FDA/PI stained, BUNV-infected A549/HuH-7 spheroids, at 24-, 72- and 120-hpi.

Between 24- and 120-hpi, the amount of green (live) cells on the peripheries of the uninfected A549 and HuH-7 spheroids appears to decrease. This is congruent with the MTS data obtained for the uninfected spheroids (Figure 3.9), in which the relative MTS activity appears to decrease between 24- and 120-hpi, inferring a decrease in viable, living cells. However, in uninfected HuH-7 spheroids, this decrease in the amount of living cells is accompanied by a concurrent increase in the amount of red (dead) cells within the necrotic core, and in small clusters on the peripheries of the spheroids (Figure 3.10). By contrast, in uninfected A549 spheroids, the number of dead cells forming the necrotic cores appears to decrease between 24- and 120h-hpi (Figure 3.10).

At each time point, the uninfected HuH-7 spheroids show a greater proportion of live cells, and fewer dead cells, when compared to the infected spheroids, regardless of the MOI. Similarly, at 72- and 120-hpi, the uninfected A549 spheroids show fewer dead cells than the infected spheroids (Figure 3.10). However, the proportion of live cells does not appear to differ significantly between uninfected and BUNV-infected A549 spheroids at 24- and 72-hpi (except for those spheroids infected at a MOI 10 – this is discussed further below).

In both A549 and HuH-7 spheroids, BUNV infection appears to induce cell death (Figure 3.10). However, this BUNV-induced cell death is more prominent in HuH-7 spheroids, which show a greater proportion of dead cells (at all MOIs used) at 72- and 120-hpi, compared to the A549 spheroids. In the HuH-7 spheroids, there appears to be little difference between increasing MOI and the number of live/dead cells at 72- and 120-hpi; this is also the case for A549 spheroids at 24- and 72-hpi. However, at 120hpi, uninfected A549 spheroids and those

infected with BUNV at a MOI of 0.1 appear larger than those infected at MOIs of 1 and 10. These data were in contrast to the MTS data, which imply that BUNV infection has little effect on the metabolic activity (typically used to indicate cell viability) in A549/HuH-7 spheroids (Figure 3.8). As discussed in section 4.2, it is possible that, whilst BUNV infection does induce cell death (Figure 3.10), the metabolic activity of the remaining living cells could be significantly upregulated (relative to the uninfected control cells) in response to BUNV infection. It was found that infection with BUNV caused A549 spheroids to become less structurally stable and more likely to disaggregate upon mechanical stress (i.e., when staining/washing; see section 4.2.2). Due to this, when staining the A549 spheroids infected at high MOI (MOI 10), and those at 120hpi, the spheroids typically fragmented, resulting in the smaller, more irregular structures observed in (Figure 3.10), this is discussed further in section 4.2.2.

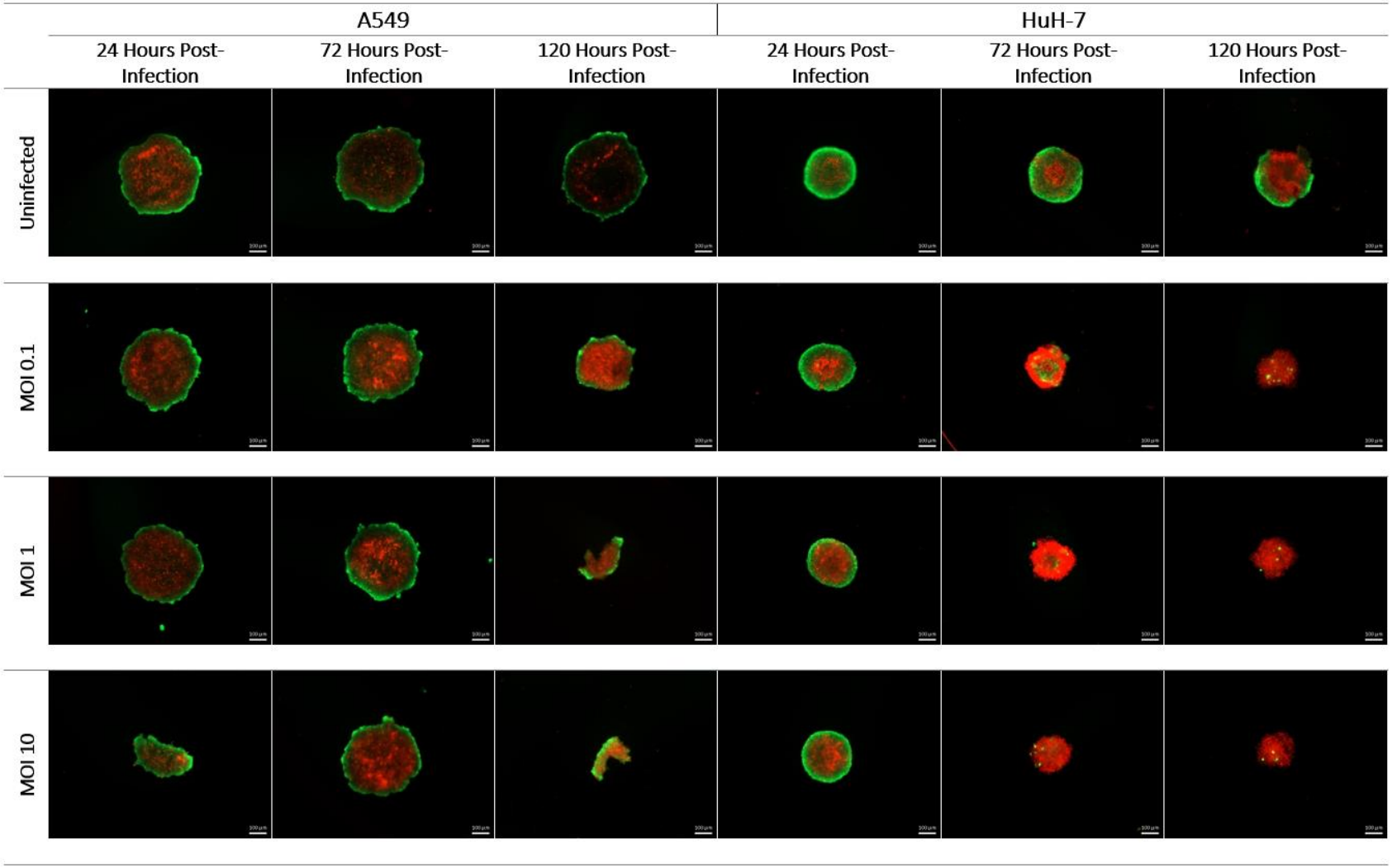

Figure 3.10. Fluorescein diacetate and propidium iodide (FDA/PI) staining of BUNV-infected A549 and HuH-7 spheroids. *FDA/PI-stained spheroids were analysed under a fluorescence microscope at 5x magnification. Utilising Zeiss Zen software, images obtained under green laser (488nm – FDA), and red laser (540nm – PI), were digitally overlaid. Uninfected control spheroids (top row) were imaged alongside spheroids infected with BUNV at MOI 0.1, 1, and 10 (rows 2 – 4, respectively). Three spheroids for each experimental condition (uninfected, MOI 0.1, MOI 1, and MOI 10), were stained and imaged at each time-point (24-, 72- and 120-hours post-infection), images are representative.*

3.2.3 Cell Death & Cell Lysis - LDH Assay

The effects of BUNV infection on the viability of A549 and HuH-7 spheroids, maintained in microfluidic devices, was determined by LDH assay. For each experimental condition (uninfected, MOI 0.1, and MOI 1), 4x spheroids were infected with BUNV/mock-infected with plain culture medium and immediately transferred into the microfluidic chips, as described in section 2.4.2. The LDH assay was performed on effluent samples, collected every 24 hours, from each chip containing 4x infected/mock-infected spheroids. After the final effluent collection (120hpi), the chips were disassembled, and the mock-infected spheroids contained within the 'uninfected' control chip were removed, lysed, and utilised as the LDH positive control as described in section 2.6.1.

At the final assay time-point (120hpi), the 4x spheroids contained within the 'uninfected' control chip had coalesced to form two, larger, spheroids. A relatively large amount of LDH was released from the control spheroids, when lysed at 120hpi, compared with the amount of LDH detected in the effluent samples collected from the chip containing the control spheroids (Figure 3.11). This indicates that the control spheroids maintain viability on-chip throughout the time-course of the experiment; the low basal release of LDH implies minimal cell death/lysis. This is supported by the large peak of LDH observed upon forced membrane damage to the control spheroids, indicating the presence of a large quantity of viable, intact, cells at 120hpi.

Contrastingly, the spheroids contained within the infected chips, at all MOIs used, appeared to have disaggregated when disassembling the chips at 120hpi. As such, it was not possible to remove these spheroids from the chips for lysis and subsequent LDH quantification. However, LDH analysis of the effluent samples collected from the chips containing BUNV-infected spheroids also showed a low LDH concentration, relative to the 'uninfected' lysate (Figure 3.11). This suggests that, throughout the experiment, the infected spheroids maintain their viability and minimal membrane damage had occurred. This is contrary to the fluorescence microscopy data shown in Figure 3.10, which shows increased membrane damage (making the cells permissive to propidium iodide staining) in A549 spheroids at 120hpi, and HuH-7 spheroids at 72- and 120-hpi. A possible explanation for this discrepancy is that due to the flow rate (2µL/min) and effluent collection intervals used (24 hours), the LDH released from the spheroids was diluted.

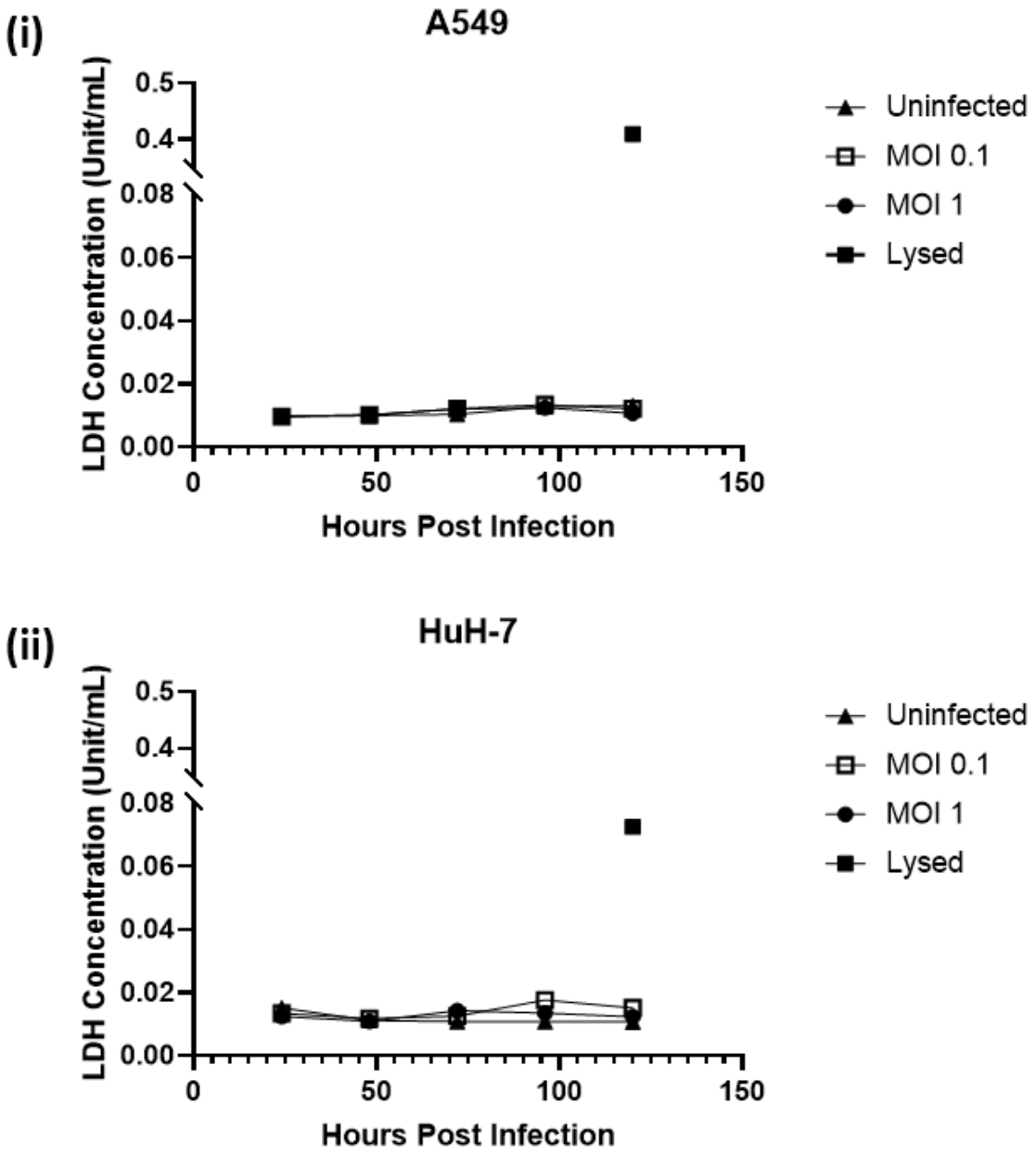

Figure 3.11. Cell viability measured by LDH release from BUNV-infected A549, and HuH-7 spheroids maintained in microfluidic devices. ***(i)*** *LDH concentration in microfluidic effluent collected from chips containing A549 spheroids infected with BUNV at MOIs of 0.1, 1, or mock-infected with plain culture medium.* ***(ii)*** *LDH concentration in effluent collected from chips containing infected/mock-infected HuH-7 spheroids. Spheroids contained within the mock-infected chip were lysed at 120hpi and used as the LDH positive control ('Lysed'). n=1.*

3.3 BUNV Effects on Exosome Release from A549 and HuH-7 Cells in 2D vs 3D Culture Models

3.3.1 Western Blotting

Western blot analysis of the exosome markers CD63 and CD81 was performed to investigate the effect of BUNV infection on exosome release. Whole cell lysates (WCLs) were prepared from 2D monolayers of A549, and HuH-7 cells as described in section 2.8.1; mock-infected cell lysates were obtained alongside lysates of cells infected with BUNV at MOIs of 0.1, 1, and 10, at 120hpi. Immediately before lysis, the supernatant was collected from each well containing mock-infected/infected cells. This supernatant was then subject to differential ultracentrifugation, with sucrose cushion purification, as described in section 2.7.2. Pellets of purified exosomes and viral particles were then lysed as described in section 2.8.1 to obtain the 'purified EV' samples for western blotting. Likewise, for 3D investigations, mock-infected/BUNV-infected A549 and HuH-7 spheroids were lysed (see section 2.8.1) to obtain 3D WCL samples for western blotting. For the 3D 'purified EV' samples, effluent was collected from microfluidic chips containing mock-infected/BUNV-infected spheroids (MOIs of 0.1, 1, and 10 were used), at 120hpi. The effluent was subject to differential ultracentrifugation with a 30% sucrose cushion (see Figure 2.12) and lysed as described in section 2.8.1.

Densitometry was performed using ImageJ software to quantify CD63, CD81 and BUNV N protein expression. All membranes were also probed for GAPDH and α-tubulin, as loading controls; both proteins have been shown to be present in exosomes (Hosseini-Beheshti et al., 2012; van Niel et al., 2018; Mashouri et al., 2019; Dar et al., 2021). However, neither GAPDH nor α-tubulin were detected in the 'purified EV' samples, for both A549 and HuH-7 cells (in 2D and 3D cultures). Protein concentration was normalised by BCA assay (see section 2.8.1) and 30µg/well of protein in each sample was loaded for gel electrophoresis. Therefore, the percentage intensity of CD63 and CD81 protein expression is presented relative to the 'uninfected' control samples, i.e., the intensity of CD63/CD81 expression in infected WCL samples are expressed as a percentage relative to the 'uninfected' WCL, and protein intensity in the infected purified EV samples are expressed as a percentage relative to the 'uninfected' purified EV sample. For BUNV N protein expression, the data are presented as arbitrary units (A.U.) as determined by Image J software analysis (Figure 3.12 – Figure 3.15).

i) BUNV Infection Appears to Increase Intracellular CD63 Expression in A549 Monolayers but Not Increase the Secretion of CD63-Enriched Exosomes

Quantification of CD63, as detected by western blotting, in lysates of A549 cells cultured as 2D monolayers revealed a BUNV-infection dependent increase in the expression of CD63 (Figure 3.12). Relative to the uninfected sample, CD63 expression was 1.67 ± 0.14x more intense in A549 cells infected with BUNV at a MOI of 0.1, at 120hpi (P=0.0746). Likewise, CD63 expression in A549 cells infected at MOI 1 was 1.71 ± 0.23x more intense than in the uninfected control cells (P=0.058). An increase in CD63 expression was also observed in A549 cells infected at MOI 10; this expression was 1.33 ± 0.42x more intense, relative to the uninfected cells (P=0.5792). However, in purified exosome lysates, the expression of CD63 is significantly decreased in response to BUNV-infection (Figure 3.12). Exosomes isolated from the supernatant of uninfected A549 monolayers showed significantly greater CD63 expression than those isolated from the supernatant of cells infected at MOIs of 0.1 (P=0.0418), 1 (0.0289), and 10 (P=0.0089). This data indicates that, while BUNV infection may be implicated in increased intracellular CD63, it does not induce the release of CD63-enriched exosomes. For both WCLs and purified EVs, there was no significant difference in CD63 expression between each of the MOIs used (Figure 3.12).

ii) Intracellular and Extracellular CD81 Expression Appears to Decrease in an MOI-dependent Manner in A549 2D Cultures

Whilst no significant difference in CD81 protein expression was found between uninfected A549 monolayers and those infected at MOI 0.1 (P=0.1416), and those infected at MOI 1 (P=0.9316) at 120hpi, CD81 expression appears visually to decrease with increasing MOI (Figure 3.12). The expression of CD81 in the WCL prepared from A549 cells infected at MOI 0.1 was 1.46 ± 0.06x more intense than in the uninfected WCL and, at MOI 1, the CD81 expression is 1.16 ± 0.11x more intense than the uninfected WCL. At MOI 10, CD81 expression is 0.40 ± 0.18x as intense as in the uninfected WCL, a significant decrease (P=0.433). Likewise, in the purified EV samples, CD81 expression is significantly decreased in exosomes isolated from the supernatant of A549 monolayers infected at MOI 10, relative to those isolated from uninfected cells (P=0.0028). Furthermore, the exosomes produced by A549 cells infected at

a MOI of 1 also show significantly decreased CD81 expression, compared to those produced by uninfected cells (P=0.0066). Relative to the exosomes purified from uninfected cells, CD81 expression is 0.46 ± 0.24x as intense in exosomes purified from A549 cells infected at MOI 0.1, but this difference was not significant (P=0.0757); this is likely due to the limited number of replicates (n=3; Figure 3.12).

iii) BUNV Infection Appears to Decrease Intracellular CD63 Expression in HuH-7 Monolayers, but CD63 Detection is Increased in Secreted Exosomes

In contrast to A549 2D cultures, the expression of CD63 in HuH-7 cell monolayers appears, visually, to decrease in BUNV infection, whilst the detection of CD63-decorated exosomes released from infected HuH-7 cells appears to increase (Figure 3.13). Relative to the exosomes isolated from uninfected cell supernatant, the detection of CD63-enriched exosomes isolated from the supernatant of cells infected at MOI 0.1 was 1.84 ± 0.12x more intense. Increasing MOI further (MOI 1) resulted in the secretion of exosomes in which CD63 detection was 1.98 ± 0.24x more intense than in exosomes isolated from uninfected cells. At MOI 10, however, CD63-enriched exosomes were found to be 0.076 ± 0.062x as intense as in the uninfected control. BUNV N protein expression is significantly lower in purified exosome/viral particle lysates obtained from the supernatant of HuH-7 monolayers infected at MOI 10, compared to those at MOI 0.1 (P=0.0194) (Figure 3.13). Perhaps this is due to the generation of DI particles at high MOIs and during long incubation periods. The generation of DI particles results in reduced infectious viral titres (Patel & Elliott, 1992), as Bunyavirus DI particles exert an inhibitory effect of viral genomic replication (Kascsak & Lyons, 1978), this would explain the decreased levels of BUNV N protein detected by western blotting in samples infected at high MOI (10) at 120hpi (Figure 3.13).

Numerous Bunyaviruses have been shown to induce apoptosis during replication in human hepatocellular carcinoma cells, including HuH-7 cells (Ding et al., 2005; Rodrigues et al., 2012; Sun et al., 2015). This hepatocytic apoptosis is thought to influence the pathology of infections with Bunyaviruses such as CCHFV and RVFV, specifically, liver necrosis and failure (see Table 1.1). Reports have indicated the presence of 'apoptotic exosomes', which are thought to play roles in inflammation and immune response, as a form of active

communication between dying and living cells (Park et al., 2018; Kakarla et al., 2020; Li et al., 2020). This could potentially explain the observation of increased CD63 expression in exosome preparations, isolated from the supernatant of infected HuH-7 cells, as CD63-enriched exosomes may be released from the cells undergoing the phenomenon of virus-induced apoptosis.

iv) BUNV Infection Appears to Decrease Intracellular CD81 Expression in HuH-7 2D Cultures

CD81 was not detected in any of the purified EV samples obtained from the supernatant of BUNV infected HuH-7 monolayers, at any of the MOIs used (Figure 3.13), although this is to be expected based on the low levels of CD81 detected in the exosome extracts produced by uninfected HuH-7 cells (Figure 3.13). In HuH-7 WCLs, however, CD81 expression appears, visually, to decrease in BUNV infection. In all replicates, no CD81 was detected in lysates of HuH-7 monolayers infected with BUNV at a MOI of 10. Relative to the uninfected control WCL, CD81 expression in the MOI 0.1 lysate was 0.57 ± 0.42x as intense, however this difference was not significant (P=0.3384). Likewise, CD81 expression in the MOI 1 lysate was 0.47 ± 0.26x as intense as the uninfected control, but this difference was also not significant (P=0.1839). This insignificance is likely due to large variation in the data obtained as illustrated by the error bars in Figure 3.13.

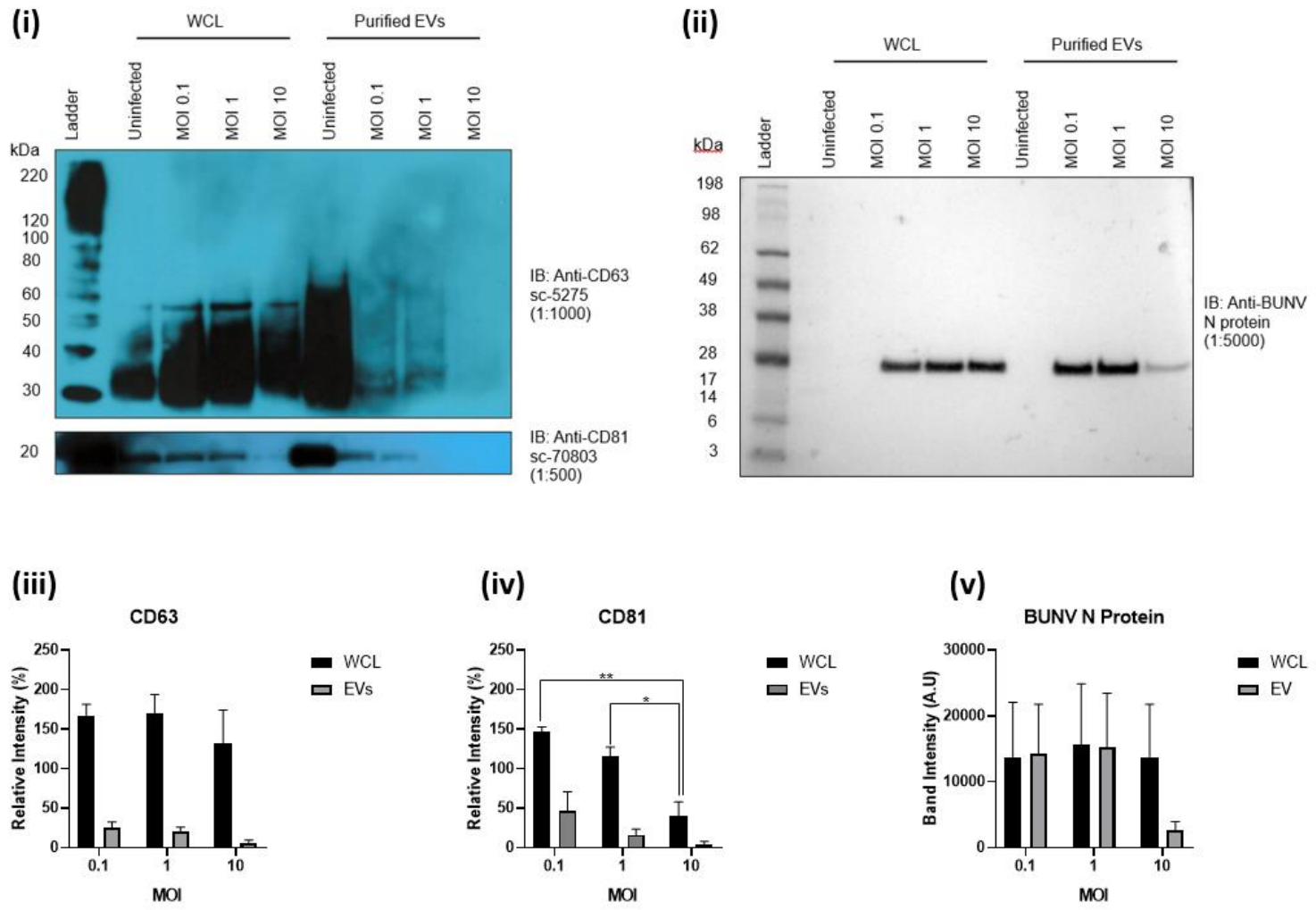

Figure 3.12. Western blot analysis of CD63, CD81 and BUNV N protein in lysates of whole cells and purified EVs from A549 2D cultures. ***(i)*** *Western blot for CD63 and CD81. Proteins were separated by denaturing but non-reducing SDS-PAGE; protein concentration was normalised by BCA assay, and 30µg of protein was loaded for each sample.* ***(ii)*** *The membrane used in blot (i) was stripped, blocked and re-probed for BUNV N protein.* ***(iii)*** *Densitometry analysis, using ImageJ, of the detected CD63 bands.* ***(iv)*** *Densitometry analysis of the detected CD81 bands. CD63/CD81 intensities in the infected samples are expressed as a percentage relative to the uninfected control samples.* ***(v)*** *Densitometry analysis of the detected BUNV N protein bands, intensity is expressed as arbitrary units (A.U), as determined by Image J software. Data are presented as mean ± 2SEM (n=3).*

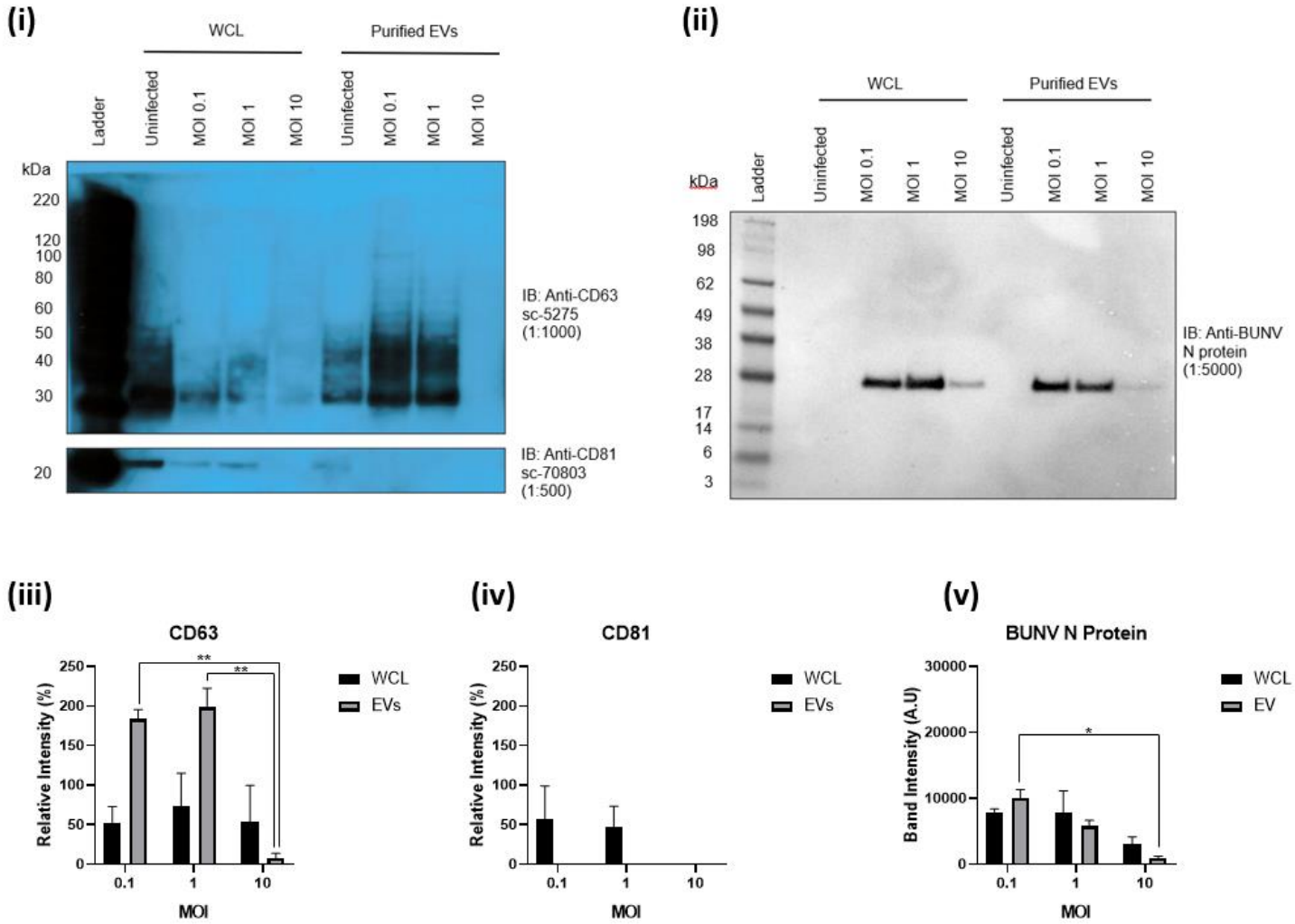

Figure 3.13. Western blot analysis of CD63, CD81 and BUNV N protein in lysates of whole cells and purified EVs from HuH-7 2D cultures. ***(i)*** *Western blot for CD63 and CD81. Proteins were separated by denaturing but non-reducing SDS-PAGE; protein concentration was normalised by BCA assay, and 30µg of protein was loaded for each sample.* ***(ii)*** *The membrane used in blot (i) was stripped, blocked and re-probed for BUNV N protein.* ***(iii)*** *Densitometry analysis, using ImageJ, of the detected CD63 bands.* ***(iv)*** *Densitometry analysis of the detected CD81 bands. CD63/CD81 intensities in the infected samples are expressed as a percentage relative to the uninfected control samples.* ***(v)*** *Densitometry analysis of the detected BUNV N protein bands, intensity is expressed as arbitrary units (A.U), as determined by Image J software. Data are presented as mean ± 2SEM (n=3).*

V) BUNV Infection Appears to Increase Intracellular CD63 and CD81 in A549 & HuH-7 Spheroids

In lysates of A549 cells cultured as 3D spheroids, BUNV infection appears to increase the expression of CD63 (Figure 3.14); as observed in 2D cultures (Figure 3.12). The expression of CD63 in A549 spheroids infected at MOI 0.1 was 1.60 ± 0.32x more intense than in uninfected spheroids, and CD63 expression in spheroids infected at MOI 1 was 1.59 ± 0.30x more intense than in uninfected spheroids, however, CD63 expression was less intense in A549 spheroids infected at MOI 10 relative to the uninfected control (0.72 ± 0.17x). Furthermore, CD63 expression was significantly reduced in A549 spheroids infected at MOI 10, compared to those infected at MOI 0.1 ($P=0.0379$), and those infected at MOI 1 ($P=0.0409$). As previously mentioned, this is potentially due to the generation of DI particles at high MOIs (MOI 10), and at 120hpi, which may attenuate BUNV infection though competitive inhibition during replication. This is supported by the observation of decreased BUNV N protein expression at MOI 10 (Figure 3.14).

Similarly, CD63 expression appears to be greater in HuH-7 3D WCLs in response to BUNV infection (Figure 3.15); this contrasts with the data observed in 2D cultures of HuH-7 cells, which show a BUNV infection dependent decrease in intracellular CD63 expression (Figure 3.13).

Very little CD63 was detected in the 'purified EV' samples, obtained from microfluidic effluent collected from chips containing A549 spheroids at 120hpi (Figure 3.14). There was no significant difference in CD63 expression between the exosomes produced by uninfected A549 spheroids (on-chip), and exosomes produced by spheroids infected at MOI 0.1 ($P=0.3642$), MOI 1 ($P=0.2107$), or MOI 10 ($P=0.1384$). No CD63 was detected in the MOI 10 A549 'purified EV' samples (Figure 3.14), nor was any CD63 detected in any of the HuH-7 'purified EV' samples (Figure 3.15). The lack of any observable CD63 bands in these samples is likely owing to the limited spheroid sample contained within the microfluidic chips (see section 5.1.2); each chip housed only 4 spheroids, seeded at an initial density of 30,000 cells (A549), or 5,000 cells (HuH-7).

In both A549 and HuH-7 3D cultures, CD81 was only detected in the WCLs obtained from spheroids infected at MOIs of 0.1 and 1. This indicates that CD81 expression is upregulated

in response to BUNV infection. However, due to the challenging nature of western blotting for these tetraspanins in purified exosome preparations, and the time-constraints of this project, it was only possible to obtain n=2 for A549 3D CD81 expression, and n=1 for HuH-7 3D CD81 expression. Further replicates would be necessary to determine the significance of BUNV infection on CD81 expression in 3D culture models using these cell lines.

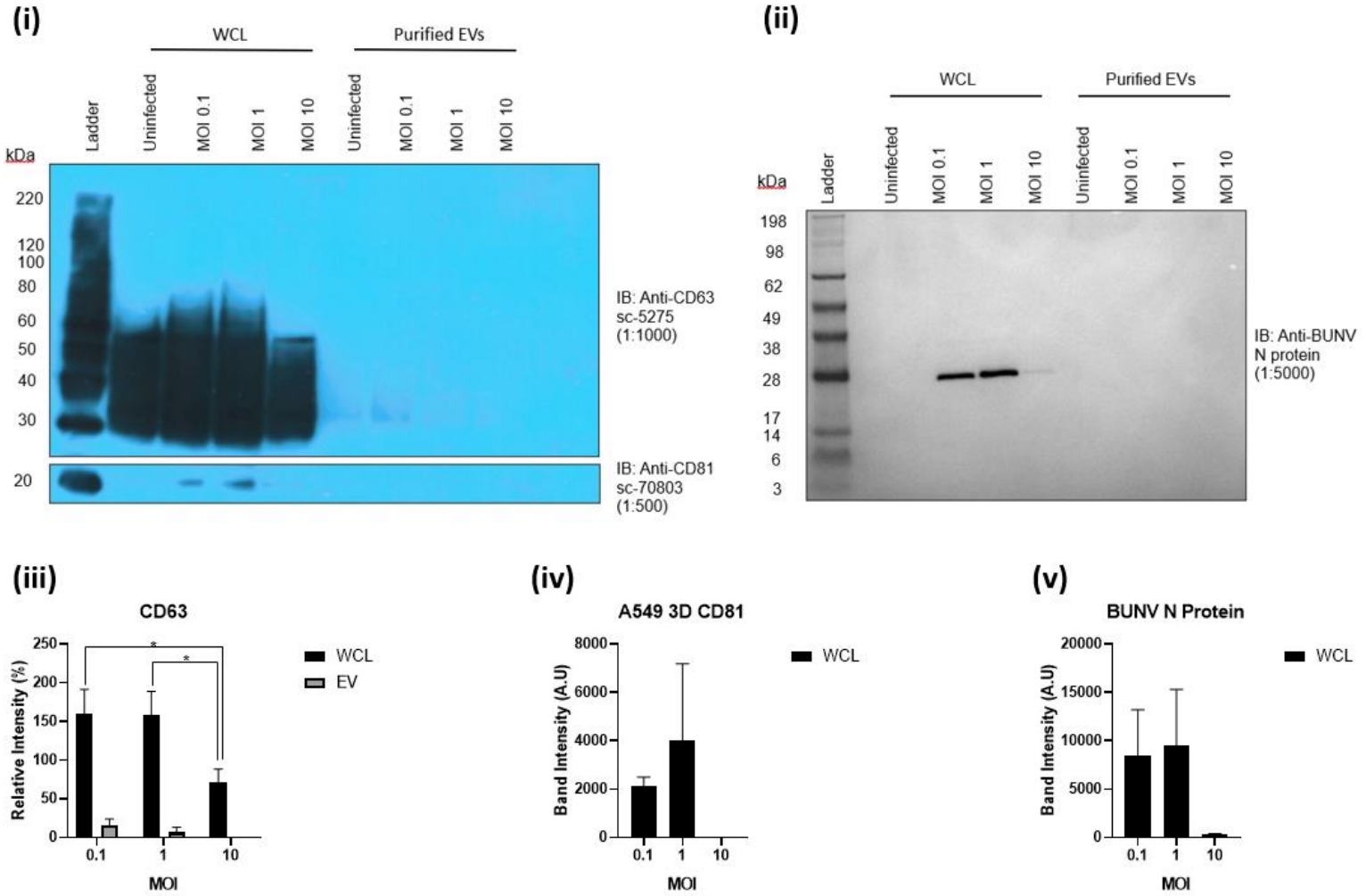

Figure 3.14. Western blot analysis of CD63, CD81 and BUNV N protein in lysates of whole cells and purified EVs from A549 3D cultures. ***(i)*** *Western blot for CD63 and CD81. Proteins were separated by denaturing but non-reducing SDS-PAGE; protein concentration was normalised by BCA assay, and 30µg of protein was loaded for each sample.* ***(ii)*** *The membrane used in blot (i) was stripped, blocked and re-probed for BUNV N protein.* ***(iii)*** *Densitometry analysis, using ImageJ, of the detected CD63 bands (n=3).* ***(iv)*** *Densitometry analysis of the detected CD81 bands (n=2). CD63/CD81 intensities in the infected samples are expressed as a percentage relative to the uninfected control samples.* ***(v)*** *Densitometry analysis of the detected BUNV N protein bands, intensity is expressed as arbitrary units (A.U), as determined by Image J software (n=2). Data are presented as mean ± 2SEM.*

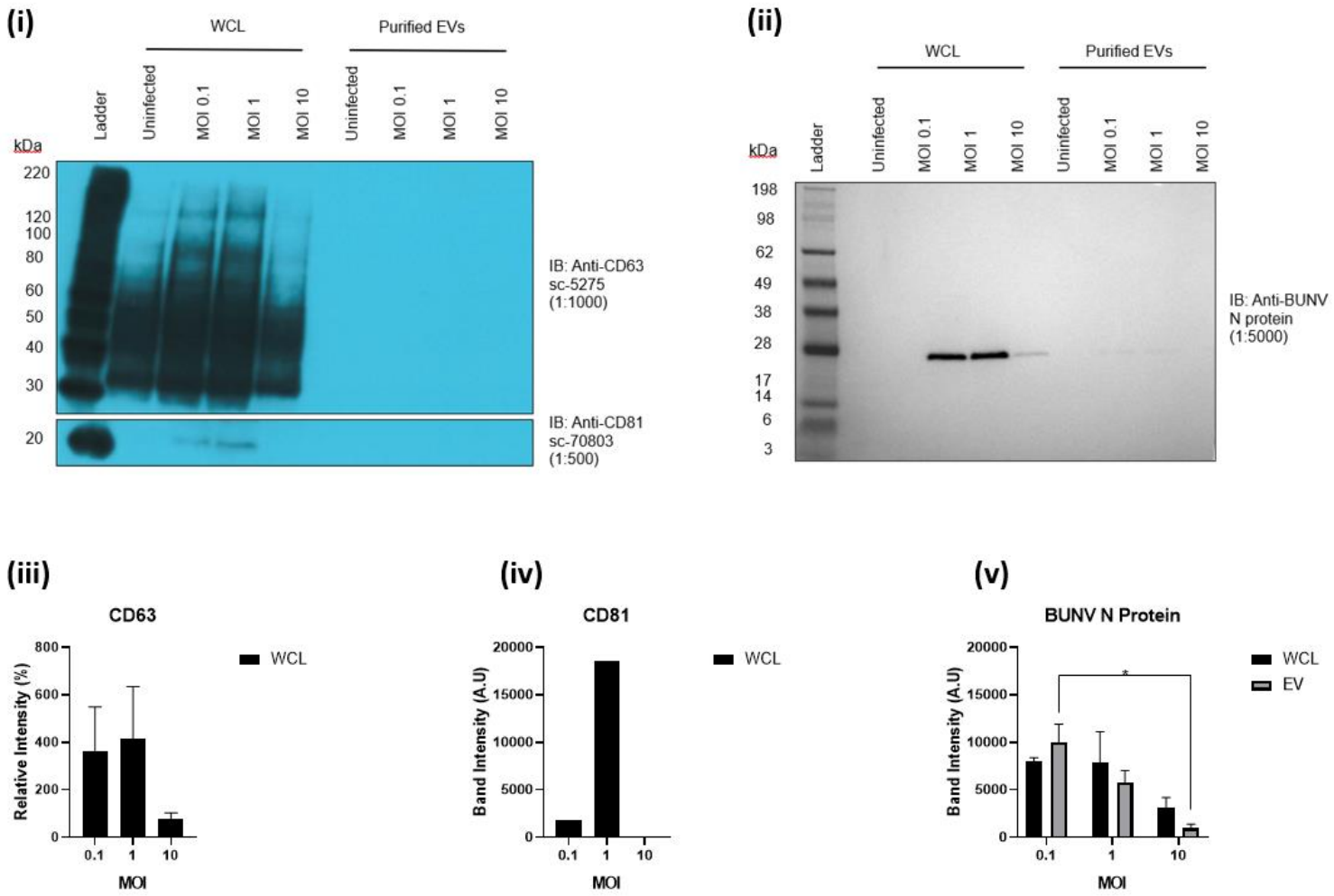

Figure 3.15. Western blot analysis of CD63, CD81 and BUNV N protein in lysates of whole cells and purified EVs from HuH-7 3D cultures. ***(i)*** *Western blot for CD63 and CD81. Proteins were separated by denaturing but non-reducing SDS-PAGE; protein concentration was normalised by BCA assay, and 30µg of protein was loaded for each sample.* ***(ii)*** *The membrane used in blot (i) was stripped, blocked and re-probed for BUNV N protein.* ***(iii)*** *Densitometry analysis, using ImageJ, of the detected CD63 bands (n=3).* ***(iv)*** *Densitometry analysis of the detected CD81 bands (n=1). CD63 intensities in the infected samples are expressed as a percentage relative to the uninfected control sample.* ***(v)*** *Densitometry analysis of the detected BUNV N protein bands, intensity is expressed as arbitrary units (A.U), as determined by Image J software (n=2). Data are presented as mean ± 2SEM.*

3.3.2 Nanoparticle Tracking Analysis (NTA)

NTA was performed on exosomes and viral particles, isolated from microfluidic effluent collected from chips containing mock-infected/BUNV infected A549/HuH-7 spheroids. Lower MOI ranges (0.1 - 1) were used, to allow successful BUNV infection of these cell types (Szemiel et al., 2012; Hover et al., 2018; Heitmann et al., 2021), to allow the cells to enter an antiviral state before lysis, as in natural infection, and to prevent the generation of DI particles as discussed in section 2.3.4. Furthermore, infectious at these MOIs was shown to yield infectious viral titres in microfluidic effluent (see below; Figure 3.16). Pellets of purified exosomes/viral particles were obtained by differential ultracentrifugation, with a 30% sucrose cushion, and fixed by resuspending in 1mL 2% (v/v) formaldehyde, made up in 20nm-filtered PBS as described in section 2.7.3. NTA was performed at 24-, 72-, and 120-hpi; each sample was diluted 1:10 with 20nm-filtered PBS prior to analysis to obtain an appropriate PPF range for NTA as described in section 2.8.2. The 20nm-filtered PBS diluent was analysed as a 'blank', at each time point, and any background interferences found in the diluent were subtracted from the sample measurements.

Before performing NTA, it was first necessary to determine whether infectious viral particles were present in the microfluidic effluent. To do this, plaque assays were performed, as described in section 2.3.2, on microfluidic effluent collected every 24 hours (up to 120hpi) from chips containing A549 and HuH-7 spheroids infected at MOIs of 0.1 and 1. Microfluidic effluent collected from BUNV-infected A549 and HuH-7 chips yielded infectious viral titres (Figure 3.16). In effluent collected from chips containing BUNV-infected A549 spheroids, the highest viral titre was obtained at 72hpi, from spheroids infected at MOI 1 ($5.9x10^6$ pfu/mL). For A549 spheroids infected at MOI 0.1, the highest viral titre was observed in the microfluidic effluent collected at 96hpi ($5.3x10^5$ pfu/mL). By contrast, HuH-7 spheroids infected at the lower MOI (MOI 0.1) produced the greatest viral titre, at 96hpi ($1.1x10^7$ pfu/mL). The highest viral titre obtained from the effluent collected from the chip containing HuH-7 spheroids infected at MOI 1 was $4.2x10^6$ pfu/mL, at 48hpi. Further in contrast to A549 microfluidic culture, in infected HuH-7 spheroids (on chip), no infectious viral particles were produced between 96- and 120hpi, for both MOIs used (Figure 3.16).

NTA allowed the determination of the concentration of particles (particles/mL) and the mean size (nm) of particles (exosomes/viral particles/any other contaminating nanoparticles) in the purified microfluidic effluent (Figure 3.17).

i) BUNV Infection Does Not Significantly Affect the Concentration or Size of Nanoparticles Isolated from A549 Microfluidic Effluent

No significant differences were found, at any time point, between the concentration of particles in microfluidic effluent collected from uninfected A549 spheroid chips, and chips containing spheroids infected at MOI 0.1 or MOI 1 (Figure 3.17). Nor was any significant difference in nanoparticle size observed between effluent from uninfected chips, and effluent from BUNV-infected A549 chips. Likewise, no significant differences in nanoparticle concentration or size were found between the effluent collected from A549 spheroid chips infected at MOI 0.1, compared to those infected at MOI 1.

i) BUNV Infection Does Not Affect the Concentration of Nanoparticles Isolated from HuH-7 Microfluidic Effluent, but Does Affect the Average Size of the Nanoparticles

As observed in A549 derived microfluidic effluent, NTA performed on effluent collected from chips containing HuH-7 spheroids (+/- BUNV infection) and subsequent statistical analysis revealed no significant differences in nanoparticle concentration, at any time point, between uninfected vs MOI 0.1, uninfected vs MOI 1, and MOI 0.1 vs MOI 1 (Figure 3.17).

However, at 24- and 72-hpi, the nanoparticles contained within the effluent collected from uninfected HuH-7 spheroid chips were significantly smaller than those in effluent collected from the chips containing HuH-7 spheroids infected at MOI 0.1 ($P=0.0004$, and $P=0.0189$, respectively). Furthermore, at 24hpi, these nanoparticles (MOI 0.1) were also significantly larger than those in the effluent collected from the MOI 1 chip ($P=0.0004$).

At 120hpi, however, the size of the nanoparticles did not significantly differ between uninfected vs MOI 0.1 ($P=0.8267$), uninfected vs MOI 1 ($P=0.2662$), or MOI 0.1 vs MOI 1 ($P=0.0977$). The major limitation of this technique is its inability to distinguish exosome

populations from viral particles due to their very similar size (see section 5.3). Without the ability to define these exosome/viral particle populations within each effluent sample, it is not possible to determine whether BUNV influences the concentration of exosomes secreted from infected cells. New technologies exist which can perform nanoparticle population differentiation and subsequent characterisation; these are reviewed in section 5.3 and Chapter 6.

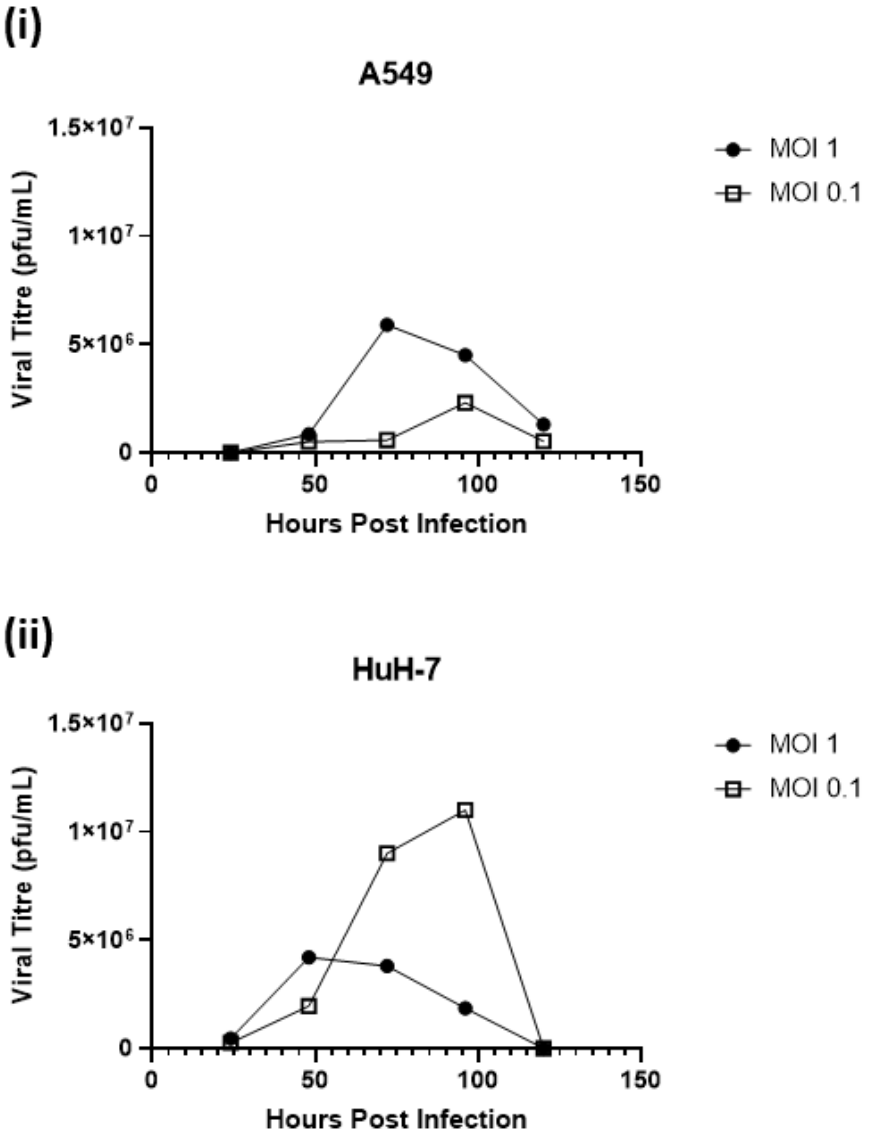

Figure 3.16. Infectious extracellular viral titres obtained from 3D microfluidic cell cultures. ***(i)*** *Infectious viral titres of microfluidic effluent collected from chips containing A549 spheroids, infected with BUNV and MOIs of 0.1 and 1, at 24-, 48-, 72-, 96-, and 120-hpi.* ***(ii)*** *Viral titres of effluent collected from chips containing infected HuH-7 spheroids. n=1.*

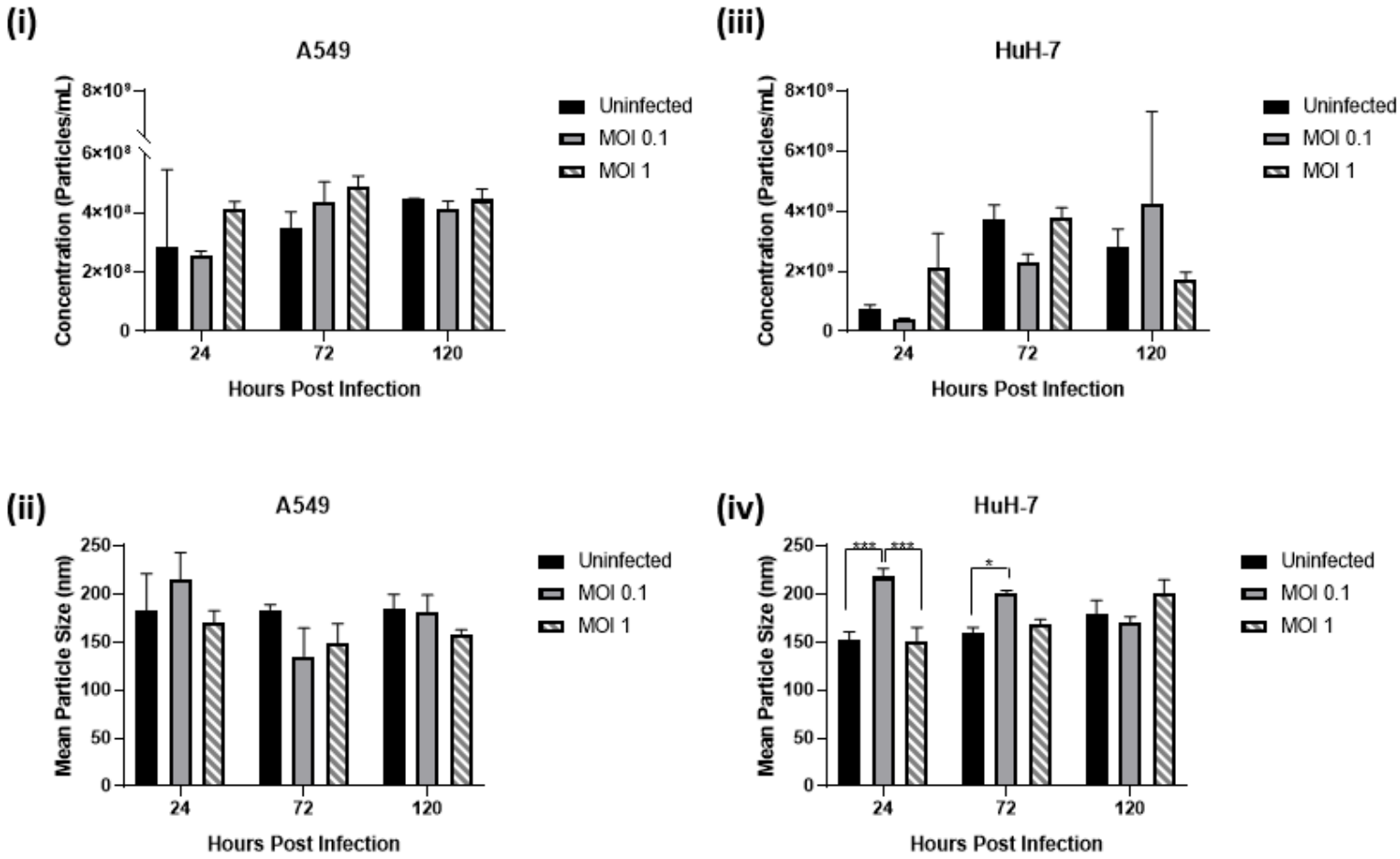

Figure 3.17. Nanoparticle tracking analysis of exosomes/viral particles isolated from microfluidic effluent. *NTA was performed using the NanoSight LM10 instrument; capture settings: 3x 60 seconds, camera level: 16, screen gain: 1, image processing settings: screen gain: 10, detection threshold: 5. Microfluidic effluent was collected from chips containing 4x mock-infected ('uninfected'), or BUNV-infected (MOI 0.1 and MOI 1) A549/HuH-7 spheroids. Exosomes/viral particles were isolated by differential ultracentrifugation with a 30% sucrose cushion, fixed in 2% (v/v) formaldehyde, and diluted 1:10 with 20nm-filtered PBS before analysis.* ***(i)*** *Nanoparticle concentration (particles/mL) in microfluidic effluent collected from chips containing A549 spheroids (+/- BUNV infection).* ***(ii)*** *Mean size (nm) of particles isolated from A549 microfluidic effluent (+/- BUNV infection).* ***(iii)*** *Nanoparticle concentration in HuH-7 microfluidic effluent.* ***(iv)*** *Mean size of particles in HuH-7 microfluidic effluent. Data are presented as mean ± 2SEM, (n=3).*

Chapter 4: Discussion

The aim of the current study was to develop a flowing, 3D-model of Bunyavirus infection, which could be utilised to investigate the effects of Bunyavirus infection on cellular secretory pathways and exosome release, by analysis of spheroids in static culture compared with those maintained in a microfluidic device. Through the development of the 3D microfluidic model of Bunyavirus infection, this study has also assessed the effects of BUNV infection on cell metabolism, cell viability, and cell death in 2D and (for the first time) 3D cultures. Furthermore, this study highlights differences in viral kinetics in 2D versus 3D culture models, contributing to the understanding of Bunyavirus dynamics and pathogenesis. The current study also documents a protocol for the optimal generation of uniform A549 and HuH-7 spheroids, in addition to an optimised protocol for the isolation and purification of exosomes and BUNV virions from cellular supernatant and microfluidic effluent. The adoption of these protocols in future studies will prove invaluable to investigate Bunyavirus infection in a more physiologically relevant model system.

Whilst 2D models have contributed tremendously to our knowledge and understanding of Bunyaviral replication, mechanisms of pathogenesis, and host-virus interactions; these models do not reflect the *in vivo* tissue architecture and microenvironment complexity. By utilising a multicellular spheroid (MCS) model, maintained in a device with continuous media perfusion, the 3D microfluidic model simulates a 3D microenvironment more analogous to the microenvironment encountered by viruses *in vivo*, by encompassing the cell-cell/cell-ECM interactions (Lee et al., 2018), gradients of nutrients and oxygen (Decarli et al., 2021), and shear stresses (Chen et al., 2019). In recent years, the role of exosomes in viral infection has gained increasing attention in the research community (Chahar et al., 2015; Madison et al., 2015; Ahsan et al., 2016; Kerviel et al., 2021), yet, little is known about the roles of exosomes in infection with single-stranded RNA viruses, such as Bunyaviruses. Understanding the functions of exosomes in Bunyavirus replication, pathogenesis, and persistence may provide valuable new insights to support the much-needed development of effective therapeutics and vaccines.

4.1 Summary of Results

The current study details a protocol for the successful generation of WT-BUNV stocks, adapted to the HuH-7 cell line (see section 3.1.3), and an optimised protocol for the generation of A549 and HuH-7 spheroids which are uniform in both size and sphericity (Table 3.1). Analysis of protein concentration in exosome/viral particle preparations revealed that the use of a sucrose cushion during ultracentrifugation yields a greater total protein concentration in all samples compared to those prepared without the use of a sucrose cushion (Figure 3.6). Furthermore, western blotting analysis of the exosome marker CD63 and BUNV N protein revealed that the use of a sucrose cushion during ultracentrifugation assists in the extraction of BUNV virions from A549-derived spent media (Figure 3.7). However, the use of sucrose cushion purification had negligible effect on the quantity of BUNV virions isolated from HuH-7-derived spent media (Figure 3.7). Moreover, the use of a sucrose cushion yielded fewer CD63-enriched exosomes using this cell line, relative to samples prepared using the standard ultracentrifugation protocol (Figure 3.7). Despite seemingly having no benefit in terms of CD63-enriched exosomes, ultracentrifugation with sucrose cushion purification (Figure 2.12) was utilised for the isolation of exosomes and BUNV virions from 2D supernatant and microfluidic effluent throughout this study; the higher total protein concentration in samples prepared this way (Figure 3.6) allowed for a greater concentration of protein in sample lysates to be loaded for gel electrophoresis, and subsequent western blotting analysis. Additionally, multiple studies have reported the use of a sucrose cushion during ultracentrifugation to purify morphologically intact Bunyavirus virions (Guardado-Calvo et al., 2016; Huang et al., 2016; Mastrodomenico et al., 2019; Mastrodomenico et al., 2020; Mo et al., 2020).

Using the MTS assay (see section 2.5.2) we have determined that BUNV infection has a greater effect on the metabolic activity of A549 and HuH-7 cells cultured as 2D monolayers than in 3D spheroids, under static conditions (Figure 3.8). This highlights the importance of employing a physiologically relevant cell culture platform, when studying host-pathogen interactions and mechanisms of pathogenesis, as analysis in standard 2D cultures may be misleading and contradictory. The differences in metabolic activity between 2D and 3D cultures seen in Figure 3.8 and Figure 3.9 may be attributed to the high surface area to volume ratio of 2D cultures, compared to 3D cultures. The poor representation of the *in vivo*

microenvironment encountered by pathogens in 2D cultures may, in part, be responsible for the high rates of failure in drug and vaccine development (Gardner & Herbst-Kralovetz, 2016; Barrila et al., 2018).

In A549 and HuH-7 spheroids, infection with BUNV appeared to have negligible effect on cellular metabolic activity (until 240hpi in A549 spheroids; Figure 3.8). The MTS data were in contrast with the fluorescence microscopy images of A549/HuH-7 spheroids, stained with FDA/PI, which illustrated a picture of BUNV-infection induced cell death; particularly in infected HuH-7 spheroids (Figure 3.10). It is possible that, whilst the relative number of living cells is fewer in infected spheroids than in uninfected controls (at the respective time points), the metabolic activity in these living cells could be significantly upregulated during BUNV infection; this is discussed further in section 4.2.

Analysis of LDH release from A549/HuH-7 spheroids, maintained under flowing conditions, indicate that BUNV infected spheroids can be maintained in microfluidic devices for up to 5 days (the maximal time point investigated in this study). Furthermore, microfluidic effluent collected from infected spheroid chips was found to contain infectious BUNV virions, as determined by viral plaque assay (Figure 3.16). These data imply that BUNV can complete a replication cycle in a 3D model, under flowing conditions. As such, this model may be utilised further to elucidate and define the poorly understood aspects of the Bunyavirus replication cycle (see section 1.1.4).

Finally, we have utilised the microfluidic model to investigate the effects of BUNV infection on cellular secretory pathways and exosome release, by western blot analysis of the tetraspanins CD63 and CD81; with a comparison of the differences in these 'exosome signatures' between the 2D and 3D models. Due to the time constraints of this project, and the limitations of sample size in the microfluidic model (see section 5.1.2), it was not possible to characterise exosomal CD63 and CD81 protein levels in microfluidic effluent. In brief, the data presented in the current study imply that intracellular CD63 expression is upregulated in response to BUNV infection, in both 2D and 3D (static) cultures of A549 cells (Figure 3.12 and Figure 3.14, respectively). Contrastingly, BUNV infection appears to reduce intracellular CD63 expression in HuH-7 monolayers (Figure 3.13), whereas CD63 expression appears to be increased in HuH-7 spheroids in response to BUNV infection (Figure 3.15). Again, this highlights that observations in 2D and 3D models may differ, as observed in the analysis of

cellular metabolic activity between 2D and 3D cultures (Figure 3.9). As such, further investigation is certainly required to elucidate which observation is a true reflection of *in vivo* infection. We also found that, in exosomes isolated from 2D A549-derived media, CD63 is not increased in response to BUNV infection (Figure 3.12). However, in HuH-7 cell monolayers, BUNV infection does appear to induce the secretion of exosomes possessing CD63 (Figure 3.13). Furthermore, in HuH-7 and A549 2D cultures, both intracellular and exosomal CD81 appear to decrease with increasing MOI (Figure 3.12). Again, this contrasts with the data observed in 3D culture models, which indicate that CD81 is increased intracellularly (in both cell lines), in response to BUNV infection (Figure 3.14 and Figure 3.15). The observation of increased intracellular CD81 in response to BUNV infection in 3D cultures of A549/HuH-7 cells is more analogous with the literature, for example; CD81 has been shown to play important roles in Influenza A virus (IAV) entry and budding; IAV is trafficked through CD81-positive endosomes, and CD81 is required for the fusion of the viral and endosomal membranes (He et al., 2013). Likewise, CD81 has been shown to play a multifunctional role in Hepatitis C virus (HCV) entry (Pileri et al., 1998; Farquhar et al., 2011; Grigorov et al., 2017). Since CD81 is manipulated by IAV and HCV, it could be postulated that other enveloped, single-stranded RNA viruses, such as Bunyaviruses, may have evolved to exploit the same mechanisms.

Nanoparticle tracking analysis (NTA) of exosomes/viral particles isolated from microfluidic effluent did not reveal any major significant differences in particle concentration/size in response to BUNV infection. However, such technology was of limited use to assess the effects of BUNV infection on exosome release, as exosomes and BUNV virions are similar in size and morphology; both are delimited by a lipid bilayer envelope, exosomes: 30-100nm, BUNV virions: 80-120nm. As such, exosomes and BUNV virions could not be differentiated with the NanoSight machine. These limitations are discussed further in section 5.3.

4.2 BUNV Effects on Cell Viability & Cell Death

4.2.1 2D Culture

It is clear from the data presented in section 3.2.1 that BUNV is implicated in reduced cellular metabolic activity in the A549 2D culture model. A549 cells infected at an MOI of 10 consistently show the lowest rates of metabolic activity of all MOIs used, relative to uninfected control cells (fig 3.8). In A549 cells infected at MOIs of 0.1 and 1, the metabolic activity is similar to uninfected cells, until 120hpi, after which the metabolic activity of infected cells (at all MOIs) decreases by approximately 50%, relative to the uninfected control cells. Classically, the MTS assay is used to quantify cell viability via the assessment of mitochondrial activity (see section 2.5.2). However, conversion of the MTS tetrazolium compound by NAD(P)H-dependent dehydrogenase enzymes implies only that the cells are metabolically active, thus, a high MTS absorbance reading correlates to higher metabolic rates, and not necessarily to a large quantity of viable cells (Devendran et al., 2019).

Numerous viruses have been shown to influence substantial alterations in cellular metabolism by the induction of mitochondrial dysfunction (Elesela & Lukacs, 2021). Mitochondria sense and respond to cellular stresses, such as infection, by rapidly increasing energy production (Osellame et al., 2012; Eisner et al., 2018). The precise role of mitochondrial dynamics in viral infection is yet to be elucidated, however, multiple studies have documented the adoption of changes to mitochondrial dynamics influenced by infections with influenza A virus (Ackermann, 1951; Ackermann & Johnson, 1953), hepatitis C virus (Kim et al., 2013; Javed & Manzoor, 2018), and respiratory syncytial virus (Owczarczyk et al., 2015; Elesela et al., 2020), to many varying downstream effects, including mitochondrion-mediated induction of apoptosis (Deng et al., 2008). Furthermore, studies have demonstrated the recruitment of mitochondria to BUNV viral factories (Fontana et al., 2008; Sanz-Sánchez & Risco, 2013) as described in section 1.1.4. Interestingly, studies have indicated that the Bunyaviral nonstructural NSs protein is involved in the induction of apoptosis; NSs mediates caspase activation and the release of mitochondrial pro-apoptotic factors such as cytochrome c (Colón-Ramos et al., 2003), through disruption of the mitochondrial membrane potential, resulting in permeabilisation (Barnwal et al., 2016). However, studies by Solà-Riera et al. (2020) show the opposite in Hantavirus infection;

whereby apoptosis is inhibited through the prevention of mitochondrial membrane potential loss and permeabilisation. Similarly, Kohl et al. (2003) show that BUNV NSs inhibits IRF-3 mediated apoptosis (see section 1.1.5), in the initial stages of infection. It is evident that mitochondrial dynamics are significantly altered in Bunyavirus infection. Future studies which elucidate the mechanisms by which the viral proteins directly dysregulate mitochondrial dynamics may improve our understanding of Bunyaviral pathogenesis. Furthermore, establishing a functional correlation between mitochondrial dynamics and the pathogenesis of Bunyaviral infections may contribute to the development of new antiviral drugs and therapeutic strategies (Ren et al., 2020).

In HuH-7 monolayers, the metabolic activity of cells infected with BUNV at MOIs of 0.1 and 1 appears to fluctuate (Figure 3.8). A possible explanation for this fluctuation in metabolic activity is the rapid doubling time of HuH-7 cells; approximately 24 hours (Jang et al., 2016). However, this is not concomitant with the basal rates of metabolic activity in HuH-7 monolayers presented in Figure 3.9, which shows no significant differences in metabolic activity between uninfected HuH-7 cells over the time course of the experiment. The observation that HuH-7 cell monolayers, infected with BUNV at an MOI of 0.1, show a significantly greater rate of metabolic activity than those infected at MOI 1 ($P=0.0079$), and those infected at MOI 10 ($P=0.0017$) at 72hpi (Figure 3.8) would support the findings by Kohl et al. (2003). Inhibition of apoptosis mediated by BUNV NSs would delay cell death and as a result, a greater proportion of viable, living cells would remain; overall resulting in higher metabolic activity. Those cells infected at the lowest MOI (MOI 0.1) more closely mimic natural infection, allowing infected cells to enter an antiviral state; an explanation for this increased metabolic activity observed in cells infected at MOI 0.1, relative to the higher MOIs used in this study.

4.2.2 3D Culture

Together the MTS data (Figure 3.8 and Figure 3.9), and fluorescence microscopy images (Figure 3.10) indicate that BUNV infection induces cell death, whilst increasing mitochondrial activity and metabolism in any living cells. Whilst no screening was conducted on the effects of BUNV on apoptotic pathways (see Chapter 6), the contrasting MTS and fluorescence

microscopy data could be explained by the phenomenon of BUNV NSs-induced mitochondrion-mediated apoptosis, as observed in studies by Colón-Ramos et al. (2003) and Barnwal et al. (2016). An upregulation of mitochondrial activity would be reflected by an increased rate of MTS conversion and thus a higher MTS absorbance recording. As such, in both HuH-7 and A549 spheroids, BUNV appears to have negligible effect on cellular metabolic activity (Figure 3.8). However, with FDA/PI staining, it is clear that BUNV infection induces cell death; in infected spheroids, there is a much larger proportion of dead cells (permissive to PI through membrane damage), than in the uninfected controls (Figure 3.10). This BUNV-induced cell death is more prominent in HuH-7 spheroids than in A549 spheroids; this may be a result of differences in the pro-apoptotic or anti-apoptotic mechanisms, mediated by BUNV nonstructural proteins, in cell types of different origin; both A549 and HuH-7 cells are interferon competent. In human lung epithelial cells (HSAECs), RVFV anti-apoptotic NSm manipulates the p53 pathway to delay apoptosis, favoring efficient viral replication and propagation (Austin et al., 2012). Whereas, in hepatocellular carcinoma cell lines (HepG2), RVFV and SFTSV have been shown to induce apoptosis through pro-apoptotic NSs protein-mediated activation of NFκB signaling, leading to aberrant cytokine and chemokine induction (Sun et al., 2015). Perhaps these differences in pathways exploited by members of the *Bunyavirales* could be explained by the evolution of distinct mechanisms to facilitate interferon antagonism by different Bunyaviruses (see Figure 1.10) (Elliott & Weber, 2009).

The low LDH release from BUNV infected A549 and HuH-7 spheroids (Figure 3.11) indicates that BUNV-infected spheroids can be maintained in a microfluidic device, in a viable state without lysis, for up to 5 days. However, upon examination of the microfluidic devices at 120hpi, the 4x BUNV-infected spheroids which were placed within microfluidic chips (see section 2.4.2) had all disaggregated (regardless of MOI). Therefore, it was not possible to determine the viability of the spheroids through lysis and examination of intracellular LDH concentration, as conducted on the uninfected control spheroids (see section 2.6.1). Perhaps the disaggregation of the infected spheroids is a result of the loss of cell-cell adhesiveness during BUNV infection. This was also observed during the microscopic examination of spheroids after FDA/PI staining (Figure 3.10), particularly in A549 spheroids infected at high MOIs, or after longer infection periods, spheroids appeared to lose structural stability and become more prone to disaggregate and fragment under mechanical stress. The shear stress

simulated by the flow rate used on the microfluidic device may have caused the infected spheroids to break apart, although the modelling of fluid flow is several orders of magnitude lower than found in vivo ((Baldwin, 2020)); single cells or small cell clusters would be able to pass through the 100 micron wide holes of the grid matrix (Figure 2.5) and flow into the effluent collection tube and be lost.

4.3 BUNV Effects on Cellular Secretory Trafficking & Exosome Release

4.3.1 Trafficking & Function of the Tetraspanins CD63 & CD81 in Mammalian Cells

The tetraspanins are a superfamily of transmembrane spanning proteins, which are associated with numerous biological processes including: signal transduction, tumorigenesis, cell adhesion, activation, differentiation, migration (Pols & Klumperman, 2009; Zou et al., 2018; Jankovičová et al., 2020), extracellular vesicle (EV) biogenesis, EV cargo selection and EV targeting and uptake (Andreu & Yáñez-Mó, 2014). The CD subfamily is largest of the tetraspanins and comprises all CD tetraspanins, except for CD63, which constitutes its own subfamily (Pols & Klumperman, 2009). Within mammalian cells, the majority of CD63 and CD81 is localised within late endosomes (LEs), lysosomes and multivesicular bodies (MVBs) (see figure 1.12), although a small pool is present at the cell surface (Pols & Klumperman, 2009). CD63 and CD81 are enriched within intraluminal vesicles (ILVs) inside MVBs (Escola et al., 1998). As such, these proteins are classically used as exosome markers (Escola et al., 1998; Raposo & Stoorvogel, 2013). Incorporation of these proteins into ILVs is believed to be both ESCRT-dependent (van Niel et al., 2011) and ESCRT-independent (see section 1.2.2), likely requiring ceramide (Trajkovic et al., 2008).

The specific functions of intracellular CD63 and CD81 are yet to be elucidated. However, evidence suggests that CD63 may be able to regulate the trafficking of its interaction partners; such as the sorting of major histocompatibility complexes I- and II (MHC-I and MHC-II) to B- T- and dendric cell-derived exosomes (Escola et al., 1998; Théry et al., 1999; Buschow et al., 2009). Yoshida et al. (2008) show that a CD63 mutant inhibits HIV-1 infection by mis-trafficking the cell surface associated receptor, CXCR4, to late endosomes and lysosomes. Furthermore, studies by Ninomiya et al. (2021) found that CD63 associates with hepatitis B virus (HBV), which contributes to the assembly and release of infectious HBV virions. CD81 plays an important role in the maturation, intracellular trafficking, and function of CD19 in B cells (Shoham et al., 2003; Shoham et al., 2006).

Increasing evidence points to the pivotal role of tetraspanins (such as CD63 and CD81) in the pathogenesis of viral infections (Martin et al., 2005; Florin & Lang, 2018; Cabañas et al., 2019). To enter and traffic through mammalian cells, viruses must interact with cellular membrane systems. Due to the localization of tetraspanins in membranes, associations must exist between the tetraspanins and viruses, during different stages of their replication cycle. As such, it is reasonable to hypothesise that viruses may have evolved to exploit these proteins (as with the cellular machinery involved in exosome biogenesis, discussed in section 1.2.2), to favour their entry, assembly, and non-lytic egress to produce new infectious progeny.

4.3.2 BUNV Infection Induces Changes in Intracellular CD63 & CD81

Quantification of CD63 and CD81, as detected by western blotting, in lysates of A549/HuH-7 cells (cultured as 2D monolayers and 3D spheroids) revealed that BUNV infection induces alterations in intracellular CD63 and CD81 levels. In 2D cultures of both cell lines, CD81 decreases intracellularly in response to BUNV infection (Figure 3.12 –Figure 3.13). By contrast, BUNV infection appears to increase intracellular CD81 expression in both A549 and HuH-7 spheroids (Figure 3.14 - Figure 3.15). Moreover, the effects of BUNV infection on CD63 expression was not consistent between the two cell lines, or between the 2D and 3D culture models (Figure 3.12 – Figure 3.15). In A549 monolayers and spheroids, CD63 appears to be increased intracellularly in response to BUNV infection, but the release of CD63-enriched exosomes is not induced. Contrastingly, in HuH-7 monolayers, BUNV infection appears to decrease intracellular CD63 expression, whereas the detection of CD63-enriched exosomes from BUNV-infected HuH-7 cells is increased in relation to the detection of CD63-enriched exosomes isolated from uninfected control cells at 120hpi (Figure 3.13); this is discussed further in section 4.3.3. However, in HuH-7 spheroids, CD63 expression appears to be increased intracellularly in response to BUNV infection (Figure 3.15).

Numerous studies have evidenced a dramatic remodeling of Golgi compartments during Bunyavirus assembly (Salanueva et al., 2003; Novoa Reyes et al., 2005; Fontana et al., 2008). Tetraspanins, including CD63, are palmitoylated in the Golgi complex (Yang et al., 2002). Palmitoylation is thought to be critical for the formation of tetraspanin interactions with other cell surface proteins (Yang et al., 2002). Studies by Flannery et al. (2010) identify a

palmitoylation-dependent association between CD63 and trafficking of synaptotagmin VII (Sty VII) to lysosomes. Perhaps this could explain the observation of increased intracellular CD63 in BUNV-infected A549 cells; disruption to the normal functioning of the Golgi body during the assembly of the Bunyavirus 'viral factory' (Fontana et al., 2008) and Bunyavirus maturation (see section 1.1.4) may interfere with CD63 palmitoylation, resulting its retention and accumulation in early compartments of the biosynthetic pathway; the endoplasmic reticulum or the Golgi (Charollais & Van Der Goot, 2009; Flannery et al., 2010).

The re-organisation of intracellular membranes, and the manipulation of cellular secretory pathways by RNA viruses to promote efficient replication and propagation is also well documented in the literature (Salanueva et al., 2003; Novoa Reyes et al., 2005; Mages et al., 2008; Hsu et al., 2010b; Barbosa et al., 2018; Hassan et al., 2021). However, the mechanisms by which viruses induce membrane rearrangements and affect changes to secretory pathways remains largely unclear. In HBV infection, activation of Rab7 drives a dramatic mobilisation of the endo-lysosomal and autophagic pathways, resulting in the extension of viral tubules from MVBs which aid in HBV secretion at the plasma membrane (Inoue et al., 2015). Additionally, Ninomiya et al. (2021) show that CD63 is essential for HBV assembly, release, and infectivity. For the closely related Orthobunyavirus, Oropouche virus (OROV), it is thought that trafficking from the *trans*-Golgi network to the cell periphery, and subsequent egress, is mediated though manipulation of ESCRT machineries (see section 1.1.4) (Barbosa et al., 2018) and in BUNV, through associations with actin filament bundles and multilamellar structures (MLS) on the basal surface of the infected cell (Sanz-Sánchez & Risco, 2013). Interestingly, a recent study has found that the *Phlebovirus,* SFTSV, induces autophagic flux for its assembly and egress (Yan et al., 2022). This mechanism of autophagic flux exploitation to mediate viral egress is distinct from those mechanisms of egress discussed above for BUNV and OROV. Yan et al. (2022) demonstrate that SFTSV not only assembles in autophagosomes derived from the ER-Golgi intermediate compartment and Golgi complex, but SFTSV also utilises autophagic vesicles for egress. Furthermore, studies by Wang et al. (2019) also show that Hantaviruses manipulate autophagic flux and induce mitophagy in the early stages of infection to evade host innate immunity through Gn protein interactions, which inhibit IFN responses. Moreover, Perez Vidakovics et al. (2019) demonstrate the induction of autophagy in A549 cells infected with the Arenavirus Junín virus. The precise role of autophagy in the

Bunyaviral replication cycle remains poorly understood. Further study is certainly required to elucidate the molecular mechanisms of autophagic manipulation, mediated by Bunyaviruses, and to determine whether these manipulations of autophagy to promote assembly and egress (Perez Vidakovics et al., 2019; Yan et al., 2022) and innate immune response suppression (Wang et al., 2019), are conserved across the *Bunyavirales.* Haeussler et al. (2020) propose that the induction of autophagy compensates for defects in mitochondrial dynamics (as discussed in section 4.2.1), leading to elevated metabolic activity and increased mitochondrial membrane potential to restore mitochondrial and cellular homeostasis. Based on the above proposal by Haeussler et al. (2020) (although based on an invertebrate model), and the documented ability of Bunyaviruses to induce autophagy (Wang et al., 2019; Yan et al., 2022), it could be speculated that the increase in metabolic activity implied by the data in this study (Figure 3.8), may be a result of BUNV-induced autophagy in A549 and HuH-7 cells, however, further studies are certainly required to confirm this hypothesis.

Furthermore, in the studies by Sanz-Sánchez and Risco (2013), it is suggested that the formation of MLS during BUNV infection alters the adhesive capacity of cells. It is speculated that, during egress, virus-induced assembly of actin bundles causes a loss of adherence, which triggers the formation of MLS from plasma membrane reservoirs to reinforce attachment to substrates. A possible hypothesis for the observed loss of cell-cell adhesiveness in A549 spheroids, as discussed in section 4.4.2, could be that the induction of MLS formation in infected cells may increase cell adherence to the housing substrates (i.e., the culture plate/microfluidic chip), discouraging cell-cell adhesiveness. However, due to the ultra-low adhesive nature of the spheroid plates, and the shear stress of the flow rate used on the microfluidic device, this is unlikely.

As a mechanism of innate immune response suppression, multiple Bunyaviruses (including BUNV) have evolved to block interferon production; NSs directly dysregulates RNA polymerase II, inhibiting host gene transcription (see fig. 1.9b) (Billecocq et al., 2004; Thomas et al., 2004; van Knippenberg et al., 2010; Eifan et al., 2013; Barry et al., 2014). The observation of increased intracellular CD63 expression in A549 monolayers (fig. 3.12) and A549/HuH-7 spheroids (fig. 3.14 and fig. 3.15) suggests that CD63 can be modulated by BUNV, or by the antiviral state of the cell, as the general transcriptional block induced by BUNV NSs would shut-off synthesis of cellular proteins that not are essential for BUNV replication.

4.3.3 HuH-7 Cells Secrete CD63-enriched Exosomes in Response to BUNV Infection

Western blot analysis of exosomes and BUNV virions, purified from HuH-7 derived spent media, suggest that BUNV infection induces the secretion of CD63-enriched exosomes (Figure 3.13). However, as mentioned previously, the detection of intracellular CD63 decreases in response to BUNV infection in these cells. Discussed briefly in sections 3.3.1 and 4.2.2, this observation could potentially be explained by the phenomenon of virus induced apoptosis (Roulston et al., 1999) and the secretion of 'apoptotic exosomes' (Park et al., 2018; Kakarla et al., 2020; Li et al., 2020). Apoptotic exosomes have been shown to possess CD63 (but not CD81), in addition to other markers associated with cellular stress; including LAMP1 and heat shock protein 70 (HSP70) (Kakarla et al., 2020). Since Bunyavirus infection has been shown to induce hepatocytic apoptosis (Ding et al., 2005; Sun et al., 2015), and given the presence of CD63 on apoptotic exosomes (Kakarla et al., 2020), the findings in this study would certainly support this theory. However, we cannot be certain that BUNV induces the release of apoptotic exosomes in HuH-7 cells without, i) further assessment of markers of apoptosis in infected cells, and ii) further characterisation of the exosomes secreted from infected cells to distinguish apoptotic exosomes from other EV subtypes (see Chapter 6).

The data presented in this study suggest that CD63 plays a significant role in the cellular secretory trafficking pathways affected by BUNV infection, however, the distinct mechanisms and interactions between CD63 and BUNV during different stages of the viral replication cycle remain to be elucidated, and certainly warrant further investigation. The observation of increased CD63-enriched exosome release from BUNV infected HuH-7 cells is concordant with studies by Silvas et al. (2016), who show that CD63 is increased in EVs produced from cells infected with SFTSV. Furthermore, Silvas et al. (2016) show that these CD63-positive EVs harbour infectious SFTSV virions, which can be delivered to, and establish infection in, naïve cells. This mechanism of receptor-independent transmission, mediated by exosomes, is also exploited by hepatitis C virus, which incorporates infectious RNA into exosomes to evade host immune responses and infect new cells (Ramakrishnaiah et al., 2013) and other examples reviewed in Kerviel et al. (2021) who introduce the concept on vesicle-mediated en block transmission. Further studies are certainly required to determine whether this mechanism of

transmission is shared with other members of the *Bunyavirales*, and to reveal the significance of this in contribution to viral pathogenesis.

Chapter 5: Limitations

5.1 Model Systems

5.1.1 Cell Lines

In recent years, the experimental relevance of established cell lines, such as those used in this study, has been debated in the research community (Mullard, 2018). Whilst immortalised cells have made immense contributions to biological research, the long-term storage and passage of these cells has resulted in questionable authenticity. Troublingly, a study on six different established cancer cell lines found that the cell lines shared more resemblance to each other, than to clinical samples of the respective cancer types (Gillet et al., 2011). As such, primary cells are often preferentially used to strengthen the validity of key findings (Kaur & Dufour, 2012). As a precaution, the HuH-7 cell line used in this study was referred to a genetic testing laboratory for authentication (see section 2.1.2). The A549 cell line was not authenticated as it was recently purchased from the ECACC, which are subject to scrutiny before delivery to ensure the integrity of their cell lines. Furthermore, all cell lines were regularly screened for mycoplasma infection, and preserved at low passage to allow the regeneration of new stocks when required (see section 2.1.1).

5.1.2 Small Sample Size in Microfluidic Devices

Figures 3.14 and 3.15 show faint, or no, detection of CD63 or CD81 in exosomes isolated from microfluidic effluent. It is likely that this is due to the small number of cells which are maintained in the microfluidic device, compared to the millions of cells maintained in monolayer culture. This could be rectified by pooling effluent from multiple chips; however, this would result in a greater volume of effluent requiring ultracentrifugation. The TLA-110 fixed-angle rotor used in this study is suitable for use with OptiSeal polypropylene 4.7mL centrifuge tubes only. Larger ultracentrifuge tubes (and adapted rotors) are available, however acquisition of these was not financially viable in the scope of this project.

5.2 Cell Viability Assessment

Few protocols have been standardised to assess cell viability in 3D spheroid models. The MTS protocol used in this study utilises longer incubation times in 3D culture (4 hours) than in 2D culture (1 hour) to allow the MTS reagent to penetrate the spheroids (Sennett, 2019). Specialised 3D cell viability assays have been developed, such as the CellTiter-Glo 3D cell viability assay, which quantifies intracellular ATP content; this has been found to assess cell viability more accurately than the MTS assay in 3D models (Dominijanni et al., 2021). A major limitation of the LDH assay is the high background LDH activity in FBS (Aslantürk, 2018). We combatted this limitation in the current study by utilising a reduced concentration of FBS (2% v/v), and any background interference caused by the assay medium is accounted for by measuring a media blank (see section 2.6.1). Moreover, whilst the LDH assay allows quantitative assessment of cell death, it does not provide information regarding the nature of cell death, nor will it detect cellular senescence (Aslantürk, 2018). Regarding the fluorescence microscopy used in this study, limitations include the low processing power of the conventional microscopes used, and the damage caused to spheroids by staining/washing. Microscopes with higher penetrating power may be utilised, such as multiphoton confocal microscopes. However studies have found that this still requires the cryosectioning of the spheroids, as only spheroid sections <100µm in thickness can be focused in detail (Sennett, 2019).

5.3 Exosome and Viral Particle Isolation

Both exosomes and BUNV virions are delimited by a lipid bilayer; exosomes are approximately 30-100nm in size (Théry et al., 2006), whilst BUNV virions are typically 80-120nm (Överby et al., 2008) (see section 1.1.3). Likewise, exosomes and Bunyavirus virions have similar densities; 1.06-1.11g/cm^3 (McNamara & Dittmer, 2020) and 1.16-1.17g/cm^3 (Schmaljohn et al., 1983), respectively. The sedimentation coefficient is a value, based on the Stokes-Einstein equation, that describes a particles migration through a medium (Cvjetkovic et al., 2014). Due to the similarities in size, density, morphology and hence, the sedimentation coefficients of exosomes and viral particles, the techniques reported in the literature their isolation are also very similar (McNamara & Dittmer, 2020). Differential ultracentrifugation is commonly used

to isolate exosomes from biological fluids (Théry et al., 2006; Momen-Heravi et al., 2013). Differential ultracentrifugation protocols which utilise sucrose cushion purification, such as the protocol used in this study (Figure 2.12), have been employed by numerous research groups to purify intact, functional Bunyavirus virions (Guardado-Calvo et al., 2016; Huang et al., 2016; Mastrodomenico et al., 2019; Mastrodomenico et al., 2020; Mo et al., 2020). However, a major limitation to the method is its inability to isolate exosomes from viral particles, as both are pelleted together given their similar sedimentation rates (McNamara & Dittmer, 2020). Separation of exosomes and viruses is not possible using techniques based on the particle's sedimentation coefficient, such as differential ultracentrifugation, and even density gradient ultracentrifugation (Nolte-'t Hoen et al., 2016). This was problematic for subsequent nanoparticle tracking analysis (NTA); the inability to separate and define populations of exosomes and BUNV virions meant that the data produced by NTA was of limited use to study BUNV infection effects on exosome release. No significant differences in nanoparticle concentration in microfluidic effluent were found between BUNV-infected and uninfected A549/HuH-7 spheroids maintained on-chip (Figure 3.17). This was contrary to the expectation that nanoparticle concentration would be greater in infected samples versus uninfected samples, particularly at 72hpi, as at this point it was shown that infectious BUNV virions were present in the effluent (Figure 3.16). However, as the NTA technology used in this study does encompass any nanoparticle characterisation (such as surface marker differentiation which is possible with nano flow-assisted cell sorting (nanoFACS), see Chapter 6), we were unable to define changes in the specific concentrations of exosomes and BUNV virions (if present) between the analysed samples.

Chapter 6: Conclusions & Future Direction

This study presents, for the first time, a physiologically relevant 3D microfluidic system that is permissive to BUNV infection. Such models, which can more accurately reflect the intricate architecture of native tissues and the complexity of the microenvironment encountered by human viruses, are the key to better understanding host-virus interactions; thus, enhancing their translational utility. However, it must be noted that this model employs only one cell type, therefore the interactions between different cell types (i.e., immune cells), observed *in vivo* is not simulated. The inability of 2D systems to recapitulate the *in vivo* environment fully has contributed to high rates of failure in vaccine and antiviral drug development (Lawko et al., 2021). The development of this flowing 3D model, which simulates an interactive 3D microenvironment and shear stress more comparable to an *in vivo* model of BUNV infection, may be utilised in future studies, i) to define poorly understood aspects of the Bunyaviral replication cycle, as discussed in section1.1.4, ii) to identify much-needed new potential therapeutic targets, and iii) to assess the efficacy of novel therapeutics. Furthermore, this model is suitable for the maintenance of spheroids formed from many different cell types; therefore, it may be utilised to study a variety of different viruses by employing the various cell types permissive to the virus of interest.

In recent years, numerous studies have revealed pivotal, previously unappreciated, roles of exosomes in viral diseases (Anderson et al., 2016; Chaudhari et al., 2022). Exosomes are able to act as immunomodulators and increase viral pathogenicity through cloaking viral RNA, DNA and complete virions within exosomes (Gould et al., 2003; Wiley & Gummuluru, 2006; Ariza et al., 2013; Klaus et al., 2013; Ramakrishnaiah et al., 2013; Longatti, 2015; Silvas et al., 2015; Ahsan et al., 2016)(Kerviel et al., 2021). The clinical applications of exosomes are gaining increasing attention in the viral research community; exosomes may serve as potential prognostic or diagnostic biomarkers of viral disease, and the viral components contained within exosomes may be targeted to impede further receptor-independent viral transmission and to reduce viral pathogenicity (Chaudhari et al., 2022). As discussed in section 1.2.3, many viruses hijack host cell endosomal sorting pathways, which are also utilised by exosomes. As such, engineered exosomes (serving as anti-viral drug delivery vehicles) represent a promising novel therapeutic option in the targeted treatment of viral diseases (Popowski et al., 2021).

Furthermore, enhancing the knowledge of the mechanisms by which viruses manipulate exosomes and exosome biogenesis machinery is also crucial to the understanding of poorly defined aspects of the Bunyaviral life cycle, particularly viral egress.

Interestingly, the data produced in this study implies that CD63-enriched exosomes are secreted by HuH-7 cells in response to BUNV infection (Figure 3.13). As discussed in section 4.3.3, we speculate that these exosomes may be apoptotic in nature, however, further investigation is needed to confirm this hypothesis. Furthermore, this observation is only made in the 2D model of infection, as it was not possible to detect CD63, CD81, or BUNV N protein in exosome/viral particle preparations from microfluidic effluent, owing to limitations in sample size (see section 5.1.2). Due to the time and budget constraints of this project, it was not possible to further optimise the microfluidic model to permit greater exosome/viral particle yield. However, by pooling microfluidic effluent and utilising ultracentrifugation equipment suitable for larger sample volumes, it may be possible to attain greater and observable levels of these proteins of interest.

Future studies that employ this microfluidic model should utilise different techniques to isolate exosomes and viral particles, to define a gold-standard protocol. Other methods of size-based isolation include ultrafiltration, size exclusion chromatography, and polymer precipitation (Gurunathan et al., 2019). However, as with ultracentrifugation, due the similarities in size between exosomes and Bunyavirus virions, these isolation methods would also struggle to allow the two populations to be differentiated. Immunoaffinity purification can be utilised to isolate specific exosome populations (such as those enriched with CD63), from a homogenous solution containing different biological components. This technique employs magnetic beads which can be coupled with high affinity to capture antibodies; this allows specific exosome subpopulations to be selected, based on the presence of their defining surface antigens (Greening et al., 2015b; Sharma et al., 2018; Filipović et al., 2022). Furthermore, recent studies have employed the principle of conventional immunoaffinity purification in microfluidic-based technologies to allow for the high-throughput extraction of specific EV subpopulations and subsequent characterisation (Kanwar et al., 2014; Contreras-Naranjo et al., 2017). These microfluidic-based immunoaffinity capture (Mf-IAC) platforms are able to recover exosomes with intact RNA (Kanwar et al., 2014). As such, future studies could manipulate these newly established Mf-IAC platforms to further characterise the

exosomes secreted from BUNV infected cells, including profiling of exosomal RNAs. It would be interesting to determine whether the exosomes secreted from BUNV infected cells contain any viral components, for example genomic RNA, and whether these exosomes are able to establish infection in naïve cells; as reported in SFTSV infection by Silvas et al. (2015).

Whilst this suggests that BUNV infection induces alterations in CD63-enriched exosome secretion, further research is certainly required to further characterise these exosomes. As discussed in section 4.3.3, it was not possible to distinguish exosomes from viral particles from the data produced by NTA. This technique would be more applicable if immunoaffinity purification was utilised first to isolate the CD63-positive exosomes, however, due to time and financial constraints this was not possible in the current project. Newer technologies have been developed that utilise flow cytometry to discriminate between exosomes and viral particle; nano flow-assisted cell sorting (nanoFACS). Future studies may employ such technologies to sort functional exosome and viral subsets whilst preserving their morphology, surface protein specificity and RNA cargo (Morales-Kastresana et al., 2019).

Further studies are required to investigate the nature of the exosomes secreted by HuH-7 cells in response to BUNV infection. In this study, we report the observation of increased CD63-enriched exosome secretion in response to BUNV infection in HuH-7 monolayers and speculate that these exosomes could be apoptotic exosomes (see section 4.3.3), a recently discovered entity (Kakarla et al., 2020). Markers unique to apoptotic exosomes are poorly defined in the literature (Gould & Raposo, 2013; Lotvall et al., 2014). However, Park et al. (2018) show that CD63, LAMP1, and HSP70 are found on apoptotic exosomes. If the exosomes secreted from BUNV infected HuH-7 cells are apoptotic in nature, we would expect an increased detection of LAMP1 and HSP70 by western blotting analysis of these exosomes, as observed with CD63 (fig 3.13). Additionally, further studies which interrogate the pathways by which these exosomes are secreted from BUNV infected cells, and analyses of their internal cargoes would be required to support the apoptotic exosome hypothesis. Studies have shown that apoptotic exosomes are produced by an MVB maturation pathway that is distinct from conventional exosome biogenesis (Sirois et al., 2011; Sirois et al., 2012), and the internal cargoes within apoptotic exosomes are also distinct from conventional exosomes (Park et al., 2018; Abramowicz et al., 2019). These studies could be further supported by assays to detect and quantify cellular events associated with apoptosis in HuH-

7 cells infected with BUNV. This may include flow cytometry of annexin V binding, analysis of caspase activation and caspase substrate (PARP) cleavage, cytochrome C release, mitochondrial membrane potential decrease, nuclear condensation, DNA fragmentation, and membrane blebbing.

At present, much of our knowledge regarding Bunyaviruses is based upon studies using traditional 2D cell culture systems which significantly undermine the intricacies of *in vivo* infection. Whilst the 3D microfluidic model of BUNV infection established in this study is single-celled and lacks entire complexity encountered by pathogens *in vivo,* this model represents a novel approach to Bunyaviral research, which may be utilised for many varying downstream applications, such as investigating novel mechanisms of pathogenesis, determining efficacy of therapeutics, and, importantly, defining poorly understood aspects of the Bunyaviral replication cycle. The global threat that is posed by the emergence of Bunyaviruses (Mehand et al., 2018) is exacerbated by the current lack of any licensed vaccines or effective therapeutics. The development of new drugs and vaccines is a time-consuming and costly process with up to 80% of therapeutics which pass preclinical trials failing during trials with human subjects (Miller & Spence, 2017). This highlights the importance of *ex vivo* models that embody the *in vivo* properties which influence disease pathology and therapeutic responses. Further optimisation of the microfluidic model is required to allow for the downstream characterisation of exosomes secreted from spheroids in response to Bunyavirus infection; a major barrier to overcome is the optimisation of effective, high-yield, and specific exosome isolation techniques. It is clear that cellular secretory pathways and exosome release are altered in BUNV infection. Further investigations based on the findings of this study, through characterisation of the nature of the exosomes that are secreted in response to BUNV infection, and the intracellular processes which drive their production will greatly contribute to our understanding of Bunyavirus-host interactions. Future studies must determine whether the exosomes produced during Bunyavirus infection enhance replicative fitness or trigger neighbouring host cell innate immunity to suppress infection. This knowledge is key to the future of exosome-based applications for the treatment of Bunyaviral infections. Furthermore, these studies will reveal important information to contribute to our understanding of ill-defined aspects of the Bunyaviral replication cycle, specifically viral egress, and receptor-independent transmission.

References

Abramowicz, A., Wojakowska, A., Marczak, L., Lysek-Gladysinska, M., Smolarz, M., Story, M. D., Polanska, J., Widlak, P. & Pietrowska, M. (2019) Ionizing radiation affects the composition of the proteome of extracellular vesicles released by head-and-neck cancer cells in vitro. *Journal of radiation research*, 60(3), 289-297.

Abudurexiti, A., Adkins, S., Alioto, D., Alkhovsky, S. V., Avšič-Županc, T., Ballinger, M. J., Bente, D. A., Beer, M., Bergeron, É., Blair, C. D., Briese, T., Buchmeier, M. J., Burt, F. J., Calisher, C. H., Cháng, C., Charrel, R. N., Choi, I. R., Clegg, J. C. S., de la Torre, J. C., de Lamballerie, X., Dèng, F., Di Serio, F., Digiaro, M., Drebot, M. A., Duàn, X., Ebihara, H., Elbeaino, T., Ergünay, K., Fulhorst, C. F., Garrison, A. R., Gāo, G. F., Gonzalez, J. J., Groschup, M. H., Günther, S., Haenni, A. L., Hall, R. A., Hepojoki, J., Hewson, R., Hú, Z., Hughes, H. R., Jonson, M. G., Junglen, S., Klempa, B., Klingström, J., Kòu, C., Laenen, L., Lambert, A. J., Langevin, S. A., Liu, D., Lukashevich, I. S., Luò, T., Lǚ, C., Maes, P., de Souza, W. M., Marklewitz, M., Martelli, G. P., Matsuno, K., Mielke-Ehret, N., Minutolo, M., Mirazimi, A., Moming, A., Mühlbach, H. P., Naidu, R., Navarro, B., Nunes, M. R. T., Palacios, G., Papa, A., Pauvolid-Corrêa, A., Pawęska, J. T., Qiáo, J., Radoshitzky, S. R., Resende, R. O., Romanowski, V., Sall, A. A., Salvato, M. S., Sasaya, T., Shěn, S., Shí, X., Shirako, Y., Simmonds, P., Sironi, M., Song, J. W., Spengler, J. R., Stenglein, M. D., Sū, Z., Sūn, S., Táng, S., Turina, M., Wáng, B., Wáng, C., Wáng, H., Wáng, J., Wèi, T., Whitfield, A. E., Zerbini, F. M., Zhāng, J., Zhāng, L., Zhāng, Y., Zhang, Y. Z., Zhāng, Y., et al (2019) Taxonomy of the order Bunyavirales: update 2019. *Arch Virol*, 164(7), 1949-1965.

Ackermann, W. W. (1951) The relation of the Krebs cycle to viral synthesis. II. The effect of sodium fluoroacetate on the propagation of influenza virus in mice. *J Exp Med*, 93(6), 635-42.

Ackermann, W. W. & Johnson, R. B. (1953) Some energy relations in a host-virus system. *J Exp Med*, 97(3), 315-22.

Adams, M. J., Lefkowitz, E. J., King, A. M. Q., Harrach, B., Harrison, R. L., Knowles, N. J., Kropinski, A. M., Krupovic, M., Kuhn, J. H., Mushegian, A. R., Nibert, M., Sabanadzovic, S., Sanfaçon, H., Siddell, S. G., Simmonds, P., Varsani, A., Zerbini, F. M., Gorbalenya, A. E. & Davison, A. J. (2017) Changes to taxonomy and the International Code of Virus Classification and Nomenclature ratified by the International Committee on Taxonomy of Viruses (2017). *Arch Virol*, 162(8), 2505-2538.

Afonso, A., Abrahantes, J. C., Conraths, F., Veldhuis, A., Elbers, A., Roberts, H., Van der Stede, Y., Méroc, E., Gache, K. & Richardson, J. (2014) The Schmallenberg virus epidemic in Europe-2011-2013. *Prev Vet Med*, 116(4), 391-403.

Ahsan, N. A., Sampey, G. C., Lepene, B., Akpamagbo, Y., Barclay, R. A., Iordanskiy, S., Hakami, R. M. & Kashanchi, F. (2016) Presence of Viral RNA and Proteins in Exosomes from Cellular Clones Resistant to Rift Valley Fever Virus Infection. *Front Microbiol*, 7, 139.

Albornoz, A., Hoffmann, A. B., Lozach, P. Y. & Tischler, N. D. (2016) Early Bunyavirus-Host Cell Interactions. *Viruses*, 8(5).

Alem, F., Olanrewaju, A. A., Omole, S., Hobbs, H. E., Ahsan, N., Matulis, G., Brantner, C. A., Zhou, W., Petricoin, E. F., Liotta, L. A., Caputi, M., Bavari, S., Wu, Y., Kashanchi, F. & Hakami, R. M. (2021) Exosomes originating from infection with the cytoplasmic single-stranded RNA virus Rift Valley fever virus (RVFV) protect recipient cells by inducing RIG-I mediated IFN-B response that leads to activation of autophagy. *Cell & Bioscience*, 11(1), 220.

Alenquer, M. & Amorim, M. J. (2015) Exosome Biogenesis, Regulation, and Function in Viral Infection. *Viruses*, 7(9), 5066-5083.

Aly, H. H., Shimotohno, K. & Hijikata, M. (2009) 3D cultured immortalized human hepatocytes useful to develop drugs for blood-borne HCV. *Biochem Biophys Res Commun*, 379(2), 330-4.

Ancel, S. & Feige, J. N. (2021) Young extracellular vesicles rejuvenate aged muscle. *Nature Aging*, 1(12), 1078-1080.

Andaloussi, S. E., Lakhal, S., Mäger, I. & Wood, M. J. (2013) Exosomes for targeted siRNA delivery across biological barriers. *Advanced drug delivery reviews*, 65(3), 391-397.

Anderson, M. R., Kashanchi, F. & Jacobson, S. (2016) Exosomes in Viral Disease. *Neurotherapeutics : the journal of the American Society for Experimental NeuroTherapeutics*, 13(3), 535-546.

Andrei, G., Duraffour, S., Van den Oord, J. & Snoeck, R. (2010) Epithelial raft cultures for investigations of virus growth, pathogenesis and efficacy of antiviral agents. *Antiviral Research*, 85(3), 431-449.

Andrei, G., van den Oord, J., Fiten, P., Opdenakker, G., De Wolf-Peeters, C., De Clercq, E. & Snoeck, R. (2005) Organotypic epithelial raft cultures as a model for evaluating compounds against alphaherpesviruses. *Antimicrob Agents Chemother*, 49(11), 4671-80.

Andreu, Z. & Yáñez-Mó, M. (2014) Tetraspanins in extracellular vesicle formation and function. *Frontiers in immunology*, 5, 442.

Antoni, D., Burckel, H., Josset, E. & Noel, G. (2015) Three-dimensional cell culture: a breakthrough in vivo. *Int J Mol Sci*, 16(3), 5517-27.

Ariza, M. E., Rivailler, P., Glaser, R., Chen, M. & Williams, M. V. (2013) Epstein-Barr virus encoded dUTPase containing exosomes modulate innate and adaptive immune responses in human dendritic cells and peripheral blood mononuclear cells. *PLoS One*, 8(7), e69827.

Aslantürk, Ö. S. (2018) In vitro cytotoxicity and cell viability assays: principles, advantages, and disadvantages. *Genotoxicity-A predictable risk to our actual world*, 2, 64-80.

Austin, D., Baer, A., Lundberg, L., Shafagati, N., Schoonmaker, A., Narayanan, A., Popova, T., Panthier, J. J., Kashanchi, F., Bailey, C. & Kehn-Hall, K. (2012) p53 Activation following Rift

Valley fever virus infection contributes to cell death and viral production. *PLoS One*, 7(5), e36327.

Babst, M. (2011) MVB vesicle formation: ESCRT-dependent, ESCRT-independent and everything in between. *Current Opinion in Cell Biology*, 23(4), 452-457.

Baldwin, L. (2020) *Development of a dual flow microfluidic device for the study of barrier systems* PhD Biomedical Sciences Thesis. University of Hull, October 2020.

Balzarini, J., Andrei, G., Balestra, E., Huskens, D., Vanpouille, C., Introini, A., Zicari, S., Liekens, S., Snoeck, R., Holý, A., Perno, C. F., Margolis, L. & Schols, D. (2013) A multi-targeted drug candidate with dual anti-HIV and anti-HSV activity. *PLoS Pathog*, 9(7), e1003456.

Barbosa, N. S., daSilva, L. L. P., Crump, C. M. & Graham, S. C. (2020) Oropouche virus glycoprotein topology and cellular requirements for virus-like particle assembly. *bioRxiv*, 2020.05.28.122689.

Barbosa, N. S., Mendonça, L. R., Dias, M. V. S., Pontelli, M. C., da Silva, E. Z. M., Criado, M. F., da Silva-Januário, M. E., Schindler, M., Jamur, M. C., Oliver, C., Arruda, E. & daSilva, L. L. P. (2018) ESCRT machinery components are required for Orthobunyavirus particle production in Golgi compartments. *PLOS Pathogens*, 14(5), e1007047.

Barnwal, B., Karlberg, H., Mirazimi, A. & Tan, Y. J. (2016) The Non-structural Protein of Crimean-Congo Hemorrhagic Fever Virus Disrupts the Mitochondrial Membrane Potential and Induces Apoptosis. *J Biol Chem*, 291(2), 582-92.

Barr, J. N. (2007) Bunyavirus mRNA synthesis is coupled to translation to prevent premature transcription termination. *RNA (New York, N.Y.)*, 13(5), 731-736.

Barr, J. N., Elliott, R. M., Dunn, E. F. & Wertz, G. W. (2003) Segment-specific terminal sequences of Bunyamwera bunyavirus regulate genome replication. *Virology*, 311(2), 326-38.

Barr, J. N., Rodgers, J. W. & Wertz, G. W. (2006) Identification of the Bunyamwera bunyavirus transcription termination signal. *J Gen Virol*, 87(Pt 1), 189-198.

Barr, J. N. & Wertz, G. W. (2004) Bunyamwera bunyavirus RNA synthesis requires cooperation of 3'- and 5'-terminal sequences. *Journal of virology*, 78(3), 1129-1138.

Barrila, J., Crabbé, A., Yang, J., Franco, K., Nydam Seth, D., Forsyth Rebecca, J., Davis Richard, R., Gangaraju, S., Ott, C. M., Coyne Carolyn, B., Bissell Mina, J. & Nickerson Cheryl, A. (2018) Modeling Host-Pathogen Interactions in the Context of the Microenvironment: Three-Dimensional Cell Culture Comes of Age. *Infection and Immunity*, 86(11), e00282-18.

Barry, G., Varela, M., Ratinier, M., Blomström, A. L., Caporale, M., Seehusen, F., Hahn, K., Schnettler, E., Baumgärtner, W., Kohl, A. & Palmarini, M. (2014) NSs protein of Schmallenberg virus counteracts the antiviral response of the cell by inhibiting its transcriptional machinery. *J Gen Virol*, 95(Pt 8), 1640-1646.

Bebelman, M. P., Smit, M. J., Pegtel, D. M. & Baglio, S. R. (2018) Biogenesis and function of extracellular vesicles in cancer. *Pharmacol Ther*, 188, 1-11.

Berto, A., Van der Poel, W. H., Hakze-van der Honing, R., Martelli, F., La Ragione, R. M., Inglese, N., Collins, J., Grierson, S., Johne, R., Reetz, J., Dastjerdi, A. & Banks, M. (2013) Replication of hepatitis E virus in three-dimensional cell culture. *J Virol Methods*, 187(2), 327-32.

Billecocq, A., Spiegel, M., Vialat, P., Kohl, A., Weber, F., Bouloy, M. & Haller, O. (2004) NSs Protein of Rift Valley Fever Virus Blocks Interferon Production by Inhibiting Host Gene Transcription. *Journal of Virology*, 78(18), 9798-9806.

Blakqori, G., Delhaye, S., Habjan, M., Blair, C. D., Sánchez-Vargas, I., Olson, K. E., Attarzadeh-Yazdi, G., Fragkoudis, R., Kohl, A., Kalinke, U., Weiss, S., Michiels, T., Staeheli, P. & Weber, F. (2007) La Crosse bunyavirus nonstructural protein NSs serves to suppress the type I interferon system of mammalian hosts. *J Virol*, 81(10), 4991-9.

Blight, K. J., McKeating, J. A. & Rice, C. M. (2002) Highly permissive cell lines for subgenomic and genomic hepatitis C virus RNA replication. *J Virol*, 76(24), 13001-14.

Blitvich, B. J., Beaty, B. J., Blair, C. D., Brault, A. C., Dobler, G., Drebot, M. A., Haddow, A. D., Kramer, L. D., LaBeaud, A. D., Monath, T. P., Mossel, E. C., Plante, K., Powers, A. M., Tesh, R. B., Turell, M. J., Vasilakis, N. & Weaver, S. C. (2018) Bunyavirus Taxonomy: Limitations and Misconceptions Associated with the Current ICTV Criteria Used for Species Demarcation. *Am J Trop Med Hyg*, 99(1), 11-16.

Booth, A. M., Fang, Y., Fallon, J. K., Yang, J. M., Hildreth, J. E. & Gould, S. J. (2006) Exosomes and HIV Gag bud from endosome-like domains of the T cell plasma membrane. *J Cell Biol*, 172(6), 923-35.

Boulant, S., Stanifer, M. & Lozach, P.-Y. (2015) Dynamics of virus-receptor interactions in virus binding, signaling, and endocytosis. *Viruses*, 7(6), 2794-2815.

Bowden, T. A., Bitto, D., McLees, A., Yeromonahos, C., Elliott, R. M. & Huiskonen, J. T. (2013) Orthobunyavirus ultrastructure and the curious tripodal glycoprotein spike. *PLoS pathogens*, 9(5), e1003374-e1003374.

Breslin, S. & O'Driscoll, L. (2013) Three-dimensional cell culture: the missing link in drug discovery. *Drug Discov Today*, 18(5-6), 240-9.

Bridgen, A. & Elliott, R. M. (1996) Rescue of a segmented negative-strand RNA virus entirely from cloned complementary DNAs. *Proceedings of the National Academy of Sciences*, 93(26), 15400-15404.

Bridgen, A., Weber, F., Fazakerley, J. K. & Elliott, R. M. (2001) Bunyamwera bunyavirus nonstructural protein NSs is a nonessential gene product that contributes to viral

pathogenesis. *Proceedings of the National Academy of Sciences of the United States of America*, 98(2), 664-669.

Buschow, S. I., Nolte-'t Hoen, E. N., Van Niel, G., Pols, M. S., Ten Broeke, T., Lauwen, M., Ossendorp, F., Melief, C. J., Raposo, G. & Wubbolts, R. (2009) MHC II in dendritic cells is targeted to lysosomes or T cell-induced exosomes via distinct multivesicular body pathways. *Traffic*, 10(10), 1528-1542.

Cabañas, C., Yáñez-Mó, M. & van Spriel, A. B. (2019) Editorial: Functional Relevance of Tetraspanins in the Immune System. *Frontiers in Immunology*, 10.

Carlton-Smith, C. & Elliott, R. M. (2012) Viperin, MTAP44, and protein kinase R contribute to the interferon-induced inhibition of Bunyamwera Orthobunyavirus replication. *Journal of virology*, 86(21), 11548-11557.

Casel, M. A., Park, S. J. & Choi, Y. K. (2021) Severe fever with thrombocytopenia syndrome virus: emerging novel phlebovirus and their control strategy. *Experimental & Molecular Medicine*, 53(5), 713-722.

CDC *Hantavirus.* Available online: https://www.cdc.gov/hantavirus/technical/hanta/virology.html [Accessed 13/01/2022].

Chahar, H. S., Bao, X. & Casola, A. (2015) Exosomes and Their Role in the Life Cycle and Pathogenesis of RNA Viruses. *Viruses*, 7(6), 3204-3225.

Charollais, J. & Van Der Goot, F. G. (2009) Palmitoylation of membrane proteins (Review). *Molecular Membrane Biology*, 26(1-2), 55-66.

Chaudhari, P., Ghate, V., Nampoothiri, M. & Lewis, S. (2022) Multifunctional role of exosomes in viral diseases: From transmission to diagnosis and therapy. *Cell Signal*, 94, 110325.

Chen, H., Wang, L., Zeng, X., Schwarz, H., Nanda, H. S., Peng, X. & Zhou, Y. (2021) Exosomes, a New Star for Targeted Delivery. *Front Cell Dev Biol*, 9, 751079.

Chen, H., Yu, Z., Bai, S., Lu, H., Xu, D., Chen, C., Liu, D. & Zhu, Y. (2019) Microfluidic models of physiological or pathological flow shear stress for cell biology, disease modeling and drug development. *TrAC Trends in Analytical Chemistry*, 117, 186-199.

Chen, S. Y., Matsuoka, Y. & Compans, R. W. (1991) Assembly and polarized release of Punta Toro virus and effects of brefeldin A. *Journal of Virology*, 65(3), 1427-1439.

Chen, W., Feng, Y., Chen, D. & Wandinger-Ness, A. (1998) Rab11 is required for trans-golgi network-to-plasma membrane transport and a preferential target for GDP dissociation inhibitor. *Mol Biol Cell*, 9(11), 3241-57.

Cho, N. J., Elazar, M., Xiong, A., Lee, W., Chiao, E., Baker, J., Frank, C. W. & Glenn, J. S. (2009) Viral infection of human progenitor and liver-derived cells encapsulated in three-dimensional PEG-based hydrogel. *Biomed Mater*, 4(1), 011001.

Collins, T., Pyne, E., Christensen, M., Iles, A., Pamme, N. & Pires, I. M. (2021) Spheroid-on-chip microfluidic technology for the evaluation of the impact of continuous flow on metastatic potential in cancer models in vitro. *Biomicrofluidics*, 15(4), 044103-044103.

Colón-Ramos, D. A., Irusta, P. M., Gan, E. C., Olson, M. R., Song, J., Morimoto, R. I., Elliott, R. M., Lombard, M., Hollingsworth, R., Hardwick, J. M., Smith, G. K. & Kornbluth, S. (2003) Inhibition of translation and induction of apoptosis by Bunyaviral nonstructural proteins bearing sequence similarity to reaper. *Mol Biol Cell*, 14(10), 4162-72.

Contreras-Naranjo, J. C., Wu, H.-J. & Ugaz, V. M. (2017) Microfluidics for exosome isolation and analysis: enabling liquid biopsy for personalized medicine. *Lab on a Chip*, 17(21), 3558-3577.

Cui, X., Hartanto, Y. & Zhang, H. (2017) Advances in multicellular spheroids formation. *J R Soc Interface*, 14(127).

Cvjetkovic, A., Lötvall, J. & Lässer, C. (2014) The influence of rotor type and centrifugation time on the yield and purity of extracellular vesicles. *J Extracell Vesicles*, 3.

Dar, G. H., Mendes, C. C., Kuan, W.-L., Speciale, A. A., Conceição, M., Görgens, A., Uliyakina, I., Lobo, M. J., Lim, W. F., El Andaloussi, S., Mäger, I., Roberts, T. C., Barker, R. A., Goberdhan, D. C. I., Wilson, C. & Wood, M. J. A. (2021) GAPDH controls extracellular vesicle biogenesis and enhances the therapeutic potential of EV mediated siRNA delivery to the brain. *Nature Communications*, 12(1), 6666.

de Boer, S. M., Kortekaas, J., de Haan, C. A. M., Rottier, P. J. M., Moormann, R. J. M. & Bosch, B. J. (2012) Heparan sulfate facilitates Rift Valley fever virus entry into the cell. *Journal of virology*, 86(24), 13767-13771.

Decarli, M. C., Amaral, R., Santos, D. P. D., Tofani, L. B., Katayama, E., Rezende, R. A., Silva, J., Swiech, K., Suazo, C. A. T., Mota, C., Moroni, L. & Moraes Â, M. (2021) Cell spheroids as a versatile research platform: formation mechanisms, high throughput production, characterization and applications. *Biofabrication*, 13(3).

Deng, L., Adachi, T., Kitayama, K., Bungyoku, Y., Kitazawa, S., Ishido, S., Shoji, I. & Hotta, H. (2008) Hepatitis C Virus Infection Induces Apoptosis through a Bax-Triggered, Mitochondrion-Mediated, Caspase 3-Dependent Pathway. *Journal of Virology*, 82(21), 10375-10385.

Devendran, C., Carthew, J., Frith, J. E. & Neild, A. (2019) Cell adhesion, morphology, and metabolism variation via acoustic exposure within microfluidic cell handling systems. *Advanced Science*, 6(24), 1902326.

Deyde, V. M., Khristova, M. L., Rollin, P. E., Ksiazek, T. G. & Nichol, S. T. (2006) Crimean-Congo Hemorrhagic Fever Virus Genomics and Global Diversity. *Journal of Virology*, 80(17), 8834-8842.

Ding, X., Xu, F., Chen, H., Tesh, R. B. & Xiao, S. Y. (2005) Apoptosis of hepatocytes caused by Punta Toro virus (Bunyaviridae: Phlebovirus) and its implication for Phlebovirus pathogenesis. *Am J Pathol*, 167(4), 1043-9.

Dominijanni, A. J., Devarasetty, M., Forsythe, S. D., Votanopoulos, K. I. & Soker, S. (2021) Cell Viability Assays in Three-Dimensional Hydrogels: A Comparative Study of Accuracy. *Tissue Eng Part C Methods*, 27(7), 401-410.

Dunn, E. F., Pritlove, D. C., Jin, H. & Elliott, R. M. (1995) Transcription of a recombinant bunyavirus RNA template by transiently expressed bunyavirus proteins. *Virology*, 211(1), 133-43.

Edmondson, R., Broglie, J. J., Adcock, A. F. & Yang, L. (2014) Three-dimensional cell culture systems and their applications in drug discovery and cell-based biosensors. *Assay Drug Dev Technol*, 12(4), 207-18.

Eifan, S., Schnettler, E., Dietrich, I., Kohl, A. & Blomström, A.-L. (2013) Non-structural proteins of arthropod-borne bunyaviruses: roles and functions. *Viruses*, 5(10), 2447-2468.

Eisner, V., Picard, M. & Hajnóczky, G. (2018) Mitochondrial dynamics in adaptive and maladaptive cellular stress responses. *Nature Cell Biology*, 20(7), 755-765.

Ekert, J. E., Johnson, K., Strake, B., Pardinas, J., Jarantow, S., Perkinson, R. & Colter, D. C. (2014) Three-dimensional lung tumor microenvironment modulates therapeutic compound responsiveness in vitro--implication for drug development. *PloS one*, 9(3), e92248-e92248.

Elesela, S. & Lukacs, N. W. (2021) Role of Mitochondria in Viral Infections. *Life (Basel)*, 11(3).

Elesela, S., Morris, S. B., Narayanan, S., Kumar, S., Lombard, D. B. & Lukacs, N. W. (2020) Sirtuin 1 regulates mitochondrial function and immune homeostasis in respiratory syncytial virus infected dendritic cells. *PLoS Pathog*, 16(2), e1008319.

Elliott, R. M. (2009) Bunyaviruses and climate change. *Clinical Microbiology and Infection*, 15(6), 510-517.

Elliott, R. M. (2014) Orthobunyaviruses: recent genetic and structural insights. *Nat Rev Microbiol*, 12(10), 673-85.

Elliott, R. M., Blakqori, G., van Knippenberg, I. C., Koudriakova, E., Li, P., McLees, A., Shi, X. & Szemiel, A. M. (2013) Establishment of a reverse genetics system for Schmallenberg virus, a newly emerged orthobunyavirus in Europe. *J Gen Virol*, 94(Pt 4), 851-859.

Elliott, R. M. & Weber, F. (2009) Bunyaviruses and the type I interferon system. *Viruses*, 1(3), 1003-21.

Enders, J. F., Weller, T. H. & Robbins, F. C. (1949) Cultivation of the Lansing Strain of Poliomyelitis Virus in Cultures of Various Human Embryonic Tissues. *Science*, 109(2822), 85-7.

Escola, J.-M., Kleijmeer, M. J., Stoorvogel, W., Griffith, J. M., Yoshie, O. & Geuze, H. J. (1998) Selective Enrichment of Tetraspan Proteins on the Internal Vesicles of Multivesicular Endosomes and on Exosomes Secreted by Human B-lymphocytes*. *Journal of Biological Chemistry*, 273(32), 20121-20127.

Fang, L., Meyers, C., Budgeon, L. R. & Howett, M. K. (2006) Induction of productive human papillomavirus type 11 life cycle in epithelial cells grown in organotypic raft cultures. *Virology*, 347(1), 28-35.

Farquhar, M. J., Harris, H. J. & McKeating, J. A. (2011) Hepatitis C virus entry and the tetraspanin CD81. *Biochemical Society Transactions*, 39(2), 532-536.

Filipović, L., Spasojević, M., Prodanović, R., Korać, A., Matijaševic, S., Brajušković, G., de Marco, A. & Popović, M. (2022) Affinity-based isolation of extracellular vesicles by means of single-domain antibodies bound to macroporous methacrylate-based copolymer. *New Biotechnology*, 69, 36-48.

Flannery, A. R., Czibener, C. & Andrews, N. W. (2010) Palmitoylation-dependent association with CD63 targets the Ca2+ sensor synaptotagmin VII to lysosomes. *J Cell Biol*, 191(3), 599-613.

Flick, R., Elgh, F. & Pettersson, R. F. (2002) Mutational analysis of the Uukuniemi virus (Bunyaviridae family) promoter reveals two elements of functional importance. *J Virol*, 76(21), 10849-60.

Florin, L. & Lang, T. (2018) Tetraspanin Assemblies in Virus Infection. *Frontiers in Immunology*, 9.

Fontana, J., López-Montero, N., Elliott, R. M., Fernández, J. J. & Risco, C. (2008) The unique architecture of Bunyamwera virus factories around the Golgi complex. *Cellular Microbiology*, 10(10), 2012-2028.

Frey, O., Misun, P. M., Fluri, D. A., Hengstler, J. G. & Hierlemann, A. (2014) Reconfigurable microfluidic hanging drop network for multi-tissue interaction and analysis. *Nature Communications*, 5(1), 4250.

Gangoda, L., Boukouris, S., Liem, M., Kalra, H. & Mathivanan, S. (2015) Extracellular vesicles including exosomes are mediators of signal transduction: are they protective or pathogenic? *Proteomics*, 15(2-3), 260-71.

Gardner, J. K. & Herbst-Kralovetz, M. M. (2016) Three-Dimensional Rotating Wall Vessel-Derived Cell Culture Models for Studying Virus-Host Interactions. *Viruses*, 8(11), 304.

Garrison, A. R., Radoshitzky, S. R., Kota, K. P., Pegoraro, G., Ruthel, G., Kuhn, J. H., Altamura, L. A., Kwilas, S. A., Bavari, S., Haucke, V. & Schmaljohn, C. S. (2013) Crimean-Congo hemorrhagic fever virus utilizes a clathrin- and early endosome-dependent entry pathway. *Virology*, 444(1-2), 45-54.

Garrus, J. E., von Schwedler, U. K., Pornillos, O. W., Morham, S. G., Zavitz, K. H., Wang, H. E., Wettstein, D. A., Stray, K. M., Côté, M., Rich, R. L., Myszka, D. G. & Sundquist, W. I. (2001) Tsg101 and the Vacuolar Protein Sorting Pathway Are Essential for HIV-1 Budding. *Cell*, 107(1), 55-65.

Gavrilovskaya, I. N., Brown, E. J., Ginsberg, M. H. & Mackow, E. R. (1999) Cellular entry of hantaviruses which cause hemorrhagic fever with renal syndrome is mediated by beta3 integrins. *Journal of virology*, 73(5), 3951-3959.

Gavrilovskaya, I. N., Shepley, M., Shaw, R., Ginsberg, M. H. & Mackow, E. R. (1998) β3 integrins mediate the cellular entry of hantaviruses that cause respiratory failure. *Proceedings of the National Academy of Sciences*, 95(12), 7074-7079.

Gerber, P. P., Cabrini, M., Jancic, C., Paoletti, L., Banchio, C., von Bilderling, C., Sigaut, L., Pietrasanta, L. I., Duette, G., Freed, E. O., Basile Gde, S., Moita, C. F., Moita, L. F., Amigorena, S., Benaroch, P., Geffner, J. & Ostrowski, M. (2015) Rab27a controls HIV-1 assembly by regulating plasma membrane levels of phosphatidylinositol 4,5-bisphosphate. *J Cell Biol*, 209(3), 435-52.

Gillet, J.-P., Calcagno, A. M., Varma, S., Marino, M., Green, L. J., Vora, M. I., Patel, C., Orina, J. N., Eliseeva, T. A., Singal, V., Padmanabhan, R., Davidson, B., Ganapathi, R., Sood, A. K., Rueda, B. R., Ambudkar, S. V. & Gottesman, M. M. (2011) Redefining the relevance of established cancer cell lines to the study of mechanisms of clinical anti-cancer drug resistance. *Proceedings of the National Academy of Sciences*, 108(46), 18708-18713.

Goodwin, T. J., McCarthy, M., Osterrieder, N., Cohrs, R. J. & Kaufer, B. B. (2013) Three-dimensional normal human neural progenitor tissue-like assemblies: a model of persistent varicella-zoster virus infection. *PLoS Pathog*, 9(8), e1003512.

Gori-Savellini, G., Valentini, M. & Cusi, M. G. (2013) Toscana virus NSs protein inhibits the induction of type I interferon by interacting with RIG-I. *Journal of virology*, 87(12), 6660-6667.

Gould, S. J., Booth, A. M. & Hildreth, J. E. (2003) The Trojan exosome hypothesis. *Proc Natl Acad Sci U S A*, 100(19), 10592-7.

Gould, S. J. & Raposo, G. (2013) As we wait: coping with an imperfect nomenclature for extracellular vesicles. *Journal of Extracellular Vesicles*, 2(1), 20389.

Greening, D. W., Gopal, S. K., Xu, R., Simpson, R. J. & Chen, W. (2015a) Exosomes and their roles in immune regulation and cancer. *Semin Cell Dev Biol*, 40, 72-81.

Greening, D. W., Xu, R., Ji, H., Tauro, B. J. & Simpson, R. J. (2015b) A protocol for exosome isolation and characterization: evaluation of ultracentrifugation, density-gradient separation, and immunoaffinity capture methods. *Methods Mol Biol*, 1295, 179-209.

Grigorov, B., Reungoat, E., Gentil dit Maurin, A., Varbanov, M., Blaising, J., Michelet, M., Manuel, R., Parent, R., Bartosch, B. & Zoulim, F. (2017) Hepatitis C virus infection propagates through interactions between Syndecan‐1 and CD81 and impacts the hepatocyte glycocalyx. *Cellular Microbiology*, 19(5), e12711.

Guardado-Calvo, P., Bignon, E. A., Stettner, E., Jeffers, S. A., Pérez-Vargas, J., Pehau-Arnaudet, G., Tortorici, M. A., Jestin, J. L., England, P., Tischler, N. D. & Rey, F. A. (2016) Mechanistic Insight into Bunyavirus-Induced Membrane Fusion from Structure-Function Analyses of the Hantavirus Envelope Glycoprotein Gc. *PLoS Pathog*, 12(10), e1005813.

Gubbins, S., Richardson, J., Baylis, M., Wilson, A. J. & Abrahantes, J. C. (2014) Modelling the continental-scale spread of Schmallenberg virus in Europe: approaches and challenges. *Prev Vet Med*, 116(4), 404-11.

Gupta, S., Rawat, S., Arora, V., Kottarath, S. K., Dinda, A. K., Vaishnav, P. K., Nayak, B. & Mohanty, S. (2018) An improvised one-step sucrose cushion ultracentrifugation method for exosome isolation from culture supernatants of mesenchymal stem cells. *Stem Cell Research & Therapy*, 9(1), 180.

Gurunathan, S., Kang, M.-H., Jeyaraj, M., Qasim, M. & Kim, J.-H. (2019) Review of the Isolation, Characterization, Biological Function, and Multifarious Therapeutic Approaches of Exosomes. *Cells*, 8(4), 307.

Gurung, S., Perocheau, D., Touramanidou, L. & Baruteau, J. (2021) The exosome journey: from biogenesis to uptake and intracellular signalling. *Cell Communication and Signaling*, 19(1), 47.

György, B., Szabó, T. G., Pásztói, M., Pál, Z., Misják, P., Aradi, B., László, V., Pállinger, É., Pap, E., Kittel, Á., Nagy, G., Falus, A. & Buzás, E. I. (2011) Membrane vesicles, current state-of-the-art: emerging role of extracellular vesicles. *Cellular and Molecular Life Sciences*, 68(16), 2667-2688.

Habjan, M., Penski, N., Wagner, V., Spiegel, M., Överby, A. K., Kochs, G., Huiskonen, J. T. & Weber, F. (2009) Efficient production of Rift Valley fever virus-like particles: The antiviral protein MxA can inhibit primary transcription of bunyaviruses. *Virology*, 385(2), 400-408.

Haeussler, S., Köhler, F., Witting, M., Premm, M. F., Rolland, S. G., Fischer, C., Chauve, L., Casanueva, O. & Conradt, B. (2020) Autophagy compensates for defects in mitochondrial dynamics. *PLoS Genet*, 16(3), e1008638.

Haisler, W. L., Timm, D. M., Gage, J. A., Tseng, H., Killian, T. C. & Souza, G. R. (2013) Three-dimensional cell culturing by magnetic levitation. *Nat Protoc*, 8(10), 1940-9.

Han, S. J., Kwon, S. & Kim, K. S. (2021) Challenges of applying multicellular tumor spheroids in preclinical phase. *Cancer Cell International*, 21(1), 152.

Harb, A., Fakhreddine, M., Zaraket, H. & Saleh, F. A. (2021) Three-Dimensional Cell Culture Models to Study Respiratory Virus Infections Including COVID-19. *Biomimetics (Basel)*, 7(1).

Hart, T. J., Kohl, A. & Elliott, R. M. (2009) Role of the NSs protein in the zoonotic capacity of Orthobunyaviruses. *Zoonoses Public Health*, 56(6-7), 285-96.

Hassan, Z., Kumar, N. D., Reggiori, F. & Khan, G. (2021) How Viruses Hijack and Modify the Secretory Transport Pathway. *Cells*, 10(10), 2535.

He, B., Chen, G. & Zeng, Y. (2016) Three-dimensional cell culture models for investigating human viruses. *Virol Sin*, 31(5), 363-379.

He, J., Sun, E., Bujny, M. V., Kim, D., Davidson, M. W. & Zhuang, X. (2013) Dual function of CD81 in influenza virus uncoating and budding. *PLoS Pathog*, 9(10), e1003701.

Heitmann, A., Gusmag, F., Rathjens, M. G., Maurer, M., Frankze, K., Schicht, S., Jansen, S., Schmidt-Chanasit, J., Jung, K. & Becker, S. C. (2021) Mammals Preferred: Reassortment of Batai and Bunyamwera orthobunyavirus Occurs in Mammalian but Not Insect Cells. *Viruses*, 13(9).

Heng, B. C., Cowan, C. M. & Basu, S. (2009) Comparison of enzymatic and non-enzymatic means of dissociating adherent monolayers of mesenchymal stem cells. *Biol Proced Online*, 11, 161-9.

Henne, William M., Buchkovich, Nicholas J. & Emr, Scott D. (2011) The ESCRT Pathway. *Developmental Cell*, 21(1), 77-91.

Hermonat, P. L., You, H., Chiriva-Internati, C. M. & Liu, Y. (2005) Analysis of adeno-associated virus and HPV interaction. *Methods Mol Med*, 119, 397-409.

Hessvik, N. P. & Llorente, A. (2018) Current knowledge on exosome biogenesis and release. *Cell Mol Life Sci*, 75(2), 193-208.

Hoffmann, B., Scheuch, M., Höper, D., Jungblut, R., Holsteg, M., Schirrmeier, H., Eschbaumer, M., Goller, K. V., Wernike, K., Fischer, M., Breithaupt, A., Mettenleiter, T. C. & Beer, M. (2012) Novel orthobunyavirus in Cattle, Europe, 2011. *Emerg Infect Dis*, 18(3), 469-72.

Hollidge Bradley, S., Nedelsky Natalia, B., Salzano, M.-V., Fraser Jonathan, W., González-Scarano, F. & Soldan Samantha, S. (2012) Orthobunyavirus Entry into Neurons and Other Mammalian Cells Occurs via Clathrin-Mediated Endocytosis and Requires Trafficking into Early Endosomes. *Journal of Virology*, 86(15), 7988-8001.

Hollidge, B. S., Nedelsky, N. B., Salzano, M. V., Fraser, J. W., González-Scarano, F. & Soldan, S. S. (2012) Orthobunyavirus entry into neurons and other mammalian cells occurs via clathrin-mediated endocytosis and requires trafficking into early endosomes. *J Virol*, 86(15), 7988-8001.

Hoogstraal, H. (1979) The epidemiology of tick-borne Crimean-Congo hemorrhagic fever in Asia, Europe, and Africa. *J Med Entomol*, 15(4), 307-417.

Hossain, M. J., Mori, I., Dong, L., Liu, B. & Kimura, Y. (2008) Fetal calf serum inhibits virus genome expression in Madin-Darby canine kidney cells persistently infected with influenza A virus. *Med Microbiol Immunol*, 197(1), 21-7.

Hosseini-Beheshti, E., Pham, S., Adomat, H., Li, N. & Tomlinson Guns, E. S. (2012) Exosomes as biomarker enriched microvesicles: characterization of exosomal proteins derived from a panel of prostate cell lines with distinct AR phenotypes. *Mol Cell Proteomics*, 11(10), 863-85.

Hover, S., Foster, B., Fontana, J., Kohl, A., Goldstein, S. A. N., Barr, J. N. & Mankouri, J. (2018) Bunyavirus requirement for endosomal K+ reveals new roles of cellular ion channels during infection. *PLoS Pathog*, 14(1), e1006845.

Hover, S., King, B., Hall, B., Loundras, E. A., Taqi, H., Daly, J., Dallas, M., Peers, C., Schnettler, E., McKimmie, C., Kohl, A., Barr, J. N. & Mankouri, J. (2016) Modulation of Potassium Channels Inhibits Bunyavirus Infection. *J Biol Chem*, 291(7), 3411-22.

Hsu, C., Morohashi, Y., Yoshimura, S.-i., Manrique-Hoyos, N., Jung, S., Lauterbach, M. A., Bakhti, M., Grønborg, M., Möbius, W., Rhee, J., Barr, F. A. & Simons, M. (2010a) Regulation of exosome secretion by Rab35 and its GTPase-activating proteins TBC1D10A–C. *Journal of Cell Biology*, 189(2), 223-232.

Hsu, N. Y., Ilnytska, O., Belov, G., Santiana, M., Chen, Y. H., Takvorian, P. M., Pau, C., van der Schaar, H., Kaushik-Basu, N., Balla, T., Cameron, C. E., Ehrenfeld, E., van Kuppeveld, F. J. & Altan-Bonnet, N. (2010b) Viral reorganization of the secretory pathway generates distinct organelles for RNA replication. *Cell*, 141(5), 799-811.

Huang, B., Firth, C., Watterson, D., Allcock, R., Colmant, A. M., Hobson-Peters, J., Kirkland, P., Hewitson, G., McMahon, J., Hall-Mendelin, S., van den Hurk, A. F. & Warrilow, D. (2016) Genetic Characterization of Archived Bunyaviruses and their Potential for Emergence in Australia. *Emerg Infect Dis*, 22(5), 833-40.

Hughes, H. R., Adkins, S., Alkhovskiy, S., Beer, M., Blair, C., Calisher, C. H., Drebot, M., Lambert, A. J., de Souza, W. M., Marklewitz, M., Nunes, M. R. T., Shí 石晓宏, X. & Ictv Report, C. (2020) ICTV Virus Taxonomy Profile: Peribunyaviridae. *J Gen Virol*, 101(1), 1-2.

Hukkanen, V., Mikola, H., Nykänen, M. & Syrjänen, S. (1999) Herpes simplex virus type 1 infection has two separate modes of spread in three-dimensional keratinocyte culture. *J Gen Virol*, 80 (Pt 8), 2149-2155.

Hurley, J. H. (2008) ESCRT complexes and the biogenesis of multivesicular bodies. *Current Opinion in Cell Biology*, 20(1), 4-11.

Hurley, J. H. (2015) ESCRTs are everywhere. *The EMBO Journal*, 34(19), 2398-2407.

Inoue, J., Krueger, E. W., Chen, J., Cao, H., Ninomiya, M. & McNiven, M. A. (2015) HBV secretion is regulated through the activation of endocytic and autophagic compartments mediated by Rab7 stimulation. *J Cell Sci*, 128(9), 1696-706.

Ipinmoroti, A. O. & Matthews, Q. L. (2020) Extracellular Vesicles: Roles in Human Viral Infections, Immune-Diagnostic, and Therapeutic Applications. *Pathogens*, 9(12).

Israr, M., Mitchell, D., Alam, S., Dinello, D., Kishel, J. J. & Meyers, C. (2010) Effect of the HIV protease inhibitor amprenavir on the growth and differentiation of primary gingival epithelium. *Antivir Ther*, 15(2), 253-65.

Israr, M., Mitchell, D., Alam, S., Dinello, D., Kishel, J. J. & Meyers, C. (2011) The HIV protease inhibitor lopinavir/ritonavir (Kaletra) alters the growth, differentiation and proliferation of primary gingival epithelium. *HIV Med*, 12(3), 145-56.

Jang, J.-W., Song, Y., Kim, K. M., Kim, J.-S., Choi, E. K., Kim, J. & Seo, H. (2016) Hepatocellular carcinoma-targeted drug discovery through image-based phenotypic screening in co-cultures of HCC cells with hepatocytes. *BMC Cancer*, 16(1), 810.

Jankovičová, J., Sečová, P., Michalková, K. & Antalíková, J. (2020) Tetraspanins, More than Markers of Extracellular Vesicles in Reproduction. *Int J Mol Sci*, 21(20).

Javed, F. & Manzoor, S. (2018) HCV non-structural NS4A protein of genotype 3a induces mitochondria mediated death by activating Bax and the caspase cascade. *Microbial Pathogenesis*, 124, 346-355.

Jiang, X. L., Zhang, S., Jiang, M., Bi, Z. Q., Liang, M. F., Ding, S. J., Wang, S. W., Liu, J. Y., Zhou, S. Q., Zhang, X. M., Li, D. X. & Xu, A. Q. (2015) A cluster of person-to-person transmission cases caused by SFTS virus in Penglai, China. *Clinical Microbiology and Infection*, 21(3), 274-279.

Johnstone, R. M., Adam, M., Hammond, J. R., Orr, L. & Turbide, C. (1987) Vesicle formation during reticulocyte maturation. Association of plasma membrane activities with released vesicles (exosomes). *J Biol Chem*, 262(19), 9412-20.

Jones, K. H. & Senft, J. A. (1985) An improved method to determine cell viability by simultaneous staining with fluorescein diacetate-propidium iodide. *J Histochem Cytochem*, 33(1), 77-9.

Kaja, S., Payne, A. J., Naumchuk, Y. & Koulen, P. (2017) Quantification of Lactate Dehydrogenase for Cell Viability Testing Using Cell Lines and Primary Cultured Astrocytes. *Curr Protoc Toxicol*, 72, 2.26.1-2.26.10.

Kakarla, R., Hur, J., Kim, Y. J., Kim, J. & Chwae, Y. J. (2020) Apoptotic cell-derived exosomes: messages from dying cells. *Exp Mol Med*, 52(1), 1-6.

Kalluri, R. & LeBleu, V. S. (2020) The biology, function, and biomedical applications of exosomes. *Science*, 367(6478), eaau6977.

Kanwar, S. S., Dunlay, C. J., Simeone, D. M. & Nagrath, S. (2014) Microfluidic device (ExoChip) for on-chip isolation, quantification and characterization of circulating exosomes. *Lab on a Chip*, 14(11), 1891-1900.

Kapałczyńska, M., Kolenda, T., Przybyła, W., Zajączkowska, M., Teresiak, A., Filas, V., Ibbs, M., Bliźniak, R., Łuczewski, Ł. & Lamperska, K. (2018) 2D and 3D cell cultures - a comparison of different types of cancer cell cultures. *Arch Med Sci*, 14(4), 910-919.

Kasai, F., Hirayama, N., Ozawa, M., Iemura, M. & Kohara, A. (2016) Changes of heterogeneous cell populations in the Ishikawa cell line during long-term culture: Proposal for an in vitro clonal evolution model of tumor cells. *Genomics*, 107(6), 259-66.

Kascsak, R. J. & Lyons, M. J. (1978) Bunyamwera virus II. The generation and nature of defective interfering particles. *Virology*, 89(2), 539-546.

Kaur, G. & Dufour, J. M. (2012) Cell lines: Valuable tools or useless artifacts. *Spermatogenesis*, 2(1), 1-5.

Kerviel, A., Zhang, M. & Altan-Bonnet, N. (2021) A New Infectious Unit: Extracellular Vesicles Carrying Virus Populations. *Annual Review of Cell and Developmental Biology*, 37(1), 171-197.

Khawar, I. A., Park, J. K., Jung, E. S., Lee, M. A., Chang, S. & Kuh, H.-J. (2018) Three Dimensional Mixed-Cell Spheroids Mimic Stroma-Mediated Chemoresistance and Invasive Migration in hepatocellular carcinoma. *Neoplasia*, 20(8), 800-812.

Kielian, M. & Rey, F. A. (2006) Virus membrane-fusion proteins: more than one way to make a hairpin. *Nat Rev Microbiol*, 4(1), 67-76.

Kim, S. J., Khan, M., Quan, J., Till, A., Subramani, S. & Siddiqui, A. (2013) Hepatitis B virus disrupts mitochondrial dynamics: induces fission and mitophagy to attenuate apoptosis. *PLoS Pathog*, 9(12), e1003722.

Kim, W. Y., Choi, W., Park, S.-W., Wang, E. B., Lee, W.-J., Jee, Y., Lim, K. S., Lee, H.-J., Kim, S.-M., Lee, S.-O., Choi, S.-H., Kim, Y. S., Woo, J. H. & Kim, S.-H. (2015) Nosocomial Transmission of Severe Fever With Thrombocytopenia Syndrome in Korea. *Clinical Infectious Diseases*, 60(11), 1681-1683.

Klaus, J. P., Eisenhauer, P., Russo, J., Mason, A. B., Do, D., King, B., Taatjes, D., Cornillez-Ty, C., Boyson, J. E. & Thali, M. (2013) The intracellular cargo receptor ERGIC-53 is required for the

production of infectious arenavirus, coronavirus, and filovirus particles. *Cell host & microbe*, 14(5), 522-534.

Kohl, A., Clayton, R. F., Weber, F., Bridgen, A., Randall, R. E. & Elliott, R. M. (2003) Bunyamwera virus nonstructural protein NSs counteracts interferon regulatory factor 3-mediated induction of early cell death. *J Virol*, 77(14), 7999-8008.

Kohl, A., Dunn, E., Lowen, A. & Elliott, R. (2004) Complementarity, sequence and structural elements within the 3' and 5' non-coding regions of the Bunyamwera orthobunyavirus S segment determine promoter strength. *The Journal of general virology*, 85, 3269-78.

Koles, K., Nunnari, J., Korkut, C., Barria, R., Brewer, C., Li, Y., Leszyk, J., Zhang, B. & Budnik, V. (2012) Mechanism of evenness interrupted (Evi)-exosome release at synaptic boutons. *J Biol Chem*, 287(20), 16820-34.

Kowal, E. J. K., Ter-Ovanesyan, D., Regev, A. & Church, G. M. (2017) Extracellular Vesicle Isolation and Analysis by Western Blotting. *Methods Mol Biol*, 1660, 143-152.

Kowal, J., Arras, G., Colombo, M., Jouve, M., Morath, J. P., Primdal-Bengtson, B., Dingli, F., Loew, D., Tkach, M. & Théry, C. (2016) Proteomic comparison defines novel markers to characterize heterogeneous populations of extracellular vesicle subtypes. *Proceedings of the National Academy of Sciences*, 113(8), E968-E977.

Kumar, P., Nagarajan, A. & Uchil, P. D. (2018) Analysis of Cell Viability by the Lactate Dehydrogenase Assay. *Cold Spring Harb Protoc*, 2018(6).

Laemmli, U. K. (1970) Cleavage of structural proteins during the assembly of the head of bacteriophage T4. *Nature*, 227(5259), 680-5.

Lai, T.-Y., Cao, J., Ou-Yang, P., Tsai, C.-Y., Lin, C.-W., Chen, C.-C., Tsai, M.-K. & Lee, C.-Y. (2022) Different methods of detaching adherent cells and their effects on the cell surface expression of Fas receptor and Fas ligand. *Scientific Reports*, 12(1), 5713.

Langhans, S. A. (2018) Three-Dimensional in Vitro Cell Culture Models in Drug Discovery and Drug Repositioning. *Front Pharmacol*, 9, 6.

Larios, J., Mercier, V., Roux, A. & Gruenberg, J. (2020) ALIX- and ESCRT-III–dependent sorting of tetraspanins to exosomes. *Journal of Cell Biology*, 219(3).

Lawko, N., Plaskasovitis, C., Stokes, C., Abelseth, L., Fraser, I., Sharma, R., Kirsch, R., Hasan, M., Abelseth, E. & Willerth, S. M. (2021) 3D tissue models as an effective tool for studying viruses and vaccine development. *Frontiers in Materials*, 8, 80.

Le May, N., Dubaele, S., De Santis, L. P., Billecocq, A., Bouloy, M. & Egly, J.-M. (2004) TFIIH Transcription Factor, a Target for the Rift Valley Hemorrhagic Fever Virus. *Cell*, 116(4), 541-550.

Le May, N., Mansuroglu, Z., Léger, P., Josse, T., Blot, G., Billecocq, A., Flick, R., Jacob, Y., Bonnefoy, E. & Bouloy, M. (2008) A SAP30 complex inhibits IFN-beta expression in Rift Valley fever virus infected cells. *PLoS pathogens*, 4(1), e13-e13.

Lee, H. W., Lee, P. W. & Johnson, K. M. (1978) Isolation of the etiologic agent of Korean Hemorrhagic fever. *J Infect Dis*, 137(3), 298-308.

Lee, Y. B., Kim, E. M., Byun, H., Chang, H. K., Jeong, K., Aman, Z. M., Choi, Y. S., Park, J. & Shin, H. (2018) Engineering spheroids potentiating cell-cell and cell-ECM interactions by self-assembly of stem cell microlayer. *Biomaterials*, 165, 105-120.

Léonard, V. H., Kohl, A., Hart, T. J. & Elliott, R. M. (2006) Interaction of Bunyamwera Orthobunyavirus NSs protein with mediator protein MED8: a mechanism for inhibiting the interferon response. *J Virol*, 80(19), 9667-75.

Li, M., Liao, L. & Tian, W. (2020) Extracellular Vesicles Derived From Apoptotic Cells: An Essential Link Between Death and Regeneration. *Front Cell Dev Biol*, 8, 573511.

Li, Z. & Cui, Z. (2014) Three-dimensional perfused cell culture. *Biotechnol Adv*, 32(2), 243-54.

Lievaart-Peterson, K., Luttikholt, S., Van den Brom, R. & Vellema, P. (2012) Schmallenberg virus infection in small ruminants–First review of the situation and prospects in Northern Europe. *Small ruminant research*, 106(2-3), 71-76.

Lin, C.-H., Chao, C.-H. & Lan, C.-W. (2007) Low azeotropic solvent for bonding of PMMA microfluidic devices. *Sensors and Actuators B: Chemical*, 121, 698-705.

Lippincott-Schwartz, J., Yuan, L. C., Bonifacino, J. S. & Klausner, R. D. (1989) Rapid redistribution of Golgi proteins into the ER in cells treated with brefeldin A: evidence for membrane cycling from Golgi to ER. *Cell*, 56(5), 801-13.

Liu, S., Chen, R. & Hagedorn, C. H. (2014) Direct visualization of hepatitis C virus-infected Huh7.5 cells with a high titre of infectious chimeric JFH1-EGFP reporter virus in three-dimensional Matrigel cell cultures. *J Gen Virol*, 95(Pt 2), 423-433.

Livshits, M. A., Khomyakova, E., Evtushenko, E. G., Lazarev, V. N., Kulemin, N. A., Semina, S. E., Generozov, E. V. & Govorun, V. M. (2015) Isolation of exosomes by differential centrifugation: Theoretical analysis of a commonly used protocol. *Scientific Reports*, 5(1), 17319.

Longatti, A. (2015) The Dual Role of Exosomes in Hepatitis A and C Virus Transmission and Viral Immune Activation. *Viruses*, 7(12), 6707-15.

Longatti, A., Boyd, B. & Chisari, F. V. (2015) Virion-independent transfer of replication-competent hepatitis C virus RNA between permissive cells. *J Virol*, 89(5), 2956-61.

Lotvall, J., Hill, A., Hochberg, F., Buzas, w. E., Di Vizio, D., Gardiner, C., Gho, Y., Kurochkin, I., Mathivanan, S. & Quesenberry, P. (2014) Minimal experimental requirements for definition of extracellular vesicles and their functions: a position statement from the International Society for Extracellular Vesicles. *J Extracell Vesicles*, 3(26913), 10.3402.

Lozach, P.-Y., Mancini, R., Bitto, D., Meier, R., Oestereich, L., Overby, A. K., Pettersson, R. F. & Helenius, A. (2010a) Entry of bunyaviruses into mammalian cells. *Cell host & microbe*, 7(6), 488-499.

Lozach, P. Y., Kühbacher, A., Meier, R., Mancini, R., Bitto, D., Bouloy, M. & Helenius, A. (2011) DC-SIGN as a receptor for phleboviruses. *Cell Host Microbe*, 10(1), 75-88.

Lozach, P. Y., Mancini, R., Bitto, D., Meier, R., Oestereich, L., Overby, A. K., Pettersson, R. F. & Helenius, A. (2010b) Entry of bunyaviruses into mammalian cells. *Cell Host Microbe*, 7(6), 488-99.

Madison, M. N., Jones, P. H. & Okeoma, C. M. (2015) Exosomes in human semen restrict HIV-1 transmission by vaginal cells and block intravaginal replication of LP-BM5 murine AIDS virus complex. *Virology*, 482, 189-201.

Mages, J., Freimüller, K., Lang, R., Hatzopoulos, A. K., Guggemoos, S., Koszinowski, U. H. & Adler, H. (2008) Proteins of the secretory pathway govern virus productivity during lytic gammaherpesvirus infection. *J Cell Mol Med*, 12(5b), 1974-89.

Maltezou, H. C. & Papa, A. (2010) Crimean–Congo hemorrhagic fever: Risk for emergence of new endemic foci in Europe? *Travel Medicine and Infectious Disease*, 8(3), 139-143.

Martin, F., Roth, D. M., Jans, D. A., Pouton, C. W., Partridge, L. J., Monk, P. N. & Moseley, G. W. (2005) Tetraspanins in Viral Infections: a Fundamental Role in Viral Biology? *Journal of Virology*, 79(17), 10839-10851.

Martin, Y. & Vermette, P. (2005) Bioreactors for tissue mass culture: design, characterization, and recent advances. *Biomaterials*, 26(35), 7481-503.

Mashouri, L., Yousefi, H., Aref, A. R., Ahadi, A. m., Molaei, F. & Alahari, S. K. (2019) Exosomes: composition, biogenesis, and mechanisms in cancer metastasis and drug resistance. *Molecular Cancer*, 18(1), 75.

Mastrodomenico, V., Esin, J. J., Graham, M. L., Tate, P. M., Hawkins, G. M., Sandler, Z. J., Rademacher, D. J., Kicmal, T. M., Dial, C. N. & Mounce, B. C. (2019) Polyamine Depletion Inhibits Bunyavirus Infection via Generation of Noninfectious Interfering Virions. *Journal of Virology*, 93(14), e00530-19.

Mastrodomenico, V., Esin, J. J., Qazi, S., Khomutov, M. A., Ivanov, A. V., Mukhopadhyay, S. & Mounce, B. C. (2020) Virion-Associated Polyamines Transmit with Bunyaviruses to Maintain Infectivity and Promote Entry. *ACS Infect Dis*, 6(9), 2490-2501.

Matsuoka, Y., Chen, S. Y. & Compans, R. W. (1994) A signal for Golgi retention in the bunyavirus G1 glycoprotein. *J Biol Chem*, 269(36), 22565-73.

McNamara, R. P. & Dittmer, D. P. (2020) Modern Techniques for the Isolation of Extracellular Vesicles and Viruses. *Journal of Neuroimmune Pharmacology*, 15(3), 459-472.

Mehand, M. S., Al-Shorbaji, F., Millett, P. & Murgue, B. (2018) The WHO R&D Blueprint: 2018 review of emerging infectious diseases requiring urgent research and development efforts. *Antiviral Res*, 159, 63-67.

Meng, B. & Lever, A. M. L. (2021) The Interplay between ESCRT and Viral Factors in the Enveloped Virus Life Cycle. *Viruses*, 13(2).

Meyers, C. (1996) Organotypic (raft) epithelial tissue culture system for the differentiation-dependent replication of papillomavirus. *Methods in Cell Science*, 18(3), 201-210.

Meyers, C., Andreansky, S. S. & Courtney, R. J. (2003) Replication and interaction of herpes simplex virus and human papillomavirus in differentiating host epithelial tissue. *Virology*, 315(1), 43-55.

Miller, A. J. & Spence, J. R. (2017) In Vitro Models to Study Human Lung Development, Disease and Homeostasis. *Physiology (Bethesda)*, 32(3), 246-260.

Mo, Q., Xu, Z., Deng, F., Wang, H. & Ning, Y. J. (2020) Host restriction of emerging high-pathogenic bunyaviruses via MOV10 by targeting viral nucleoprotein and blocking ribonucleoprotein assembly. *PLoS Pathog*, 16(12), e1009129.

Momen-Heravi, F., Balaj, L., Alian, S., Mantel, P.-Y., Halleck, A. E., Trachtenberg, A. J., Soria, C. E., Oquin, S., Bonebreak, C. M., Saracoglu, E., Skog, J. & Kuo, W. P. (2013) Current methods for the isolation of extracellular vesicles. *Biological Chemistry*, 394(10), 1253-1262.

Monteil, V., Kwon, H., Prado, P., Hagelkrüys, A., Wimmer, R. A., Stahl, M., Leopoldi, A., Garreta, E., Hurtado del Pozo, C., Prosper, F., Romero, J. P., Wirnsberger, G., Zhang, H., Slutsky, A. S., Conder, R., Montserrat, N., Mirazimi, A. & Penninger, J. M. (2020) Inhibition of SARS-CoV-2 Infections in Engineered Human Tissues Using Clinical-Grade Soluble Human ACE2. *Cell*, 181(4), 905-913.e7.

Morales-Kastresana, A., Musich, T. A., Welsh, J. A., Telford, W., Demberg, T., Wood, J. C. S., Bigos, M., Ross, C. D., Kachynski, A., Dean, A., Felton, E. J., Van Dyke, J., Tigges, J., Toxavidis, V., Parks, D. R., Overton, W. R., Kesarwala, A. H., Freeman, G. J., Rosner, A., Perfetto, S. P., Pasquet, L., Terabe, M., McKinnon, K., Kapoor, V., Trepel, J. B., Puri, A., Kobayashi, H., Yung, B., Chen, X., Guion, P., Choyke, P., Knox, S. J., Ghiran, I., Robert-Guroff, M., Berzofsky, J. A. & Jones, J. C. (2019) High-fidelity detection and sorting of nanoscale vesicles in viral disease and cancer. *J Extracell Vesicles*, 8(1), 1597603.

Morzunov, S. P., Feldmann, H., Spiropoulou, C. F., Semenova, V. A., Rollin, P. E., Ksiazek, T. G., Peters, C. J. & Nichol, S. T. (1995) A newly recognized virus associated with a fatal case of hantavirus pulmonary syndrome in Louisiana. *J Virol*, 69(3), 1980-3.

Muinao, T., Pal, M. & Boruah, H. P. D. (2018) Cytosolic and Transmembrane Protein Extraction Methods of Breast and Ovarian Cancer Cells: A Comparative Study. *J Biomol Tech*, 29(3), 71-78.

Mullard, A. (2018) Can you trust your cancer cell lines? *Nature Reviews Drug Discovery*, 17(9), 613-613.

Murakami, K., Ishii, K., Ishihara, Y., Yoshizaki, S., Tanaka, K., Gotoh, Y., Aizaki, H., Kohara, M., Yoshioka, H., Mori, Y., Manabe, N., Shoji, I., Sata, T., Bartenschlager, R., Matsuura, Y., Miyamura, T. & Suzuki, T. (2006) Production of infectious hepatitis C virus particles in three-dimensional cultures of the cell line carrying the genome-length dicistronic viral RNA of genotype 1b. *Virology*, 351(2), 381-392.

Murakami, S., Takenaka-Uema, A., Kobayashi, T., Kato, K., Shimojima, M., Palmarini, M. & Horimoto, T. (2017) Heparan Sulfate Proteoglycan Is an Important Attachment Factor for Cell Entry of Akabane and Schmallenberg Viruses. *Journal of virology*, 91(15), e00503-17.

Nakabayashi, H., Taketa, K., Miyano, K., Yamane, T. & Sato, J. (1982) Growth of Human Hepatoma Cell Lines with Differentiated Functions in Chemically Defined Medium. *Cancer Research*, 42(9), 3858-3863.

Newton Susan, E., Short Nicholas, J. & Dalgarno, L. (1981) Bunyamwera Virus Replication in Cultured Aedes albopictus (Mosquito) Cells: Establishment of a Persistent Viral Infection. *Journal of Virology*, 38(3), 1015-1024.

Nichol, S. T., Spiropoulou, C. F., Morzunov, S., Rollin, P. E., Ksiazek, T. G., Feldmann, H., Sanchez, A., Childs, J., Zaki, S. & Peters, C. J. (1993) Genetic identification of a hantavirus associated with an outbreak of acute respiratory illness. *Science*, 262(5135), 914-7.

Ninomiya, M., Inoue, J., Krueger, E. W., Chen, J., Cao, H., Masamune, A. & McNiven, M. A. (2021) The Exosome‐Associated Tetraspanin CD63 Contributes to the Efficient Assembly and Infectivity of the Hepatitis B Virus. *Hepatology communications*, 5(7), 1238-1251.

Nolte-'t Hoen, E., Cremer, T., Gallo, R. C. & Margolis, L. B. (2016) Extracellular vesicles and viruses: Are they close relatives? *Proceedings of the National Academy of Sciences*, 113(33), 9155-9161.

Novoa Reyes, R., Calderita, G., Cabezas, P., Elliott Richard, M. & Risco, C. (2005) Key Golgi Factors for Structural and Functional Maturation of Bunyamwera Virus. *Journal of Virology*, 79(17), 10852-10863.

Noya, F., Balagué, C., Banerjee, N. S., Curiel, D. T., Broker, T. R. & Chow, L. T. (2003) Activation of adenovirus early promoters and lytic phase in differentiated strata of organotypic cultures of human keratinocytes. *J Virol*, 77(11), 6533-40.

Osellame, L. D., Blacker, T. S. & Duchen, M. R. (2012) Cellular and molecular mechanisms of mitochondrial function. *Best Practice & Research Clinical Endocrinology & Metabolism*, 26(6), 711-723.

Osterman, A., Stellberger, T., Gebhardt, A., Kurz, M., Friedel, C. C., Uetz, P., Nitschko, H., Baiker, A. & Vizoso-Pinto, M. G. (2015) The Hepatitis E virus intraviral interactome. *Sci Rep*, 5, 13872.

Ostrowski, M., Carmo, N. B., Krumeich, S., Fanget, I., Raposo, G., Savina, A., Moita, C. F., Schauer, K., Hume, A. N., Freitas, R. P., Goud, B., Benaroch, P., Hacohen, N., Fukuda, M., Desnos, C., Seabra, M. C., Darchen, F., Amigorena, S., Moita, L. F. & Thery, C. (2010) Rab27a and Rab27b control different steps of the exosome secretion pathway. *Nature Cell Biology*, 12(1), 19-30.

Överby, A. K., Pettersson, R. F., Grünewald, K. & Huiskonen, J. T. (2008) Insights into bunyavirus architecture from electron cryotomography of Uukuniemi virus. *Proceedings of the National Academy of Sciences*, 105(7), 2375-2379.

Owczarczyk, A. B., Schaller, M. A., Reed, M., Rasky, A. J., Lombard, D. B. & Lukacs, N. W. (2015) Sirtuin 1 Regulates Dendritic Cell Activation and Autophagy during Respiratory Syncytial Virus-Induced Immune Responses. *J Immunol*, 195(4), 1637-46.

Park, S. J., Kim, J. M., Kim, J., Hur, J., Park, S., Kim, K., Shin, H.-J. & Chwae, Y.-J. (2018) Molecular mechanisms of biogenesis of apoptotic exosome-like vesicles and their roles as damage-associated molecular patterns. *Proceedings of the National Academy of Sciences*, 115(50), E11721-E11730.

Pastula, D. M., Hoang Johnson, D. K., White, J. L., Dupuis, A. P., 2nd, Fischer, M. & Staples, J. E. (2015) Jamestown Canyon Virus Disease in the United States-2000-2013. *The American journal of tropical medicine and hygiene*, 93(2), 384-389.

Patel, A. H. & Elliott, R. M. (1992) Characterization of Bunyamwera virus defective interfering particles. *J Gen Virol*, 73 (Pt 2), 389-96.

Patterson, J. L., Holloway, B. & Kolakofsky, D. (1984) La Crosse virions contain a primer-stimulated RNA polymerase and a methylated cap-dependent endonuclease. *J Virol*, 52(1), 215-22.

Peperkamp, N. H., Luttikholt, S. J., Dijkman, R., Vos, J. H., Junker, K., Greijdanus, S., Roumen, M. P., van Garderen, E., Meertens, N., van Maanen, C., Lievaart, K., van Wuyckhuise, L. & Wouda, W. (2014) Ovine and Bovine Congenital Abnormalities Associated With Intrauterine Infection With Schmallenberg Virus. *Veterinary Pathology*, 52(6), 1057-1066.

Perez-Hernandez, D., Gutiérrez-Vázquez, C., Jorge, I., López-Martín, S., Ursa, A., Sánchez-Madrid, F., Vázquez, J. & Yáñez-Mó, M. (2013) The intracellular interactome of tetraspanin-enriched microdomains reveals their function as sorting machineries toward exosomes. *J Biol Chem*, 288(17), 11649-61.

Perez Vidakovics, M. L. A., Ure, A. E., Arrías, P. N., Romanowski, V. & Gómez, R. M. (2019) Junín virus induces autophagy in human A549 cells. *PLoS One*, 14(6), e0218730.

Pileri, P., Uematsu, Y., Campagnoli, S., Galli, G., Falugi, F., Petracca, R., Weiner, A. J., Houghton, M., Rosa, D. & Grandi, G. (1998) Binding of hepatitis C virus to CD81. *Science*, 282(5390), 938-941.

Pinto, B., Henriques, A. C., Silva, P. M. A. & Bousbaa, H. (2020) Three-Dimensional Spheroids as In Vitro Preclinical Models for Cancer Research. *Pharmaceutics*, 12(12).

Pols, M. S. & Klumperman, J. (2009) Trafficking and function of the tetraspanin CD63. *Experimental Cell Research*, 315(9), 1584-1592.

Popowski, K. D., Dinh, P. U. C., George, A., Lutz, H. & Cheng, K. (2021) Exosome therapeutics for COVID‐19 and respiratory viruses. *View*, 2(3), 20200186.

Qin, Z.-l., Ju, H.-p., Liu, Y., Gao, T.-t., Wang, W.-b., Aurelian, L., Zhao, P. & Qi, Z.-t. (2013) Fetal bovine serum inhibits hepatitis C virus attachment to host cells. *Journal of Virological Methods*, 193(2), 261-269.

R. Daubney, J. R. H., P. C. Garnham (1931) Enzootic hepatitis or rift valley fever. An undescribed virus disease of sheep cattle and man from east africa. *The Journal of Pathology and Bacteriology*, 34(4), 545-579.

Rajalakshmy, A. R., Malathi, J., Madhavan, H. N. & Samuel, J. K. (2015) Mebiolgel, a thermoreversible polymer as a scaffold for three dimensional culture of Huh7 cell line with improved hepatocyte differentiation marker expression and HCV replication. *Indian J Med Microbiol*, 33(4), 554-9.

Ramakrishnaiah, V., Thumann, C., Fofana, I., Habersetzer, F., Pan, Q., de Ruiter, P. E., Willemsen, R., Demmers, J. A., Stalin Raj, V., Jenster, G., Kwekkeboom, J., Tilanus, H. W., Haagmans, B. L., Baumert, T. F. & van der Laan, L. J. (2013) Exosome-mediated transmission of hepatitis C virus between human hepatoma Huh7.5 cells. *Proc Natl Acad Sci U S A*, 110(32), 13109-13.

Raposo, G. & Stoorvogel, W. (2013) Extracellular vesicles: Exosomes, microvesicles, and friends. *Journal of Cell Biology*, 200(4), 373-383.

Reguera, J., Weber, F. & Cusack, S. (2010) Bunyaviridae RNA polymerases (L-protein) have an N-terminal, influenza-like endonuclease domain, essential for viral cap-dependent transcription. *PLoS Pathog*, 6(9), e1001101.

Ren, Z., Zhang, X., Ding, T., Zhong, Z., Hu, H., Xu, Z. & Deng, J. (2020) Mitochondrial Dynamics Imbalance: A Strategy for Promoting Viral Infection. *Front Microbiol*, 11, 1992.

Rodrigues, R., Paranhos-Baccalà, G., Vernet, G. & Peyrefitte, C. N. (2012) Crimean-Congo hemorrhagic fever virus-infected hepatocytes induce ER-stress and apoptosis crosstalk. *PLoS One*, 7(1), e29712.

Roulston, A., Marcellus, R. C. & Branton, P. E. (1999) Viruses and apoptosis. *Annu Rev Microbiol*, 53, 577-628.

Rowe, R. K., Suszko, J. W. & Pekosz, A. (2008) Roles for the recycling endosome, Rab8, and Rab11 in hantavirus release from epithelial cells. *Virology*, 382(2), 239-249.

Sainz, B., TenCate, V. & Uprichard, S. L. (2009) Three-dimensional Huh7 cell culture system for the study of Hepatitis C virus infection. *Virology Journal*, 6(1), 103.

Salahudeen, A. A., Choi, S. S., Rustagi, A., Zhu, J., van Unen, V., de la O, S. M., Flynn, R. A., Margalef-Català, M., Santos, A. J. M., Ju, J., Batish, A., Usui, T., Zheng, G. X. Y., Edwards, C. E., Wagar, L. E., Luca, V., Anchang, B., Nagendran, M., Nguyen, K., Hart, D. J., Terry, J. M., Belgrader, P., Ziraldo, S. B., Mikkelsen, T. S., Harbury, P. B., Glenn, J. S., Garcia, K. C., Davis, M. M., Baric, R. S., Sabatti, C., Amieva, M. R., Blish, C. A., Desai, T. J. & Kuo, C. J. (2020) Progenitor identification and SARS-CoV-2 infection in human distal lung organoids. *Nature*, 588(7839), 670-675.

Salanueva, I. J., Novoa, R. R., Cabezas, P., López-Iglesias, C., Carrascosa, J. L., Elliott, R. M. & Risco, C. (2003) Polymorphism and structural maturation of bunyamwera virus in Golgi and post-Golgi compartments. *Journal of virology*, 77(2), 1368-1381.

Saleh, F., Harb, A., Soudani, N. & Zaraket, H. (2020) A three-dimensional A549 cell culture model to study respiratory syncytial virus infections. *Journal of Infection and Public Health*, 13(8), 1142-1147.

Santos, R. I., Rodrigues, A. H., Silva, M. L., Mortara, R. A., Rossi, M. A., Jamur, M. C., Oliver, C. & Arruda, E. (2008) Oropouche virus entry into HeLa cells involves clathrin and requires endosomal acidification. *Virus Res*, 138(1-2), 139-43.

Sanz-Sánchez, L. & Risco, C. (2013) Multilamellar structures and filament bundles are found on the cell surface during bunyavirus egress. *PLoS One*, 8(6), e65526.

Satsuka, A., Yoshida, S., Kajitani, N., Nakamura, H. & Sakai, H. (2010) Novel human papillomavirus type 18 replicon and its application in screening the antiviral effects of cytokines. *Cancer Sci*, 101(2), 536-42.

Schmaljohn, C. S., Hasty, S. E., Harrison, S. A. & Dalrymple, J. M. (1983) Characterization of Hantaan virions, the prototype virus of hemorrhagic fever with renal syndrome. *J Infect Dis*, 148(6), 1005-12.

Schöneberg, J., Lee, I.-H., Iwasa, J. H. & Hurley, J. H. (2017) Reverse-topology membrane scission by the ESCRT proteins. *Nature Reviews Molecular Cell Biology*, 18(1), 5-17.

Sciaky, N., Presley, J., Smith, C., Zaal, K. J. M., Cole, N., Moreira, J. E., Terasaki, M., Siggia, E. & Lippincott-Schwartz, J. (1997) Golgi Tubule Traffic and the Effects of Brefeldin A Visualized in Living Cells. *Journal of Cell Biology*, 139(5), 1137-1155.

Sedda, L. & Rogers, D. J. (2013) The influence of the wind in the Schmallenberg virus outbreak in Europe. *Sci Rep*, 3, 3361.

Sennett, C. (2019) *Response of brain tumour spheroids to therapeutic agents in a microfluidic environment.* MSc (by Research) Biomedical Science Thesis. University of Hull, December 2019.

Sharma, P., Ludwig, S., Muller, L., Hong, C. S., Kirkwood, J. M., Ferrone, S. & Whiteside, T. L. (2018) Immunoaffinity-based isolation of melanoma cell-derived exosomes from plasma of patients with melanoma. *J Extracell Vesicles*, 7(1), 1435138.

Shelke, G. V., Lässer, C., Gho, Y. S. & Lötvall, J. (2014) Importance of exosome depletion protocols to eliminate functional and RNA-containing extracellular vesicles from fetal bovine serum. *J Extracell Vesicles*, 3.

Shen, S., Duan, X., Wang, B., Zhu, L., Zhang, Y., Zhang, J., Wang, J., Luo, T., Kou, C., Liu, D., Lv, C., Zhang, L., Chang, C., Su, Z., Tang, S., Qiao, J., Moming, A., Wang, C., Abudurexiti, A., Wang, H., Hu, Z., Zhang, Y., Sun, S. & Deng, F. (2018) A novel tick-borne phlebovirus, closely related to severe fever with thrombocytopenia syndrome virus and Heartland virus, is a potential pathogen. *Emerging Microbes & Infections*, 7(1), 1-14.

Shi, X., Botting, C. H., Li, P., Niglas, M., Brennan, B., Shirran, S. L., Szemiel, A. M. & Elliott, R. M. (2016) Bunyamwera orthobunyavirus glycoprotein precursor is processed by cellular signal peptidase and signal peptide peptidase. *Proc Natl Acad Sci U S A*, 113(31), 8825-30.

Shi, X., Kohl, A., Léonard, V. H., Li, P., McLees, A. & Elliott, R. M. (2006) Requirement of the N-terminal region of orthobunyavirus nonstructural protein NSm for virus assembly and morphogenesis. *J Virol*, 80(16), 8089-99.

Shi, X., Kohl, A., Li, P. & Elliott, R. M. (2007) Role of the cytoplasmic tail domains of Bunyamwera orthobunyavirus glycoproteins Gn and Gc in virus assembly and morphogenesis. *Journal of virology*, 81(18), 10151-10160.

Shi, X., Lappin, D. F. & Elliott, R. M. (2004) Mapping the Golgi targeting and retention signal of Bunyamwera virus glycoproteins. *Journal of virology*, 78(19), 10793-10802.

Shoham, T., Rajapaksa, R., Boucheix, C., Rubinstein, E., Poe, J. C., Tedder, T. F. & Levy, S. (2003) The Tetraspanin CD81 Regulates the Expression of CD19 During B Cell Development in a Postendoplasmic Reticulum Compartment 1. *The Journal of Immunology*, 171, 4062 - 4072.

Shoham, T., Rajapaksa, R., Kuo, C.-C., Haimovich, J. & Levy, S. (2006) Building of the Tetraspanin Web: Distinct Structural Domains of CD81 Function in Different Cellular Compartments. *Molecular and Cellular Biology*, 26(4), 1373-1385.

Silvas, J. A., Popov, V. L., Paulucci-Holthauzen, A. & Aguilar, P. V. (2015) Extracellular Vesicles Mediate Receptor-Independent Transmission of Novel Tick-Borne Bunyavirus. *Journal of virology*, 90(2), 873-886.

Silvas, J. A., Popov, V. L., Paulucci-Holthauzen, A. & Aguilar, P. V. (2016) Extracellular Vesicles Mediate Receptor-Independent Transmission of Novel Tick-Borne Bunyavirus. *J Virol*, 90(2), 873-86.

Simon, M., Johansson, C. & Mirazimi, A. (2009) Crimean-Congo hemorrhagic fever virus entry and replication is clathrin-, pH- and cholesterol-dependent. *J Gen Virol*, 90(Pt 1), 210-5.

Sirois, I., Groleau, J., Pallet, N., Brassard, N., Hamelin, K., Londono, I., Pshezhetsky, A. V., Bendayan, M. & Hébert, M.-J. (2012) Caspase activation regulates the extracellular export of autophagic vacuoles. *Autophagy*, 8(6), 927-937.

Sirois, I., Raymond, M., Brassard, N., Cailhier, J., Fedjaev, M., Hamelin, K., Londono, I., Bendayan, M., Pshezhetsky, A. & Hébert, M. (2011) Caspase-3-dependent export of TCTP: a novel pathway for antiapoptotic intercellular communication. *Cell Death & Differentiation*, 18(3), 549-562.

Skryabin, G. O., Komelkov, A. V., Savelyeva, E. E. & Tchevkina, E. M. (2020) Lipid Rafts in Exosome Biogenesis. *Biochemistry (Moscow)*, 85(2), 177-191.

Solà-Riera, C., García, M., Ljunggren, H. G. & Klingström, J. (2020) Hantavirus inhibits apoptosis by preventing mitochondrial membrane potential loss through up-regulation of the pro-survival factor BCL-2. *PLoS Pathog*, 16(2), e1008297.

Soldan, S. S. & González-Scarano, F. (2005) Emerging infectious diseases: the Bunyaviridae. *J Neurovirol*, 11(5), 412-23.

Souza, G. R., Molina, J. R., Raphael, R. M., Ozawa, M. G., Stark, D. J., Levin, C. S., Bronk, L. F., Ananta, J. S., Mandelin, J., Georgescu, M. M., Bankson, J. A., Gelovani, J. G., Killian, T. C., Arap, W. & Pasqualini, R. (2010) Three-dimensional tissue culture based on magnetic cell levitation. *Nat Nanotechnol*, 5(4), 291-6.

Straub, T. M., Bartholomew, R. A., Valdez, C. O., Valentine, N. B., Dohnalkova, A., Ozanich, R. M., Bruckner-Lea, C. J. & Call, D. R. (2011) Human norovirus infection of caco-2 cells grown as a three-dimensional tissue structure. *J Water Health*, 9(2), 225-40.

Straub, T. M., Höner zu Bentrup, K., Orosz-Coghlan, P., Dohnalkova, A., Mayer, B. K., Bartholomew, R. A., Valdez, C. O., Bruckner-Lea, C. J., Gerba, C. P., Abbaszadegan, M. & Nickerson, C. A. (2007) In vitro cell culture infectivity assay for human noroviruses. *Emerg Infect Dis*, 13(3), 396-403.

Stuffers, S., Sem Wegner, C., Stenmark, H. & Brech, A. (2009) Multivesicular Endosome Biogenesis in the Absence of ESCRTs. *Traffic*, 10(7), 925-937.

Subedi, P., Schneider, M., Philipp, J., Azimzadeh, O., Metzger, F., Moertl, S., Atkinson, M. J. & Tapio, S. (2019) Comparison of methods to isolate proteins from extracellular vesicles for mass spectrometry-based proteomic analyses. *Analytical Biochemistry*, 584, 113390.

Suda, Y., Fukushi, S., Tani, H., Murakami, S., Saijo, M., Horimoto, T. & Shimojima, M. (2016) Analysis of the entry mechanism of Crimean-Congo hemorrhagic fever virus, using a vesicular stomatitis virus pseudotyping system. *Arch Virol*, 161(6), 1447-54.

Sun, Q., Jin, C., Zhu, L., Liang, M., Li, C., Cardona, C. J., Li, D. & Xing, Z. (2015) Host Responses and Regulation by NFκB Signaling in the Liver and Liver Epithelial Cells Infected with A Novel Tick-borne Bunyavirus. *Scientific Reports*, 5(1), 11816.

Szemiel, A. M., Failloux, A. B. & Elliott, R. M. (2012) Role of Bunyamwera Orthobunyavirus NSs protein in infection of mosquito cells. *PLoS Negl Trop Dis*, 6(9), e1823.

Tatum, L., Pacy, J., Frazier, K., Weege, J., Baldwin, C., Hullinger, G., Bossart, G. & Altman, N. (1999) Canine LaCrosse Viral Meningoencephalomyelitis with Possible Public Health Implications. *Journal of veterinary diagnostic investigation : official publication of the American Association of Veterinary Laboratory Diagnosticians, Inc*, 11, 184-8.

Théry, C., Amigorena, S., Raposo, G. & Clayton, A. (2006) Isolation and characterization of exosomes from cell culture supernatants and biological fluids. *Curr Protoc Cell Biol*, Chapter 3, Unit 3.22.

Théry, C., Regnault, A., Garin, J., Wolfers, J., Zitvogel, L., Ricciardi-Castagnoli, P., Raposo, G. & Amigorena, S. (1999) Molecular characterization of dendritic cell-derived exosomes: selective accumulation of the heat shock protein hsc73. *The Journal of cell biology*, 147(3), 599-610.

Théry, C., Witwer, K. W., Aikawa, E., Alcaraz, M. J., Anderson, J. D., Andriantsitohaina, R., Antoniou, A., Arab, T., Archer, F., Atkin-Smith, G. K., Ayre, D. C., Bach, J.-M., Bachurski, D., Baharvand, H., Balaj, L., Baldacchino, S., Bauer, N. N., Baxter, A. A., Bebawy, M., Beckham, C., Bedina Zavec, A., Benmoussa, A., Berardi, A. C., Bergese, P., Bielska, E., Blenkiron, C., Bobis-Wozowicz, S., Boilard, E., Boireau, W., Bongiovanni, A., Borràs, F. E., Bosch, S., Boulanger, C. M., Breakefield, X., Breglio, A. M., Brennan, M. Á., Brigstock, D. R., Brisson, A., Broekman, M. L. D., Bromberg, J. F., Bryl-Górecka, P., Buch, S., Buck, A. H., Burger, D., Busatto, S., Buschmann, D., Bussolati, B., Buzás, E. I., Byrd, J. B., Camussi, G., Carter, D. R. F., Caruso, S., Chamley, L. W., Chang, Y.-T., Chen, C., Chen, S., Cheng, L., Chin, A. R., Clayton, A., Clerici, S. P., Cocks, A., Cocucci, E., Coffey, R. J., Cordeiro-da-Silva, A., Couch, Y., Coumans, F. A. W., Coyle, B., Crescitelli, R., Criado, M. F., D'Souza-Schorey, C., Das, S., Datta Chaudhuri, A., de Candia, P., De Santana, E. F., De Wever, O., del Portillo, H. A., Demaret, T., Deville, S., Devitt, A., Dhondt, B., Di Vizio, D., Dieterich, L. C., Dolo, V., Dominguez Rubio, A. P., Dominici, M., Dourado, M. R., Driedonks, T. A. P., Duarte, F. V., Duncan, H. M., Eichenberger, R. M., Ekström, K., El Andaloussi, S., Elie-Caille, C., Erdbrügger, U., Falcón-Pérez, J. M., Fatima, F., Fish, J. E.,

Flores-Bellver, M., Försönits, A., Frelet-Barrand, A., et al (2018) Minimal information for studies of extracellular vesicles 2018 (MISEV2018): a position statement of the International Society for Extracellular Vesicles and update of the MISEV2014 guidelines. *Journal of Extracellular Vesicles*, 7(1), 1535750.

Thomas, D., Blakqori, G., Wagner, V., Banholzer, M., Kessler, N., Elliott, R. M., Haller, O. & Weber, F. (2004) Inhibition of RNA polymerase II phosphorylation by a viral interferon antagonist. *J Biol Chem*, 279(30), 31471-7.

Thomas, D. W., Burns, J., Audette, J., Carroll, A., Dow-Hygelund, C. & Hay, M. (2016) Clinical development success rates 2006–2015. *BIO Industry Analysis*, 1(16), 25.

Thompson, W. H., Kalfayan, B. & Anslow, R. O. (1965) ISOLATION OF CALIFORNIA ENCEPHALITIS GROUP VIRUS FROM A FATAL HUMAN ILLNESS1. *American Journal of Epidemiology*, 81(2), 245-253.

Trajkovic, K., Hsu, C., Chiantia, S., Rajendran, L., Wenzel, D., Wieland, F., Schwille, P., Brügger, B. & Simons, M. (2008) Ceramide Triggers Budding of Exosome Vesicles into Multivesicular Endosomes. *Science*, 319(5867), 1244-1247.

Tseng, H., Gage, J. A., Raphael, R. M., Moore, R. H., Killian, T. C., Grande-Allen, K. J. & Souza, G. R. (2013) Assembly of a three-dimensional multitype bronchiole coculture model using magnetic levitation. *Tissue Eng Part C Methods*, 19(9), 665-75.

van Dongen, H. M., Masoumi, N., Witwer, K. W. & Pegtel, D. M. (2016) Extracellular Vesicles Exploit Viral Entry Routes for Cargo Delivery. *Microbiol Mol Biol Rev*, 80(2), 369-86.

van Knippenberg, I., Carlton-Smith, C. & Elliott, R. M. (2010) The N-terminus of Bunyamwera orthobunyavirus NSs protein is essential for interferon antagonism. *J Gen Virol*, 91(Pt 8), 2002-2006.

van Niel, G., Charrin, S., Simoes, S., Romao, M., Rochin, L., Saftig, P., Marks, M. S., Rubinstein, E. & Raposo, G. (2011) The tetraspanin CD63 regulates ESCRT-independent and -dependent endosomal sorting during melanogenesis. *Dev Cell*, 21(4), 708-21.

van Niel, G., D'Angelo, G. & Raposo, G. (2018) Shedding light on the cell biology of extracellular vesicles. *Nature Reviews Molecular Cell Biology*, 19(4), 213-228.

van Niel, G., Charrin, S., Simoes, S., Romao, M., Rochin, L., Saftig, P., Marks, Michael S., Rubinstein, E. & Raposo, G. (2011) The Tetraspanin CD63 Regulates ESCRT-Independent and -Dependent Endosomal Sorting during Melanogenesis. *Developmental Cell*, 21(4), 708-721.

Varela, M., Piras, I. M., Mullan, C., Shi, X., Tilston-Lunel, N. L., Pinto, R. M., Taggart, A., Welch, S. R., Neil, S. J. D., Kreher, F., Elliott, R. M. & Palmarini, M. (2017) Sensitivity to BST-2 restriction correlates with Orthobunyavirus host range. *Virology*, 509, 121-130.

Verbruggen, P., Ruf, M., Blakqori, G., Överby, A. K., Heidemann, M., Eick, D. & Weber, F. (2011) Interferon antagonist NSs of La Crosse virus triggers a DNA damage response-like degradation of transcribing RNA polymerase II. *The Journal of biological chemistry*, 286(5), 3681-3692.

Villarroya-Beltri, C., Baixauli, F., Gutiérrez-Vázquez, C., Sánchez-Madrid, F. & Mittelbrunn, M. (2014) Sorting it out: Regulation of exosome loading. *Seminars in Cancer Biology*, 28, 3-13.

von Magnus, P. (1954) Incomplete Forms of Influenza Virus, in Smith, K. M. & Lauffer, M. A. (eds), *Advances in Virus Research*Academic Press, 59-79.

Votteler, J. & Sundquist, W. I. (2013) Virus budding and the ESCRT pathway. *Cell Host Microbe*, 14(3), 232-41.

Walter, C. T. & Barr, J. N. (2011) Recent advances in the molecular and cellular biology of bunyaviruses. *Journal of General Virology*, 92(11), 2467-2484.

Wang, K., Ma, H., Liu, H., Ye, W., Li, Z., Cheng, L., Zhang, L., Lei, Y., Shen, L. & Zhang, F. (2019) The Glycoprotein and Nucleocapsid Protein of Hantaviruses Manipulate Autophagy Flux to Restrain Host Innate Immune Responses. *Cell Rep*, 27(7), 2075-2091.e5.

Wang, N., Zhang, H., Zhang, B. Q., Liu, W., Zhang, Z., Qiao, M., Zhang, H., Deng, F., Wu, N., Chen, X., Wen, S., Zhang, J., Liao, Z., Zhang, Q., Yan, Z., Yin, L., Ye, J., Deng, Y., Luu, H. H., Haydon, R. C., Liang, H. & He, T. C. (2014) Adenovirus-mediated efficient gene transfer into cultured three-dimensional organoids. *PLoS One*, 9(4), e93608.

Weber, F., Bridgen, A., Fazakerley, J. K., Streitenfeld, H., Kessler, N., Randall, R. E. & Elliott, R. M. (2002) Bunyamwera bunyavirus nonstructural protein NSs counteracts the induction of alpha/beta interferon. *J Virol*, 76(16), 7949-55.

Whelan, S. P., Barr, J. N. & Wertz, G. W. (2004) Transcription and replication of nonsegmented negative-strand RNA viruses. *Curr Top Microbiol Immunol*, 283, 61-119.

WHO *Rift Valley Fever.* Available online: https://www.who.int/news-room/fact-sheets/detail/rift-valley-fever [Accessed 13/01/2022].

Wiley, R. D. & Gummuluru, S. (2006) Immature dendritic cell-derived exosomes can mediate HIV-1 trans infection. *Proc Natl Acad Sci U S A*, 103(3), 738-43.

Windhaber, S., Xin, Q. & Lozach, P.-Y. (2021) Orthobunyaviruses: From Virus Binding to Penetration into Mammalian Host Cells. *Viruses*, 13(5).

Witwer, K. W., Buzás, E. I., Bemis, L. T., Bora, A., Lässer, C., Lötvall, J., Nolte-'t Hoen, E. N., Piper, M. G., Sivaraman, S., Skog, J., Théry, C., Wauben, M. H. & Hochberg, F. (2013) Standardization of sample collection, isolation and analysis methods in extracellular vesicle research. *J Extracell Vesicles*, 2.

Yan, J. M., Zhang, W. K., Yan, L. N., Jiao, Y. J., Zhou, C. M. & Yu, X. J. (2022) Bunyavirus SFTSV exploits autophagic flux for viral assembly and egress. *Autophagy*, 18(7), 1599-1612.

Yáñez-Mó, M., Siljander, P. R., Andreu, Z., Zavec, A. B., Borràs, F. E., Buzas, E. I., Buzas, K., Casal, E., Cappello, F., Carvalho, J., Colás, E., Cordeiro-da Silva, A., Fais, S., Falcon-Perez, J. M., Ghobrial, I. M., Giebel, B., Gimona, M., Graner, M., Gursel, I., Gursel, M., Heegaard, N. H., Hendrix, A., Kierulf, P., Kokubun, K., Kosanovic, M., Kralj-Iglic, V., Krämer-Albers, E. M., Laitinen, S., Lässer, C., Lener, T., Ligeti, E., Linē, A., Lipps, G., Llorente, A., Lötvall, J., Manček-Keber, M., Marcilla, A., Mittelbrunn, M., Nazarenko, I., Nolte-'t Hoen, E. N., Nyman, T. A., O'Driscoll, L., Olivan, M., Oliveira, C., Pállinger, É., Del Portillo, H. A., Reventós, J., Rigau, M., Rohde, E., Sammar, M., Sánchez-Madrid, F., Santarém, N., Schallmoser, K., Ostenfeld, M. S., Stoorvogel, W., Stukelj, R., Van der Grein, S. G., Vasconcelos, M. H., Wauben, M. H. & De Wever, O. (2015) Biological properties of extracellular vesicles and their physiological functions. *J Extracell Vesicles*, 4, 27066.

Yang, X., Claas, C., Kraeft, S. K., Chen, L. B., Wang, Z., Kreidberg, J. A. & Hemler, M. E. (2002) Palmitoylation of tetraspanin proteins: modulation of CD151 lateral interactions, subcellular distribution, and integrin-dependent cell morphology. *Mol Biol Cell*, 13(3), 767-81.

Yang, Y., Lyu, T., Zhou, R., He, X., Ye, K., Xie, Q., Zhu, L., Chen, T., Shen, C., Wu, Q., Zhang, B. & Zhao, W. (2019) The Antiviral and Antitumor Effects of Defective Interfering Particles/Genomes and Their Mechanisms. *Front Microbiol*, 10, 1852.

Yin, Y., Chen, H., Wang, Y., Zhang, L. & Wang, X. (2021) Roles of extracellular vesicles in the aging microenvironment and age-related diseases. *J Extracell Vesicles*, 10(12), e12154.

Yoshida, T., Kawano, Y., Sato, K., Ando, Y., Aoki, J., Miura, Y., Komano, J., Tanaka, Y. & Koyanagi, Y. (2008) A CD63 mutant inhibits T-cell tropic human immunodeficiency virus type 1 entry by disrupting CXCR4 trafficking to the plasma membrane. *Traffic*, 9(4), 540-558.

Zhang, Y., Liu, Y., Liu, H. & Tang, W. H. (2019) Exosomes: biogenesis, biologic function and clinical potential. *Cell & Bioscience*, 9(1), 19.

Zou, F., Wang, X., Han, X., Rothschild, G., Zheng, S. G., Basu, U. & Sun, J. (2018) Expression and Function of Tetraspanins and Their Interacting Partners in B Cells. *Front Immunol*, 9, 1606.